



Durham E-Theses

Elemental and isotopic insights into fluid mobility accompanying the subduction of oceanic lithosphere

INGLIS, EDWARD,CHRISTOPHER

How to cite:

INGLIS, EDWARD,CHRISTOPHER (2018) *Elemental and isotopic insights into fluid mobility accompanying the subduction of oceanic lithosphere*, Durham theses, Durham University. Available at Durham E-Theses Online: <http://etheses.dur.ac.uk/12565/>

Use policy

The full-text may be used and/or reproduced, and given to third parties in any format or medium, without prior permission or charge, for personal research or study, educational, or not-for-profit purposes provided that:

- a full bibliographic reference is made to the original source
- a [link](#) is made to the metadata record in Durham E-Theses
- the full-text is not changed in any way

The full-text must not be sold in any format or medium without the formal permission of the copyright holders.

Please consult the [full Durham E-Theses policy](#) for further details.

**Elemental and isotopic insights into
fluid mobility accompanying the
subduction of oceanic lithosphere**

Edward Christopher Inglis

A thesis submitted in partial fulfilment of the requirements for the degree of:

Doctor of Philosophy

Durham University, UK

**Department of Earth Sciences
Durham University
October 2017**

Abstract

This study presents a detailed elemental and isotopic investigation of element mobility related to high-pressure, subduction related metamorphism of oceanic lithosphere. Particular respect is paid to the mobility of key redox mediating components (e.g. multivalent elements such as iron (Fe) and sulphur (S)). The overarching aim of this work is to elucidate the contributions of different subducting lithologies to the redox budget of the sub-arc mantle. Furthermore, a comprehensive petrological characterisation of different meta-mafic and meta-ultramafic lithologies is presented.

The primary geochemical tools utilised here are iron (Fe) and zinc (Zn) stable isotopes. Iron stable isotopes are sensitive to small losses of Fe and, as such, serve as excellent tracers of Fe mobility within a high-pressure subduction setting. In addition they are fractionated in the presence of S in the form of Fe-SO_{x(aqueous)} bearing complexes. Consequently Fe isotopes can be utilised to trace the mobility of oxidising S bearing fluids during subduction zone metamorphism and slab dehydration. Zinc stable isotopes are strongly fractionated by SO_x and CO_x bearing fluids, and have been utilised here to trace the mobility of S and/or C bearing fluids within subduction zones.

Whole-rock metabasalts and metagabbros data presented here demonstrate that there is no resolvable fractionation of either Fe or Zn isotopes across prograde metamorphic facies (greenschist → blueschist → eclogite). Rather our Fe and Zn isotope data for basaltic eclogites (mean $\delta^{56}\text{Fe} = +0.12 \pm 0.11 \text{ ‰}$ and $\delta^{66}\text{Zn} = +0.27 \pm 0.09 \text{ ‰}$) overlaps with both measurements of low-grade, seafloor metabasites (mean $\delta^{56}\text{Fe} = +0.11 \pm 0.04 \text{ ‰}$ and $\delta^{66}\text{Zn} = +0.20 \pm 0.04 \text{ ‰}$) and estimates of MORB ($\delta^{56}\text{Fe} = +0.11 \pm 0.17 \text{ ‰}$ and $\delta^{66}\text{Zn} = +0.28 \pm 0.03 \text{ ‰}$; Teng et al., 2013 and Wang et al., 2017 respectively). It is noteworthy that the blueschist facies samples show trace element evidence in the form of strong enrichments in alkali fluid mobile elements, for interactions with external, sediment derived fluid(s), which has driven the Fe isotope compositions of these metagabbros towards light values. These factors together suggest that the prograde dehydration of the mafic oceanic crust within subduction zones is associated with minimal release of S or C bearing fluids. It is also apparent that the associated meta-gabbro/basalt dehydration fluids are relatively poor carriers of dissolved Fe.

In order to understand the role of subducting slab serpentinites on the redox budget of subduction zones, an exhumed section of eclogite-facies serpentinitised ultramafics from the Zermatt-Saas ophiolite have been studied, and as part of this investigation a network

of high-pressure metamorphic veins have also been documented. These veins predominantly comprise of olivine and Ti-clinohumite, and are interpreted to be high permeability zones of fluid release and migration formed during the partial dehydration of the antigorite serpentinite host.

Building on the petrographic investigation of these serpentinite dehydration features it is shown that whole rock antigorite + olivine bearing serpentinites, which are representative of serpentinites undergoing partial dehydration, display a strong negative correlation between $\delta^{56}\text{Fe}$ values and S contents. This suggests that the release of S from these rocks that controls their Fe isotope composition. Furthermore, both vein forming olivine and Ti-clinohumite display markedly light $\delta^{56}\text{Fe}$ values ($\delta^{56}\text{Fe} = -0.24 \pm 0.28 \text{ ‰}$ and $-0.12 \pm 0.11 \text{ ‰}$), demonstrating the mobility of isotopically light Fe within serpentinite-derived fluids in subduction zones. We thus conclude that serpentinite dehydration is associated with the liberation and mobilization of SO_x bearing fluids, which are isotopically light with respect to Fe.

An entire segment of oceanic lithosphere, from mafic crustal units to underlying serpentinitised peridotite, has been studied. The data presented here has enabled a greater understanding of the principal controls on fluid release and element mobility during subduction zone metamorphism. While the dehydration of metabasites clearly involve the release of fluid mobile elements it is likely that the dehydration of these lithologies play a relatively small role in the transfer of redox mediating components during subduction. Of greater significance is the process of serpentine mineral breakdown and fluid release, which is observed to play a key role in the release of highly oxidizing species within associated serpentinite derived fluids.

Declaration

I declare that this thesis, which I submit for the degree of Doctor of Philosophy at Durham University, is my own work and not substantially the same as any which has previously been submitted at this or any other university. Edward C. Inglis

Department of Earth Sciences, Durham University, October 2017

© The copyright of this thesis rests with the author. No quotation from it should be published without prior written consent and information derived from it should be acknowledged.

“Choose life”

Acknowledgements

I've been "blessed" with having a somewhat larger than normal supervisory team during the course of my PhD. Firstly, I'd like to thank Helen for getting me to Durham in the first place and introducing me to the world of (stable) isotope geochemistry, without her I would not have been given the chances I have over the last four years. Geoff has been a big help both in and out of the lab, and has never been phased with whatever accident I have had with the Neptune (even when I corrupted the new instruments software the first time I was allowed to use it). Marie-Laure encouraged me from early on, even if it did mean ditching Se for Zn (I think that was a wise decision). For this I owe her an otter. I'd like to thank Marc for not thinking I was a total idiot all of the time, especially when I confused his example of a mass fractionation line with the Pb NHRL. Easy mistake to make I know! Continuing with the gallic role of honour, enter Baptiste. At first he laughed at me, but then he realised he was stuck with me. He taught me the ways of alpine geology and serpentinite petrology – something that I will never forgive him for. In all seriousness I owe him a lot for guiding me through my PhD and helping me to write the papers that have come out of it. He is an excellent mentor. Pierre has also contributed significantly to the latter part of my project. He is a great field geologist and I was really lucky that he spent so long with me in the Alps. Without his input to both field campaigns this project wouldn't have work out the way it did, and I owe him for that. Lastly there is Kevin. He is a great geezer. He has inspired a significant amount of this project and without him the work on Zermatt would never have been realised. I could wax lyrical about him but it isn't my style. Cheers for everything dobber.

Aside from my supervisors everyone else at Durham, both in and outside of the department, has been great. The geochemistry group has provided endless support with the analytical side of things and it has been a privilege to work alongside you guys for the last four years. The postdocs and PhD students within the department have provided hours of social distraction and a few good memories. A special mention to 214 and extended family. You guys were/are great. Another mention to everyone I have been lucky to have gone on fieldwork with over the last four years – team Ísland, RHUL Scotland crew, Switzerland 2015, 2016 and 2017, all the undergrad trips – they have all been a blast. I'd also like to thank everyone at Southampton, especially Martin, for inspiring me geologically and geochemically.

Of course my family are due a big acknowledgement. You have all been amazing in the support (both emotionally and financially) you have given me ever since beginning at

Southampton and through to my time at Durham. I really couldn't have done it without you.

Lastly I'd like to thank Emma. She has been solid in supporting me through the latter part of my PhD. I'm incredibly thankful that she has put up with me (especially over the last few months!). I hope I can do the same when it is her time.

Table of Contents

1. Introduction	1
1.1 Project overview	1
1.2 The lifecycle of oceanic lithosphere	2
1.3 Alpine ophiolites as a case study for subducting oceanic lithosphere	5
1.3.1 Metamorphic evolution of the European Alps.....	5
1.3.2 The Chenaillet Massif.....	7
1.3.3 The Queyras Schiste lustrés Complex.....	8
1.3.4 Zermatt-Saas.....	9
1.4 Redox cycling in subduction zones	11
1.5 The application of non-traditional stable isotopes	12
References Cited	15

2. The Behaviour of Iron and Zinc Stable Isotopes Accompanying the Subduction of Mafic Oceanic Crust: A Case Study from Western Alpine Ophiolites	25
2.1 Introduction	26
2.2 Geological Setting and Sample Petrology	28
2.2.1 The Chenaillet Massif.....	29
2.2.2 The Queyras Schiste lustrés Complex	30
2.2.2 Zermatt-Saas	31
2.3 Analytical Methods	32
2.3.1 Major and trace element concentrations	32
2.3.2 Fe isotope measurements	33
2.3.3 Zn isotope measurements	35
2.4 Results	36
2.4.1 Major and trace element concentrations	36
2.4.2 Fe and Zn stable isotopes	40
2.5 Discussion	41

2.5.1 The effect of high-pressure metamorphism and eclogitization of mafic lithologies on Fe isotopes – Zermatt eclogites	41
2.5.2 Fe isotope fractionation in response to fluid metasomatism at blueschist facies – The Queyras meta-ophiolites	44
2.5.3 Zn isotope systematics of metabasalts and metagabbros from the Queyras and Zermatt-Saas ophiolites	47
2.5.4 Implications for slab dehydration and the redox budget of the sub-arc mantle	48
2.6 Conclusions.....	50
Acknowledgements.....	50
References Cited.....	51
Supplementary Information.....	63

3. Relicts of High-Pressure Serpentinite Dehydration in the Zermatt-Saas Ophiolite (Western Alps, Switzerland).....	71
3.1 Introduction.....	72
3.2 Geological Setting	73
3.3 Vein Occurrence and Paragenesis	75
3.3.1 Field observations of rock textures and metamorphic veins	75
3.3.2 Microscopic petrographic and textural observations	80
3.4 Discussion	82
3.4.1 Evidence for dehydration reactions	83
3.4.1.1 Python-pattern texture	83
3.4.1.2 Olivine rich veins	84
3.4.1.3 Ti-clinohumite rich veins	85
3.4.2 Carbonate and diopside occurrence	86
3.4.3 Widespread retrogression of the massif	86
3.5 Conclusions.....	87
Acknowledgements.....	88
References Cited.....	89

4. Iron isotope behaviour accompanying the dehydration of serpentinite during subduction: A mineral scale approach	97
4.1 Introduction.....	98
4.2 Geological Setting and Sample Description.....	99
4.2.1 The Zermatt-Saas Ophiolite	99
4.2.2 Serpentinised ultramafics from the Gornergrat area	100
4.2.2.1 Whole-rock antigorite + olivine serpentinites	101
4.2.2.2 Ti-clinohumite and olivine veins	101
4.2.2.1 Metasediments	103
4.3 Methods	104
4.3.1 Major and trace element and Fe isotope analysis of whole-rock serpentinites	104
4.3.1.1 Major element concentrations	104
4.3.1.2 Trace element concentrations	105
4.3.1.1 Fe isotope compositions	105
4.3.2 Micro-analysis of serpentinite mineral domains.....	107
4.3.2.1 Micro-sampling of mineral domains	107
4.3.2.2 Mineral trace element concentration	108
4.3.2.3 Mineral Fe isotope compositions	108
4.4 Results.....	109
4.4.1 Whole-rock major and trace element data.....	109
4.4.2 Mineral trace element data	111
4.4.3 Whole-rock and mineral Fe isotope data.....	112
4.5 Discussion	115
4.5.1 Trace element behaviour during high-pressure metamorphism of the Zermatt-Saas serpentinites	115
4.5.2 Fe isotope systematics during serpentinite dehydration	118
4.5.2.1 Whole rock Fe isotope behaviour	118
4.5.2.2 Mineral-scale control on Fe isotope behaviour	120
4.5.3 Implications for the nature of fluids released during deserpentinisation	122
4.6 Conclusions.....	123
References Cited.....	125
Supplementary Information.....	131

5. Conclusions and Synthesis.....	142
5.1 Key aims of this work.....	142
5.2 Overview of chapters.....	142
5.2.1 The behaviour of iron and zinc stable isotopes accompanying the subduction of mafic oceanic crust: A case study from western Alpine ophiolites.....	142
5.2.2 Relicts of High-pressure serpentinite dehydration in the Zermatt-Saas ophiolite (Western Alps, Switzerland)	144
5.2.3 Iron isotope behaviour accompanying the dehydration of serpentinite during subduction: A mineral scale approach	144
5.3 Synthesis of key findings	146
References Cited	147

Appendices

- 1) Journal formatted copy of “The behaviour of iron and zinc stable isotopes accompanying the subduction of mafic oceanic crust: A case study from western Alpine ophiolites” by *Inglis et al.*, 2017



Chapter 1.

Introduction

1.1 Project overview

The recycling of oceanic lithosphere via the process of subduction is a fundamental paradigm within the field of earth sciences. Of paramount importance is understanding the nature and quantifying the magnitude of geochemical exchanges that occur during this process. This project is specifically concerned with identifying the fluxes of key, mainly redox sensitive, elements during different stages of the metamorphic evolution of subducting oceanic lithosphere.

Specifically this study has focused on different exhumed mafic and ultramafic metamorphic terranes from the European Alps. These have been metamorphosed under different prograde conditions representative of a subduction zone gradient, and thus allow us to examine the effect of subduction zone metamorphism from a “slab perspective”. This approach has ultimately enabled us to link specific elemental and isotopic behaviour to different metamorphic reactions, and to constrain elemental mobility during the process of subduction

This thesis presents the results of three different studies, written as academic papers, which seek to address this theme. The first, entitled: “*The behaviour of iron and zinc stable isotopes accompanying the subduction of mafic oceanic crust: A case study from Western Alpine ophiolites*” examines the effect of high-pressure (HP) metamorphism of the mafic oceanic crust (meta-basalts and -gabbros), alongside the effect of metasomatic sediment interaction. The major conclusions of this study are that Fe and Zn isotopes are little fractionated by HP metamorphism but subduction zone metasomatic processes can perturb Fe isotopes.

The second paper is entitled “*Relicts of High-Pressure Serpentinite Dehydration in the Zermatt-Saas Ophiolite (Western Alps, Switzerland)*” and is concerned with the petrology of a series of olivine and titanian-clinohumite veins within an eclogite facies serpentinite body from the Zermatt-Saas ophiolite. This work presents the significant finding that this ultramafic massif preserves evidence for widespread partial dehydration of a section of slab serpentinite – a feature previously unrecognised by previous workers. In particular, we show that partial dehydration of the serpentinite produces a channelized fluid, localised within veins in which olivine and Ti-clinohumite subsequently precipitated.

Consequently we are able to chemically fingerprint this zone of fluid release during subduction.

The third paper, “*Iron isotope behaviour accompanying the dehydration of serpentinite during subduction: A mineral scale approach*” builds on the findings of the second paper and presents a detailed whole-rock and micro-scale trace element and Fe isotope study of the Zermatt serpentinites and associated metamorphic veins. By sampling both vein forming minerals and host serpentinites we identify the incorporation of isotopically light Fe within the metamorphic veins, thus suggesting that isotopically light Fe is mobilised during serpentinite dehydration. Linking this to our whole-rock data that demonstrates a strong co-variation between sulphur content and Fe isotope composition, we suggest that these fluids produced during serpentinite dehydration are a carrier of dissolved sulphate, which serves as a mechanism for fractionating Fe isotopes in this setting. Ultimately we conclude that this provides strong evidence for the liberation of highly oxidising fluids during the process of deserpentinisation.

1.2 The lifecycle of oceanic lithosphere

Oceanic lithosphere is largely formed at mid-ocean spreading centres, and is then progressively hydrated, altered and oxidised during seafloor fluid-rock interaction, before being recycled back into the mantle at subduction zones. When considering oceanic lithosphere formation it is important to understand the effect of different variables on the type of lithosphere that can be created. Factors such as: mantle potential temperature (*Langmuir & Forsyth, 2007*); composition of the mantle source (*McKenzie et al., 2005*); geometry of the ridge segment (*McDonald, 1986, Lagabrielle et al., 1998*), and; spreading rate (*Morgan and Chen, 1993*) are all known to affect the nature of lithosphere formed. Of these the rate of spreading exerts a dominant control on the type of oceanic lithosphere formed at spreading centres (*Morgan and Chen, 1993, Dick et al., 2003*). To a first order two end members can be considered with respect to fast vs. slow spreading centres, and are summarised in **Figure 1.1**.

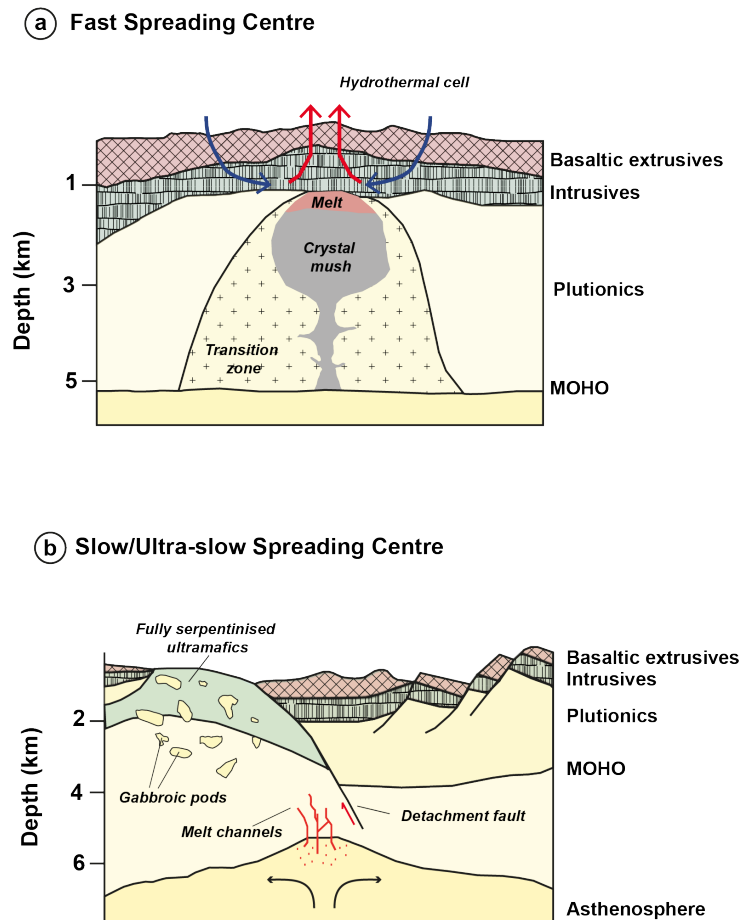


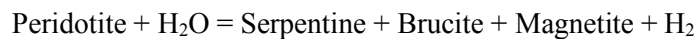
Figure 1.1. Schematic sketches showing typical across axis morphologies of (a) Fast, and, (b) Slow/ultra-slow spreading centres. Figure is modified from Bach & Fruh-Green, 2010.

After initial formation a number of secondary processes act to alter and modify the mineralogy and bulk chemistry of the oceanic lithosphere. This process of alteration and seafloor metamorphism is fundamentally controlled by fluid-rock interaction occurring between the mafic and ultramafic lithologies and seawater.

Alteration of the mafic crustal units (basalts and gabbros) is the effect of high-temperature (H-T) hydrothermal alteration, or low-temperature (L-T) seafloor weathering processes (Bach & Fruh-Green, 2010). The nature and extent of this alteration is highly variable, and influenced by such factors as local and regional heat flow, structure and faulting, lithological fabric and sediment cover (Alt, 1995, Staudigel et al., 1996, Gillis, 1995). As such, the effect of hydrothermal alteration cannot be considered uniform throughout the oceanic lithosphere. Despite this it is widely accepted that the upper basaltic units of the oceanic crust undergo a greater degree of hydration and subsequent alteration than the lower gabbroic units (Rosenberg et al., 1993, Hart et al., 1994). Much

of the H₂O sequestered within the mafic oceanic crust is controlled by a series of hydration reactions affecting primary mineral domains, such as the hydration of the typical anhydrous silicates such as pyroxene to hydrous amphibole. Additionally the formation of secondary, hydrous phyllosilicates can also contribute to the bound H₂O budget of altered oceanic crust (*Shau & Peacor, 1993 & Alt & Teagle, 2003*). These common seafloor reactions typically account for the sequestration of ~0.5 wt% H₂O within the lower gabbroic units and up to 5wt% H₂O within the extrusive basaltic sequence (*Carlson, 2003*).

In addition to alteration of the mafic crustal units we must also consider the effect of hydration upon the ultramafic sequence of oceanic lithosphere. Seawater interaction with ultramafic rocks at temperatures >250 °C results in a hydration reaction termed serpentinisation. These reactions result in the conversion of fresh mantle peridotite to a hydrated, serpentine-rich lithology termed serpentinite, as described by the generalised reaction:

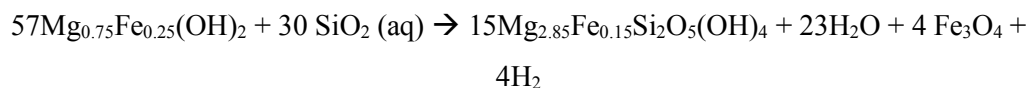


Specifically the process of serpentinisation refers to a set of hydrous mineral reactions affecting the olivine domain of protolith ultramafics. These reactions are best described by *Bach et al., 2006*:

(1) Olivine (Mg#90) → Serpentine + Brucite



(2) Fe-rich brucite + SiO₂(aq) → Serpentinite and Magnetite



(3) Orthopyroxene → Serpentinite + SiO₂ (aq)



With serpentine represented by one of three different polymorphs: lizardite, chrysotile or antigorite dependant on the *P-T* conditions. The production of magnetite and H₂ is also common during this process, but is controlled by the Fe content of the system, for at low Fe concentrations magnetite precipitation may be suppressed (*O'Hanley & Dyar, 1993*).

The formation of magnetite in seafloor serpentinite has also been suggested to occur as a function of temperature (*Klein et al., 2014*)

This sequence of reactions ultimately sees the H₂O content of primary mantle peridotite increase from <0.1 wt% to ~13wt% after serpentinisation (*Ulmer & Tromsdorff, 1995*), which consequently represents the most significant hydrous lithology within the oceanic lithosphere. The process of serpentinisation is also significant with respect to the redox budget of oceanic lithosphere. Oxidation of the bulk Fe²⁺ content of the original peridotite to an Fe³⁺ dominated serpentinite is perhaps one of the most important redox reactions to consider. Iron oxidation via the process of serpentinisation is concurrent with H₂ generation, and sees Fe³⁺ hosted mainly within serpentine and magnetite (*O'Hanley & Dyar, 1993, Evans, 2010, Greenberger et al., 2015*). By this process the bulk Fe³⁺/ΣFe of a mantle peridotite can be increased from ~0.2 when unserpentinised to ~0.7 when fully serpentinised (*e.g. Debret et al., 2014*). Additionally the role of S should also be considered, as S, notably S⁶⁺ species, serve as a powerful oxidant (1mol of S⁶⁺ can oxidise 8mol of Fe²⁺ to Fe³⁺). Until recently S storage within seafloor serpentinites was largely thought to be controlled by secondary sulfide and sulphate assemblages (*Alt et al., 2013*), but recent work has shown that S⁶⁺ can be readily incorporated within serpentine group minerals and these minerals can account for between 60-100% of the total S budget for abyssal serpentinites (*Debret et al., 2017*).

1.3 Alpine ophiolites as a case study for subducting oceanic lithosphere

The overarching theme of this work has been to identify fluxes of key elements during the subduction and ensuing devolatilisation of oceanic lithosphere. One approach in elucidating such fluxes is to study exhumed subduction zone rocks that preserve their prograde metamorphic history, and as such, can be taken as being representative of the metamorphic products of subduction zone inputs.

1.3.1 Metamorphic evolution of the European Alps

The samples that have been studied as part of this work have been collected from different ophiolites within the Western European Alps. In order to contextualise these samples the following provides a brief overview of Alpine geological evolution.

The Alpine orogenic belt represents the collisional product of convergence between the Eurasian and African plates. Prior to this orogenesis a relatively long-lived period of subduction had been established, whereby Tethyan oceanic

lithosphere was subducted beneath the overriding Eurasian plate (Coward & Dietrich, 1989). During the Cretaceous the upper Adriatic continental margin underwent oblique collision with the European passive continental margin, in what is now recognised as the onset of Alpine orogeny (Del Piaz, 2001). Continued convergence saw the closure of the oceanic basin by the Eocene and a later, second orogenic period termed the Adria-Europe collision (Del Piaz *et al.*, 2003). Despite cessation of convergence between the plates involved, uplift of the orogeny still continues today (Nocquet *et al.*, 2016). A cross-section of the north-western Alps (taken from Del Piaz *et al.*, 2003) is shown in **Figure 1.2** and illustrates the current structural arrangement of the units within this area.

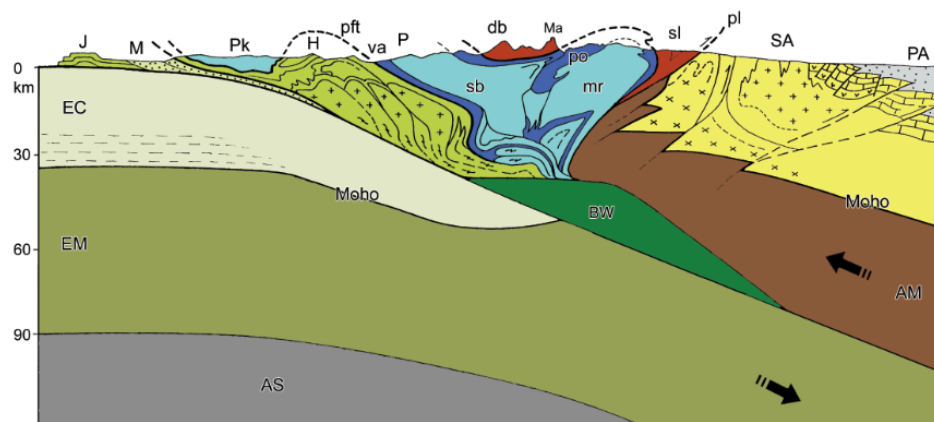


Figure 1.2. A cross section of the North western Alps showing the main structural arrangements of the units within this region. Unit abbreviations: *sl* (Sesia-Lanzo inlier); *db* (Dente Blanche); *Ma* (Matterhorn); *P* (Penninic domain); *po* (Piedmont ophiolites); *mr* (Monte Rosa); *sb* (Grand St. Bernard); *va* (Penninic Valais zone); *Pk* (Penninic klippen); *pft* (Penninic frontal thrust); *H* (Helvetic); *M* (Molasse foredeep); *J* (Jura belt); *BW* (Buried wedge); *EC* (European continental crust); *EM* (European mantle); *AS* (Asthenosphere); *SA* (Southern Alps); *AM* (Antithetic mantle); *pl* (Periodic fault system), *PA* (Padane-Adriatic foreland). Figure is taken from Dal Piaz *et al.*, 2003.

Alpine geology is dominated by nappe tectonics (e.g. Trümpy, 2001), whereby a wide range of oceanic and continental lithologies are juxtaposed in relatively coherent slivers, bounded by a series of low angle thrust faults. Of particular interest are the subduction related units of the Austroalpine-Penninic wedge, now situated within the western Alps (see **Figure 1.2**). These units represent sections of deeply subducted (~75-100km), oceanic and continental material, which underwent peak metamorphism prior to the main Adria-Europe collision. Closure

of the Piemonte basement and the onset of continent-continent collision by the late Cretaceous saw relatively rapid exhumation and obduction of these fossil subduction zone units (Avigad *et al.*, 1993). These meta-ophiolite bodies of the western Alps were likely formed at a magma-poor setting, i.e., a slow or ultra-slow spreading centre or an ocean-continent transition, during the opening of the Ligurian Ocean in the Jurassic (Lagabrielle and Cannat, 1990, Bernoulli *et al.*, 2003, Lagabrielle *et al.*, 2015).

Presently these units are preserved within the internal Alps as part of a nappe-stack arrangement. Within this structure the juxtaposition of crystalline continental massifs against meta-ophiolite bodies and sediment packages dominate (Hunziker *et al.*, 1989, Debelmas and Lemoine, 1970, Goffé and Chopin, 1986, Lemoine *et al.*, 1989).

This study draws on samples collected from three different meta-ophiolite complexes within the Western Alps: The Chenaillet Massif; Queyras Schistelustrés Complex, and; Zermatt-Saas (see **Figure 1.3**). An overview of the geology for these locations is given below.

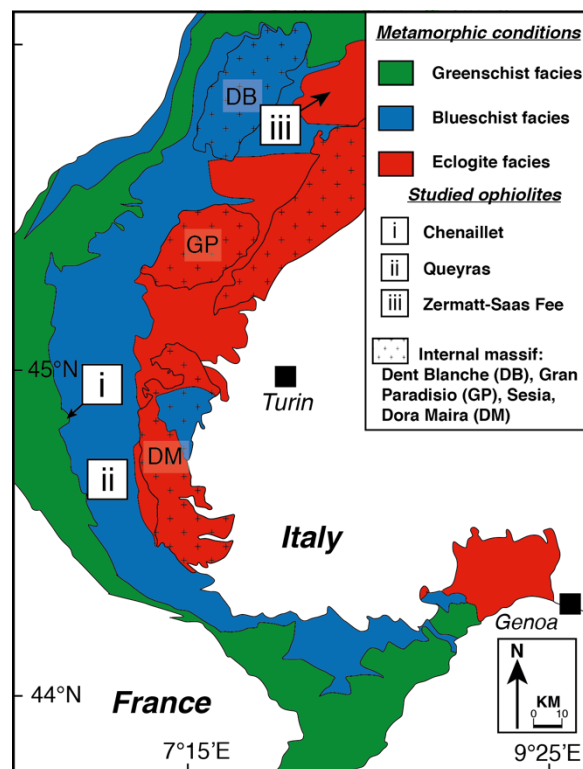


Figure 1.3. A map of the western Alps showing the apparent metamorphic conditions for each area. The study locations for work are given in the closed

squares as i) *The Chenaillet*; ii) *The Queyras Schiste Lustres*, and iii) *Zermatt-Saas*.

1.3.2 *The Chenaillet Massif*

The Chenaillet massif represents a largely undeformed, meta-ophiolite body situated within the external Piedmont zone, along the French-Italian border (**Figure 1.3**). Within its current structural arrangement the complex forms a klippe, overlying the Lago Nero-Replatte unit (*Caby, 1995*). The ~25km² complex preserves primary oceanic contacts and is characterised by a sequence of serpentinitised ultramafics, intruded by gabbro pods. These mafic rocks are overlain by an extrusive basaltic sequence and oceanic sediments (*Caby, 1995, Inglis et al., 2017*). Detailed petrological, geochemical and structural studies have suggested that this ophiolite represents a fossil oceanic core complex, like those currently formed at a slow-spreading ridge settings (*Lagabrielle et al., 1990, Chalot-Prat, 2005, Manatschal et al., 2011*).

One of the most significant features of the Chenaillet massif is the relatively low *P-T* metamorphic overprint it records compared to other Alpine meta-ophiolites. Previous workers have suggested that the ophiolitic lithologies here record a prehnite-pumpellyite to amphibolite facies metamorphic overprint (*Caby, 1995, Li et al., 2013, Inglis et al., 2017*), akin to seafloor metamorphism, as opposed to the *LP-HT* blueschist and eclogite facies overprint that is recorded by most other alpine meta-ophiolites. As such, the Chenaillet meta-ophiolite provides a good contextual reference for a slice of Ligurian oceanic lithosphere, which escaped subduction related *HP* metamorphism.

1.3.3 *The Queyras Schiste lustrés Complex*

The Queyras Schiste lustrés complex is located in the Piedmont zone of the south-western Alps (**Figure 1.3**). It represents a ~10km thick pile comprising units belonging to the distal European margin and from the nearby oceanic domain (*Lemoine et al., 1989*) that were ultimately juxtaposed during Alpine subduction and collision in the late Cretaceous to Tertiary (*Tricart, 1984*). It preserves a complex structure, resulting from successive phases of subduction, collision and obduction related deformation (*Tricart & Schwartz, 2006*). Within its present structural arrangement the complex overlies the Dora-Maira internal crystalline massif to the east and is bounded to the west by the Briançonnais zone (*Tricart et al., 2004*).

The Queyras Schiste lustrés complex is formed of ~10 meter- to kilometre-scale boudinaged meta-ophiolite bodies, embedded within a sediment rich environment. The meta-ophiolites are dominated by serpentinised ultramafics and variably deformed gabbroic bodies, all of which have been metamorphosed under blueschist facies conditions (*Lagabrielle et al., 1984, Lemoine et al., 1989*). Previous workers have suggested that these units likely evolved as a palaeo-sedimentary wedge, which formed during the late Cretaceous-early Eocene subduction of the Tethyan Ocean (*Tricart & Schwartz, 2006*).

The metamorphic evolution of the oceanic units from the complex is typified by a characteristic blueschist facies overprint. Detailed petrographic and *P-T* work has identified three tectono-metamorphic domains within the Queyras schiste lustré complex (see *Schwartz et al., 2013*). The *P-T* conditions of these domains range from low-temperature blueschist facies conditions ($P= 0.9\text{-}1.1$ GPa, $T= 320\text{-}340$ °C) in the west, to medium temperature blueschist facies conditions ($P= 1.1\text{-}1.2$ GPa, $T= 340\text{-}360$ °C) and high temperature blueschist facies conditions ($P= 1.2\text{-}1.5$ GPa, $T= 380\text{-}470$ °C) towards the east (*Schwartz et al., 2013*).

1.3.4 Zermatt-Saas

The Zermatt-Saas zone of alpine Switzerland and Italy (**Figure 1.3**) represents a continuous slice of Tethyan oceanic lithosphere, which experienced Mesozoic oceanic stage metamorphism, followed by a later Cenozoic, subduction related overprint (see *Rebay et al., 2017* and references therein). The Zermatt-Saas Zone comprises a near complete section of oceanic lithosphere, including: serpentinised ultramafics; intrusive gabbros; an intrusive and extrusive basaltic sequence, and; associated marine sediment cover (*Bearth, 1967, Meyer, 1983, Barnicoat & Fry, 1986, Bucher et al., 2005*). It is likely that the genesis of these units occurred during the Mid to Late Jurassic (*Rubatto et al., 1998*), as part of a small scale Tethyan spreading centre (*Pognante et al., 1986*).

The Zermatt-Saas Zone is located within the inner Alpine belt, between the units derived from the Adriatic margin and Briançonnais zone. Locally the Zermatt-Saas is preserved within a collisional nappe stack, underlain by the Monte Rosa continental basement, and overlain by the Dente Blanche nappe (*Angiboust et al., 2009*).

The metamorphic history of the complex is intricate but has been explained according to four key stages by *Rubatto et al., 1998*:

- 1) Mid to Late Jurassic formation of the oceanic lithosphere during basin opening. Later greenschist facies seafloor metamorphism.
- 2) High to ultra-high pressure metamorphism during the alpine collision. Numerous *P-T* estimates are suggested and summarised by *Rebay et al., 2017*. Many authors suggest a metamorphic climax in the region of 2.5-3 GPa and 550-600 °C. Recent U-Pb dating of zircons has suggested that peak metamorphism occurred at ~65Ma (*Rebay et al., 2017*).
- 3) Decompression related blueschist facies overprint.
- 4) Late exhumation related greenschist facies overprint.

One of the key features of the meta-ophiolites of the Zermatt-Saas is the preservation of primary magmatic features, in particular, mineralogy, textures and pillow structures (*Barnicoat, 1988, Bucher & Grapes, 2009*), which have survived extensive metamorphism and still remain recognisable to this day. This allows workers to test the effect of subduction related metamorphism on these lithologies, without ambiguity of the protolith.

Taken together, these metamorphic terranes are considered as being representative of the different metamorphic conditions endured by a subducted section of oceanic lithosphere along a prograde *P-T* path. This assumption is reasonable given the range of slab thermal and pressure structures suggested from computational modelling of subduction zones systems (e.g. *Stein & Stein, 1996, Syracuse et al., 2010*). It is further reinforced by numerous experimental studies designed to predict the phase equilibria of HP subduction zone metamorphism (i.e., *Nichols et al., 1994, Liu et al., 1996, Schmidt & Poli et al., 1998, Poli & Schmidt, 2002*).

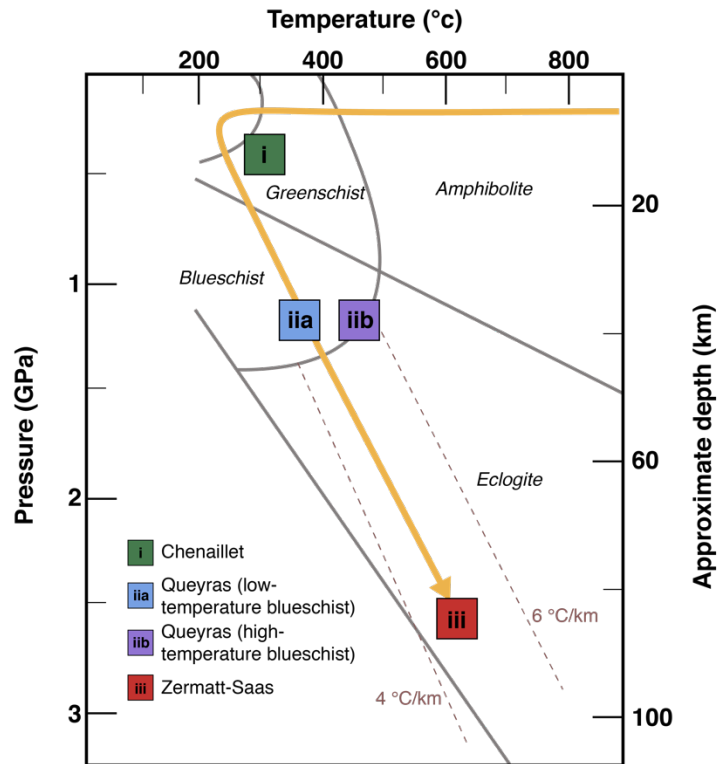


Figure 1.4. A schematic P - T grid showing the apparent peak metamorphic conditions for the Chenaillet, Queyras Schiste Lustres and Zermatt-Saas ophiolites. The P - T estimates for each location are taken from Manatschal et al., 2011, Schwartz et al., 2013 and Angiboust et al., 2009 respectively. The pale red dashed lines represent slab geotherms for hot ($6\text{ }^{\circ}\text{C}/\text{km}$) and cold ($4\text{ }^{\circ}\text{C}/\text{km}$) subduction gradients.

It should be noted that our work assumes a prograde metamorphic P - T evolution from greenschist-blueschist-eclogite facies (**Figure 1.4**), and this is supported by workers aforementioned. A notable caveat of this assumption is the degree of shear heating that a subducting slab could undergo. Indeed, it has been previously suggested that shear heating along the slab-mantle interface could see the upper lithologies (basalt) progress along a greenschist-amphibolite-granulite-eclogite path (Peacock, 1993). Taking this into consideration we suggest that our H/UHP eclogite facies rocks from Zermatt-Saas were unlikely to have evolved along such a path, as no evidence for high degrees of shear heating (e.g. melting) has been seen and they contain no evidence for amphibolite or granulite facies conditions.

1.4 Redox cycling in subduction zones

Oxygen fugacity ($f\text{O}_2$) acts as an intrinsic thermodynamic property that controls the chemical availability of oxygen and the speciation of multivalent elements (Canil, 1997, Christie et al., 1986, Wood, 1990). As such an understanding how this

parameter is controlled within Earth's reservoirs is of significant importance. Arc lavas typically display high ratios of ferric Fe to total Fe ($\text{Fe}^{3+}/\Sigma\text{Fe}$) relative to MORB and OIB, which is commonly interpreted to reflect an elevated $f\text{O}_2$ of the mantle source (Brandon & Draper, 1996, Frost & Ballhaus, 1998, Parkinson & Arculus, 1999, Kelly & Cottrell, 2009). Recently this topic has received much attention from geochemists seeking to understand global redox cycles and elucidate mechanisms for oxidation of the mantle (e.g. Evans, 2012).

The processes and mechanisms of sub-arc mantle oxidation have historically been poorly understood and heavily debated. While most workers agree that mass transfer between the subducting slab and overlying mantle wedge controls the elevated $\text{Fe}^{3+}/\Sigma\text{Fe}$ observed in arc-lavas (e.g. Kelly & Cottrell, 2009), some have suggested that this signature could be a function of crustal anatexis and fractional crystallisation during ascent and eruption of resulting melts (Lee *et al.*, 2005, 2010). Despite this, many studies have focused their attention on possible mechanisms that could account for elevated $f\text{O}_2$ of the sub-arc mantle source (e.g. Evans *et al.*, 2012, Evans, 2012, Kelly & Cottrell, 2009, Debret *et al.*, 2016, Pons *et al.*, 2016, Inglis *et al.*, 2017).

The transfer of oxidised or oxidising components between the subducting slab and sub-arc mantle is the main candidate when considering possible mechanisms for oxidation. Within this setting chemical mass transfer is mobilised within slab derived sub- (Hermann *et al.*, 2006) and/or, super-critical fluids (Kessel *et al.*, 2005), and melts (Foley *et al.*, 2000). The occurrence of which is strongly controlled by P - T - x - $f\text{O}_2$ conditions (Manning, 2004). Seeing as H_2O serves as a poor oxidising agent under mantle conditions (Frost & Ballhaus, 1998), other candidates must be considered. One possible scenario is to consider the transfer of strongly oxidising, multi-valent elements. Both S and C exist in sufficiently high concentrations within altered oceanic lithosphere (Alt *et al.*, 2003) and could be mobilised during slab dehydration or melting (Keleman & Manning, 2015, Alt *et al.*, 1993). Consequently these elements serve as some of the most likely candidates for oxidising the sub-arc mantle. An alternative possibility is to consider the mobility of Fe^{3+} within fluids and melts leaving the down-going slab. If this were to occur in sufficiently high volumes then such direct transfer could serve as the primary control on the $\text{Fe}^{3+}/\Sigma\text{Fe}$ observed within arc lavas (Kelly & Cottrell, 2009).

1.5 The application of non-traditional stable isotopes

Recent advances in mass spectrometric techniques have seen the emerging field of non-traditional stable isotope geochemistry applied to numerous scientific problems in both high- and low-temperature settings. Continual method development and refinement has enabled the stable isotopes of over 30 individual elements to be measured routinely to high levels of precision and accuracy – mainly down to advances in both Thermal Ionisation Mass Spectrometry (TIMS) and Multiple-Collector Inductively Coupled Plasma-Mass Spectrometry (MC-ICP-MS) techniques. The following chapters present a range of Fe and Zn stable isotope data, specifically applied to understand the mobility of key redox mediating elements during subduction. To this end we will concentrate on the geochemistry of Fe and Zn stable isotopes within the remainder of this section.

Iron, the fourth most abundant element in Earth's crust has four naturally occurring stable isotopes: ^{54}Fe , ^{56}Fe , ^{57}Fe and ^{58}Fe . Ratio measurements of these isotopes have been measured, predominantly by MC-ICP-MS, for the last ~15 years. There are two main issues surrounding the determination of Fe isotope ratios. The first of these is the low relative abundance of all but ^{56}Fe , which accounts for <91% of total Fe. In practice this means that accurate determination of masses ^{54}Fe , ^{57}Fe and ^{58}Fe has historically proved difficult. Rapid development of amplifier technology and sample introduction systems has largely combatted this issue, but can still prove challenging for samples of low Fe concentrations (e.g. environmental material). The second difficulty concerning Fe isotope measurements is the occurrence of polyatomic interferences on all but one of the Fe masses (see **Figure 1.5**). Although these spectral interferences can be resolved from the analyte peaks of interest, by using high-resolution (or pseudo high-resolution) capabilities of modern MC-ICP-MS instruments, this relies on an inherent stability of the magnet analysing position, as drifts in this can cause false measurement of the interference tail or analyte peak shoulder. A detailed explanation of the Fe isotope methods used to determine the stable isotope composition of samples analysed as part of this work is presented within each of the subsequent chapters.

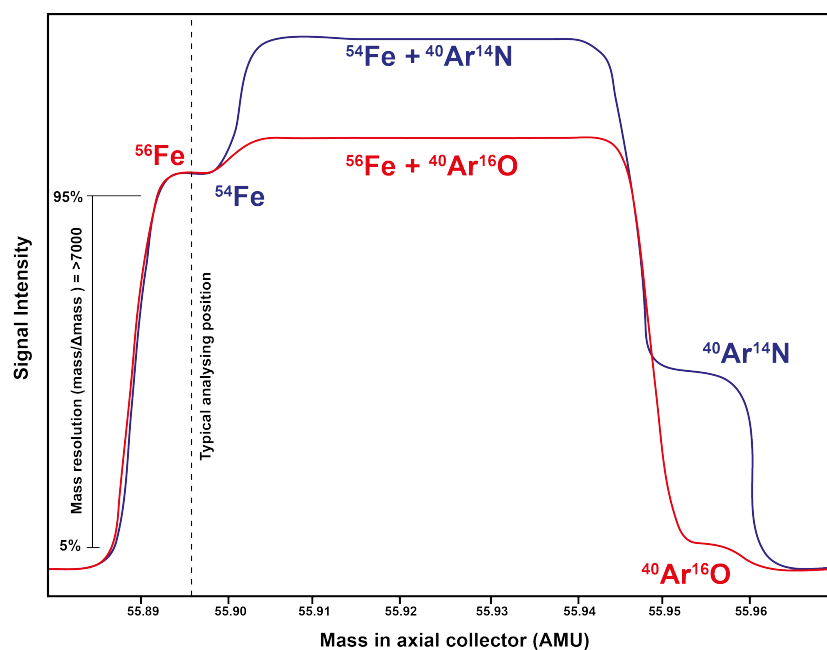


Figure 1.5. A mass-scan across the nominal mass 56 space. The red trace shows the axial collector (C) that is set to collect ^{56}Fe - denoted by the black dashed vertical line. The blue trace shows the low mass collector (LI) that is set to collect ^{54}Fe . The wide mass scan shows different polyatomic interferences that can block both ^{54}Fe and ^{56}Fe .

When considering different processes that may fractionate the stable isotopes of a given material, a simple set of governing qualitative principals can be considered. These are best described by *Schauble, 2004* and are summarized here:

- 1) Smaller equilibrium isotopic fractionations are expected at higher temperatures. The magnitude of such fractionations is roughly proportional to $1/T^2$.
- 2) Typically fractionations are greatest for the lighter elements and isotopes of very different mass, when all else is equal.
- 3) At equilibrium the heavy isotopes of a given element will be concentrated in substances where that given element forms the stiffest bonds. The magnitude of the resulting isotopic fractionation will be roughly proportional to the differences in bond stiffness between the equilibrated substances. The shortest and strongest (thus stiffest) bonds are commonly associated with features such as high oxidation states, bonding with elements towards the top of the periodic table, and low coordination numbers. It should be noted that when the element of interest is

directly bonded to a hydrogen atom, or is part of a low mass molecule, then the expected enrichment in heavy isotopes might not be apparent.

This theory predicts that Fe isotopes can experience mass-dependent fractionation in response to changes in redox, with the heavier isotopes of Fe mirroring Fe^{3+} when a system is in equilibrium (Polyakov & Mineev, 2000). Within the field of high temperature geochemistry the analysis of natural sample suites has shown that resolvable variations in Fe isotopes can occur in response to such as mantle melting (Williams *et al.*, 2004; 2005; 2009; 2014, Weyer and Ionov, 2007, Dauphas *et al.*, 2014), igneous differentiation (Sossi *et al.*, 2012, Telus *et al.*, 2012, Schuessler *et al.*, 2009, Teng *et al.*, 2011; 2013,) and changes in mantle redox state (Williams *et al.*, 2004, Dauphas *et al.*, 2009). Consequently Fe isotopes serve as a powerful tool to understand redox processes in subduction.

Unlike Fe, Zn stable isotopes present less of an analytical challenge in their determination. The five isotopes of Zn are largely free from spectral interference, and masses 64, 66, 67 and 68 all occur in relative high abundance. The same mass-dependant stable isotope theory applies, in that Zn isotope can be fractionated in response to changes in coordination chemistry, bonding environment and ligand binding, but unlike Fe there is thought to be no redox effect. One of the key aspects of Zn isotope geochemistry that is drawn upon here is the effect of S and C. Ab initio calculations predict strong isotopic fractions of Zn within the presence of aqueous S and C, in the form of Zn-S and Zn-C species (Fujii *et al.*, 2011). Consequently, we have utilised Zn isotopes this work to serve as a tracer of these species during subduction zone mass transfer.

Ultimately this study has applied Fe and Zn stable isotopes, which are fractionated by geochemical processes, to allow us to comment of the transfer of redox mediating components during subduction zone mass transfer.

References Cited

Alt, J.C. and Teagle, D.A., 2003. Hydrothermal alteration of upper oceanic crust formed at a fast-spreading ridge: mineral, chemical, and isotopic evidence from ODP Site 801. *Chemical Geology*, 201(3), pp.191-211.

Alt, J.C., 1995. Subseafloor Processes in Mid-Ocean Ridge Hydrothermal Systems. *Seafloor Hydrothermal Systems: Physical, chemical, biological, and geological interactions*, pp.85-114.

Alt, J.C., Schwarzenbach, E.M., Früh-Green, G.L., Shanks, W.C., Bernasconi, S.M., Garrido, C.J., Crispini, L., Gaggero, L., Padrón-Navarta, J.A. and Marchesi, C., 2013. The role of serpentinites in cycling of carbon and sulfur: seafloor serpentinization and subduction metamorphism. *Lithos*, 178, pp.40-54.

Angiboust, S., Agard, P., Jolivet, L. and Beyssac, O., 2009. The Zermatt-Saas ophiolite: the largest (60km wide) and deepest (c. 70–80 km) continuous slice of oceanic lithosphere detached from a subduction zone? *Terra Nova*, 21(3), pp.171-180.

Avigad, D., Chopin, C., Goffe, B. and Michard, A., 1993. Tectonic model for the evolution of the western Alps. *Geology*, 21(7), pp.659-662.

Bach, W., Paulick, H., Garrido, C.J., Ildefonse, B., Meurer, W.P. and Humphris, S.E., 2006. Unraveling the sequence of serpentinization reactions: petrography, mineral chemistry, and petrophysics of serpentinites from MAR 15 N (ODP Leg 209, Site 1274). *Geophysical research letters*, 33(13).

Bach, W. and Früh-Green, G.L., 2010. Alteration of the oceanic lithosphere and implications for seafloor processes. *Elements*, 6(3), pp.173-178.

Barnicoat, A.C. and Fry, N., 1986. High-pressure metamorphism of the Zermatt-Saas ophiolite zone, Switzerland. *Journal of the Geological Society*, 143(4), pp.607-618.

Barnicoat, A.C., 1988. Zoned high-pressure assemblages in pillow lavas of the Zermatt-Saas ophiolite zone, Switzerland. *Lithos*, 21(3), pp.227-236.

Bearth, P., 1967. *Die Ophiolithe der Zone von Zermatt-Saas Fee*. Kümmerly & Frey.

Bernoulli, D., Manatschal, G., Desmurs, L. and Muntener, O., 2003. Where did Gustav Steinmann see the trinity? Back to the roots of an Alpine ophiolite concept. *Special Papers-Geological Society of America*, pp.93-110.

Brandon, A.D. and Draper, D.S., 1996. Constraints on the origin of the oxidation state of mantle overlying subduction zones: an example from Simcoe, Washington, USA. *Geochimica et Cosmochimica Acta*, 60(10), pp.1739-1749.

Bucher, K. and Grapes, R., 2009. The eclogite-facies Allalin Gabbro of the Zermatt–Saas ophiolite, Western Alps: a record of subduction zone hydration. *Journal of Petrology*, 50(8), pp.1405-1442.

Bucher, K., Fazis, Y., Capitani, C.D. and Grapes, R., 2005. Blueschists, eclogites, and decompression assemblages of the Zermatt-Saas ophiolite: High-pressure metamorphism of subducted Tethys lithosphere. *American mineralogist*, 90(5-6), pp.821-835.

Caby, R., 1995. Plastic deformation of gabbros in a slow-spreading Mesozoic ridge: Example of the Montgenevre ophiolite, Western Alps. In *Mantle and Lower Crust Exposed in Oceanic Ridges and in Ophiolites* (pp. 123-145). Springer, Dordrecht.

Canil, D., 1997. Vanadium partitioning and the oxidation state of Archaean komatiite magmas. *Nature*, 389(6653), p.842.

Carlson, R.L., 2003. Bound water content of the lower oceanic crust estimated from modal analyses and seismic velocities of oceanic diabase and gabbro. *Geophysical research letters*, 30(22).

Chalot-Prat, F., 2005. An undeformed ophiolite in the Alps: field and geochemical evidence for a link between volcanism and shallow plate tectonic processes. *Special Papers – Geological Society of America*, 388, p.751.

Christie, D.M., Carmichael, I.S. and Langmuir, C.H., 1986. Oxidation states of mid-ocean ridge basalt glasses. *Earth and Planetary Science Letters*, 79(3-4), pp.397-411.

Coward, M. & Dietrich, D. (1989) Alpine tectonics – an overview. In: *Alpine Tectonics* (Ed. by Coward M.P., Dietrich D. & Park R.) Geol. Soc. London Spec. Publ., 45, 1–29.

Dal Piaz, G. V. (2001). History of tectonic interpretations of the Alps. *Journal of Geodynamics*, 32, 99-114.

Dal Piaz, G. V., Bistacchi, A., & Massironi, M. (2003). Geological outline of the Alps. *Episodes*, 26(3), 175-180

Dauphas, N., Craddock, P.R., Asimow, P.D., Bennett, V.C., Nutman, A.P. and Ohnenstetter, D., 2009. Iron isotopes may reveal the redox conditions of mantle melting from Archean to Present. *Earth and Planetary Science Letters*, 288(1), pp.255-267.

Dauphas, N., Roskosz, M., Alp, E.E., Neuville, D.R., Hu, M.Y., Sio, C.K., Tissot, F.L.H., Zhao, J., Tissandier, L., Médard, E. and Cordier, C., 2014. Magma redox and structural controls on iron isotope variations in Earth's mantle and crust. *Earth and Planetary Science Letters*, 398, pp.127-140.

Debelmas, J. and Lemoine, M., 1970. The western Alps: palaeogeography and structure. *Earth-Science Reviews*, 6(4), pp.221-256.

Debret, B., Andreani, M., Delacour, A., Rouméjon, S., Trcera, N. and Williams, H., 2017. Assessing sulfur redox state and distribution in abyssal serpentinites using XANES spectroscopy. *Earth and Planetary Science Letters*, 466, pp.1-11.

Debret, B., Millet, M.A., Pons, M.L., Bouilhol, P., Inglis, E. and Williams, H., 2016. Isotopic evidence for iron mobility during subduction. *Geology*, 44(3), pp.215-218.

Dick, H.J., Lin, J. and Schouten, H., 2003. An ultraslow-spreading class of ocean ridge. *Nature*, 426(6965), p.405.

Evans, B.W., 2010. Lizardite versus antigorite serpentinite: Magnetite, hydrogen, and life (?). *Geology*, 38(10), pp.879-882.

Evans, K.A., 2012. The redox budget of subduction zones. *Earth-Science Reviews*, 113(1), pp.11-32.

Evans, K.A., Elburg, M.A. and Kamenetsky, V.S., 2012. Oxidation state of subarc mantle. *Geology*, 40(9), pp.783-786.

Foley, S.F., Barth, M.G. and Jenner, G.A., 2000. Rutile/melt partition coefficients for trace elements and an assessment of the influence of rutile on the trace element characteristics of subduction zone magmas. *Geochimica et Cosmochimica Acta*, 64(5), pp.933-938.

Frost, B.R. and Ballhaus, C., 1998. Comment on " Constraints on the origin of the oxidation state of mantle overlying subduction zones: an example from Simcoe, Washington, USA" by AD Brandon and DS Draper. *Geochimica et Cosmochimica Acta*, 62, pp.329-332.

Fujii, T., Moynier, F., Pons, M.L. and Albarède, F., 2011. The origin of Zn isotope fractionation in sulfides. *Geochimica et Cosmochimica Acta*, 75(23), pp.7632-7643

Gillis, K.M., 1995. Controls on hydrothermal alteration in a section of fast-spreading oceanic crust. *Earth and Planetary Science Letters*, 134(3-4), pp.473-489.

Goffe, B. and Chopin, C., 1986. High-pressure metamorphism in the Western Alps: zoneography of metapelites, chronology and consequences. *Schweizerische mineralogische und petrographische Mitteilungen*, 66(1-2), pp.41-52.

Greenberger, R.N., Mustard, J.F., Cloutis, E.A., Pratt, L.M., Sauer, P.E., Mann, P., Turner, K., Dyar, M.D. and Bish, D.L., 2015. Serpentinization, iron oxidation, and aqueous conditions in an ophiolite: Implications for hydrogen production and habitability on Mars. *Earth and Planetary Science Letters*, 416, pp.21-34.

Hart, S.R., Blusztajn, J., Dick, H.J. and Lawrence, J.R., 1994. Fluid circulation in the oceanic crust: Contrast between volcanic and plutonic regimes. *Journal of Geophysical Research: Solid Earth*, 99(B2), pp.3163-3173.

Hermann, J., Spandler, C., Hack, A. and Korsakov, A.V., 2006. Aqueous fluids and hydrous melts in high-pressure and ultra-high pressure rocks: implications for element transfer in subduction zones. *Lithos*, 92(3), pp.399-417.

Hunziker, J.C., Desmons, J. and Martinotti, G., 1989. Alpine thermal evolution in the central and the western Alps. *Geological Society, London, Special Publications*, 45(1), pp.353-367.

Inglis, E.C., Debret, B., Burton, K.W., Millet, M.A., Pons, M.L., Dale, C.W., Bouilhol, P., Cooper, M., Nowell, G.M., McCoy-West, A. and Williams, H.M., 2017. The behaviour of iron and zinc stable isotopes accompanying the subduction of mafic

oceanic crust: A case study from Western Alpine Ophiolites. *Geochemistry, Geophysics, Geosystems*.

Kelemen, P.B. and Manning, C.E., 2015. Reevaluating carbon fluxes in subduction zones, what goes down, mostly comes up. *Proceedings of the National Academy of Sciences*, 112(30), pp.E3997-E4006.

Kelley, K.A. and Cottrell, E., 2009. Water and the oxidation state of subduction zone magmas. *Science*, 325(5940), pp.605-607.

Kessel, R., Schmidt, M.W., Ulmer, P. and Pettke, T., 2005. Trace element signature of subduction-zone fluids, melts and supercritical liquids at 120-180 km depth. *Nature*, 437(7059), p.724.

Klein, F., Bach, W., Humphris, S.E., Kahl, W.A., Jöns, N., Moskowitz, B. and Berquó, T.S., 2014. Magnetite in seafloor serpentinite—Some like it hot. *Geology*, 42(2), pp.135-138.

Lagabrielle, Y. and Cannat, M., 1990. Alpine Jurassic ophiolites resemble the modern central Atlantic basement. *Geology*, 18(4), pp.319-322.

Lagabrielle, Y. and Cannat, M., 1990. Alpine Jurassic ophiolites resemble the modern central Atlantic basement. *Geology*, 18(4), pp.319-322.

Lagabrielle, Y., Bideau, D., Cannat, M., Karson, J.A. and MéVel, C., 1998. Ultramafic and Mafic Plutonic Rock Suites Exposed Along the Mid-Atlantic Ridge (10° N-30° N). Symmetrical/Asymmetrical Distribution and Implications for Seafloor Spreading Processes. *Faulting and Magmatism at Mid-Ocean Ridges*, pp.153-176.

Lagabrielle, Y., Brovarone, A.V. and Ildefonse, B., 2015. Fossil oceanic core complexes recognized in the blueschist metaophiolites of Western Alps and Corsica. *Earth-Science Reviews*, 141, pp.1-26.

Langmuir, C.H. and Forsyth, D.W., 2007. Mantle melting beneath mid-ocean ridges. *Oceanography*, 20(1), pp.78-89

Lee, C.T.A., Leeman, W.P., Canil, D. and Li, Z.X.A., 2005. Similar V/Sc systematics in MORB and arc basalts: implications for the oxygen fugacities of their mantle source regions. *Journal of Petrology*, 46(11), pp.2313-2336.

Lee, C.T.A., Luffi, P., Le Roux, V., Dasgupta, R., Albarède, F. and Leeman, W.P., 2010. The redox state of arc mantle using Zn/Fe systematics. *Nature*, 468(7324), p.681.

Lemoine, M., Tricart, P. and Boillot, G., 1987. Ultramafic and gabbroic ocean floor of the Ligurian Tethys (Alps, Corsica, Apennines): In search of a genetic imodel. *Geology*, 15(7), pp.622-625.

Li, X.H., Faure, M., Lin, W. and Manatschal, G., 2013. New isotopic constraints on age and magma genesis of an embryonic oceanic crust: The Chenaillet Ophiolite in the Western Alps. *Lithos*, 160, pp.283-291.

Liu, J., Bohlen, S.R. and Ernst, W.G., 1996. Stability of hydrous phases in subducting oceanic crust. *Earth and Planetary Science Letters*, 143(1-4), pp.161-171.

Macdonald, K.C., 1986. The crest of the Mid-Atlantic Ridge: Models for crustal generation processes and tectonics. *The Geology of North America*, pp.51-68.

Manatschal, G., Sauter, D., Karpoff, A.M., Masini, E., Mohn, G. and Lagabrielle, Y., 2011. The Chenaillet Ophiolite in the French/Italian Alps: An ancient analogue for an oceanic core complex?. *Lithos*, 124(3), pp.169-184.

Manning, C.E., 2004. The chemistry of subduction-zone fluids. *Earth and Planetary Science Letters*, 223(1), pp.1-16.

McKenzie, D., Jackson, J. and Priestley, K., 2005. Thermal structure of oceanic and continental lithosphere. *Earth and Planetary Science Letters*, 233(3), pp.337-349.

Meyer, J., ms, 1983, Mineralogie und Petrologie des Allalingabbros: Inauguraldissertation Universität Basel.

Morgan, J.P. and Chen, Y.J., 1993. The genesis of oceanic crust: Magma injection, hydrothermal circulation, and crustal flow. *Journal of Geophysical Research: Solid Earth*, 98(B4), pp.6283-6297.

Nichols, G.T., Wyllie, P.J. and Stern, C.R., 1996. Experimental melting of pelagic sediment, constraints relevant to subduction. *Subduction top to bottom*, pp.293-298.

Nocquet, J.M., Sue, C., Walpersdorf, A., Tran, T., Lenôtre, N., Vernant, P., Cushing, M., Jouanne, F., Masson, F., Baize, S. and Chery, J., 2016. Present-day uplift of the western Alps. *Scientific reports*, 6, p.28404.

O'Hanley, D.S. and Dyar, M., 1993. The composition of lizardite 1T and, the formation of magnetite in serpentinites. *American Mineralogist*, 78, pp.391-404.

Parkinson, I.J. and Arculus, R.J., 1999. The redox state of subduction zones: insights from arc-peridotites. *Chemical Geology*, 160(4), pp.409-423.

Peacock, S.M., 1993. The importance of blueschist→ eclogite dehydration reactions in subducting oceanic crust. *GSA Bulletin*, 105(5), pp.684-694.

Pognante, U., Perotto, A., Salino, C. and Toscani, L., 1986. The ophiolitic peridotites of the Western Alps: Record of the evolution of a small oceanic-type basin in the Mesozoic Tethys. *Tschermaks mineralogische und petrographische Mitteilungen*, 35(1), pp.47-65.

Poli, S. and Schmidt, M.W., 2002. Petrology of subducted slabs. *Annual Review of Earth and Planetary Sciences*, 30(1), pp.207-235

Polyakov, V.B. and Mineev, S.D., 2000. The use of Mössbauer spectroscopy in stable isotope geochemistry. *Geochimica et Cosmochimica Acta*, 64(5), pp.849-865.

Pons, M.L., Debret, B., Bouilhol, P., Delacour, A. and Williams, H., 2016. Zinc isotope evidence for sulfate-rich fluid transfer across subduction zones. *Nature communications*, 7, p.13794.

Rebay, G., Zanoni, D., Langone, A., Luoni, P., Tiepolo, M. and Spalla, M.I., 2017. Dating of ultramafic rocks from the Western Alps ophiolites discloses Late Cretaceous subduction ages in the Zermatt-Saas Zone. *Geological Magazine*, pp.1-18.

Rosenberg, N.D., Spera, F.T. and Haymon, R.M., 1993. The relationship between flow and permeability field in seafloor hydrothermal systems. *Earth and Planetary Science Letters*, 116(1), pp.135-153.

Rubatto, D., Gebauer, D. and Fanning, M., 1998. Jurassic formation and Eocene subduction of the Zermatt–Saas-Fee ophiolites: implications for the geodynamic evolution of the Central and Western Alps. *Contributions to Mineralogy and Petrology*, 132(3), pp.269-287.

Schauble, E.A., 2004. Applying stable isotope fractionation theory to new systems. *Reviews in Mineralogy and Geochemistry*, 55(1), pp.65-111.

Schmidt, M.W. and Poli, S., 1998. Experimentally based water budgets for dehydrating slabs and consequences for arc magma generation. *Earth and Planetary Science Letters*, 163(1), pp.361-379.

Schuessler, J.A., Schoenberg, R. and Sigmarrsson, O., 2009. Iron and lithium isotope systematics of the Hekla volcano, Iceland—evidence for Fe isotope fractionation during magma differentiation. *Chemical Geology*, 258(1), pp.78-91.

Schwartz, S., Guillot, S., Reynard, B., Lafay, R., Debret, B., Nicollet, C., Lanari, P. and Auzende, A.L., 2013. Pressure–temperature estimates of the lizardite/antigorite transition in high pressure serpentinites. *Lithos*, 178, pp.197-210.

Sossi, P.A., Foden, J.D. and Halverson, G.P., 2012. Redox-controlled iron isotope fractionation during magmatic differentiation: an example from the Red Hill intrusion, S. Tasmania. *Contributions to Mineralogy and Petrology*, 164(5), pp.757-772.

Staudigel, H., Plank, T., White, B. and Schmincke, H.U., 1996. Geochemical fluxes during seafloor alteration of the basaltic upper oceanic crust: DSDP Sites 417 and 418. *Subduction top to bottom*, pp.19-38.

Stein, S. and Stein, C.A., 1996. Thermo-Mechanical Evolution of Oceanic Lithosphere: Implications for the Subduction Process and Deep Earthquakes. *Subduction top to bottom*, pp.1-17.

Syracuse, E.M., van Keken, P.E. and Abers, G.A., 2010. The global range of subduction zone thermal models. *Physics of the Earth and Planetary Interiors*, 183(1), pp.73-90.

Telus, M., Dauphas, N., Moynier, F., Tissot, F.L., Teng, F.Z., Nabelek, P.I., Craddock, P.R. and Groat, L.A., 2012. Iron, zinc, magnesium and uranium isotopic fractionation during continental crust differentiation: The tale from migmatites, granitoids, and pegmatites. *Geochimica et Cosmochimica Acta*, 97, pp.247-265.

Teng, F.Z., Dauphas, N., Helz, R.T., Gao, S. and Huang, S., 2011. Diffusion-driven magnesium and iron isotope fractionation in Hawaiian olivine. *Earth and Planetary Science Letters*, 308(3), pp.317-324.

Teng, F.Z., Dauphas, N., Huang, S. and Marty, B., 2013. Iron isotopic systematics of oceanic basalts. *Geochimica et Cosmochimica Acta*, 107, pp.12-26.

Tricart, P. and Schwartz, S., 2006. A north-south section across the Queyras Schistes lustrés (Piedmont zone, western Alps): Syn-collision refolding of a subduction wedge. *Eclogae Geologicae Helvetiae*, 99(3), pp.429-442.

Tricart, P., 1984. From passive margin to continental collision; a tectonic scenario for the Western Alps. *American Journal of Science*, 284(2), pp.97-120.

Tricart, P., Schwartz, S., Sue, C. and Lardeaux, J.M., 2004. Evidence of synextension tilting and doming during final exhumation from analysis of multistage faults (Queyras Schistes lustrés, Western Alps). *Journal of Structural Geology*, 26(9), pp.1633-1645.

Trümpy, R., 2001. Why plate tectonics was not invented in the Alps. *International Journal of Earth Sciences*, 90(3), pp.477-483.

Ulmer, P. and Trommsdorff, V., 1995. Serpentine stability to mantle depths and subduction-related magmatism. *Science*, pp.858-858.

Weyer, S. and Ionov, D.A., 2007. Partial melting and melt percolation in the mantle: the message from Fe isotopes. *Earth and Planetary Science Letters*, 259(1), pp.119-133.

Williams, H.M. and Bizimis, M., 2014. Iron isotope tracing of mantle heterogeneity within the source regions of oceanic basalts. *Earth and Planetary Science Letters*, 404, pp.396-407.

Williams, H.M., McCammon, C.A., Peslier, A.H., Halliday, A.N., Teutsch, N., Levasseur, S. and Burg, J.P., 2004. Iron isotope fractionation and the oxygen fugacity of the mantle. *Science*, 304(5677), pp.1656-1659.

Williams, H.M., Nielsen, S.G., Renac, C., Griffin, W.L., O'Reilly, S.Y., McCammon, C.A., Pearson, N., Viljoen, F., Alt, J.C. and Halliday, A.N., 2009. Fractionation of oxygen and iron isotopes by partial melting processes: implications for the interpretation of stable isotope signatures in mafic rocks. *Earth and Planetary Science Letters*, 283(1), pp.156-166.

Williams, H.M., Peslier, A.H., McCammon, C., Halliday, A.N., Levasseur, S., Teutsch, N. and Burg, J.P., 2005. Systematic iron isotope variations in mantle rocks and minerals: the effects of partial melting and oxygen fugacity. *Earth and Planetary Science Letters*, 235(1), pp.435-452.

Wood, B., Brydznia, L. and Johnson, K., 1990. Mantle oxidation state and its relationship to tectonic environment and fluid speciation. *Science*, 248(4953), pp.337-345.

Chapter 2.

The Behaviour of Iron and Zinc Stable Isotopes Accompanying the Subduction of Mafic Oceanic Crust: A Case Study from Western Alpine Ophiolites

This chapter has been published as a peer reviewed article in the journal Geochemistry, Geophysics, Geosystems. A copy of journal-formatted version of this chapter is included in the supplementary information of this thesis.

Citation: Inglis, E.C., Debret, B., Burton, K.W., Millet, M.A., Pons, M.L., Dale, C.W., Bouilhol, P., Cooper, M., Nowell, G.M., McCoy-West, A. and Williams, H.M., 2017. The behaviour of iron and zinc stable isotopes accompanying the subduction of mafic oceanic crust: A case study from Western Alpine Ophiolites. *Geochemistry, Geophysics, Geosystems*.

DOI: 10.1002/2016GC006735

Abstract

Arc lavas display elevated $\text{Fe}^{3+}/\Sigma\text{Fe}$ ratios relative to MORB. One mechanism to explain this is the mobilization and transfer of oxidised or oxidising components from the subducting slab to the mantle wedge. Here we use iron and zinc isotopes, which are fractionated upon complexation by sulfide, chloride and carbonate ligands, to remark on the chemistry and oxidation state of fluids released during prograde metamorphism of subducted oceanic crust. We present data for metagabbros and metabasalts from the Chenaillet massif, Queyras complex and the Zermatt-Saas ophiolite (Western European Alps), which have been metamorphosed at typical subduction zone P - T conditions and preserve their prograde metamorphic history. There is no systematic, detectable fractionation of either Fe or Zn isotopes across metamorphic facies, rather the isotope composition of the eclogites overlaps with published data for MORB. The lack of resolvable Fe isotope fractionation with increasing prograde metamorphism likely reflects the mass balance of the system, and in this scenario Fe mobility is not traceable with Fe isotopes. Given that Zn isotopes are fractionated by S- and C-bearing fluids, this suggests that relatively small amounts of Zn are mobilised from the mafic lithologies in within these types of dehydration fluids. Conversely, metagabbros from the Queyras that are in close proximity to metasediments display a significant Fe isotope fractionation. The

covariation of $\delta^{56}\text{Fe}$ of these samples with selected fluid mobile elements suggests the infiltration of sediment derived fluids with an isotopically light signature during subduction.

2.1. Introduction

Oceanic lithosphere formed at mid-ocean ridges is progressively hydrated, altered and oxidised by interaction with seawater before being recycled into the deep mantle at convergent plate margins. During the subduction of oceanic lithosphere the increase in pressure and temperature (P - T) conditions leads to the destabilisation of hydrous mineral phases via a series of metamorphic reactions and the release of dehydration fluids and/or slab derived melts into the overlying crust and sub-arc mantle (e.g. *Schmidt and Poli, 2014, Hermann and Green, 2001, Bouilhol et al., 2015*). Alongside the release of structurally bound H_2O from subducted sediments, mafic and ultramafic sections of the slab, the mechanical compaction of sediments at shallower depths (<20km) can result in pore fluid expulsion in the fore arc region (*Henson et al., 2004, Rüpke et al., 2004*) and localised metasomatism of lithologies in the residual subducting slab (e.g. *Marschall et al., 2009, Penniston-Dorland et al., 2012, Vitale-Brovarone et al., 2014, Debret et al., 2016a*). The release of slab derived sub- (*Hermann et al., 2006*) or super-critical (*Kessel et al., 2005*) fluids, and melts (*Foley et al., 2000*) has been invoked to explain a number of distinct geochemical signatures observed in arc lavas relative to Mid-Ocean Ridge (MORB) and Ocean Island Basalts (OIB), including the enrichment of fluid mobile elements (*Hawkesworth et al., 1993*) and their elevated $\text{Fe}^{3+}/\Sigma\text{Fe}$ ratios (*Brandon and Draper, 1996, Frost and Ballhaus, 1998, Parkinson and Arculus, 1999, Kelley and Cottrell, 2009*). At the same time, residual oceanic crust is ultimately recycled back into the deep mantle, providing a source for the geochemical heterogeneity that is sampled by MORBs and OIBs. Consequently, developing a clear understanding of the processes that govern element mobility during subduction zone metamorphism and metasomatism is crucial for elucidating both the controls on arc magmatism and the long-term chemical evolution of the mantle (*Magni et al., 2014*). This study aims to examine the effect of subduction zone metamorphism and metasomatism on the redox budget of subducted mafic oceanic crust using the stable iron (Fe) and zinc (Zn) isotopes as tracers of elemental mobility, which are thought to be sensitive to complexation by aqueous sulfate (SO_x) and carbonate (CO_x) ligands (*Fujii et al., 2011, Hill et al., 2010, Black et al., 2011*).

Recent advances in mass spectrometric techniques have seen the emerging field of non-traditional stable isotope geochemistry applied to numerous scientific problems in both

high- and low-temperature natural settings. Theory predicts that equilibrium stable isotope fractionation decreases with increasing temperature ($1/T^2$) (Urey, 1947, Schauble, 2003). Nonetheless, high-precision Fe and Zn stable isotope measurements have shown that both of these systems are sensitive to high temperature petrogenetic processes, such as mantle melting (Weyer *et al.*, 2005, Williams *et al.*, 2004; 2005; 2009; 2015, Weyer and Ionov, 2007, Dauphas *et al.*, 2014, Konter *et al.*, 2016), igneous differentiation (Sossi *et al.*, 2012, Telus *et al.*, 2012, Chen *et al.*, 2013, Schuessler *et al.*, 2009, Teng *et al.*, 2011; 2013, Doucet *et al.*, 2016) and for Fe, changes in redox state (Williams *et al.*, 2004, Dauphas *et al.*, 2009). It is now well established from both radiogenic and stable isotopes that the loss of fluid mobile elements from sediments imparts a distinct signature to arc lavas (e.g. Pearce, 1982, Plank and Langmuir, 1993, Elliott *et al.*, 1997, Nebel *et al.*, 2010, Freymuth *et al.*, 2015), and the dissolution of carbonate sediments during subduction may play a role in controlling the redox budget of the sub-arc mantle (Frezzotti *et al.*, 2011, Evans, 2012). Despite this, it has been suggested that subducted sediments exert little influence on the Fe isotope composition of arc lavas, and that Fe isotope variations in erupted arc products result from depletion of the mantle source and fractional crystallization of the resulting melt (Nebel *et al.*, 2015). Additionally, the release of sulfur from the subducting slab could serve as a powerful oxidizing agent in this setting, as if sulfur was to be released from the slab as sulfate, then 1 mol of sulfur could serve to oxidise 8 mol of reduced Fe^{2+} to oxidized Fe^{3+} .

More recently both Fe and Zn stable isotopes have been utilized to trace the mobility of Fe and oxidising sulfate (SO_x) and/or carbonate (CO_x) species during the prograde devolatilisation of subducted slab serpentinites (Debret *et al.*, 2016b, Pons *et al.*, 2016). However, while element depletion has been shown to occur from some parts of the mafic oceanic crust (e.g. Dale *et al.*, 2007), the nature of those fluids remains poorly constrained. This study aims to examine the effect of subduction zone metamorphism on redox sensitive elements in mafic oceanic crust. To this end we have measured stable Fe and Zn isotope in the metamorphic rocks of an exhumed subducted slab to trace the mobility of redox sensitive Fe and oxidizing SO_x/CO_x -rich fluids during the subduction related, prograde metamorphism and metasomatism of the mafic oceanic crust.

One approach to assessing the controls on Fe and Zn isotopes during subduction-related metamorphism is to compare their behaviour in oceanic crustal rocks across a range of P - T conditions. This study uses samples of metabasalts and metagabbros from three meta-ophiolite massifs in the Western European Alps - Chenaillet, Queyras and Zermatt-Saas. These meta-ophiolites record prograde metamorphic conditions that range from

greenschist to blueschist to eclogite, that are taken to be representative of a P - T path for subducting mafic oceanic crust (e.g. Guillot *et al.*, 2009) (**Figure 2.1a**). Samples have also been selected based on varying degree of fluid related slab metasomatism (i.e. those that show evidence for interaction with externally derived fluids released from proximal subducting sediments), thus allowing us to not only examine the effect of prograde metamorphism but also how metasomatic modification could potentially alter the Fe and Zn isotope composition of down-going mafic lithologies.

2.2. Geological Setting and Sample Petrology

The ophiolite complexes of the Western European Alps provide a unique insight into the processes acting upon oceanic lithosphere during subduction (e.g. Scambelluri and Philippot, 2001, Guillot *et al.*, 2009, Debret *et al.*, 2013, Vils *et al.*, 2011, Evans *et al.*, 1979, Hermann *et al.*, 2000, Scambelluri *et al.*, 2001; 2014). These meta-ophiolites were formed in a magma-poor setting, i.e. a slow or ultra-slow spreading centre or an ocean-continent transition, during the opening of the Ligurian Ocean in the Jurassic (Lagabrielle and Cannat, 1990, Bernoulli *et al.*, 2003, Lagabrielle *et al.*, 2014), before being subsequently metamorphosed at various P - T conditions and exhumed during the Alpine orogeny (Rubatto *et al.*, 1998, Brouwer *et al.*, 2004). This study is focused on three Alpine ophiolitic complexes that record different P - T paths during alpine evolution (**Figure 2.1a**). These are the Chenaillet massif, the Queyras Schiste-Lustrés and Zermatt-Saas ophiolitic complexes. The Chenaillet massif mainly preserves low-pressure “ocean floor” parageneses, while the Queyras Schiste-Lustrés and Zermatt-Saas ophiolite complexes record the high-pressure transformation of subducted oceanic lithosphere, ranging from blueschist to eclogite facies, respectively.

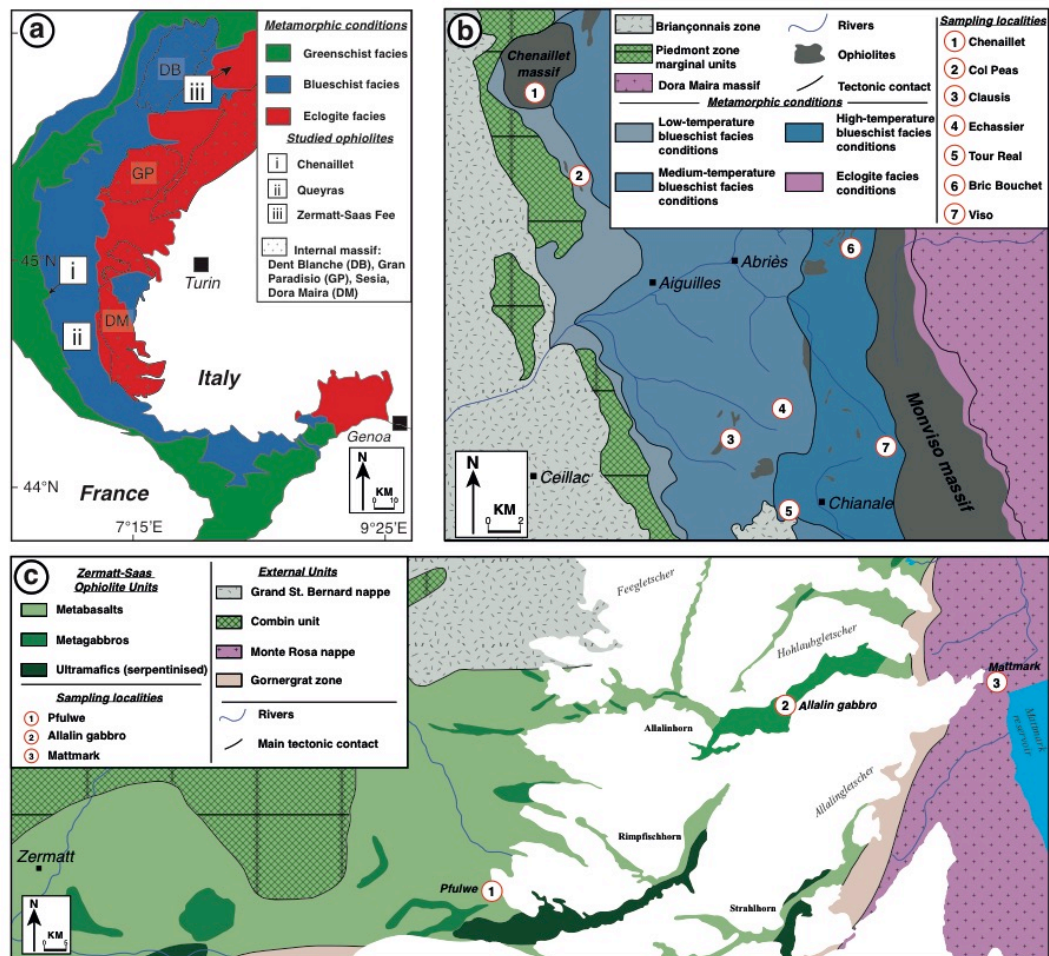


Figure 2.1. Inset **A** shows the location of the three Western Alps ophiolitic complexes (Chenaillet, Queyras Schiste Lustrés and Zermatt Saas) that were sampled as part of this study, within the context of Alpine metamorphic conditions. Inset **B** shows the sampling localities for the Chenaillet massif and Queyras Schiste Lustré complex and the tectono-metamorphic conditions within the area (modified after Schwartz et al., 2013). Inset **C** shows the sampling localities for the Zermatt-Saas area and the key lithological units of the complex.

2.2.1 The Chenaillet massif

The Chenaillet massif is located in the external Piedmont zone, 6 km west of Briançon (**Figure 2.1b**). It is a structural klippe, overlying the Lago Nero-Replatte unit (Caby, 1995). The massif preserves a classic sequence of oceanic lithosphere comprising, from top to bottom, oceanic sediments and/or basalts overlying gabbroic pods and serpentinised mantle peridotite. Detailed petrological, geochemical and structural studies have suggested that this ophiolite represents a fossil oceanic core complex, likely formed at a slow-spreading ridge setting (Lagabrielle et al., 1990, Charlot-Prat, 2005, Manatschal et al., 2011).

Unlike the majority of the western Alpine ophiolites, the Chenaillet massif was only weakly affected by alpine subduction (Mevel, 1978, Debret *et al.*, 2016a). Instead, the metagabbros here mainly record a low-pressure metamorphic overprint, ranging from amphibolite to greenschist facies conditions (Mevel *et al.*, 1978, Debret *et al.*, 2016a). One coarse-grained metagabbro sample (PR4) was analysed in this study. This sample represents an undeformed metagabbro, mainly composed of plagioclase and clinopyroxene. The clinopyroxene crystals display small (~20 μm) coronas of green and brown amphibole. Minor amounts (<10%) of actinolite are also observed, both within the plagioclase domain and associated with the amphibole coronas.

2.2.2 Queyras Schiste lustrés complex

The Queyras Schiste lustrés complex is located in the Piedmont zone of the south-western Alps (**Figure 2.1b**). It comprises units belonging to the distal European margin and from the nearby oceanic domain (Lemoine *et al.*, 1987) that were juxtaposed during alpine subduction and collision in the Late Cretaceous to Tertiary (Tricart, 1984). This complex comprises ~10% meta-ophiolite bodies embedded in a sedimentary-rich environment, consisting of Jurassic to Lower Cretaceous clastic and metasedimentary rocks (Lagabrielle *et al.*, 1984, Lemoine *et al.*, 1987) and has previously been interpreted to represent a palaeo-sedimentary wedge (Tricart and Schwartz, 2006).

Three tectono-metamorphic domains have been identified within the complex by Schwartz *et al.*, (2013). The P - T conditions of these domains range from low-temperature blueschist facies conditions ($P= 0.9\text{-}1.1$ GPa, $T= 320\text{-}340$ °C) in the west, to medium-temperature blueschist facies conditions ($P= 1.0\text{-}1.2$ GPa, $T= 340\text{-}360$ °C) and high-temperature blueschist facies conditions ($P= 1.2\text{-}1.5$ GPa, $T= 380\text{-}470$ °C) towards the east (**Figure 2.1b**).

Eight metagabbros were collected from the medium- and high-temperature blueschist domains within five different metagabbroic massifs. Four metagabbro samples were collected from the Echassier (CE7 and CE12) and Clausis (QE1 and QE10) meta-ophiolites that belong to the medium temperature domain (**Figure 2.1b**). These samples predominantly display coarse-grained textures and are typically composed of clinopyroxene, partially recrystallized to glaucophane, while plagioclase is no longer present and is replaced by fine aggregate of lawsonite, chlorite and albite with minor amounts of ilmenite, titanite and late

zoisite. Within these massifs the interface between metasedimentary lithologies and metagabbros is demarked by metasomatic contacts, which represent a zone of intense localised fluid circulation, which has occurred during subduction (*Debret et al.*, 2016a). In order to constrain the nature of the fluid circulating within these zones during subduction, we selected a sample from one metasomatic contact (CE8a) from the Echassier meta-ophiolite. This sample comprises glaucophane, chlorite, quartz, epidote and titanite. Four samples from the high temperature domain were collected from the Refuge du Viso (RV7), Tour Real (TR6 and TR9) and the Bric Bouchet (BB1) meta-ophiolites (**Figure 2.1b**). The sample RV7 preserves relicts of brown amphibole associated with green amphibole coronas and partially recrystallized into glaucophane, while the plagioclase domain is recrystallized to fine aggregates (<10 µm) of lawsonite, chlorite, quartz and magnetite. Samples TR6 and TR9 consist of lawsonite, magnetite, chlorite and glaucophane without any low-pressure relicts, while BB1 displays a similar coarse-grained texture as the Tour Real samples but is composed of stretched porphyroblasts of brown amphibole in association with needles of tremolite and actinolite. In this sample the plagioclase domain is finely recrystallized to aggregates of cloudy plagioclase and zoisite.

In addition to the metagabbro samples, two sedimentary lithologies from the low- and high-temperature domains were also collected. One sediment sample (CP1) was taken from the Col Peas area within the low-temperature blueschist domain, while the second sediment sample (RV5) comes from the Refuge du Viso within the high-temperature domain. These samples are proximal within tens of meters to the sampled metagabbros. Both of these samples are similar in mineralogy and are comprised of calcite, quartz aggregates, stringy magnetite, phengite, chlorite and titanite, with both preserving a well-developed foliation.

2.2.3 Zermatt-Saas

The Zermatt-Saas complex of Alpine Switzerland (**Figure 2.1c**) represents a continuous slice of oceanic lithosphere, including ultramafic, mafic and metasedimentary lithologies, which have been metamorphosed under eclogite facies conditions during subduction (*Bucher et al.*, 2005). The Zermatt-Saas ophiolite is preserved within a collisional nappe stack, underlain by the Monte Rosa continental basement, and overlain by the Dent Blanche nappe (*Angiboust et al.*, 2009). Twelve metabasaltic and metagabbroic rocks were sampled in three different areas of the complex, which record various P-T conditions (**Figure**

2.1c): the Pfulwe area located to the east of the town of Zermatt which records a metamorphic climax of 24-26 kbar and 550-600 °C (*Bucher et al.*, 2005); the Allalin gabbro which is situated between Zermatt and Saas-Fee and records a metamorphic climax of 2.5 GPa and 610 °C (*Bucher & Grapes*, 2009); and the terminal moraine of the Hohlaub and Allalin glaciers at the Mattmark dam area, which derives from the Allalin gabbro and corresponds to the same peak metamorphic conditions as given for the Allalin gabbro (*Dale et al.*, 2007). These samples are discussed in detail in *Dale et al.*, 2007; 2009.

Two different types of metabasalt were collected at Pfulwe. The first of these being samples of eclogitised pillow basalts that comprise garnet, omphacite, quartz, zoisite, paragonite and phengite. Samples were collected from both the core (S02/75iiiC) and rim (S02/75iiR & S02/75iiiR) of individual pillows. The second type of metabasalt collected at Pfulwe are massive basaltic eclogites (S02/41ii & S02/41v), which comprise garnet, omphacite, glaucophane, epidote, paragonite and phengite. In addition to the basaltic eclogites a range of metagabbros from the Allalin and Mattmark areas have also been studied. The three metagabbro samples collected from the Allalin gabbro body display a range in mineralogy. Samples S01/5G and S02/83viiiG consist of olivine, fresh and dusty plagioclase and pyroxene without any evidence of an eclogitic overprint, while sample S01/35iiix is a gabbroic eclogite and is composed of garnet, glaucophane, talc, zoisite, omphacite, paragonite and rutile. The occurrence of both primary gabbroic and metamorphic eclogitic assemblages within the Allalin metagabbros has been noted before (*Meyer*, 1983, *Dale et al.*, 2007, *Bucher & Grapes*, 2009) and is attributed to a combination of the relatively anhydrous nature of the gabbroic protolith, and the short period and only moderate peak temperature of metamorphism. Of the samples collected from the Mattmark moraine, three (S01/40viix, S02/85ixE, S01/40vx) display typical eclogitic assemblages of coronitic garnet, omphacite, paragonite, glaucophane, phengite and quartz, while S02/85ixB shows evidence for late retrogression (barroisite, talc, zoisite and chlorite).

2.3. Analytical Methods

2.3.1 Major and trace element concentrations

Samples from Zermatt-Saas have been previously characterised for major and trace element concentrations by *Dale et al.*, (2007). Samples from the Chenaillet

and Queyras meta-ophiolites were analysed for major element concentration by wavelength dispersive X-Ray Fluorescence at the University of Edinburgh after the method detailed by *Fitton et al.*, (1998). An external international rock standard (USGS BHVO-1) was measured alongside the samples as a check on precision and accuracy. Measured major element values of this geostandard compare well with the average values obtained in Edinburgh (<5%) and with accepted values published elsewhere (*Govindaraju, 1994*; <5%). The loss on ignition corrected major element concentrations of the samples and standards analysed as part of this study are presented in supplementary information (**Table 2.1**)

Trace element concentrations for the Chenaillet and Queyras samples were determined at the National Oceanography Centre, Southampton. Sample powders were digested using concentrated HF and HNO₃ acids, evaporated to dryness and re-dissolved in 3% HNO₃ spiked with 5 ppb In and Re and 20 ppb Be for use as internal standards. The samples were analysed on a Thermo X-Series 2 Quadrupole Inductively Coupled Plasma-Mass Spectrometer (ICP-MS), calibrated against 5 international rock standards, with JA-2 and BHVO-2 run as unknowns. Analysis of these unknowns compare well to the published values, with the external reproducibility being <5% for Sc, Ti, V, Ni, Cu, As, Rb, Sr, Y, Cd, Sb, Ba, La, Ce, Nd, Sm, Eu, Gd, Tb, Ho, Tm, Lu, Li, Co, Pr, Dy, Er and Yb and between 5-10% for all other elements. The trace element concentrations are presented in supplementary information (**Table 2.1**)

2.3.2 Fe isotope measurements

The Fe isotope measurements were carried out on whole rock powders at Durham University. Isotope ratios are reported as $\delta^{56}\text{Fe}$ in permil notation relative to IRMM-014 external standard, and $\delta^{57}\text{Fe}$ is given to demonstrate mass dependency of the measurements. All reported errors are 2SD unless stated otherwise.

$$\delta^{56}\text{Fe} = \left(\frac{{}^{56}\text{Fe}/{}^{54}\text{Fe}_{\text{sample}}}{{}^{56}\text{Fe}/{}^{54}\text{Fe}_{\text{IRMM-014}}} - 1 \right) * 1000$$

$$\delta^{57}\text{Fe} = \left(\frac{{}^{57}\text{Fe}/{}^{54}\text{Fe}_{\text{sample}}}{{}^{57}\text{Fe}/{}^{54}\text{Fe}_{\text{IRMM-014}}} - 1 \right) * 1000$$

The procedure for the chemical separation of Fe is described in detail by *Williams et al.*, (2009) but is briefly outlined here. Samples were dissolved using concentrated HF and HNO₃ acids in 7 mL PTFE Teflon square body beakers with

wrench top closures in an oven at 165 °C for 3 days. These were then further attacked with a 1:1 mix of concentrated HCl and HNO₃ to ensure all refractory phases, such as spinel and rutile, were fully digested. Finally samples were brought into solution in 6M HCl prior to column chemistry. Quantitative purification of Fe was achieved by chromatographic exchange, using Biorad AG1-X4 anion exchange resin in an HCl medium. All reagents used in the chemistry and mass spectrometry procedures were distilled in sub-boiling Teflon two-bottle stills at Durham University. The total amount of Fe processed through the columns was typically around 650 µg. The total procedural blank contribution was <10 ng of Fe, which is negligible compared to the amount of Fe in the samples. Isotope measurements follow that of *Weyer and Schwieters, 2003* but briefly described here. Measurements were performed by multiple-collector (MC) ICP-MS (Thermo Scientific Neptune Plus) in medium-resolution mode, using an Elemental Scientific Instruments Apex HF desolvating nebuliser for sample introduction. The mass resolution, which is defined as $\text{mass}/\Delta\text{mass}$ at 95% and 5% of the beam intensity of the ⁵⁶Fe peak edge, ranged between 7500-9000 depending on daily tuning of the instrument as well as the age of the medium resolution beam slit. At this resolution it was possible to adequately resolve the ⁴⁰Ar¹⁶O+, ⁴⁰Ar¹⁶O¹H+, ⁴⁰Ar¹⁸O+ and ⁴⁰Ar¹⁴N+ polyatomic species that can interfere on the ⁵⁶Fe, ⁵⁷Fe, ⁵⁸Fe and ⁵⁴Fe masses respectively. Instrumental mass bias was corrected for by sample-standard bracketing, where the beam intensities of the bracketing standard and sample were matched to within 10%. Both sample and standard solutions were run at 2ppm, giving a beam intensity of between 35-50 V on ⁵⁶Fe, depending on daily sensitivity. In addition to all Fe masses, ⁵³Cr and ⁶⁰Ni were also monitored and an online Cr and Ni correction was applied to account for any isobaric interferences from ⁵⁴Cr and ⁵⁸Ni on the ⁵⁴Fe and ⁵⁸Fe masses. These corrections, were either negligible or non-existent due to the effective separation of Fe from Cr and Ni during column chemistry. An in-house standard of FeCl₂, was analysed throughout each analytical sessions giving a mean $\delta^{56}\text{Fe}$ value of $-0.70 \pm 0.06\text{‰}$ and mean $\delta^{57}\text{Fe}$ value of -1.05 ± 0.06 , where $n=69$, these values are in excellent agreement with previously published measurements of this standard (*Mikutta et al., 2009*). In addition to this internal standard, an external geostandard, USGS BIR-1, was processed through chemistry and analysed alongside samples. The BIR-1 analysis gave a mean value of $+0.06 \pm 0.02\text{‰}$ for $\delta^{56}\text{Fe}$ and $+0.08 \pm 0.03\text{‰}$ for $\delta^{57}\text{Fe}$ based on nine measurements from different analytical sessions on the same dissolution. This value is in good agreement with previously published values (*Millet et al., 2012*,

Hibbert *et al.*, 2012, Sossi *et al.*, 2015), which notably were carried out at both high- and low-resolution modes on Nu Plasma and Thermo Neptune instruments.

2.3.3 Zn isotope measurements

The method used for the chemical purification of Zn is based on that of Moynier *et al.*, (2006), adapted by Pons *et al.*, (2011). Depending on the Zn concentration of samples, between 30-50 mg of rock powder was digested in a 2:1 mix of concentrated HF-HNO₃ in 7 mL PTFE Teflon square body beakers with wrench top closures in an oven at 165 °C for 3 days. As Zn is likely to partition into the fluoride phase as ZnF₂, it is important that all fluorides are fully decomposed prior to column separation, and this was achieved by repeated refluxes of the sample residue in 6M and concentrated HCl. All samples were visually inspected for the presence of fluorides before being evaporated to dryness and brought back into solution in 1.5M HBr, ready for column chemistry.

Quantitative separation of Zn from matrix elements was achieved using Teflon shrink fit columns filled with 0.5ml of Biorad AG1-X4 anion exchange resin. The resin was cleaned on the column by 4 repeated passes of 0.5M HNO₃ and Milli-Q (MQ) ultrapure (18.2 MΩ) H₂O, before conditioning in 3 ml of 1.5M HBr. The sample solution was then added to the column and the matrix eluted in 3 ml of 1.5M HBr. Zn was collected from the column in 0.5M HNO₃. To ensure total separation of Zn from matrix elements this column separation procedure was repeated twice. With the exception of the HBr, which was purchased from ROMIL Ltd. at ultra pure “UpA” grade, all reagents were distilled by sub-boiling in Teflon stills at Durham University. The total procedural blank is <20ng of Zn, which is negligible compared to the >2 µg of sample Zn processed.

Isotope ratio measurements were performed on a Thermo Scientific Neptune Plus MC-ICPMS at Durham University running in low-resolution mode. Samples were introduced via an ESI PFA 50 µl/min nebuliser attached to an ESI cinnabar glass spray chamber. Sample solutions were run at a concentration of 750 ppb Zn in 0.5M HNO₃, this typically gives signal intensities of ~3-4 V on ⁶⁴Zn. To correct for the effect of instrumental mass bias a combined standard-sample bracketing and empirical external normalisation method was adopted. This method applies an external normalisation correction (Maréchal *et al.*, 1999, Mason *et al.*, 2004, Chen *et al.*, 2009) by doping both sample and standard solutions with a pure Cu solution (Alfa-Aesar) at a Zn/Cu ratio of 3/1. In

addition, each sample analysis was bracketed against measurement of Alfa-Aesar pure Zn standard solution, which had been matched to the same concentration as the sample. During analysis the masses of ^{63}Cu , ^{64}Zn , ^{65}Cu , ^{66}Zn , ^{67}Zn and ^{68}Zn were collected, as well as ^{62}Ni to correct, using Ni natural abundances, for ^{64}Ni that is isobaric on ^{64}Zn . In all cases no on- or off-line Ni correction was performed, as the calculated contribution of ^{64}Ni to the 64 mass peaks was always lower than 0.5% of the total beam intensity.

The Zn isotope composition of the sample is presented as a delta value in permil notation relative to the JMC-Lyon isotopic standard.

$$\delta^{66}\text{Zn} = ((^{66}\text{Zn} / ^{64}\text{Zn}_{\text{sample}}) / (^{66}\text{Zn} / ^{64}\text{Zn}_{\text{JMC-Lyon}}) - 1) * 1000$$

Due to a limited supply of the JMC-Lyon standard solution, samples were measured relative to an Alfa-Aesar pure Zn solution. This standard is offset from JMC-Lyon by 0.27 ‰ for $\delta^{66}\text{Zn}$ (2sd = 0.04 ‰; n = 87; over four different analytical sessions); as such we were able to correct our measured value by this factor and present our data relative to JMC-Lyon, as is widely accepted. Precision and accuracy were assessed using the international rock reference material, USGS BCR-2. This rock was processed through chemistry alongside sample powders and measured during analytical sessions. The value obtained for $\delta^{66}\text{Zn}$ was $+0.30\text{‰} \pm 0.04\text{‰}$ based on five measurements of the same sample aliquot during two analytical sessions. This value agrees well with published results of BCR-2 (*Herzog et al.*, 2009, *Moeller et al.*, 2012).

2.4. Results

2.4.1 Major and trace element data

Major and trace element data for all samples analysed in this study are given in the supplementary material (**Table 2.1**).

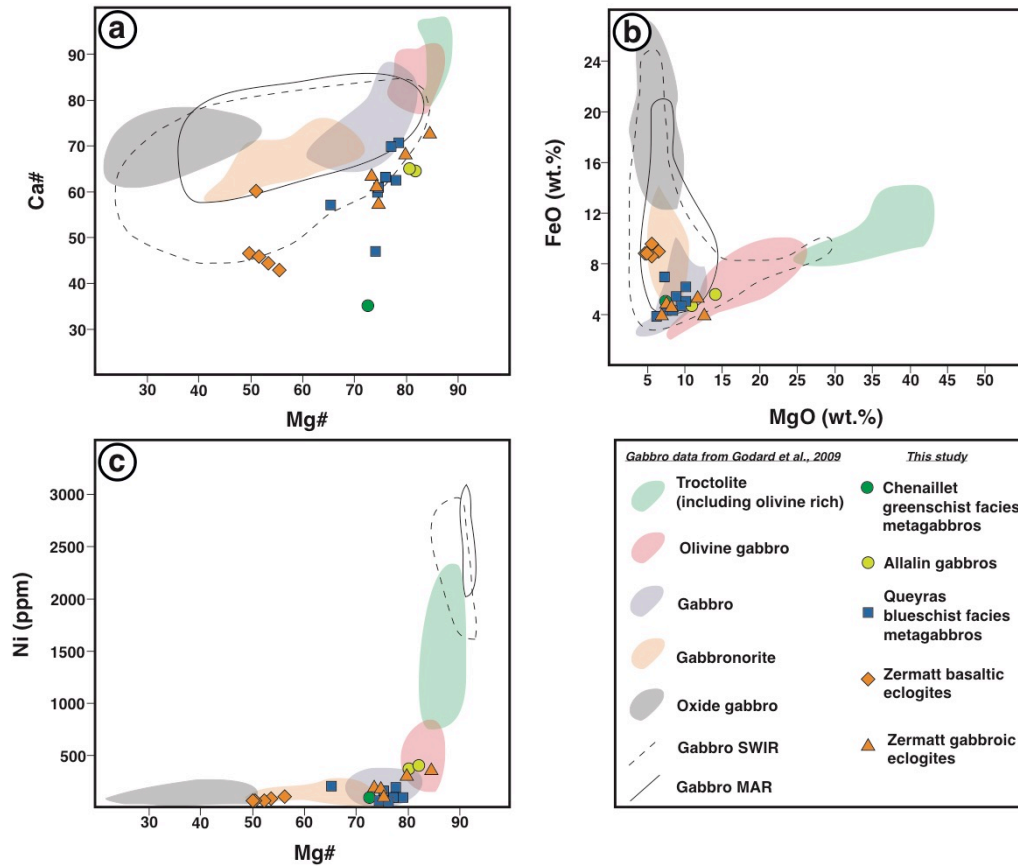


Figure 2.2. Major element plots of the metagabbroic and metabasaltic samples analysed as part of this study. The samples are compared to the fields for oceanic gabbros defined by Godard et al., 2009. Ca# is defined as $Ca_{TOT} [moles]/Ca_{TOT} [moles] + Na_{TOT} [moles]$ and Mg# as $Mg_{TOT} [moles]/Mg_{TOT} [moles] + Fe_{TOT} [moles]$. The field defined by the black dashed line is compiled data from Mid-Atlantic Ridge gabbros, while the field defined by the black solid line is compiled data from South-West Indian Ridge gabbros. Both of these compilations are taken from Godard et al., 2009.

With respect to **Figure 2.2b** and **c**, it is apparent that the range in Mg# ($[Mg_{Moles}]/([Mg_{Moles}] + [Fe_{Moles}])$) (51-84), MgO (5.6-14.3 wt%), FeO (4.1 -9.6 wt%) and Ni (45 -385 ppm) is consistent with the fields defined for gabbronorite, gabbro and olivine gabbro by previous work (Godard et al., 2009), with the majority of samples falling within the gabbro field. The Ca# ($[Ca_{Moles}]/([Ca_{Moles}] + [Na_{Moles}])$) of the analysed samples are lower than those of seafloor oceanic gabbros (**Figure 2.2a**), with a range between 36-73.

The major element composition of the metasediments (RV5 and CP1) and metasomatic contact zone (CE8a) from Queyras are not shown but presented alongside the data for the metabasalt and metagabbros samples in supplementary

material (**Table 2.1**). With the exception of SiO₂, CaO and Na₂O, the two metasediment samples are broadly similar to estimates of the mean major element composition of global subducted sediments (*Plank and Langmuir, 1998*). The metasomatic contact zone (CE8a) is best compared directly to metagabbros from the same meta-ophiolite (CE7 and CE12). Relative to these samples CE8a shows depletion in SiO₂ (37.1 wt%), Al₂O₃ (11.3 wt%), CaO (10.4 wt%), K₂O (<0.1 wt%) and Na₂O (2.5 wt%), whilst it is enriched in Fe₂O₃ (23.9 wt%), TiO₂ (3.9 wt%), MnO (0.4 wt%) and P₂O₅ (0.3 wt%) and a consistent MgO concentration (8.4 wt%).

Trace element data are presented for all of the samples used for this study, grouped by locality, in the form of multi-element spidergrams (**Figure 2.3**). Where available, relevant published data is presented alongside our sample data for comparison.

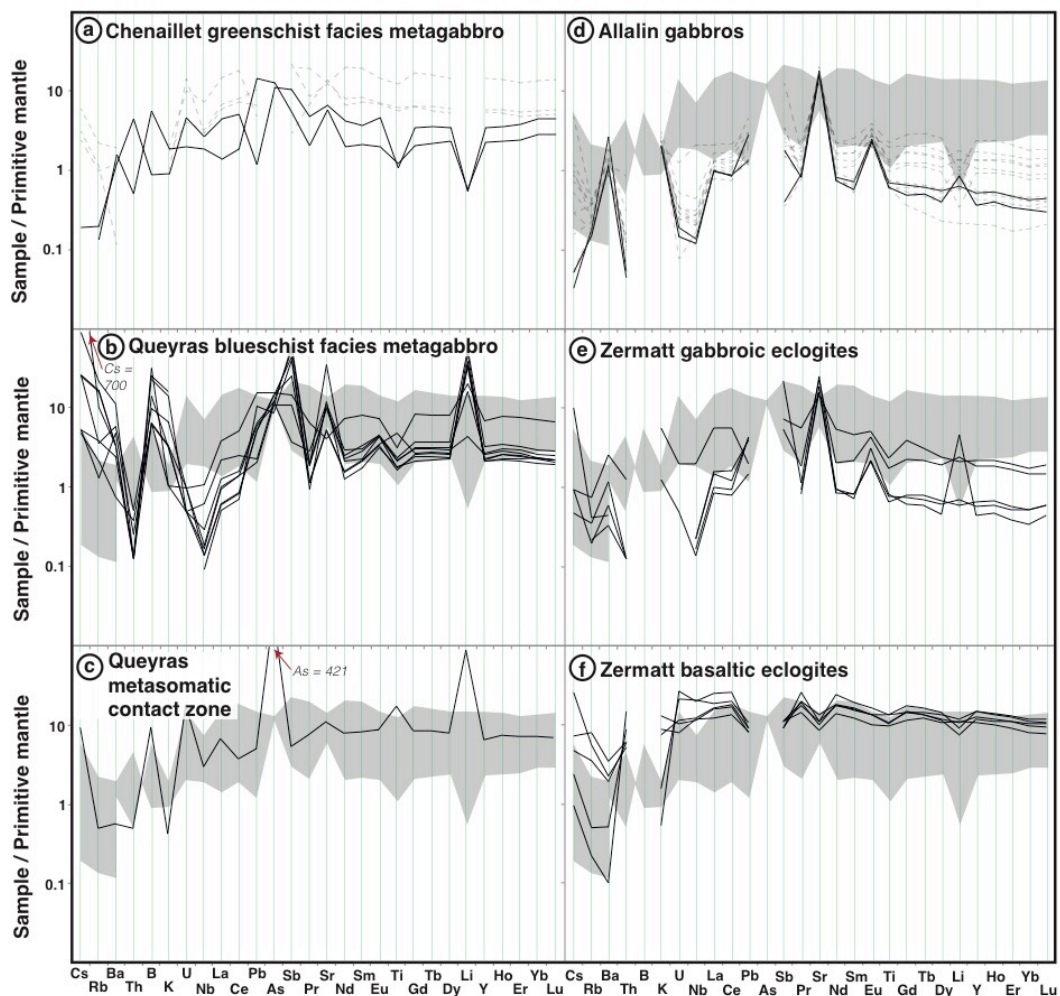


Figure 2.3. Multi element spidergrams of selected elements for samples analysed as part of this study. Elements are arranged along the horizontal axis according to degree of

compatibility. The grey field shown in b, c, d, e and f outline the “oceanic field” compiled from the Chenaillet metagabbros. Solid black lines denote samples used as part of this study. Dashed black lines represent literature data of comparable samples. The dashed black lines in panel a are metagabbro data for the Chenaillet taken from Charlot-Prat et al., 2004, while the dashed black lines in panel d are literature data for the Allalin gabbros taken from Dale et al., 2007. Breaks in the sample profiles indicate elements that were not analysed. The primitive mantle normalization factors are taken from McDonough and Sun et al., 1995.

The Chenaillet metagabbros elemental patterns (PR1 and PR4) are in good agreement with previous studies (e.g. Charlot-Prat et al., 2005) (**Figure 2.3a**). They are characterized by a relatively flat trace element profile ($Ce_N/Y_N = 0.8-1.4$; N: primitive mantle normalized), with notable depletions in Li ($Li_N/Y_N = 0.2-0.3$) and an enrichment in Sr ($Sr_N/Nd_N = 1.5-2.9$). The blueschist facies metagabbros (CE7, CE12, QE1, QE10, RV7, TR6, TR9 and BB1) (**Figure 2.3b**) and metasomatic contact (CE8a) (**Figure 2.3c**) from the Queyras display similar trace element patterns to those of Chenaillet samples, but show significant enrichment in fluid mobile elements (e.g. $Sb_N/Pr_N = 1.3-42.3$, $B_N/K_N = 1.5-30.5$ and $Li/Li^* = 1.8-25.8$; **Table 2.1**).

The trace element profiles for the Zermatt-Saas samples are presented in **Figures 2.3d to e**. The two samples from the Allalin gabbro are plotted alongside additional data from Dale et al., (2007) and compared to the Chenaillet metagabbros (grey field). All of the Allalin gabbros display trace element profiles that are consistent with each other, but are overall of lower concentrations than the patterns of the Chenaillet metagabbros. The trace element profiles are characterized by an enrichment in LREE relative to HREE ($La_N/Lu_N = 2.2-3.3$), positive anomalies in Sr ($Sr_N/Nd_N = 21.3-22$), Ba ($Ba_N/Th_N = 25.7-49.1$) and Eu ($Eu_N/Ti_N = 3.5-3.8$) and negative anomalies in U ($U_N/K_N = 0.1$) and Nb ($Nb_N/La_N = 0.1$). The Zermatt gabbroic eclogites (**Figure 2.3e**) display similar trace element patterns to that of the Allalin gabbros (**Figure 2.3d**), with positive anomalies in Sr ($Sr_N/Nd_N = 2.7-25.5$), Eu ($Eu_N/Ti_N = 2.2-3.9$), and Ba ($Ba_N/Th_N = 2-9.5$), and depletions in Rb ($Rb_N/Ba_N = 0.29-0.3$) and Nb ($Nb_N/La_N = 0.1-0.4$). The basaltic eclogites from Zermatt are shown in **Figure 2.3f**. With the exception of K, they show consistent profiles for all elements, this is marked by broadly flat lying profile between LREE to HREE ($La_N/Lu_N = 1.5-2.1$) and varying

depletions in Ba ($Ba_N/Th_N = 0.01-0.6$), Sr ($Sr_N/Nd_N = 0.5-0.7$) and Li ($Li_N/Y_N = 0.6-1$).

2.4.2 Fe and Zn stable isotopes

The whole rock Fe isotope compositions are reported as $\delta^{56}Fe$ and all errors as two standard deviations (2sd) of repeat analyses of the same sample aliquot. The $\delta^{56}Fe$ values are presented in the supplementary information **Table 2.2**. The range of $\delta^{56}Fe$ values for all samples analysed here is between $-0.02 \pm 0.03\text{‰}$ to $+0.30 \pm 0.06\text{‰}$. The only greenschist facies metagabbro from the Chenaillet that has been analysed for Fe isotopes (PR4) yields a $\delta^{56}Fe$ of $+0.14 \pm 0.06\text{‰}$, which is in good agreement with MORB analysed by *Teng et al.*, 2013 and other basaltic rocks (*Sossi et al.*, 2015). The blueschist facies metagabbros from the Queyras display a range of $\delta^{56}Fe$ of between $0.00 \pm 0.06\text{‰}$ to $+0.16 \pm 0.04\text{‰}$, with no systematic co-variation between metamorphic facies. The metasomatic contact zone sample, CE8a, yields the lightest $\delta^{56}Fe$ observed: $-0.02 \pm 0.03\text{‰}$. The two metasediments from the Queyras, RV5 and CP1 display $\delta^{56}Fe$ values of $+0.09 \pm 0.03\text{‰}$ and $+0.05 \pm 0.04\text{‰}$ respectively. The samples from the Zermatt-Saas ophiolite display the greatest range in Fe isotope composition ($\delta^{56}Fe = +0.03 \pm 0.04\text{‰}$ to $+0.29 \pm 0.04\text{‰}$). Of the two Allalin gabbros selected, one – S02/83viiiixG, displays the heaviest $\delta^{56}Fe$ value of any of the samples ($+0.30 \pm 0.06\text{‰}$), whilst the other preserves a value indistinguishable from MORB ($+0.11 \pm 0.04\text{‰}$). The $\delta^{56}Fe$ values of the gabbroic eclogites from Zermatt ranges between $+0.03 \pm 0.04\text{‰}$ to $+0.29 \pm 0.04\text{‰}$, while the basaltic eclogites show similar $\delta^{56}Fe$ values ranging between $+0.05 \pm 0.07\text{‰}$ to $+0.18 \pm 0.02\text{‰}$.

The zinc isotope composition is reported as $\delta^{66}Zn$, with all errors again being given as 2sd of n . The $\delta^{66}Zn$ values of all of the samples analysed here are presented alongside the Fe isotope compositions in the supplementary information **Table 2.2**. The $\delta^{66}Zn$ values of the samples analysed here ranges from $0.00 \pm 0.02\text{‰}$ to $+0.33 \pm 0.03\text{‰}$. As with Fe isotopes, there is no covariation between $\delta^{66}Zn$ and metamorphic facies. The greenschist facies metagabbro displays a $\delta^{66}Zn$ value of $+0.20 \pm 0.04\text{‰}$, lower than the suggested MORB value of $+0.27 \pm 0.03 \text{‰}$ (*Wang et al.*, 2017). Significant variation is observed within the blueschist facies metagabbros, which range between $+0.03 \pm 0.02\text{‰}$ to $+0.26 \pm 0.03\text{‰}$. The metasomatic contact zone from the Queyras has a $\delta^{66}Zn$ of $+0.03 \pm 0.02\text{‰}$, while the two metasediments show $\delta^{66}Zn$ of $0.00 \pm$

0.02‰ to $+0.13 \pm 0.02$ ‰. Samples from Zermatt display the greatest overall range in $\delta^{66}\text{Zn}$, being between $+0.05 \pm 0.03$ ‰ to $+0.33 \pm 0.03$ ‰.

2.5. Discussion

The overall goal of this study is to examine the effects of prograde metamorphism and metasomatism on the Zn and Fe isotope budget of the oceanic crust. To this end we have characterised a suite of metagabbros and metabasalts from three Western Alps ophiolite complexes. These samples display different parageneses from greenschist facies in the Chenaillet massif, representative of seafloor fluid interaction and oceanic crust hydration, to blueschist facies in the Queyras complex, which shows evidence for sediment interaction during subduction, through to high-pressure eclogite facies in the Zermatt-Saas ophiolite. This transect is taken to be representative of P - T path for subducting oceanic lithosphere and allows us to assess the effect of subduction zone metamorphism on the mafic portion of the subducting slab (e.g. *Guillot et al.*, 2009, *Schwartz et al.*, 2013). Furthermore samples from the Queyras meta-ophiolites were selected as they have previously been demonstrated on the basis of strong enrichments in fluid mobile elements to have been affected by fluid metasomatism from proximal devolatilization of metasedimentary rocks (*Debret et al.*, 2016a).

2.5.1 The effect of high-pressure metamorphism and eclogitization of mafic lithologies on Fe isotopes – Zermatt eclogites

The basaltic eclogites from Zermatt show MORB-like $\delta^{56}\text{Fe}$ (between 0.07 to 0.14 ‰; *Teng et al.*, 2013), ranging between +0.05 to +0.18 ‰, with an average of $+0.12 \pm 0.11$ ‰ (2sd, $n=5$) suggesting that they retain their primary magmatic composition. To full examine the effect of high-pressure dehydration we present a simple Rayleigh distillation model (shown in supplementary information 2.3), which has been calculated according to the equation below.

$$\delta_{\text{final}} - \delta_{\text{initial}} = (\delta_{\text{initial}})(F^{(\alpha-1)} - 1)$$

Where δ_{final} and δ_{initial} is taken as the average Zermatt basaltic eclogite composition and the average MORB value taken from *Teng et al.*, 2013, respectively. The variable F represents the amount of Fe removed from the rock, and α is the fractionation factor between the rock and fluid. Here we have derived the α empirically, choosing to match the modeled $\delta^{56}\text{Fe}$ to our average measured $\delta^{56}\text{Fe}$ from the Zermatt basaltic eclogites.

Given that the solubility of Fe in aqueous Cl-poor subduction zone fluids is low (Kessel *et al.*, 2004), and considering the relatively small volume of H₂O released during eclogite facies dehydration, it can be taken that the loss of Fe would not exceed 1 wt %. Across the range of possible Fe concentrations (F) we show that the derived fractionation factor is insufficient to significantly perturb the whole-rock Fe isotope composition of the fully dehydrated eclogite, even with the maximum loss of Fe possible. Thus we suggest that, owing to mass balance constraints, Fe isotopes serve as poor tracers of Fe mobility within these particular rocks.

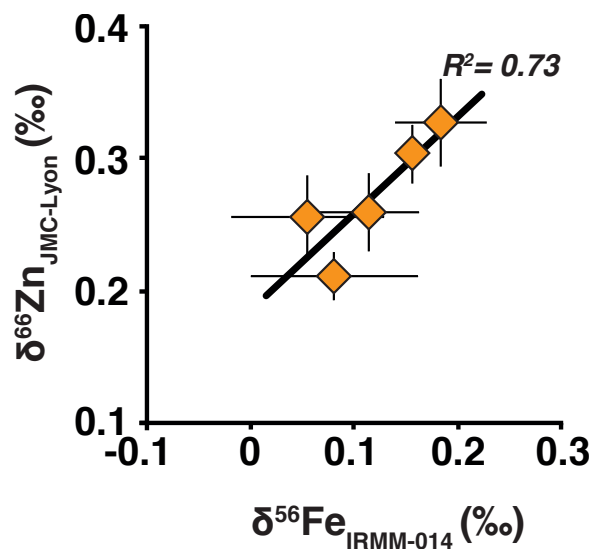


Figure 2.4. The strong correlation ($R^2=0.73$) between the $\delta^{56}\text{Fe}$ and $\delta^{66}\text{Zn}$ of the basaltic eclogites from the Zermatt-Saas suggest that both the Fe and Zn stable isotopes composition of these samples is controlled by the same process. All errors are 2sd of the mean of n .

Similarly the positive correlation ($R^2 = 0.78$) between the $\delta^{56}\text{Fe}$ and $\delta^{66}\text{Zn}$ values of basaltic eclogite (**Figure 2.4**) suggests that both isotope systems are little affected by prograde metamorphism during subduction.

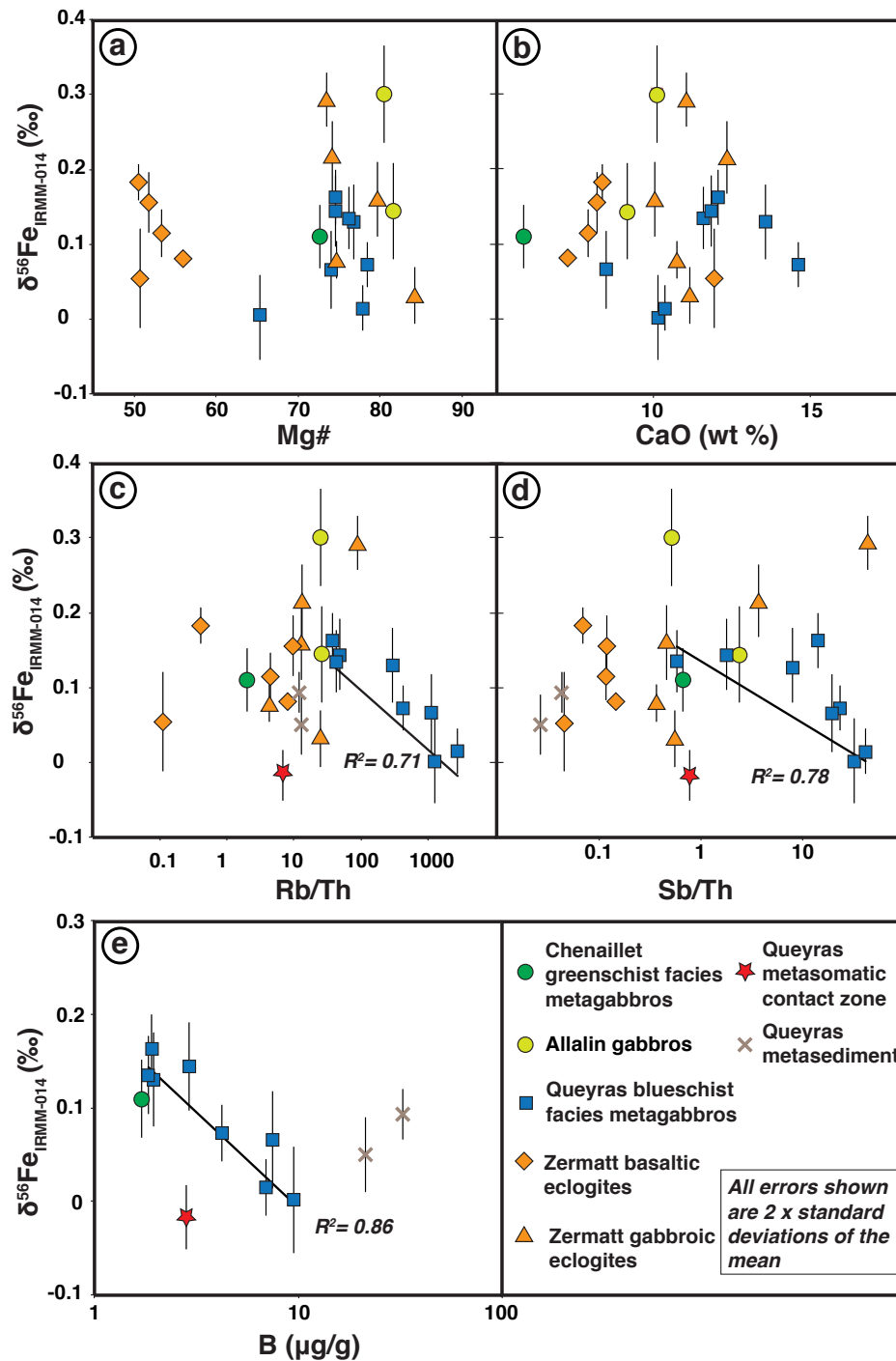


Figure 2.5. Iron isotope compositions ($\delta^{56}\text{Fe}$) plotted against indices of magmatic differentiation (panel a and b) and fluid-rock interaction (panel c, d and e). The Queyras metasomatic contact zone and the metasediments are not plotted on a and b as they have not undergone magmatic differentiation. Panels c and d present ratios of fluid mobile (Rb and Sb) and immobile (Th) elements. The linear regression lines and associated R^2 values plotted on c, d and e are for the Queyras blueschist metagabbro data only. Boron concentration data was only

available for the Chenaillet and Queyras samples. Error bars represent two standard deviations of the mean of n

Many of the Zermatt metagabbro samples display $\delta^{56}\text{Fe}$ values outside of the range seen in MORB (between 0.07 to 0.14 ‰; Teng *et al.*, 2013). Although Fe isotopes can be fractionated in response to magmatic differentiation (Schuessler *et al.*, 2009; Weyer and Seitz, 2012, Teng *et al.*, 2008), there are no systematic co-variations between the $\delta^{56}\text{Fe}$ of the gabbroic eclogites and any indicator of magmatic differentiation (Mg# and CaO) (**Figure 2.5a** and **b**). One possible explanation for the level of $\delta^{56}\text{Fe}$ variation observed is seafloor fluid interaction and alteration of gabbroic oceanic crust, and in particular the incorporation of isotopically light Fe into secondary alteration minerals (including hydrothermal sulfides), which leaves the residual highly altered silicate minerals enriched in heavier Fe isotopes (Rouxel *et al.*, 2003). Although this could account for such isotopic compositions, the absence of chalcophile element enrichment within the whole rock make it unlikely that these lithologies have been affect by hydrothermal alteration and the formation of secondary sulfides. Another possibility is that Fe isotope fractionation took place during prograde metamorphism and associated metasomatism or dehydration of the Zermatt metagabbro protoliths. However, no co-variation between metamorphic grade and Fe isotope composition are observed. It should be noted, however, that the gabbroic eclogite with the heaviest $\delta^{56}\text{Fe}$ (S02/85ixB) shows the most evidence for blueschist facies retrogression, and it is possible that retrograde processes could have modified the $\delta^{56}\text{Fe}$ of these samples.

2.5.2 Fe isotope fractionation in response to fluid metasomatism at blueschist facies – The Queyras meta-ophiolites

A single metagabbro sample from the Chenaillet possesses a $\delta^{56}\text{Fe}$ value of $+0.11 \pm 0.04$ ‰, which is in good agreement with published values obtained for MORB of between $+0.11$ to $+0.17$ ‰ (Teng *et al.*, 2013). The blueschist metagabbros from the Queyras meta-ophiolites display a similar range of Fe isotope compositions to the gabbroic eclogites from Zermatt but, on average are offset towards lighter $\delta^{56}\text{Fe}$ values, with a mean $\delta^{56}\text{Fe}$ of $+0.09 \pm 0.12$ ‰, (2sd, $n=8$) as opposed to $+0.16 \pm 0.21$ ‰, (2sd, $n=5$) for the Zermatt gabbroic eclogites.

A notable feature of the samples from the Queyras is the substantial enrichment in fluid mobile elements, such as Rb, B, Sb and Li (**Figure 2.3b**). This

enrichment is thought to result from fluid infiltration from the surrounding metasediments and the incorporation of fluid mobile elements during recrystallisation under blueschist facies conditions. This type of high-pressure interaction between external fluids and surrounding lithologies, which results in the enrichment in fluid mobile elements has been noted elsewhere globally (Marschall *et al.*, 2009, Penniston-Dorland *et al.*, 2012, Vitale Brovarone *et al.*, 2014). Consequently, it is possible to use these samples to document the effect of high-pressure fluid infiltration during subduction on the behavior of Fe (and Zn) isotopes. Owing to the low solubility of Th and B relative to Rb and Sb in aqueous fluids (e.g. Kessel *et al.*, 2005, Zach *et al.*, 2007), we have used the ratios of Rb/Th and Sb/Th alongside elemental concentrations of B in these samples as an indicator of fluid-rock interaction occurring during subduction. A negative correlation is observed between indices of fluid-rock interaction (Rb/Th, Sb/Th and B) and the $\delta^{56}\text{Fe}$ values of the samples (**Figure 2.5c, d, and e**). This correlation provides evidence for a relationship between fluid infiltration and Fe isotope systematics in the blueschist facies metagabbros in the Queyras. The perturbation of the bulk rock $\delta^{56}\text{Fe}$ by an external fluid can be accounted for by two possible mechanisms: 1) isotopically heavy Fe is preferentially complexed into the fluid and lost from the metagabbros, leaving the residual rock enriched in light Fe isotopes, or; 2) isotopically light Fe is transported via the external fluid and incorporated into one or more of the blueschist facies minerals that make up the metagabbros, thus enriching the bulk rock in light Fe isotopes. Mechanism 1, the loss of isotopically heavy Fe, appears unlikely, because previous work has demonstrated the preferential mobility of isotopically light Fe in slab derived dehydration fluids (Debret *et al.*, 2016b). Specifically, it would be expected that the heavy isotopes of Fe would have a preference for Fe^{3+} complexes (Polyakov and Mineev, 2000), and the solubility of Fe^{3+} relative to Fe^{2+} in aqueous solution is known to be low (Ding and Seyfried, 1992). Consequently, it seems much more likely that the light Fe isotope composition of the metagabbros is caused by the incorporation of externally derived low- $\delta^{56}\text{Fe}$ fluids (mechanism 2).

Fluids can acquire distinctively light Fe isotope compositions through different means. These include: kinetic processes (i.e. enhanced mobility of isotopically light Fe); preferential dissolution of low- $\delta^{56}\text{Fe}$ phases; or, equilibrium partitioning, where isotopically light Fe is preferentially complexed by aqueous SO_x (Hill *et al.*, 2010) and Cl (Testemale *et al.*, 2009) ligands, as suggested to be the case for Western Alps subducted serpentinites (Debret *et al.*, 2016b). Because

there is no observed co-variation between the $\delta^{56}\text{Fe}$ and $\delta^{66}\text{Zn}$ of the blueschist facies metagabbros we suggest that kinetic processes are not responsible, as if this was to be the case we would expect to see the two systems co-vary accordingly. Alternatively it could be considered that preferential dissolution of a low- $\delta^{56}\text{Fe}$ phase within the sediments, such as a sulfide, could result in an isotopically light metasomatising fluid. The metasediments analysed here do show isotopically light Fe isotope compositions relative to the metagabbros from the same area, but show no evidence of sulfur bearing phase dissolution (supplementary information **2.1** and **2.2**). In order to test this further we have applied a simple mass balance calculation using the equation shown below.

$$\delta^{56}\text{Fe}_{\text{mixture}} = (([\text{Fe}]_{\text{rock}} \times \delta^{56}\text{Fe}_{\text{rock}}) + ([\text{Fe}]_{\text{fluid}} \times \delta^{56}\text{Fe}_{\text{fluid}})) / ([\text{Fe}]_{\text{rock}} \times [\text{Fe}]_{\text{fluid}})$$

If we were to take the sediment composition as being representative of the fluid compositions, then mass balance suggests that we would have to add near ~60% of the sediment to the metagabbro reservoir to generate the lightest $\delta^{56}\text{Fe}$ observed. As this is unrealistic we can only suggest that the Fe isotope composition of the bulk sediments analysed does not reflect that of the fluid. Hence, we are unable to precisely identify which reaction in the metasedimentary rocks could generate a fluid with an isotopically light Fe signature. Hydrothermal fluids from mid-ocean ridges are known to be isotopically light with respect to Fe (*Rouxel et al.*, 2004; 2008, *Beard et al.*, 2003), if we were to assume that these fluids are representative of the type of fluids cycling in subduction zones, and that have been responsible for metasomatising the metagabbros in the Queyras, the mass balance suggests that addition of ~20% fluid with a $\delta^{56}\text{Fe}$ of -0.5‰ to the metagabbro could account for the light $\delta^{56}\text{Fe}$ observed. The role of infiltrating fluids derived from other lithologies such as serpentinites could also be considered here. Indeed, it has been shown that the devolatilization of serpentinitised ultramafic rocks can release fluids enriched in isotopically light Fe and heavy Zn, interpreted to reflect the release of sulphate-bearing fluids during serpentinite devolatilization (*Debret et al.*, 2016b and *Pons et al.*, 2016). If such fluids were to be released from proximal serpentinite bodies in the Queyras, and be the key metasomatic agent for the metagabbros here then we would expect to see a consistent, coupled Fe and Zn isotope variation. As we only see the process of fluid metasomatism reflected in the Fe isotope composition of the metagabbros, then we can only suggest that the fluids, and associated isotopically light Fe originates from the sediments.

2.5.3 Zn isotope systematics of metabasalts and metagabbros from the Queyras and Zermatt-Saas ophiolites

The igneous samples (metabasalts and metagabbros) analysed here possess $\delta^{66}\text{Zn}$ isotope compositions that range from $+0.03 \pm 0.02 \text{ ‰}$ to $+0.30 \pm 0.02 \text{ ‰}$, with a mean $\delta^{66}\text{Zn}$ value of $+0.21 \pm 0.16 \text{ ‰}$ (2sd; $n=21$). Recent work by Wang *et al.*, 2017 suggests that MORB possesses a Zn isotope composition of $\delta^{66}\text{Zn} = +0.28 \pm 0.03 \text{ ‰}$ ($n = 6$; samples from Carlsberg and North Atlantic), which is indistinguishable within error of the studied samples. The absence of any variation between Zn concentration and $\delta^{66}\text{Zn}$ within the sample set suggests that the overall $\delta^{66}\text{Zn}$ is not the result of Zn mobility during fluid loss under eclogite facies conditions. To demonstrate this we have modelled the evolution of $\delta^{66}\text{Zn}$ within the dehydrated eclogite according to the same Rayleigh distillation equation given in section 2.5.1, the result of which is shown in the supplementary information 2.4. This model confirms that the solubility of Zn, even in the presence of aqueous SO_x and/or CO_x species, is too low to explain the Zn isotope variation observed in the basaltic eclogites.

In the case of the Queyras blueschist facies metagabbros, the lack of a correlation between $\delta^{66}\text{Zn}$ and fluid mobile elements (supplementary material 2.5), suggests that the blueschist facies sediment interaction, which has affected Fe isotopes, has not perturbed the whole rock Zn isotope systematics of these samples. However it is possible that the external metasomatic fluid either possesses Zn concentrations that are too low to significantly affect the Zn isotope composition of the metagabbros, or else that the sediment derived fluid preserves a Zn isotope composition indistinguishable to that of the metagabbros, and owing to the mass balance this interaction is not traceable with Zn isotopes. It is notable that the metasomatic contact between metagabbros and metasedimentary rocks analysed here preserves the lightest $\delta^{66}\text{Zn}$ ($+0.03 \pm 0.02 \text{ ‰}$) and $\delta^{56}\text{Fe}$ ($-0.02 \pm 0.03 \text{ ‰}$) values. Previous studies have shown that kinetic fractionation can occur along such type of metasomatic interfaces (Teng *et al.*, 2006, Marschall *et al.*, 2007, Penniston-Dorland *et al.*, 2010, Pogge von Strandman *et al.*, 2015) resulting in a decrease of isotopic values. These compositions arise from a preferential diffusive partitioning of the lighter isotopes relative to the heavier isotopes. It is thus conceivable that similar processes locally occur in the Queyras, however further work would be required to comment on this conclusively.

Recently Zn isotopes have been shown to be sensitive to mantle partial melting (Doucet *et al.*, 2016, Wang *et al.*, 2017) and igneous differentiation (Chen *et al.*, 2013), but owing to the complex metasomatic and metamorphic history of the studied samples, coupled with the lack of a comprehensive study of Zn isotopes in global MORB and oceanic gabbros, it is difficult to conclude if the variations in Zn isotope composition observed here reflect primary magmatic process or modification by late stage alteration and metasomatic processes. While it has previously been stated that the process of low temperature seafloor alteration of the upper, basaltic oceanic lithosphere has little effect on Zn isotopes, the same study demonstrated that high temperature (>350 °C) hydrothermal circulation and complexing of light Zn isotopes in hydrothermal fluids could drive the Zn isotope composition towards heavier $\delta^{66}\text{Zn}$ values in the gabbroic portion of the oceanic lithosphere (Huang *et al.*, 2016). This observation could be invoked to explain the range of $\delta^{66}\text{Zn}$ values observed in the Zermatt and Queyras metagabbros, but as the samples now preserve a subduction related, alpine overprint to their mineralogy it is not possible to unambiguously conclude on the effect of seafloor hydrothermal activity on the Zn isotope compositions of these rocks.

2.5.4 Implications for slab dehydration and the redox budget of the sub-arc mantle

Mass transfer from the subducted slab can be considered with respect to three components: sediments; mafic oceanic crust, and; the serpentinised slab mantle. Of these, the serpentinised slab mantle has received much attention as the main carrier of fluids into subduction zones, as hydrated peridotite can contain up to 13wt% H₂O (Ulmer and Trommsdorff, 1995). Indeed, the prograde dehydration of subducting serpentinites has been demonstrated to contribute significantly to the fluid budget of the sub-arc mantle (Scambelluri and Tonarini, 2012). When considered with the findings of Debret *et al.*, 2016b and Pons *et al.*, 2016, who show clear fractionation of both Fe and Zn stable isotopes with increasing subduction metamorphism, it is likely that serpentinite-derived fluids, in combination with sediment melts, exert a strong control on the transfer of redox mediating elements between the slab and overlying sub-arc-arc. This is consistent with the results of many studies that have highlighted the importance of distinct contributions from serpentinite-derived slab fluids and sediment melts in the source regions of arc lavas (e.g. Plank and Langmuir, 1993, Elliott *et al.*, 1997, Freymuth *et al.*, 2015, Nebel *et al.*, 2015, Sossi *et al.*, 2016).

We have demonstrated that the effect of high-pressure subduction zone metamorphism and associated dehydration at eclogite facies, has no detectable effect on the whole rock Fe and Zn stable isotope composition of subducted metabasalts and metagabbros (**Figure 2.6**). This is significant with respect to two aspects. Firstly we show that an absence of resolvable Fe isotope variation at eclogite facies, with respect to a MORB protolith, demonstrates that Fe isotopes are not fractionated in response to loss of Fe during dehydration of mafic lithologies in subduction. Secondly we show that Zn isotopes remain unfractionated, suggesting that the dehydration fluids released by the process of eclogitization are not major carriers of aqueous Zn-SO_x and/or Zn-CO_x complexes.

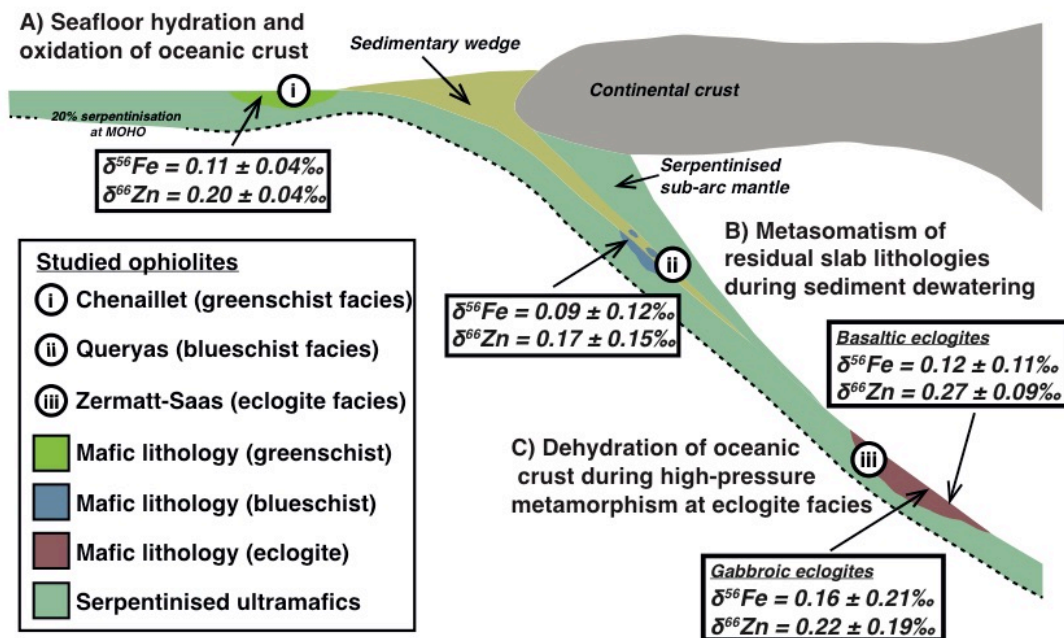


Figure 2.6. Schematic diagram (modified after Debret et al., 2016a) showing the approximate location of the metaophiolites studied as part of this work: i) Chenaillet massif; ii) Queyras complex; and iii) Zermatt-Saas ophiolite. Each of these metaophiolites has been metamorphosed under conditions representative of a subduction gradient (greenschist to blueschist to eclogite) and allows us to examine the effect of slab metamorphism and metasomatism on the mafic oceanic crust. For each of these ophiolites the average $\delta^{56}\text{Fe}$ and $\delta^{66}\text{Zn}$ values are presented.

The results from this study, at least, suggest that high-pressure subduction zone metamorphism has no detectable effect on Fe or Zn isotope composition of the mafic lithologies within the subducting slab. Consequently, the mafic slab

component that is recycled back into the mantle preserves a MORB-like Fe and Zn isotope signature.

2.6. Conclusions

We have analysed a suite of metagabbros and metabasalts, which have been metamorphosed under the different conditions of a subduction zone gradient, and are taken to be representative of the mafic oceanic crust during subduction. Our data show that fluids released from subducting sediments can interact and metasomatise mafic slab lithologies. This metasomatism is capable of modifying bulk rock Fe isotope composition, with the samples displaying the most evidence for fluid interaction recording the lightest Fe isotope compositions. This is likely due to the incorporation of an isotopically light Fe component, which is derived from the associated subducted sediments. Within the same samples zinc isotopes show no evidence of being perturbed by this metasomatic process. Consequently we conclude that Fe isotopes in subducting oceanic crust are sensitive tracers of slab metasomatism, relating to fluid released from subducting sediments

Contrary to this it is apparent that no systematic variation in isotopic composition across metamorphic grade is observed, suggesting that the mobility of Fe during the dehydration of the mafic lithologies in subduction zones is too low to lead to significant isotopic variations within the dehydrated lithologies. Additionally, our Zn isotope data demonstrate that the fluids released by these dehydration reactions are not major carriers of dissolved Zn-SO_x/CO_x complexes.

Acknowledgements

This work was supported by an ERC Starting Grant (HabitablePlanet; 306655) and a NERC Deep Volatiles Consortium Grant (NE/M0003/1) awarded to HW. BD and MLP were supported as PDRAs on the HabitablePlanet grant, while the Ph. D studentship to EI was funded as part of the same project. PB wishes to acknowledge ERC Starting Grant (MASE; 279828) awarded to J. van Hunen and his Auvergne Fellowship (2016). MAM was funded by a Durham University International Junior Fellowship. Careful and constructive reviews from Oliver Nebel, Paolo Sossi, Horst Marschall and an anonymous reviewer greatly improved the quality of this manuscript. Janne Blichert-Toft is also acknowledged for her patient editorial handling. We thank Christian Nicollet (LMV, Clermont-Ferrand, France) for discussions in the field and for providing the metagabbro samples from the Queyras and Chenaillet ophiolites. The full major and trace element composition of all of the samples presented in this study can be found within the

supplementary information. The Fe and Zn isotope data are also included within the supplementary information.

References Cited

Angiboust, S., P. Agard, L. Jolivet and O. Beyssac (2009), The Zermatt-Saas ophiolite: the largest (60-km wide) and deepest (c. 70–80 km) continuous slice of oceanic lithosphere detached from a subduction zone? *Terra Nova*, 21(3), 171-180.

Ben Othman, D., J. M. Luck, A. Tchalikian, and F. Albarède (2003), Cu-Zn isotope systematics in terrestrial basalts. In: *EGS-AGU-EUG Joint Assembly*, 1, 9669.

Bernoulli, D., G. Manatschal, L. Desmurs, and O. Muntener (2003), Where did Gustav Steinmann see the trinity? Back to the roots of an Alpine ophiolite concept. *Geological Society Of America Special Papers*, 373, 93-110.

Black, J. R., A. Kavner, and E. A. Schauble (2011), Calculation of equilibrium stable isotope partition function ratios for aqueous zinc complexes and metallic zinc. *Geochimica et Cosmochimica Acta* 75(3), 769-783.

Brandon, A. D. and D. S. Draper (1996), Constraints on the origin of the oxidation state of mantle overlying subduction zones: an example from Simcoe, Washington, USA. *Geochimica et Cosmochimica Acta*, 60(10), 1739-1749.

Brouwer, F. M., D. M. A. Van De Zedde, M. J. R. Wortel, and R. L. M. Vissers (2004), Late-orogenic heating during exhumation: Alpine PTt trajectories and thermomechanical models. *Earth and Planetary Science Letters*, 220(1), 185-199.

Vitale Brovarone, A. and O. Beyssac (2014), Lawsonite metasomatism: A new route for water to the deep Earth. *Earth and Planetary Science Letters*, 393, 275-284.

Bouilhol, P., V. Magni, J. van Hunen, and L. Kaislaniemi (2015), A numerical approach to melting in warm subduction zones. *Earth and Planetary Science Letters*, 411, 37-44.

Bucher, K., Y. Fazis, C. D. Capitani, and R. Grapes (2005), Blueschists, eclogites, and decompression assemblages of the Zermatt-Saas ophiolite: High-pressure metamorphism of subducted Tethys lithosphere. *American Mineralogist*, 90(5-6), 821-835.

Bucher, K. and R. Grapes (2009), The eclogite-facies Allalin Gabbro of the Zermatt–Saas ophiolite, Western Alps: a record of subduction zone hydration. *Journal of Petrology*, 50(8), 1405-1442.

Caby, R. (1995), Plastic deformation of gabbros in a slow-spreading Mesozoic ridge: Example of the Montgenevre ophiolite, Western Alps. In: *Mantle and Lower Crust Exposed in Oceanic Ridges and in Ophiolites, 1*, 123-145.

Chalot-Prat, F. (2005), An undeformed ophiolite in the Alps: field and geochemical evidence for a link between volcanism and shallow plate tectonic processes. *Geological Society of America Special Papers*, 388, 751-780.

Chen, H., P. S. Savage, F. Z. Teng, R. T. Helz, and F. Moynier (2013), Zinc isotope fractionation during magmatic differentiation and the isotopic composition of the bulk Earth. *Earth and Planetary Science Letters*, 369, 34-42.

Chen, J., J. Gaillardet, P. Louvat, and S. Huon (2009), Zn isotopes in the suspended load of the Seine River, France: Isotopic variations and source determination. *Geochimica et Cosmochimica Acta*, 73(14), 4060-4076.

Dale, C. W., A. Gannoun, K. W. Burton, T. W. Argles, and I. J. Parkinson (2007), Rhenium–osmium isotope and elemental behaviour during subduction of oceanic crust and the implications for mantle recycling. *Earth and Planetary Science Letters*, 253(1), 211-225.

Dale, C. W., K. W. Burton, D. G. Pearson, A. Gannoun, Olivier Alard, T. W. Argles, and I. J. Parkinson (2009), Highly siderophile element behaviour accompanying subduction of oceanic crust: whole rock and mineral-scale insights from a high-pressure terrain. *Geochimica et Cosmochimica Acta* 73(5), 1394-1416.

Dauphas, N., P. R. Craddock, P. D. Asimow, V. C. Bennett, A. P. Nutman, and D. Ohnenstetter (2009) Iron isotopes may reveal the redox conditions of mantle melting from Archean to Present. *Earth and Planetary Science Letters*, 288(1), 255-267.

Dauphas, N., M. Roskosz, E. E. Alp, D. R. Neuville, M. Y. Hu, C. K. Sio and F. L. H. Tissot (2014), Magma redox and structural controls on iron isotope variations in Earth's mantle and crust. *Earth and Planetary Science Letters* 398, 127-140.

Debret, B., K. T. Koga, F. Cattani, C. Nicollet, G. Van den Bleeken and S. Schwartz (2016a) Volatile (Li, B, F and Cl) mobility during amphibole breakdown in subduction zones. *Lithos*, 244, 165-181.

Debret, B., M. A. Millet, M. L. Pons, P. Bouilhol, E. Inglis and H. Williams (2016b), Isotopic evidence for iron mobility during subduction. *Geology*, 44(3), 215-218.

Debret, B., C. Nicollet, M. Andreani, S. Schwartz, and M. Godard (2013), Three steps of serpentinization in an eclogitized oceanic serpentinization front (Lanzo Massif–Western Alps). *Journal of Metamorphic Geology* 31(2), 165-186.

Ding, K. and W. E. Seyfried (1992), Determination of Fe-Cl complexing in the low pressure supercritical region (NaCl fluid): Iron solubility constraints on pH of subseafloor hydrothermal fluids. *Geochimica et Cosmochimica Acta*, 56(10), 3681-3692.

Doucet, L. S., N. Mattielli, D. A. Ionov, W. Deboige, and A. V. Golovin (2016), Zn isotopic heterogeneity in the mantle: A melting control? *Earth and Planetary Science Letters* 451, 232-240.

Elliott, T., T. Plank, A. Zindler, W. White and B. Bourdon (1997) Element transport from slab to volcanic front at the Mariana arc. *Journal of Geophysical Research: Solid Earth*, 102(B7), 14991-15019.

Evans, K. A. (2012), The redox budget of subduction zones. *Earth-Science Reviews*, 113(1), 11-32.

Evans, B. W., V. Trommsdorff, and W. Richter (1979), Petrology of an eclogite-metarodingite suite at Cima di Gagnone, Ticino, Switzerland. *American Mineralogist* 64(1-2), 15-31.

Fitton, J. G., A. D. Saunders, L. M. Larsen, B. S. Hardarson, and M. J. Norry (1998), Volcanic Rocks From The Southeast Greenland Margin At 63 N: Composition, Petrogenesis, and Mantle Sources. *Proceedings of the Ocean Drilling Program, Scientific Results*, 152(28).

Foley, S. F., M. G. Barth, and G. A. Jenner (2000), Rutile/melt partition coefficients for trace elements and an assessment of the influence of rutile on the trace element characteristics of subduction zone magmas. *Geochimica et Cosmochimica Acta* 64(5) 933-938.

Freyduth, H., F. Vils, M. Willbold, R. N. Taylor and Elliott, T. (2015), Molybdenum mobility and isotopic fractionation during subduction at the Mariana arc. *Earth and Planetary Science Letters*, 432, 176-186.

Frezzotti, M. L., J. Selverstone, Z. D. Sharp, and R. Compagnoni, (2011) Carbonate dissolution during subduction revealed by diamond-bearing rocks from the Alps. *Nature Geoscience*, 4(10), 703-706.

Frost, B. R. and C. Ballhaus (1998), Comment on "Constraints on the origin of the oxidation state of mantle overlying subduction zones: an example from Simcoe, Washington, USA" by A. D. Brandon and D. S. Draper. *Geochimica et Cosmochimica Acta*, 62, 329-332.

Fujii, T., F. Moynier, M. L. Pons, and F. Albarède (2011), The origin of Zn isotope fractionation in sulfides. *Geochimica et Cosmochimica Acta*, 75(23), 7632-7643.

Godard, M., S. Awaji, H. Hansen, E. Hellebrand, D. Brunelli, K. Johnson, T. Yamasaki, J. Maeda, M. Abratis, D. Christie, and Y. Kato (2009), Geochemistry of a long in-situ section of intrusive slow-spread oceanic lithosphere: Results from IODP Site U1309 (Atlantis Massif, 30 N Mid-Atlantic-Ridge). *Earth and Planetary Science Letters*, 279(1), 110-122.

Govindaraju, K. (1994), Compilation of working values and sample descriptions for 383 geostandards. *Geostandards Newsletter*, 18, 1-55.

Guillot, S, K. Hattori, P. Agard, S. Schwartz, and O. Vidal (2009) Exhumation processes in oceanic and continental subduction contexts: a review. *Subduction zone geodynamics*, 175-205.

Hawkesworth, C. J., K. Gallagher, J. M. Hergt, and F. McDermott (1993), Mantle and slab contribution in arc magmas. *Annual Review of Earth and Planetary Sciences*, 21, 175-204.

Hensen, C., K. Wallmann, M. Schmidt, C. R. Ranero, and E. Suess (2004), Fluid expulsion related to mud extrusion off Costa Rica—a window to the subducting slab. *Geology*, 32(3), 201-204.

Hermann, J., O. Müntener, and M. Scambelluri (2000), The importance of serpentinite mylonites for subduction and exhumation of oceanic crust. *Tectonophysics* 327(3), 225-238.

Hermann, J., and D. H. Green (2001), Experimental constraints on high pressure melting in subducted crust. *Earth and Planetary Science Letters* 188(1), 149-168.

Hermann, J., C. Spandler, A. Hack and A. V. Korsakov (2006), Aqueous fluids and hydrous melts in high-pressure and ultra-high pressure rocks: implications for element transfer in subduction zones. *Lithos*, 92(3), 399-417.

Hibbert, K. E. J., H. M. Williams, A. C. Kerr, and I. S. Puchtel (2012), Iron isotopes in ancient and modern komatiites: evidence in support of an oxidised mantle from Archean to present. *Earth and Planetary Science Letters*, 321, 198-207.

Hill, P. S., E. A. Schauble, and E. D. Young (2010), Effects of changing solution chemistry on Fe³⁺/Fe²⁺ isotope fractionation in aqueous Fe–Cl solutions. *Geochimica et Cosmochimica Acta* 74(23), 6669-6689.

Herzog, G. F., F. Moynier, F. Albarède, and A. A. Berezhnoy (2009) Isotopic and elemental abundances of copper and zinc in lunar samples, Zagami, Pele's hairs, and a terrestrial basalt. *Geochimica et Cosmochimica Acta*, 73(19), 5884-5904.

Huang, J., S.-A. Liu, Y. Gao, Y. Xiao, and S. Chen (2016), Copper and zinc isotope systematics of altered oceanic crust at IODP Site 1256 in the eastern equatorial Pacific, *J. Geophys. Res. Solid Earth*, 121, doi:10.1002/2016JB013095.

Jenner, F. E. and H. S. C. O'Neill (2012), Analysis of 60 elements in 616 ocean floor basaltic glasses. *Geochemistry, Geophysics, Geosystems*, 13(2), 1-11.

Kelley, K. A. and E. Cottrell (2009), Water and the oxidation state of subduction zone magmas. *Science*, 325(5940), 605-607.

Kessel, R., P. Ulmer, T. Pettke, M. W. Schmidt and A. B. Thompson (2004), A novel approach to determine high-pressure high-temperature fluid and melt compositions using diamond-trap experiments. *American Mineralogist*, 89(7), 1078-1086.

, R., M. W. Schmidt, P. Ulmer, and T. Pettke (2005), Trace element signature of subduction-zone fluids, melts and supercritical liquids at 120–180 km depth. *Nature*, 437(7059), 724-727.

Konter, J. G., A. J. Pietruszka, B. B. Hanan, V. A. Finlayson, P. R. Craddock, M. G. Jackson, and N. Dauphas (2016), Unusual $\delta^{56}\text{Fe}$ values in Samoan rejuvenated lavas generated in the mantle. *Earth and Planetary Science Letters*, 450, 221-232.

Lagabrielle, Y., R. Polino, J. M. Auzende, R. Blanchet, R. Caby, S. Fudral, M. Lemoine, C. Mével, M. Ohnenstetter, D. Robert, and P. Tricart (1984), Les témoins d'une tectonique intra-océanique dans le domaine téthysien: analyse des rapports entre les ophiolites et leurs couvertures métasédimentaires dans la zone piémontaise des Alpes franco-italiennes. *Ophioliti*, 9, 67–88

Lagabrielle, Y. and M. Cannat (1990), Alpine Jurassic ophiolites resemble the modern central Atlantic basement. *Geology*, 18(4), 319-322.

Lagabrielle, Y., S. Fudraland, J. R. Kienast (1990), La couverture océanique des ultrabasites de Lanzo (Alpes occidentales): arguments lithostratigraphiques et pétrologiques. *Geodinamica Acta*, 4(1), 43-55.

Lagabrielle, Y., A. Vitale Brovarone, and B. Ildefonse (2015), Fossil oceanic core complexes recognized in the blueschist metaophiolites of Western Alps and Corsica. *Earth-Science Reviews*, 141, 1-26.

Lemoine, M., P. Tricart, and G. Boillot (1987), Ultramafic and gabbroic ocean floor of the Ligurian Tethys (Alps, Corsica, Apennines): In search of a genetic imodel. *Geology*, 15(7), 622-625.

Li, D.-Y., Xiao, Y. L., Li, W.-Y., Zhu, X., Williams, H. M. and Li, Y.-L. (2016), Iron isotopic systematics of UHP eclogites respond to oxidizing fluid during exhumation. *J. Metamorph. Geol.*, doi:10.1111/jmg.12217

Magni, V., P. Bouilhol, and J. van Hunen (2014), Deep water recycling through time. *Geochemistry, Geophysics, Geosystems*, 15(11), 4203-4216.

Manatschal, G., D. Sauter, A. M. Karpoff, E. Masini, G. Mohn, and Y. Lagabriele (2011), The Chenaillet Ophiolite in the French/Italian Alps: An ancient analogue for an oceanic core complex? *Lithos*, 124(3), 169-184.

Maréchal, C. N., P. Télouk, and F. Albarède (1999), Precise analysis of copper and zinc isotopic compositions by plasma-source mass spectrometry. *Chemical Geology*, 156(1), 251-273.

Marschall, H. R., P. A. E. Pogge von Strandmann, H.-M. Seitz, T. Elliott, and Y. Niu (2007), The lithium isotopic composition of orogenic eclogites and deep subducted slabs. *Earth and Planetary Science Letters*, 262(3), 563-580.

Marschall, H. R., R. Altherr, K. Gméling, and Z. Kasztovszky (2009), Lithium, boron and chlorine as tracers for metasomatism in high-pressure metamorphic rocks: a case study from Syros (Greece). *Mineralogy and Petrology*, 95(3-4), 291-302.

Mason, T. F., D. J. Weiss, M. Horstwood, R. R. Parrish, S. S. Russell, E. Mullane, and B. J. Coles (2004), High-precision Cu and Zn isotope analysis by plasma source mass spectrometry Part 2. Correcting for mass discrimination effects. *Journal of Analytical Atomic Spectrometry*, 19(2), 218-226.

McDonough, W. F. and S. S. Sun (1995), The composition of the Earth. *Chemical geology*, 120(3), 223-253.

Mevel, C., R. Caby and J. R. Kienast (1978), Amphibolite facies conditions in the oceanic crust: Example of amphibolitized flaser-gabbro and amphibolites from the Chenaillet ophiolite massif (Hautes Alpes, France). *Earth and Planetary Science Letters*, 39(1), 98-108.

Meyer, J. (1983), The development of the high-pressure metamorphism in the Allalin metagabbro (Switzerland). *Terra Cognita*, 3(2-3), 187.

Mikutta, C., J. G. Wiederhold, O. A. Cirpka, T. B. Hofstetter, B. Bourdon, and U. Von

Gunten (2009), Iron isotope fractionation and atom exchange during sorption of ferrous iron to mineral surfaces. *Geochimica et Cosmochimica Acta*, 73(7), 1795-1812.

Millet, M. A., J. A. Baker and C. E. Payne (2012), Ultra-precise stable Fe isotope measurements by high resolution multiple-collector inductively coupled plasma mass spectrometry with a ^{57}Fe – ^{58}Fe double spike. *Chemical Geology*, 304, 18-25.

Moeller, K., R. Schoenberg, R. B. Pedersen, D. Weiss, and S. Dong (2012), Calibration of the New Certified Reference Materials ERM-AE633 and ERM-AE647 for Copper and IRMM-3702 for Zinc Isotope Amount Ratio Determinations. *Geostandards and Geoanalytical Research* 36(2), 177-199.

Moynier, F., F. Albarède and G. F. Herzog (2006), Isotopic composition of zinc, copper, and iron in lunar samples. *Geochimica et Cosmochimica Acta*, 70(24), 6103-6117.

Nebel, O., P. Z. Vroon, D. F. Wiggers de Vries, F. E. Jenner, and J. A. Mavrogenes (2010) Tungsten isotopes as tracers of core–mantle interactions: the influence of subducted sediments. *Geochimica et Cosmochimica Acta* 74(2), 751-762.

Nebel, O., P. A. Sossi, A. Benard, M. Wille, P. Z. Vroon, and R. J. Arculus (2015), Redox-variability and controls in subduction zones from an iron-isotope perspective. *Earth and Planetary Science Letters* 432, 142-151.

Parkinson, I. J. and R. J. Arculus (1999) The redox state of subduction zones: insights from arc-peridotites. *Chemical Geology*, 160(4), 409-423.

Pearce, J. A. (1982), Trace element characteristics of lavas from destructive plate boundaries. *Andesites* 8, 525-548.

Penniston-Dorland, S. C., G. E. Bebout, P. A. P. von Strandmann, T. Elliott and S. S. Sorensen (2012), Lithium and its isotopes as tracers of subduction zone fluids and metasomatic processes: Evidence from the Catalina Schist, California, USA. *Geochimica et Cosmochimica Acta*, 77, 530-545.

Penniston-Dorland, S. C., S. S. Sorensen, R. D. Ash and S. V., Khadke (2010), Lithium isotopes as a tracer of fluids in a subduction zone mélange: Franciscan Complex, CA. *Earth and Planetary Science Letters*, 292(1), 181-190

Plank, T. and C. H. Langmuir (1993), Tracing trace elements from sediment input to volcanic output at subduction zones. *Nature*, 362(6422), 739-743.

Plank, T. and C. H. Langmuir (1998), The chemical composition of subducting sediment and its consequences for the crust and mantle. *Chemical geology*, 145(3), 325-394.

Polyakov, V. B. and S. D. Mineev (2000), The use of Mössbauer spectroscopy in stable isotope geochemistry. *Geochimica et Cosmochimica Acta*, 64(5), 849-865.

Pons, M. L., B. Debret, P. Bouilhol, A. Delacour and H. Williams (2016), Zinc isotope evidence for sulfate-rich fluid transfer across subduction zones. *Nature Communications*, 7.

Pons, M. L., G. Quitté, T. Fujii, M. T. Rosing, B. Reynard, F. Moynier, C. Douchet and F. Albarède (2011), Early Archean serpentine mud volcanoes at Isua, Greenland, as a niche for early life. *Proceedings of the National Academy of Sciences*, 108(43), 17639-17643.

Richter, F. M., N. Dauphas, and F. Z. Teng (2009), Non-traditional fractionation of non-traditional isotopes: evaporation, chemical diffusion and Soret diffusion. *Chemical Geology*, 258(1), 92-103.

Rouxel, O., N. Dobbek, J. Ludden and Y. Fouquet (2003), Iron isotope fractionation during oceanic crust alteration. *Chemical Geology*, 202(1), 155-182.

Rubatto, D., D. Gebauer and M. Fanning (1998), Jurassic formation and Eocene subduction of the Zermatt–Saas-Fee ophiolites: implications for the geodynamic evolution of the Central and Western Alps. *Contributions to Mineralogy and Petrology*, 132(3), 269-287.

Rüpke, L. H., J. P. Morgan, M. Hort, and J. A. Connolly (2004), Serpentine and the subduction zone water cycle. *Earth and Planetary Science Letters*, 223(1), 17-34.

Scambelluri, M. and P. Philippot (2001), Deep fluids in subduction zones. *Lithos*, 55(1), 213-227.

Scambelluri, M., T. Pettke, E. Rampone, M. Godard, and E. Reusser (2014), Petrology and trace element budgets of high-pressure peridotites indicate subduction dehydration of serpentinitized mantle (Cima di Gagnone, Central Alps, Switzerland). *Journal of Petrology* 55(3), 459-498.

Scambelluri, M., E. Rampone, and G. B. Piccardo (2001), Fluid and element cycling in subducted serpentinite: a trace-element study of the Erro–Tobbio high-pressure ultramafites (Western alps, NW Italy). *Journal of Petrology*, 42(1), 55-67.

Schauble, E. A., (2004), Applying Stable Isotope Fractionation Theory to New Systems. In: *Geochemistry of Non-Traditional Stable Isotopes (Reviews in Mineralogy and Geochemistry)*, 55, 65-102.

Schmidt, M. W., and S. Poli (2014), Devolatilisation During Subduction. In: *Treatise on Geochemistry (Second Edition)* 4(4.19), 669-701.

Schuessler, J. A., R. Schoenberg and O. Sigmarsson (2009), Iron and lithium isotope systematics of the Hekla volcano, Iceland—evidence for Fe isotope fractionation during magma differentiation. *Chemical Geology*, 258(1), 78-91.

Schwartz, S., S. Guillot, B. Reynard, R. Lafay, B. Debret, C. Nicollet, P. Lanari, and A. L. Auzende (2013), Pressure–temperature estimates of the lizardite/antigorite transition in high pressure serpentinites. *Lithos*, 178, 197-210.

Sossi, P. A., G. P. Halverson, O. Nebel, and S. M. Eggins. (2015), Combined separation of Cu, Fe and Zn from rock matrices and improved analytical protocols for stable isotope determination. *Geostandards and Geoanalytical Research*, 39(2), 129-149.

Sossi, P. A., O. Nebel and J. Foden, (2016). Iron isotope systematics in planetary reservoirs. *Earth and Planetary Science Letters*, 452, 295-308.

Teng, F.-Z., W. F. McDonough, R. L. Rudnick, and R. J. Walker (2006), Diffusion-driven extreme lithium isotopic fractionation in country rocks of the Tin Mountain pegmatite. *Earth and Planetary Science Letters* 243(3), 701-710.

Teng, F. Z., N. Dauphas, and R. T. Helz (2008), Iron isotope fractionation during magmatic differentiation in Kilauea Iki lava lake. *Science*, 320(5883), 1620-1622.

Teng, F. Z., N. Dauphas, S. Huang and B. Marty (2013), Iron isotopic systematics of oceanic basalts. *Geochimica et Cosmochimica Acta*, 107, 12-26.

Tricart, P. (1984), From passive margin to continental collision; a tectonic scenario for the Western Alps. *American Journal of Science*, 284(2), 97-120.

Tricart, P. and, S. Schwartz (2006), A north-south section across the Queyras Schistes lustrés (Piedmont zone, western Alps): Syn-collision refolding of a subduction wedge. *Eclogae Geologicae Helvetiae*, 99(3), 429-442.

Ulmer, P. and V. Trommsdorff (1995). Serpentine stability to mantle depths and subduction-related magmatism. *Science*, 268(5212), 858.

Urey, H. C. (1947), The thermodynamic properties of isotopic substances. *Journal of the Chemical Society (Resumed)*, 562-581.

Vils, F., O. Müntener, A. Kalt, and T. Ludwig (2011), Implications of the serpentine phase transition on the behaviour of beryllium and lithium–boron of subducted ultramafic rocks. *Geochimica et Cosmochimica Acta*, 75(5), 1249-1271.

Vitale Brovarone, A. and O. Beyssac (2014), Lawsonite metasomatism: A new route for water to the deep Earth. *Earth and Planetary Science Letters*, 393, 275-284.

Wang, Z.-Z., S.-A. Liu, J. Liu, J. Huang, Y. Xiao, Z.-Y. Chu, X.-M. Zhao and L. Tang (2017), Zinc isotope fractionation during mantle melting and constraints on the Zn isotope composition of Earth's upper mantle. *Geochimica et Cosmochimica Acta* 198, 151-167.

Weyer, S., A. D. Anbar, G. P. Brey, C. Münker, K. Mezger, and A. B. Woodland (2005). Iron isotope fractionation during planetary differentiation. *Earth and Planetary Science Letters*, 240(2), 251-264.

Weyer, S. and D. A. Ionov (2007), Partial melting and melt percolation in the mantle: the message from Fe isotopes. *Earth and Planetary Science Letters*, 259(1), 119-133.

Weyer, S., and J. B. Schwieters (2003), High precision Fe isotope measurements with high mass resolution MC-ICPMS. *International Journal of Mass Spectrometry* 226(3), 355-368.

Weyer, S. and, H. M Seitz (2012), Coupled lithium-and iron isotope fractionation during magmatic differentiation. *Chemical Geology*, 294, 42-50.

Williams, H. M., C. A. McCammon, A. H. Peslier, A. N. Halliday, N. Teutsch, S. Levasseur, and J. P., Burg (2004), Iron isotope fractionation and the oxygen fugacity of the mantle. *Science*, 304(5677), 1656-1659.

Williams, H. M., A. H. Peslier, C. McCammon, A. N. Halliday, S. Levasseur, N. Teutsch, and J. P. Burg (2005), Systematic iron isotope variations in mantle rocks and minerals: the effects of partial melting and oxygen fugacity. *Earth and Planetary Science Letters*, 235(1), 435-452.

Williams, H. M., S. G. Nielsen, C. Renac, W. L. Griffin, S. Y. O'Reilly, C. A. McCammon, N. Pearson, F. Viljoen, J. C. Alt, and A. N. Halliday (2009), Fractionation of oxygen and iron isotopes by partial melting processes: implications for the interpretation of stable isotope signatures in mafic rocks. *Earth and Planetary Science Letters*, 283(1), 156-166.

Williams, H. M. and M. Bizimis (2014), Iron isotope tracing of mantle heterogeneity within the source regions of oceanic basalts. *Earth and Planetary Science Letters*, 404, 396-407.

Wolfe, A. L., B. W Stewart, R. C. Capo, R. Liu, D. A. Dzombak, G. W. Gordon, and A. D. Anbar (2016), Iron isotope investigation of hydrothermal and sedimentary pyrite and their aqueous dissolution products. *Chemical Geology*, 427, 73-82.

Zack, T. and T. John (2007). An evaluation of reactive fluid flow and trace element mobility in subducting slabs. *Chemical Geology*, 239(3), 199-216.

Chapter 2. Supplementary Information

Supplementary information 2.1 (Table) – Major and trace element data

Supplementary information 2.2 (Table) – Fe and Zn isotope data

Supplementary information 2.3 (Figure) – Fe Rayleigh distillation model

Supplementary information 2.4 (Figure) – Zn Rayleigh distillation model

Supplementary information 2.5 (Figure) – Zn isotope plots

Supplementary information 2.1 - Major and Trace element concentrations

Table 2.1a (All major elements and trace elements Li to Rb)

Sample	Major Elements (by XRF) – Weight percent (wt%)										Trace Elements (by ICP-MS) – Parts Per Million (ppm)										
	SiO ₂	Al ₂ O ₃	Fe ₂ O ₃	MgO	CaO	Na ₂ O	K ₂ O	TiO ₂	MnO	P ₂ O ₅	Li	B	Sc	Ti	V	Cr	Co	Ni	Cu	Zn	Rb
Greenschist facies metagabbro																					
PR4	58.38	15.28	5.76	7.72	5.87	5.97	0.06	0.26	0.12	0.02	0.91	1.71	25.78	-	79.32	1197	10.97	77.19	5.02	16.18	0.08
Blueschist facies metagabbro																					
CE7	51.01	14.14	5.62	10.35	14.64	3.29	0.09	0.49	0.12	0.01	88.07	4.23	58.49	-	203	112.1	28.68	88.97	54.02	27.45	6.16
CE12	52.43	19.12	4.55	6.74	12.06	4.34	0.03	0.36	0.08	0.03	61.62	1.91	29.5	-	103.4	47.8	22.76	74.3	76.11	22.31	0.77
QE1	52.15	16.61	7.95	7.56	10.14	4.18	0.03	0.99	0.14	0.01	56.64	9.78	34.52	-	130.6	545.7	30.53	185	80.93	30.42	9.77
QE10	54.03	15.84	5.52	9.80	10.38	3.43	0.43	0.34	0.11	0.01	51.50	6.93	31.30	-	120.8	503.2	27.6	166.8	74.3	27.7	9.6
RV7	50.72	14.48	7.09	10.49	11.84	4.17	0.20	0.64	0.22	0.10	32.54	2.92	28.97	-	136.4	156.3	17.5	119.9	5.0	101.7	2.2
TR6	52.85	17.55	5.14	8.30	11.61	3.72	0.10	0.45	0.10	0.03	6.98	1.84	29.10	-	115.3	23.8	25.3	59.5	41.4	26.0	1.3
TR9	52.01	16.14	5.25	8.79	13.57	3.16	0.10	0.43	0.11	0.02	25.60	1.95	43.14	-	158.1	50.2	24.4	61.2	45.9	29.1	2.3
BB1	54.67	14.88	6.31	9.09	8.49	5.22	0.47	0.37	0.12	0.01	78.38	7.47	33.97	-	140.6	60.9	30.4	91.1	17.0	39.6	12.8
Metasomatic Contact																					
CE8A	37.06	11.27	23.91	8.41	10.37	2.46	0.01	3.91	0.40	0.26	144.5	2.8	50.9	-	586.0	2069	163.6	789.8	61.3	238.6	0.3
Metasediments																					
RV5	51.84	15.63	7.19	2.75	17.10	0.68	2.46	0.69	0.19	0.12	54.39	32.57	13.27	-	100.40	119.3	15.74	60.06	39.13	92.77	107.2
CP1	47.00	7.43	3.51	1.78	35.87	0.12	1.92	0.40	0.08	0.08	24.28	21.39	6.03	-	46.63	45.29	3.32	16.54	18.35	39.39	56.19
Allalin Gabbros																					
S01/SG	47.58	19.78	6.30	14.17	9.16	2.77	0.06	0.12	0.10	0.02	1.35	-	6.05	-	18.77	143.29	46.06	384.58	64.06	30.62	0.09
S02/83xiixG	48.70	21.33	5.19	10.79	10.12	3.01	0.06	0.14	0.08	0.02	1.01	-	5.95	-	28.39	195.72	39.78	348.67	46.80	26.52	0.11
Basaltic eclogites																					
S02/75iir	50.65	16.74	9.92	5.38	8.20	5.25	0.39	2.12	0.17	0.38	12.06	-	28.05	-	235.25	129.95	27.29	72.82	46.63	79.21	4.81
S02/75iiic	51.22	16.72	9.82	5.68	7.91	5.44	0.22	2.17	0.18	0.37	17.24	-	27.68	-	249.61	135.80	29.33	71.47	50.68	76.49	2.14
S02/75iiir	51.37	15.64	10.26	6.59	7.26	5.41	0.26	2.00	0.16	0.35	18.00	-	26.59	-	231.62	128.90	35.22	92.73	43.12	96.99	3.40
S02/41ii	47.58	17.43	10.08	5.25	11.94	4.36	0.02	2.78	0.23	0.26	14.52	-	30.56	-	274.40	66.97	25.91	45.53	21.79	60.91	0.13
S02/41v	49.55	16.55	10.80	5.57	8.37	5.28	0.05	2.75	0.17	0.40	18.71	-	29.71	-	278.99	57.49	30.33	55.99	29.67	96.86	0.30
Gabbroic eclogites																					
S01/35iiix	49.19	23.26	4.75	7.08	10.74	4.44	0.16	0.47	0.07	0.11	3.43	-	9.76	-	79.40	224.85	31.05	124.04	34.10	26.33	0.45
S01/40viix	48.62	20.70	4.69	12.65	11.16	2.27	0.04	0.14	0.08	0.01	0.95	-	11.04	-	43.32	816.85	37.31	349.39	44.02	20.93	0.21
S02/85ixE	49.41	21.07	4.79	6.95	12.34	4.26	0.04	0.36	0.08	0.02	3.93	-	25.53	-	97.46	440.76	25.36	149.13	20.15	24.12	0.12
S02/85ixB	46.36	24.27	5.64	7.90	11.06	3.54	0.04	0.17	0.07	0.02	7.40	-	1.41	-	17.85	28.87	32.22	187.14	8.98	43.58	0.25
S01/40vx	48.27	20.96	6.17	12.23	10.04	2.52	0.03	0.16	0.14	0.02	1.12	-	8.05	-	31.99	204.04	41.18	292.30	39.91	28.62	0.13

Table 2.1b (Trace elements Sr to Er)

Sample	Trace Elements (by ICP-MS) – Parts Per Million (ppm)																			
	Sr	Y	Zr	Nb	Mo	Sn	Sb	Cs	Ba	La	Ce	Pr	Nd	Sm	Eu	Gd	Tb	Dy	Ho	Er
Greenschist facies metagabbro																				
PR4	114.10	9.60	7.77	1.22	-	1.61	0.03	0.00	10.62	0.91	3.09	0.53	2.50	0.85	0.31	1.12	0.22	1.57	0.35	1.07
Blueschist facies metagabbro																				
CE7	201.90	13.88	20.06	0.11	-	0.21	0.33	14.69	22.18	0.61	2.35	0.51	3.12	1.34	0.68	2.01	0.37	2.45	0.51	1.44
CE12	688.60	9.09	16.08	0.19	-	0.19	0.29	0.11	31.20	0.83	2.66	0.48	2.68	0.93	0.66	1.33	0.24	1.58	0.33	0.94
QE1	104.70	9.89	9.05	0.09	-	0.44	0.24	0.55	22.39	0.40	1.41	0.30	1.96	0.88	0.53	1.44	0.27	1.80	0.38	1.09
QE10	102.50	9.45	5.94	0.09	-	0.19	0.14	0.52	21.91	0.39	1.37	0.29	1.89	0.85	0.52	1.40	0.26	1.73	0.38	1.05
RV7	80.53	29.67	7.92	0.71	-	0.95	0.08	0.55	38.26	2.49	8.59	1.64	9.10	3.28	1.11	4.47	0.81	5.37	1.15	3.27
TR6	220.00	10.98	19.00	0.41	-	0.39	0.02	0.10	4.95	1.40	4.22	0.72	3.69	1.24	0.69	1.63	0.30	1.98	0.42	1.18
TR9	197.30	11.63	13.98	0.12	-	0.27	0.06	0.11	15.81	0.66	2.34	0.48	2.84	1.16	0.66	1.72	0.31	2.10	0.45	1.28
BB1	235.70	9.08	9.34	0.06	-	0.17	0.22	1.87	73.39	0.33	1.16	0.24	1.57	0.70	0.49	1.15	0.22	1.53	0.34	0.99
Metasomatic Contact																				
CE8A	222.80	28.47	65.41	1.99	-	9.72	0.03	0.20	3.79	4.45	6.37	1.88	9.87	3.36	1.35	4.58	0.84	5.39	1.12	3.21
Metasediments																				
RV5	302.60	24.08	62.73	11.24	-	52.22	0.38	5.00	189.90	31.50	62.15	7.51	27.76	5.23	1.07	4.47	0.66	3.96	0.81	2.37
CPI	484.40	23.98	44.55	5.45	-	9.67	0.12	2.30	151.60	16.43	31.07	4.11	16.25	3.42	0.76	3.39	0.55	3.36	0.69	1.89
Allalin Gabbros																				
S01/5G	319.08	1.58	3.27	0.08	0.07	0.12	0.01	0.00	7.56	0.64	1.41	0.21	0.94	0.23	0.36	0.27	0.05	0.27	0.06	0.15
S02/83xiiiG	361.42	2.28	4.74	0.09	0.06	0.10	0.00	0.00	17.42	0.62	1.45	0.23	1.03	0.29	0.38	0.36	0.06	0.37	0.08	0.21
Basaltic eclogites																				
S02/75iiR	217.32	50.07	15.39	7.62	0.31	2.67	0.06	0.15	22.87	10.43	28.56	4.46	21.68	6.43	2.06	8.09	1.33	7.64	1.67	4.80
S02/75iiiC	202.27	54.51	17.01	8.05	0.22	2.44	0.06	0.10	12.71	10.55	30.02	4.85	22.55	6.55	2.07	7.80	1.35	8.04	1.75	4.91
S02/75iiiR	171.35	46.80	23.82	7.70	0.22	2.19	0.06	0.54	14.89	7.84	22.65	3.71	17.59	4.92	1.57	6.21	1.21	7.27	1.49	3.97
S02/41ii	219.70	64.17	36.34	12.93	0.20	3.17	0.05	0.02	0.66	15.98	43.75	6.68	29.98	7.94	2.54	9.37	1.64	9.61	2.05	5.65
S02/41v	266.96	63.86	34.15	13.57	0.16	3.14	0.05	0.05	3.41	12.06	32.94	5.02	22.77	6.27	2.07	7.73	1.44	9.00	1.98	5.51
Gabbroic eclogites																				
S01/35iiix	285.39	9.32	2.48	1.31	0.84	0.63	0.04	0.02	16.86	3.62	9.40	1.41	6.72	1.87	0.79	2.11	0.31	1.63	0.33	0.88
S01/40viiix	369.05	2.82	2.17	0.09	0.06	0.10	0.00	0.01	7.87	0.55	1.32	0.21	1.06	0.33	0.33	0.43	0.08	0.46	0.10	0.25
S02/85ixE	460.62	8.11	6.36	0.15	0.05	0.22	0.03	0.02	3.97	1.03	2.76	0.48	2.59	0.89	0.66	1.22	0.22	1.30	0.28	0.73
S02/85ixB	495.16	1.91	1.33	0.15	0.04	0.13	0.12	0.21	2.97	0.96	2.03	0.29	1.22	0.29	0.49	0.33	0.06	0.31	0.07	0.17
S01/40vx	320.88	2.50	1.16	0.11	0.05	0.12	0.00	0.00	2.21	0.66	1.56	0.24	1.16	0.33	0.34	0.41	0.07	0.41	0.09	0.23

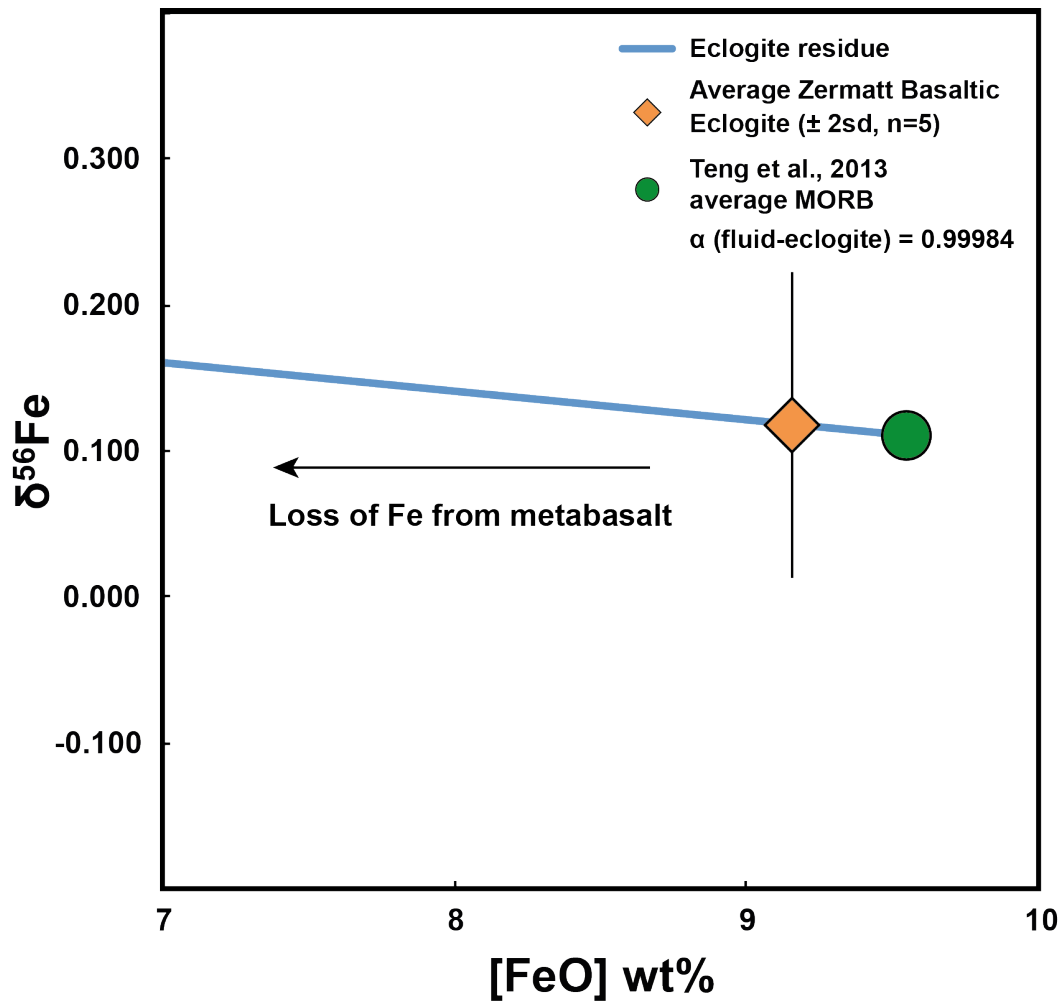
Table 2.1c (Trace elements Yb to U)

<i>Trace Elements (by ICP-MS) – Parts Per Million (ppm)</i>							
<i>Sample</i>	<i>Yb</i>	<i>Lu</i>	<i>Hf</i>	<i>Ta</i>	<i>Pb</i>	<i>Th</i>	<i>U</i>
<i>Greenschist facies metagabbro</i>							
PR4	1.24	0.19	0.32	0.21	2.17	0.04	0.04
<i>Blueschist facies metagabbro</i>							
CE7	1.31	0.19	0.63	0.00	0.89	0.01	0.01
CE12	0.88	0.13	0.47	0.02	0.95	0.02	0.01
QE1	1.00	0.15	0.37	0.01	0.80	0.01	0.02
QE10	0.99	0.14	0.28	0.06	0.76	0.00	0.01
RV7	3.08	0.45	0.40	0.08	2.28	0.04	0.02
TR6	1.03	0.15	0.57	0.06	0.34	0.03	0.01
TR9	1.14	0.17	0.48	0.04	0.31	0.01	0.02
BB1	1.03	0.15	0.35	0.01	1.58	0.01	0.00
<i>Metasomatic Contact</i>							
CE8A	3.17	0.47	1.86	0.15	0.75	0.04	0.37
<i>Metasediments</i>							
RV5	0.35	1.70	0.76	26.21	8.74	1.81	0.35
CP1	0.23	1.22	0.38	5.80	4.26	1.11	0.23
<i>Allalin Gabbros</i>							
<i>S01/5G</i>	0.02	0.08	0.01	0.42	0.00	0.00	0.02
<i>S02/83xiiixG</i>	0.03	0.12	0.01	0.20	0.00	0.00	0.03
<i>Basaltic eclogites</i>							
S02/75iiR	0.64	0.34	0.51	1.20	0.49	0.21	0.64
S02/75iiiC	0.69	0.85	0.50	1.38	0.48	0.23	0.69
S02/75iiiR	0.53	0.62	0.47	1.25	0.41	0.16	0.53
S02/41ii	0.79	1.24	0.78	1.37	1.18	0.55	0.79
S02/41v	0.73	0.79	0.80	1.61	0.71	0.43	0.73
<i>Gabbroic eclogites</i>							
S01/35iiix	0.13	0.10	0.08	0.30	0.10	0.04	0.13
S01/40viix	0.04	0.07	0.01	0.22	0.01	0.01	0.04
S02/85ixE	0.10	0.20	0.01	0.60	0.01	0.00	0.10
S02/85ixB	0.03	0.04	0.01	0.63	0.00	0.00	0.03
S01/40vx	0.04	0.04	0.01	0.66	0.01	0.00	0.04

Supplementary information 2.2 – Fe and Zn isotope compositions

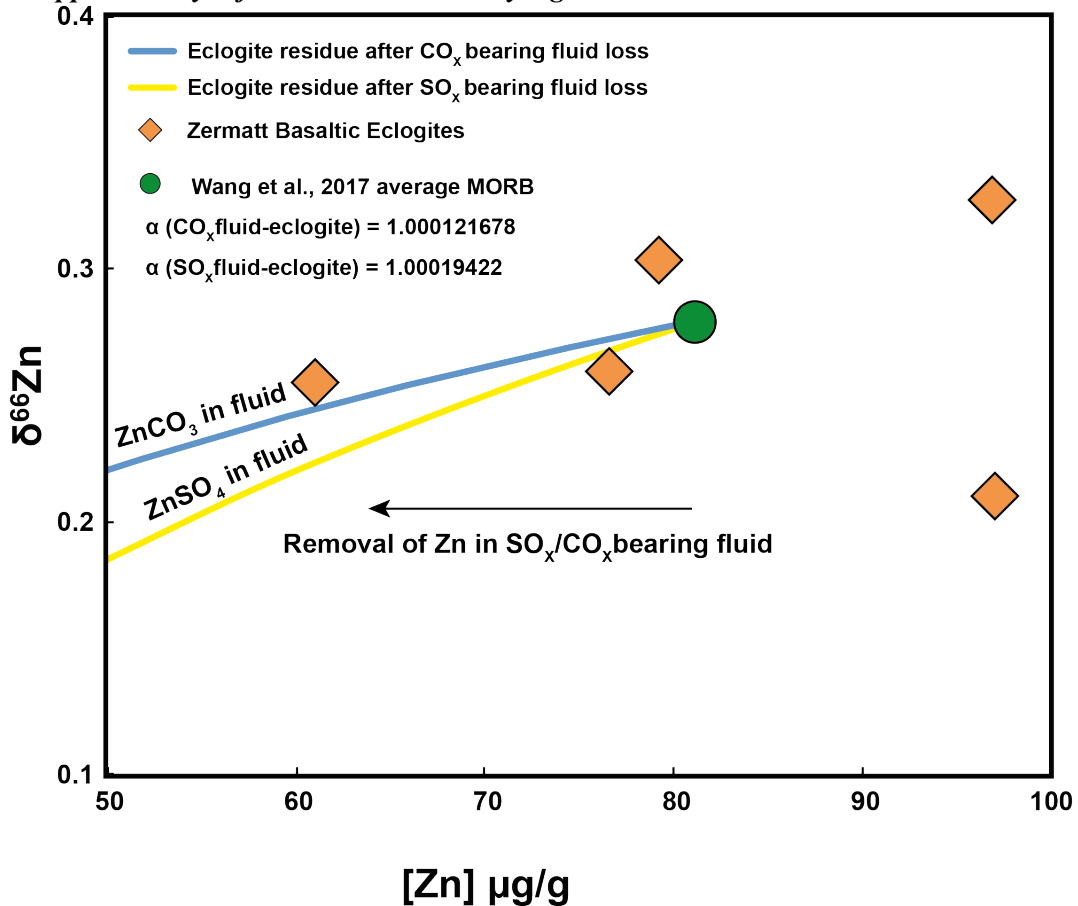
Sample	Fe isotopes (*relative to IRMM-14)					Zn isotopes (§relative to JMC-Lyon)		
	$\delta^{56}/^{54}\text{Fe}^*$	2sd	$\delta^{57}/^{54}\text{Fe}^*$	2sd	n	$\delta^{66}/^{64}\text{Zn}\S$	2sd	n
Greenschist facies metagabbro								
PR4	0.11	0.04	0.18	0.08	4	0.20	0.04	3
Blueschist facies metagabbro								
CE7	0.07	0.03	0.15	0.07	7	0.16	0.04	3
CE12	0.16	0.04	0.24	0.04	3	0.24	0.03	4
QE1	0.00	0.06	0.04	0.09	4	0.12	0.04	8
QE10	0.02	0.03	0.06	0.03	3	0.16	0.02	8
RV7	0.14	0.05	0.21	0.03	6	0.03	0.02	7
TR6	0.14	0.04	0.16	0.02	5	0.25	0.03	4
TR9	0.13	0.05	0.17	0.06	4	0.15	0.03	4
BB1	0.07	0.05	0.13	0.06	6	0.26	0.03	8
Metasomatic Contact								
CE8A	-0.02	0.03	-0.03	0.05	6	0.03	0.02	4
Metasediments								
RV5	0.09	0.03	0.13	0.04	6	0.13	0.02	4
CP1	0.05	0.04	0.10	0.06	4	0.00	0.02	4
Allalin Gabbros								
S01/5G	0.14	0.06	0.24	0.13	3	0.22	0.03	4
S02/83xiiixG	0.30	0.06	0.43	0.11	3	0.23	0.02	4
Basaltic eclogites								
S02/75iiR	0.16	0.04	0.22	0.01	3	0.30	0.02	3
S02/75iiiC	0.11	0.03	0.18	0.05	4	0.26	0.03	6
S02/75iiiR	0.08	0.01	0.13	0.08	3	0.21	0.02	8
S02/41ii	0.05	0.07	0.07	0.07	3	0.26	0.03	6
S02/41v	0.18	0.02	0.31	0.04	3	0.33	0.03	6
Gabbroic eclogites								
S01/35iiix	0.08	0.03	0.12	0.03	4	0.28	0.05	8
S01/40viiix	0.03	0.04	0.05	0.07	4	0.24	0.06	3
S02/85ixE	0.22	0.05	0.31	0.05	4	0.28	0.02	4
S02/85ixB	0.29	0.04	0.42	0.12	2	0.24	0.02	6
S01/40vx	0.16	0.05	0.23	0.06	4	0.05	0.03	3

Supplementary information 2.3 – Fe Rayleigh distillation model



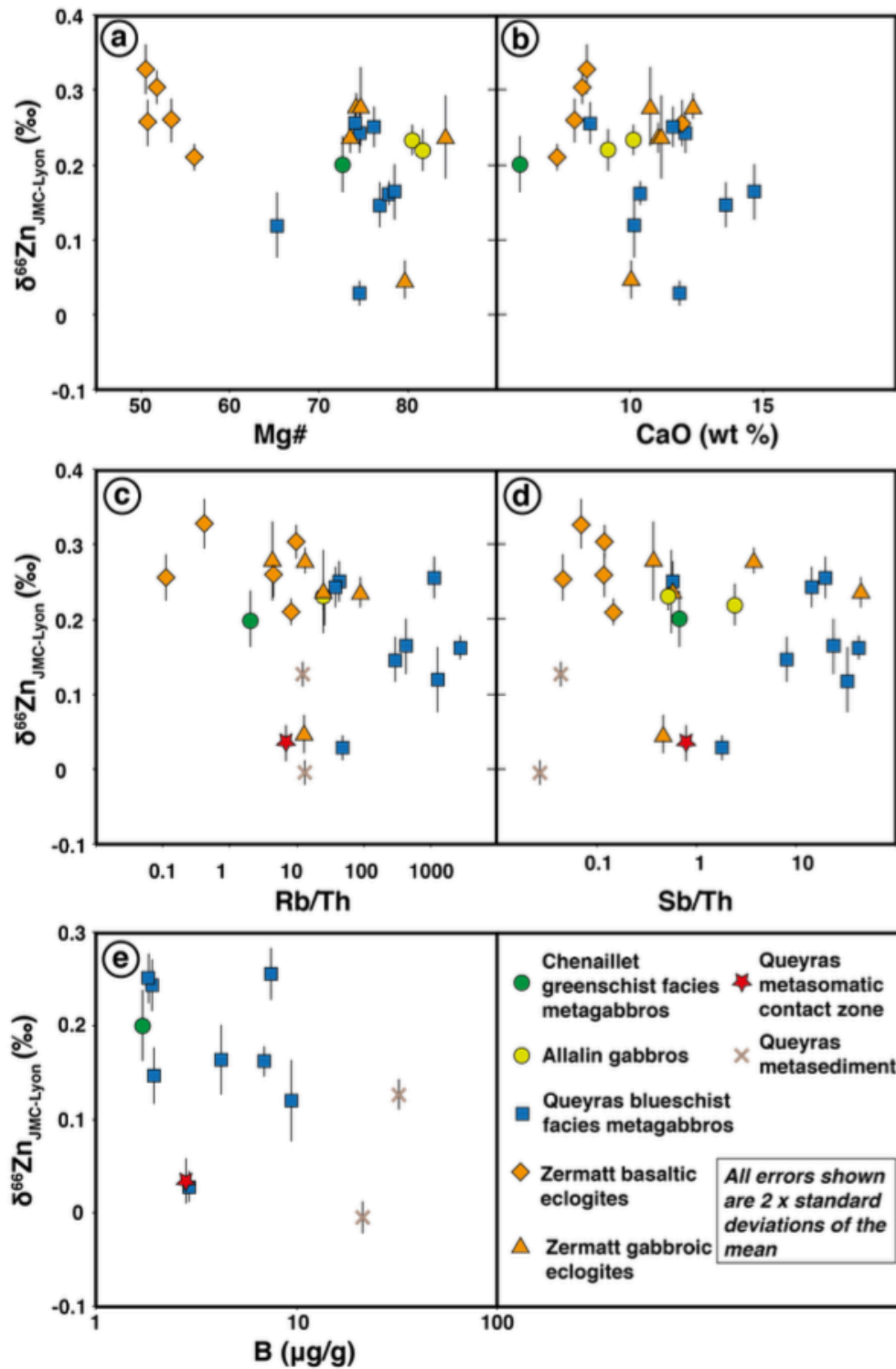
Supplementary Figure 2.3. A Rayleigh distillation model to predict the evolution of $\delta^{56}\text{Fe}$ accompanying decreasing Fe concentration with basalts. We use a starting MORB Fe concentration and Fe isotope composition from *Teng et al., 2013* and a $\alpha_{\text{fluid-rock}}$ factor of 0.99984. This $\alpha_{\text{fluid-rock}}$ was selected as it gave the best modelled prediction compared to our average measured $\delta^{56}\text{Fe}$ from the Zermatt-Saas basaltic eclogites

Supplementary information 2.4 – Zn Rayleigh distillation model



Supplementary Figure 2.4. A Rayleigh distillation model to predict the evolution of $\delta^{66}\text{Zn}$ accompanying loss of Zn in the presence of SO_x and CO_x bearing fluid. We use a starting MORB Zn concentration and Zn isotope composition from *Wang et al., 2017*. For a SO_x bearing fluid a $\alpha_{\text{fluid-rock}}$ factor of 1.00019422 is applied. For a CO_x bearing fluid a $\alpha_{\text{fluid-rock}}$ factor of 1.000121678 is applied. The α factors were calculated from *Black et al., 2011* for a fractionation between silicate-aqueous sulphate as ZnSO₄ in the fluid phase and from *Fujii et al., 2011* for a fractionation between silicate-aqueous carbonate as ZnCO₃ in the fluid phase. This assumes that all Zn in the metabasalts is stored in octahedral sites in the silicates and that fluid release from the eclogite is occurring at 600 °C.

Supplementary information 2.5 – Zn isotope plots



Supplementary Figure 2.5. Zinc isotope composition of the samples studied here plotted against indices of magmatic differentiation and selected fluid mobile elements.

Chapter 3.

Relicts of High-Pressure Serpentinite Dehydration in the Zermatt-Saas Ophiolite (Western Alps, Switzerland)

This chapter is currently in preparation for publication in the journal Lithos. It is being prepared as a short format article for submission to the “letters” section of the journal.

The following will be included as co-authors on the submitted manuscript:

Edward C. Inglis^{1}, Pierre Bouilhol², Baptiste Debret³, Helen M. Williams⁴ and Kevin W. Burton¹*

¹Department of Earth Sciences, Durham University, South Road, Durham, United Kingdom, DH1 3LE

²CRPG, Université de Lorraine, UMR7358, Vandoeuvre-Lès-Nancy, F-54501, France

³Laboratoire G-TIME, Université libre de Bruxelles, CP 160/02, Ave. F. Roosevelt 50, B-1050, Brussels, Belgium

⁴Department of Earth Sciences, University of Cambridge, Downing Street, Cambridge, United Kingdom, CB2 3EQ

Abstract

In subduction zones, deserpentinisation is one of the main processes that controls fluid mediated mass-transfer between the slab and the mantle wedge. Despite a growing interest of this series of high-pressure reactions, natural examples of deserpentinisation in exhumed metamorphic terranes is rare. Here we identify for the first time in the Zermatt-Saas eclogite facies ultramafic massif, a network of high-pressure Ti-clinohumite and olivine bearing veins hosted within partly dehydrated slab serpentinites. Ti-clinohumite veins occur either in isolation as anastomosing vein networks, or in close association with pseudomorphic olivine + magnetite. Isolated veins comprising dominant granoblastic olivine, often associated with fibrous diopside, are also observed. These observations provide strong evidence for the partial dehydration of the hydrous serpentinite massif, and also call for a reappraisal of previous *P-T* estimates for the massif. The preferential crystallization of these high-pressure minerals within veins suggests that these constitute high permeability reaction channels, which served to localise fluids during the partial deserpentinisation of the Zermatt-Saas serpentinites. Our observations provide unequivocal evidence for the partial dehydration of the Zermatt serpentinites at high-

pressure during subduction.

3.1. Introduction

Subduction zones are the principal sites for the recycling of elements between Earth's exterior and interior. Exhumed subduction related terranes within present and past orogens (e.g. European Alps, Himalaya and Dabie Shan-Sulu) serve as prime locations to study high/ultrahigh-pressure (H/UH-P) metamorphic processes, yielding invaluable constraints on the chemical and physical processes that occur during subduction. Overall, ultrahigh-pressure (UHP) metamorphic massifs are globally sparse, and only small numbers of which can be considered representative of previously subducted oceanic lithosphere (Agard *et al.*, 2009, Guillot *et al.*, 2015). Furthermore, many of these UHP massifs preserve only dismembered portion of the subducting slab, with very few comprising a full complement of crustal and mantle slab lithologies (Guillot *et al.*, 2001, Schwartz *et al.*, 2001, Federico *et al.*, 2007).

The hydrated portion of the slab mantle plays a key role in subduction systems, as serpentines are capable of sequestering up to 13 wt. % H₂O, and, as such, arguably represent the most important carrier of fluids into subduction zones - playing a key role in the global volatile cycle (Ulmer and Trommsdorff, 1995; Rüpke *et al.*, 2004; Magni *et al.* 2014). The study of serpentinised UHP slab remnants have provided invaluable insights into the petrology of subducted material (Evans and Trommsdorff, 1978, Scambelluri *et al.*, 1991; 1995; 2015, Trommsdorff *et al.*, 1998, Sanchez Viscaino *et al.*, 2005, Padron-Navarta *et al.*, 2011, Debret *et al.*, 2013a, Shen *et al.*, 2015), geochemical cycling occurring in subduction zones (Scambelluri *et al.*, 2001a; 2001b; 2004, Deschamps *et al.*, 2010; 2013, Tenthorey *et al.*, 2004, John *et al.*, 2011, Scambelluri and Tonarini, 2012; Kendrick *et al.*, 2013; Alt *et al.*, 2013, Debret *et al.*, 2016, Pons *et al.*, 2016) and the nature and mechanics of deep fluid mobility (Kasahara *et al.*, 2002, Tenthorey and Cox, 2003, Zach *et al.*, 2007, Spandler *et al.*, 2011, Plümper *et al.*, 2017). Some of the most valuable information extracted from the study of UHP serpentinites derives from insights taken from metamorphic veins that record free fluid generation and migration during the devolatilisation process. Such veins provide powerful insight into the mechanisms of fluid expulsion and the geochemical transfer occurring during subduction (John *et al.*, 2011; 2012, Debret *et al.*, 2013b; Plümper *et al.*, 2017).

Here we have revisited one of the largest coherent serpentinite-bearing massifs worldwide: the Zermatt-Saas meta-ophiolite. This meta-ophiolite represents a large-scale (~30km thick) section of oceanic lithosphere, metamorphosed under eclogite facies conditions

along a subduction gradient (*Barnicoat and Fry, 1986, Bucher et al., 2005, Angiboust et al., 2009*). This massif records a metamorphic climax (~ 2.5 GPa and 600 °C; *Rebay et al., 2017*) at the edge of the stability of antigorite (high-*P* serpentine polytype), indicating that dehydration of the serpentinites under peak metamorphic conditions was likely. Despite a pervasive retrograde overprint, which have led previous studies to conclude that the ultramafic rocks did not suffer significant HP dehydration (e.g. *Barnicoat and Fry, 1986; Li et al., 2004a*), we demonstrate, through field and petrographic evidence, that the massif has indeed preserved evidence for antigorite breakdown. Dehydration patterns and olivine bearing veins provide direct evidence for fluid generation and migration during subduction zone metamorphism. This finding sets the grounds for a further understanding of slab processes to be gleaned from the Zermatt-Saas meta-ophiolite.

3.2. Geological Setting

The Zermatt-Saas meta-ophiolite forms part of the Zermatt-Saas Zone, which is located in the Western European Alps and covers an area spanning from Saas-Fee (Switzerland) in the North to Valtouranche (Italy) in the South (**Figure 3.1**). The terrane comprises a full sequence of ophiolitic lithologies, including serpentinitised ultramafics, metabasites and associated metamorphosed marine sediments (*Bearth, 1953; 1959, Barnicoat and Fry, 1986, Rubatto et al., 1998, Bucher et al., 2005, Angiboust et al., 2009, Rebay et al., 2017*). Structurally the Zermatt-Saas member sits above the internal Monte-Rosa basement units and is over thrust by the crystalline Dent-Blanche nappe (*Barnicoat and Fry, 1986*). The ophiolite is taken to represent a ~ 30 km thick section of Jurassic Liguro-piemontese oceanic lithosphere, which underwent subduction to ~ 75 km depth during the Eocene and subsequent exhumation as part of the Alpine orogeny (*Rubatto et al., 1998, Skora et al., 2015*). A varying metamorphic history is given for the ophiolite (summarized in *Rebay et al., 2017*) but it is accepted that it provides an excellent example of a largely cohesive eclogite facies terrane (e.g. *Angiboust et al., 2009*). This study focuses on the ultramafic lithologies between the Gornergrat and Trockner Steg area of the meta-ophiolite (**Figure 3.1**).

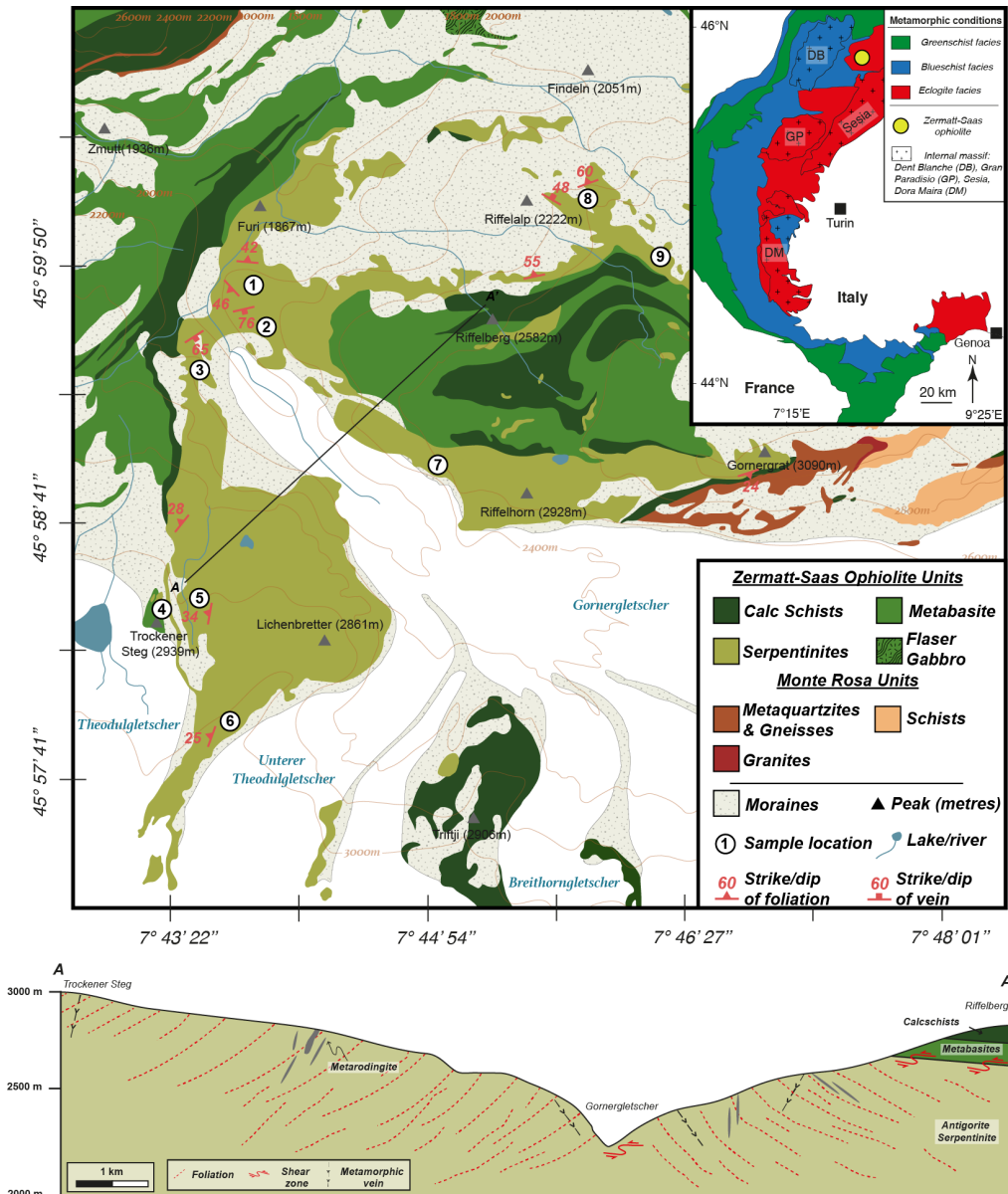


Figure 3.1. The inset map shows the apparent metamorphic conditions of the European Alps and the position of the Zermatt-Saas ophiolite in this context. The main body map shows the geology and key structural data for this study area. The localities of samples used as part of this study are denoted by the closed circle symbols. The cross section is drawn from the line of section (A-A') as shown on the main body. The main map is redrawn after Bearth, 1953.

The ultramafics from this area are composed of heavily deformed basal and upper units, characterised by a series of NE-SW striking shear planes, and a less deformed central unit, dominated by foliated serpentinites surrounding meter-scale boundaries of massive serpentinite and meta-rodinrites. The serpentinites of the Zermatt-Saas likely formed from a hartzburgitic protolith (Li et al., 2004a, Selverstone and Sharp, 2013; this study [see major element data within Chapter 4]) and constitute the volumetrically most

significant lithology within the meta-ophiolite (*Butcher et al., 2005*). In their current structural arrangement, this ultramafic sequence sits below associated metabasite and calc-schistose marine sediments (*Bearth, 1953, Figure 3.1*)

3.3. Vein Occurrence and Paragenesis

3.3.1 Field observations of rock textures and metamorphic veins

Throughout the massif, most of the ultramafic body is formed from dark-green, variably foliated serpentinites, which comprise an aphanitic antigorite groundmass. Subordinate mm-scale magnetite and Titanium-clinohumite (Ti-Chm) is commonly observed, alongside rare, chlorite and olivine bearing horizons. Intense deformation is mostly restricted to some mylonitic corridors typically found at the base and the top of the ultramafic unit. The whole body is at first monotonous, but in some areas, and especially where the foliation is weak, networks of veins and veinlets are observed. This veining can be so intense that the host serpentinite can appear to be almost totally replaced by the vein forming minerals (**Figure 3.2**).

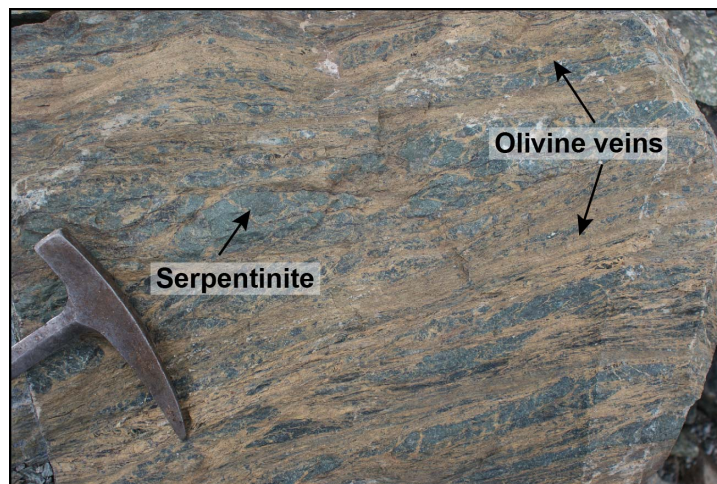


Figure 3.2. Field photograph showing the pervasive nature of olivine veining in parts of the serpentinite massif. Here the host serpentinite appears ~75% replaced by olivine veins

In the most massive areas, these vein networks are often associated with a distinctive macro-texture, where cm-size light-green patches, sometimes containing Ti-Chm cores (**Figure 3.3a**), are associated with cm-wide strips and appear in contrast with the dark green groundmass. This distinctive textural arrangement is referred to here after as a “python pattern”. A key outcrop where the python pattern is most well developed in association with several generations of metamorphic

veins offers the best example of the field relationships and has been studied and sampled in detail (See locality 7 on **Figure 3.1**; 45° 99. 209' N, 007° 73. 442' W).

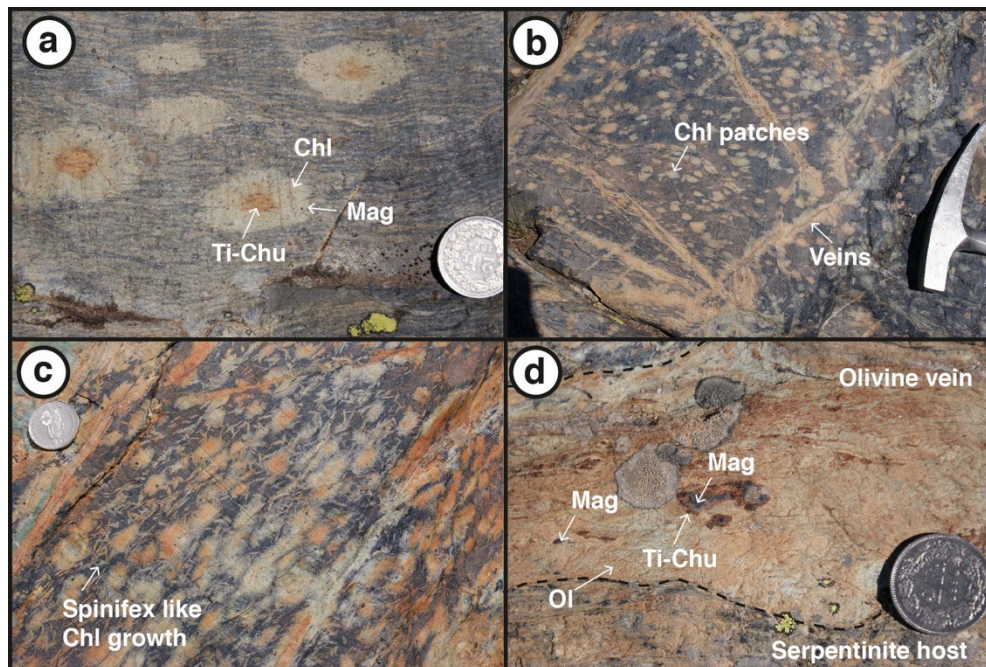


Figure 3.3. A multipanel of images taken from the “key outcrop”. (a) shows individual patches of chlorite growth that surround Ti-chu grains. (b) shows the development of the python-pattern across the surface of the serpentinites. (c) shows the relationship between chlorite patches and spinifex like chlorite growth. (d) shows an olivine vein (Type 1 olivine) that preserves nests of magnetite and Ti-Chu within. This type of Ti-Chu is termed Type 2 Ti-Chu.

At this key outcrop, the well-developed python pattern shows light green patches often coalescing into a network of anastomosing veinlets and veins, that in turn display a pervasive relationship with the serpentinites (**Figure 3.3b**). Rarely, patches and veins are associated with tiny needles, which can be observed radiating around patches, or randomly oriented and closely associated with such patches (**Figure 3.3c**). These tiny needles resemble a spinifex-like texture. In this location, veins can also be sharp, and cross cut the python pattern. In addition we also note cm-wide, laterally continuous veins of coarse white olivine and aggregated Ti-Chu. Within such veins it is common to observe nests of magnetite that are rimmed by Ti-Chu (**Figure 3.3d**). Olivine observed within this manner is termed Type 1 olivine. An additional generation of olivine is also observed at this key outcrop whereby veins and capillary networks comprising relict Ti-Chm cores are now surrounded by beige olivine and minor chlorite (**Figure 3.4**). This generation of olivine is termed Type 2 olivine.

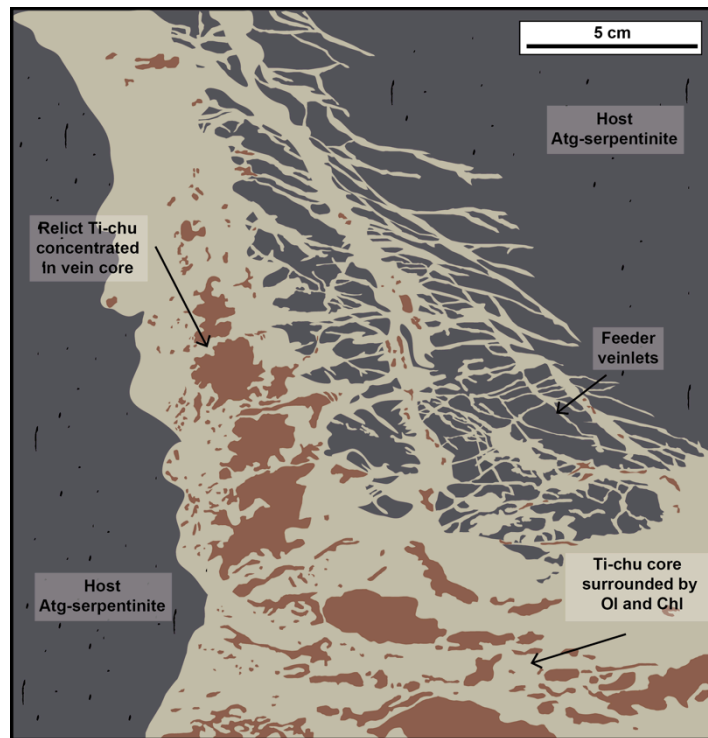


Figure 3.4. A field sketch showing the occurrence of Type 2 olivine. This olivine generation occurs in association with minor chlorite, surrounding relict Ti-Chu veins. Ti-Chu occurring in this manner is termed Type 3 Ti-Chu. These vein networks resemble a feeder system of interconnected smaller veinlets that join with a larger vein.

Although this outcrop provides us with the best example of these textures, this pattern is in fact ubiquitous throughout the massif, but often obscured and overprinted by deformation and retrogression (e.g. **Figure 3.5a**).

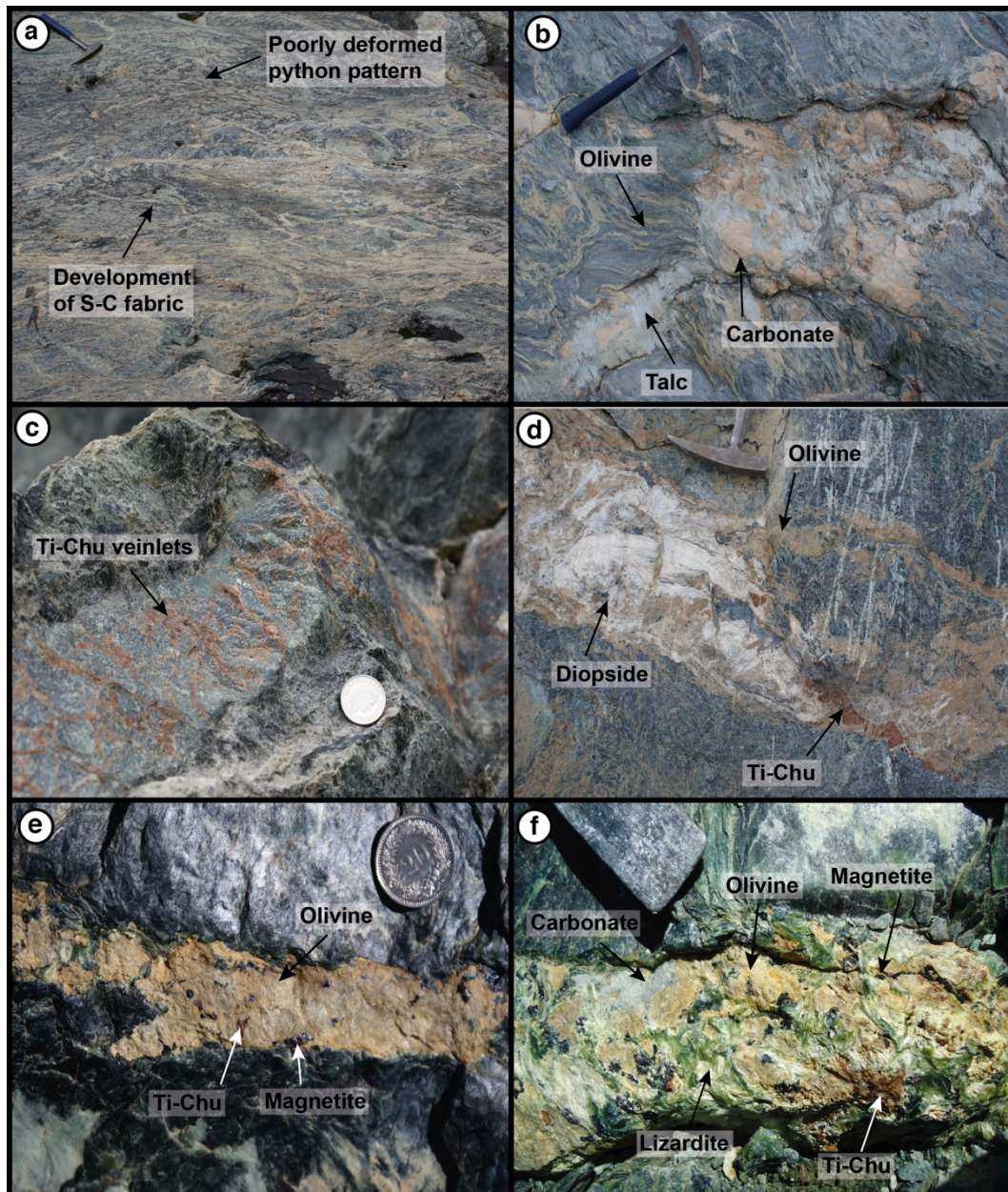


Figure 3.5. A multipanel of images taken from different localities across the massif. **(a)** A section of serpentinite showing a deformed example of the python-pattern. Within the lower part of the photograph a poorly developed S-C fabric can be seen to obscure the python pattern. Towards the top of the picture a poorly deformed section shows the well-formed python pattern. **(b)** Carbonate and talc rich regions of serpentinite in association with olivine veins. This outcrop occurs ~5m from the contact with overlying sedimentary units. **(c)** shows a section of anastomosing Ti-chu veinlets appearing to cut the foliation of the host serpentinite (Type 4 Ti-Chu). **(d)** A thick olivine, diopside and Ti-Chu vein within a serpentinite located at the top of the massif, towards the contact with overlying sedimentary units. **(e)** Pinching olivine dominated vein that contains disseminated grains of Ti-Chu and magnetite. Olivine occurring in this form is termed Type 3 olivine, whilst this type of Ti-Chu is termed Type 2 Ti-Chu. **(f)** Veined carbonate in association with

olivine. Magnetite and Ti-Chu are also observed as vein forming phases. Green patches are of late lizardite.

Across the massif the metamorphic veins show numerous structures and relationships with the serpentinites, as well as a diverse mineralogy, with olivine and Ti-Chm being the most common vein forming phases. Carbonates, commonly associated with olivine, Ti-Chm and talc are also present, but mainly appear close to the upper contact with the overlying crustal and sedimentary units (**Figure 3.5b**).

Metamorphic veins range between 1-10 m in length and anywhere from mm-scale capillaries (**Figure 3.5c**) up to channels 10 cm in width (**Figure 3.5d**). Although some appear laterally continuous across the outcrop, often they taper and pinch out. Additionally it is common to observe veins forming as tension gashes, which display sharp boundaries and appear to either cut the foliation, or open along shear planes oblique to the foliation – subsequently defining C-planes. Anastomosing vein networks are sometimes affected by heterogeneous deformation, where shear planes only affect part of the network.

The abundance of vein bearing phases varies significantly between outcrops and the structural level of the massif. Olivine is usually abundant as the groundmass of most of the veins, with three main types being defined here. The first and second type of vein forming olivine were best observed at the key outcrop, and have been described and defined above. The third type of vein forming olivine is prevalent throughout the massif and shows coarse, white olivine occurring in association with cm-scale, disseminated grains of Ti-Chu (**Figure 3.5e**). This generation of olivine is termed Type 3 olivine.

Four main types of Ti-Chm are identified on the basis of different macroscopic textural relationships. Ti-Chu occurs within veins associated with olivine as either: Type 1 - Fresh dark red, cm-scale crystals surrounded by olivine (e.g. **Figure 3.5e**); Type 2 - Centimetre scale aggregates within the core of olivine veins appearing to surround nests of magnetite (e.g. **Figure 3.3d**), or as; Type 3 - Relict aggregates within the core of olivine veins entirely surrounded and enveloped by olivine (e.g. **Figure 3.4**). A fourth type of Ti-Chu (Type 4) is defined appearing to occur in isolation as anastomosing veinlets parallel to the foliation of the host serpentinite (e.g. **Figure 3.5c**).

Chlorite is most commonly occurs as a phase with olivine in veins and pods at the aforementioned “key outcrop”. Near the contact with the overlying crust, olivine and carbonates coexist in the veins, with a fine olivine matrix containing Ti-Chu and magnetite, and isolated mm- to cm-sized carbonates (**Figure 3.5f**). Typically these are overprinted by a diopside matrix, which often forms as cm-scale fibrous blades surrounding and isolating angular olivine clusters, ultimately forming a brecciated texture. It is common to observe large strips of Ti-chum being dismembered by cracks in which a fine-grained olivine matrix crystallized (**Figure 3.6**).

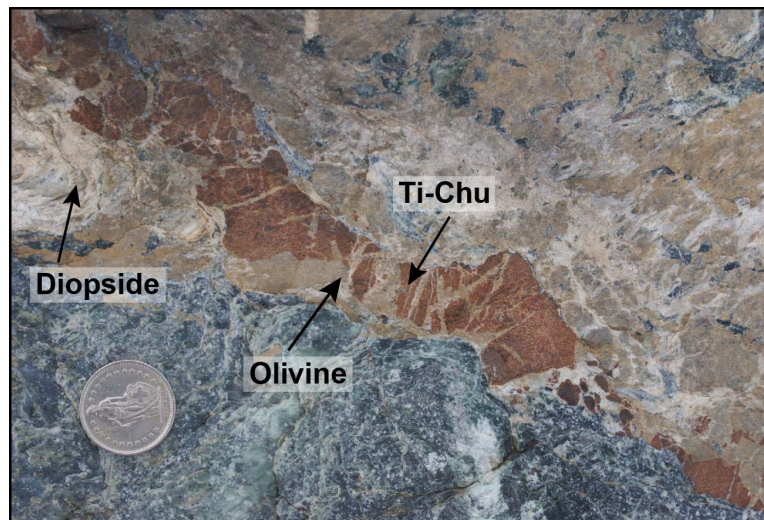


Figure 3.6. *Dismembered Ti-Chu intruded by olivine along cracks. Diopside is also observed to coexists.*

At the contact with the crustal lithologies, veining is intense, and carbonates veins and pods are associated with talc, overprinting all the previously cited textures.

3.3.2 Microscopic petrographic and textural observations

In thin section both foliated and massive serpentinite bodies are dominated by fresh, <0.1 mm antigorite and ~1mm disseminated magnetite, which either forms as elongate stringers or rounded grains hosted within groundmass antigorite. Groundmass olivine is found within both the foliated and massive serpentinites. In these samples groundmass olivine occurs either as, <0.1 mm disseminated grains supported within antigorite groundmass, or as microscopic <mm-scale pinching veinlets, often associated with magnetite, and commonly seen to be being replaced by laths of antigorite (**Figure 3.7a**). Rare groundmass Ti-

clinohumite is also observed as a minor phase within the foliated and massive serpentinites, typically occurring as <0.1mm anhedral disseminated grains.

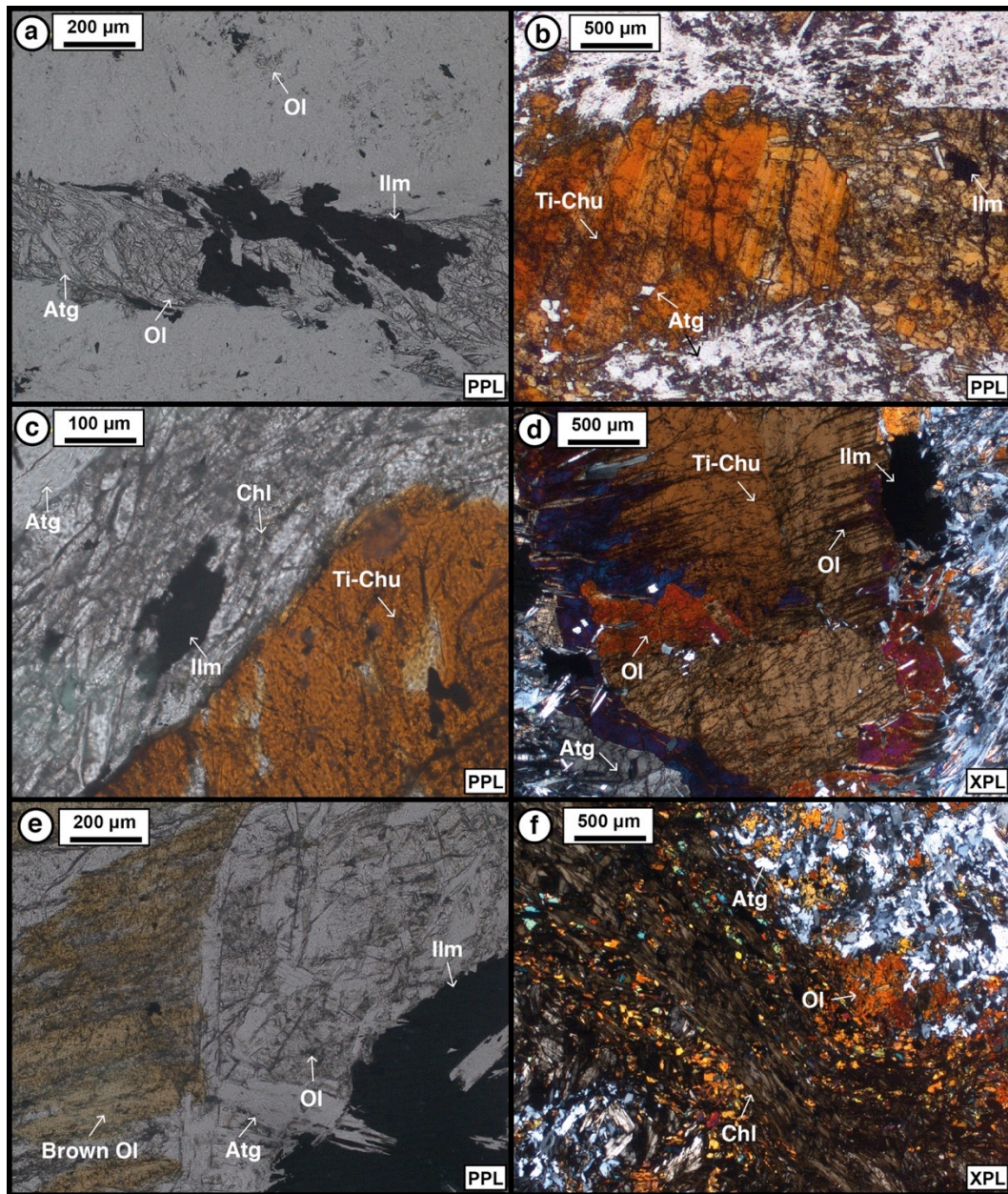


Figure 3.7. A selection of thin section photomicrographs showing (a) Millimetre-scale olivine and ilmenite veinlet hosted with an antigorite groundmass. Olivine within the vein is partially replaced by laths of antigorite. Smaller (<mm) disseminated olivine grains occur within the antigorite groundmass. (b) Subhedral Ti-clinohumite crystal surrounded by antigorite. It is common to observe Ti-clinohumite crystals contain inclusions of antigorite and ilmenite. (c) Python-pattern Ti-clinohumite core surrounded by woody chlorite and ilmenite. (d) Relict Ti-clinohumite pseudomorphed by olivine and ilmenite within an antigorite serpentinite. (e) An assemblage of pseudomorphic brown and clear olivine with ilmenite. Note partial replacement of olivine with laths of antigorite. (f)

Woody chlorite associated with <mm-scale grains of olivine and Ti-clinohumite hosted within an antigorite matrix.

The patches forming the python-pattern described from the “key outcrop” are predominantly formed from <0.01mm laths of chlorite associated with mm-scale magnetite, in which grains of olivine ± Ti-Chm are commonly observed. Often individual patches of chlorite surround a poorly preserved cm-scale core of Ti-Chm, which display ragged grain boundaries and commonly contain inclusions of acicular antigorite (**Figure 3.7c**). When chlorite patches coalesce into vein-like structures they commonly contain thin <mm-scale cores of anhedral Ti-Chu and olivine, sometimes being associated with mm-scale grains of magnetite (**Figure 3.7f**). Type 1 olivine from this “key outcrop” appears as relatively fresh, mm-cm scale olivine grains displaying a granoblastic texture alongside mm- and cm-scale grains of magnetite, while Type 2 olivine forms as pseudomorphic fine grained aggregates of clear and brown olivine surrounding aggregated relict Ti-Chu (**Figure 3.7d and e**).

Type 1 Ti-Chu occurs as mm-scale, fresh crystals displaying equilibrium textures with granoblastic vein forming olivine. Type 2 Ti-Chu is formed of <0.1mm scale aggregates of anhedral Ti-Chu that surround cm-scale nests of magnetite. Type 3 Ti-Chu forms as ~1mm grains, that is enveloped by brown and clear olivine. Typically this Ti-Chu shows distinctive fracturing radiating inwards from the grain boundaries (**Figure 3.7d**). Along these cracks olivine is seen to partially replace Ti-Chu. Type 4 Ti-Chu comprises some of the freshest crystals observed. Here mm-scale grains show distinctive pleochroic twinning and are surrounded by smaller <0.01mm grains of Ti-Chu (**Figure 3.7b**). Often elongate intergrowths of magnetite and ilmenite are observed growing parallel to the twinning planes.

Carbonate bearing veins show equigranular, <0.1mm scale carbonate grains occurring alongside subhedral olivine and contain small laths of included antigorite. Magnetite also occurs as small, ~0.01mm disseminated grains. Diopside, when present, occurs as tube-like crystals forms alongside fresh, olivine grains. Interestingly when diopside-bearing veins seemed to be hosted by serpentinites that contains much more olivine groundmass associated with antigorite.

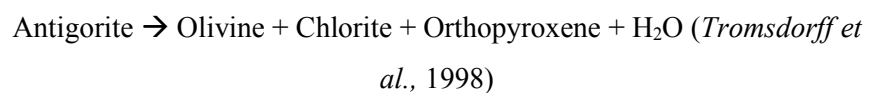
3.4. Discussion

3.4.1 Evidence for dehydration reactions

Here we have observed and described a series of HP metamorphic veins and rock textures within the Zermatt-Saas serpentinites, and link these to a series of key deserpentinisation reactions.

3.4.1.1. Python-pattern texture

The python patterned serpentinites represent the most abundant chlorite bearing lithology of the massif, and is interpreted as being a key maker of partial dehydration within the serpentinites. We suggest that chlorite growth in this manner could form owing to the static recrystallisation of the antigorite domain as a result of the reaction:



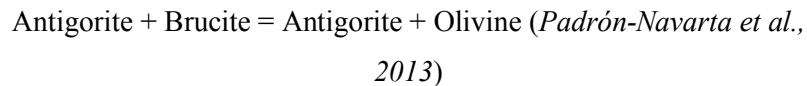
Static recrystallisation of the antigorite domain to chlorite, accompanying fluid release can account for the distinctive patterns formed. In parts this pattern is formed from isolated patches of chlorite growth, whilst elsewhere these patches coalesce into vein like structures. We interpret patchy chlorite growth to reflect in-situ dehydration of the serpentinites, whereby static replacement of the antigorite domain is occurring. Where these patches coalesce into veins it is feasible that this represents parts where fluid expulsion is occurring, and that such fluids are migrating outwards from the areas where they were generated. This could also account for olivine and Ti-Chu cores within such veins.

The spinifex-like growth is somewhat more ambiguous than the patchy chlorite growth. Seeing as these radiating needles do not appear to join together it is unlikely that these areas represent a fracturing pattern caused by fluid over-pressuring. Instead it could be the case that these represent growth of bladed diopside, rather than a texture created by dehydration mechanics (i.e. fracturing).

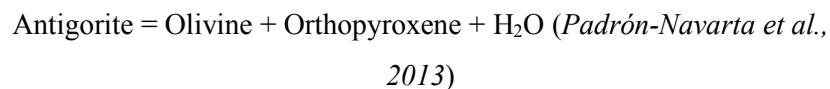
It is noteworthy that this so called python-pattern is akin to the granofels texture observed within the transitional lithologies of the Almiraz ultramafic massif (Padrón-Navarta et al., 2011)

3.4.1.2 Olivine rich veins

One of the most significant findings of this work has been the documentation of multiple types of olivine dominated metamorphic veins hosted within the serpentinites. Metamorphic olivine within subducted serpentinites could be considered with respect to two key reactions. The first of these reactions is brucite destabilisation, which proceeds as:



Owing to the suggested prograde path of the massif it is highly likely that brucite destabilisation occurred at temperatures greater than ~475 °C at ~2.4 GPa, which could be invoked to explain the occurrence of metamorphic olivine seen within the serpentinites. Despite this we suggest that the majority of vein forming olivine seen here occurs as a result of antigorite breakdown, as per the reaction:



Our main reasoning to suggest that much of the metamorphic olivine within these rocks represents antigorite destabilisation, opposed to brucite breakdown is the nature of olivine occurrence. Seeing as much of the olivine is present within widespread, pervasive vein networks, it is apparent that olivine crystallization occurred alongside relatively high degrees of fluid flow. As such we argue that brucite destabilisation did not liberate enough free H₂O to account for the structures observed, instead the relatively high volume of free fluid generated during antigorite breakdown could account for such widespread vein structures within the massif.

Further more we document clear observations of chlorite growth, which occurs at the expense of antigorite. This provides unequivocal evidence that the main deserpentinisation reaction we are observing within these lithologies is that of antigorite breakdown.

This finding is complimentary to previous studies from other partially dehydrated ultramafic massifs (e.g. Errio Tobbio [Scambelluri *et al.*, 1991]) whereby similar olivine-rich vein assemblages have been accounted for owing to the destabilisation of antigorite during HP eclogite facies metamorphism of the massif. Ultimately we suggest a similar scenario for the Zermatt-Saas ultramafics, whereby peak metamorphism occurred within the divariant antigorite + olivine stability field, triggering partial destabilisation of hydrous antigorite and the crystallisation of metamorphic olivine (e.g. stage 1 on **Figure 4**). This interpretation is consistent with key *P-T* estimates given for the massif (Bucher and Frey, 1994, Li *et al.*, 2004).

3.4.1.3 Ti-Clinohumite rich veins

Of the four types of Ti-Chu identified and described above we interpret these to reflect formation at distinct periods in the metamorphic history of the massif. The first generation of Ti-Chu (displaying equilibrium textures with olivine in veins) can be interpreted to reflect Ti-Chu formation along the prograde path, whereby Ti-Chu was stabilised within its divariant stability field, as shown on **Figure 3.8**. This initial crystallisation of Ti-Chu occurred alongside formation of metamorphic vein forming olivine, and grew within metamorphic veins. Continued metamorphism at higher *P-T* likely triggered destabilisation of Ti-Chu beyond the upper limit of the stability field, as shown in **Figure 3.8**. In this scenario prograde Ti-Chu underwent destabilisation to olivine, thus accounting for Ti-Chu, which is now surrounded and enveloped by pseudomorphic olivine and ilmenite aggregates. This observation is in agreement with the Ti-Chu breakdown mechanisms suggested for the Cerro del Almirez ultramafic massif (López Sánchez-Vizcío *et al.*, 2009). This assemblage most likely represents the peak assemblage identified as part of this study.

The other two types of Ti-Chu are interpreted to reflect Ti-Chu stabilisation within the divariant stability field during retrogressive metamorphism of the massif. We suggest that Ti-Chu surrounding ilmenite nests, and Ti-Chu present as anastomosing veinlets most likely formed as retrogressive features, whereby Ti-Chu surrounding ilmenite formed pseudomorphically after the peak olivine and ilmenite

assemblage. The fourth type of Ti-Chu recognised most likely represents a late stage generation of Ti-Chu growth, as it cuts the dominant foliation of the host serpentinite whenever observed.

3.4.2 Carbonate and diopside occurrence

The presence of both carbonate minerals and diopside within the serpentinites suggest the possible interaction with externally derived fluids, as externally sourced Ca remains the likely catalyst for the growth of these minerals. To a first order it should be noted that the occurrence of these minerals within the serpentinites proximal to the overlying sedimentary units, suggest a sedimentary origin for such fluids but without detailed geochemical tracers it is not possible to elucidate this process fully.

3.4.3 Widespread retrogression of the massif

Despite obvious evidence for a series of *HP*, prograde assemblages a pervasive retrogressive overprint is apparent. Much of the groundmass forming antigorite likely represents post peak crystallisation along the return path, and is evidenced through replacement of groundmass olivine veinlets with laths of antigorite (**Figure 3.7a**). Additionally the presence of low *P* lizardite appearing to replace olivine (**Figure 3.5f**) and lizardite and chrysotile veins cutting the main foliation of the massif further reinforces the suggestion of a retrogressive overprint to the serpentinites.

The preservation of relatively fresh peak, or near peak metamorphic assemblages is most likely a result of the relatively undeformed sections of the massif where they are located, meaning that the kinetic rate in these areas was significantly lower than in the most deformed and sheared sections, where the most evidence for late retrogression is apparent. Given that the rate of exhumation of the Zermatt-Saas Ophiolite is suggested to have occurred relatively rapidly, it is likely that that greenschist facies conditions were reached within ~4 My post peak (*Amato et al., 1999*), this could account for the preservation of the prograde dehydration features documented here.

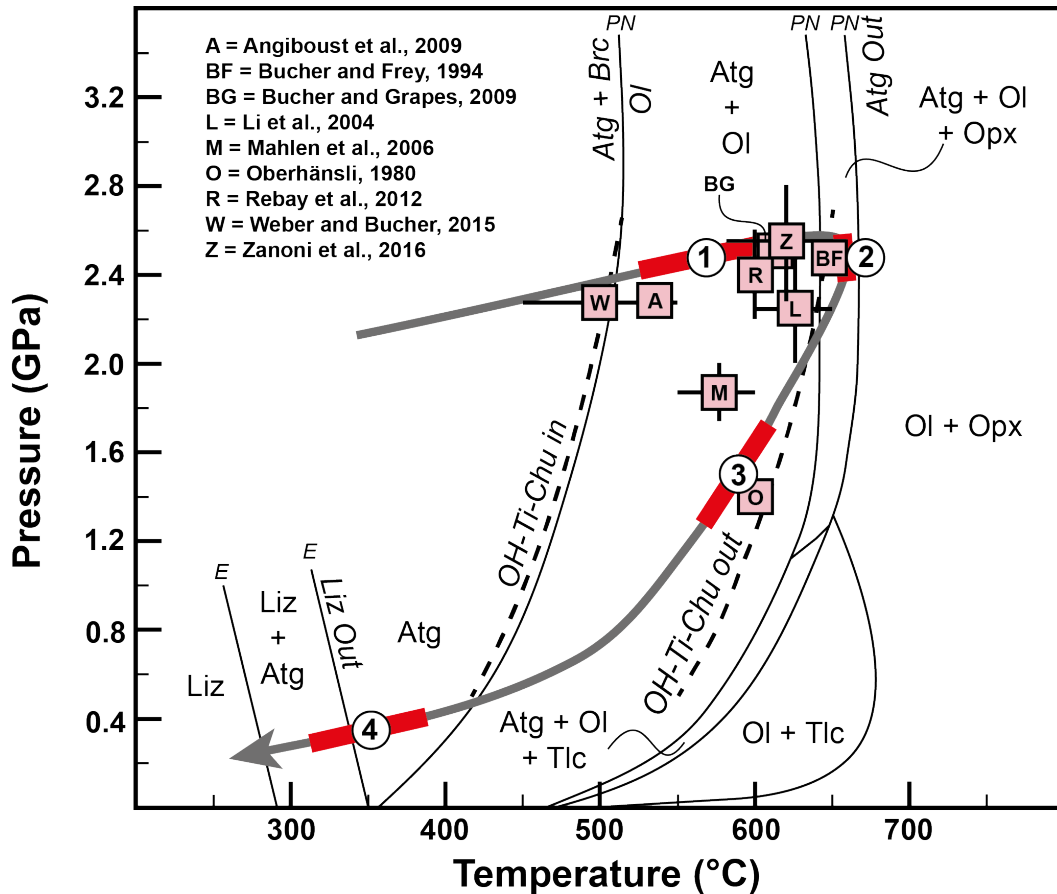


Figure 3.8. A simplified P - T grid for the Zermatt serpentinite massif. The suggested metamorphic evolution (P - T path) is shown with the thick grey arrow. Each of the red numbered boxes represent key points of the metamorphic evolution of the massif for which we have observed a defining mineral assemblage. These stages are summarised in our main text conclusions. The reaction tie lines E are taken from Evans, 2004; PN from Padrón-Navarta et al., 2013, and; SV from Sánchez-Vizcaino et al., 2009. Light red boxes with letters indicate previous P - T estimates for peak metamorphism of rocks from the Zermatt-Saas ophiolite.

3.5. Conclusions

This study documents a series of Ti-Chu and olivine bearing metamorphic veins and macroscopic rock textures, which are interpreted to be indicative features of partial dehydration of the Zermatt-Saas serpentinites – a scenario previously undiscussed. With respect to **Figure 3.8** we give a suggest P - T path of the ultramafic massif, and link our observations to previously determined metamorphic reactions. Stage 1 of this evolution is marked by formation of olivine owing to brucite breakdown and equilibration within the olivine + antigorite stability field. Concurrent with this is the formation of Ti-Chu within the divariant stability field. Stage 2 represents the peak metamorphic assemblage, whereby the antigorite out isograd is reached and olivine formation results from the

breakdown of antigorite. This stage like accompanied the greatest fluid release from these rocks. Stage 3 marks re-equilibration along the return path, whereby antigorite and Ti-Chu are stabilised and begin to overprint prograde or peak assemblages. The final stage (4) represents low P retrogression and overprinting of the massif.

In conclusion we suggest that both olivine + Ti-Chu + chlorite metamorphic assemblage most likely occurred as a result of antigorite breakdown within the serpentinites studied here. We suggest that despite being heavily retrogressed, portions of the massive preserve peak, or near peak metamorphic assemblages. In addition we also suggest that interaction with externally derived fluids has occurred at some point during the metamorphic history of the massive, but we are unable to comment conclusively on the origin or timing of this fluid interaction.

Taken together we suggest that previous studies of the Zermatt-Saas serpentinites failed to acknowledge apparent evidence for partial dehydration of these lithologies and consequently, we conclude that the Zermatt-Saas serpentinites provide an excellent example of a section of slab serpentinites that demonstrate evidence for channelized fluid flow owing to the partial dehydration of hydrous serpentinite. We advocate the future study of these rocks in the understanding of fluid flow and mass transfer occurring during serpentinite dehydration within subduction zones.

Acknowledgements

This study forms part of the Ph. D work of EI who was supported via a studentship made possible as part of an ERC Starting Grant (HabitablePlanet; 306655) awarded to HW. HW also acknowledges BD acknowledges his F.R.S.-F.N.R.S. research fellowship (Chargé de recherché). PB wishes to acknowledge ERC Starting Grant (MASE; 279828) awarded to J. van Hunen and his Auvergne Fellowship (French Government Laboratory of Excellence initiative No. ANR-10LABX-0006, ClercVoc contribution no. 253). Funding for this fieldwork was provided by a Geological Society of London grant from the Timothy Jefferson Field Research fund awarded to EI. Emma Gregory is thanked for her help in the field. The staff at Ulrich Imboden AG (Zermatt) are acknowledged for their assistance with the sampling strategy. Joerg Hermann is thanked for discussion. This paper is dedicated to the memory of Ueli Steck.

References Cited

- Agard, P., Yamato, P., Jolivet, L. and Burov, E., 2009. Exhumation of oceanic blueschists and eclogites in subduction zones: timing and mechanisms. *Earth-Science Reviews*, 92(1), pp.53-79.
- Amato, J.M., Johnson, C.M., Baumgartner, L.P. and Beard, B.L., 1999. Rapid exhumation of the Zermatt-Saas ophiolite deduced from high-precision SmNd and RbSr geochronology. *Earth and Planetary Science Letters*, 171(3), pp.425-438.
- Alt, J.C., Schwarzenbach, E.M., Früh-Green, G.L., Shanks, W.C., Bernasconi, S.M., Garrido, C.J., Crispini, L., Gaggero, L., Padrón-Navarta, J.A. and Marchesi, C., 2013. The role of serpentinites in cycling of carbon and sulfur: seafloor serpentinization and subduction metamorphism: *Lithos*, v. 178, p. 40-54.
- Angiboust, S., Agard, P., Jolivet, L. and Beyssac, O., 2009. The Zermatt- Saas ophiolite: the largest (60-km wide) and deepest (c. 70–80 km) continuous slice of oceanic lithosphere detached from a subduction zone?, *Terra Nova*, v. 21, p.171-180
- Barnicoat, A.C. and Fry, N., 1986, High-pressure metamorphism of the Zermatt-Saas ophiolite zone, Switzerland. *Journal of the Geological Society*, v. 143, p. 607-618
- Bearth, P., 1953, *Geologischer Atlas der Schweiz*. Schweizerische Geologische Komm.
- Bearth, P., 1959, Über Eklogite, Glaukophanschiefer und metamorphe Pillowlaven. *Schweizerische Mineralogische und Petrographische Mitteilungen*, v. 39, p.267-286.
- Bucher, K., Fazis, Y., Capitani, C.D. and Grapes, R., 2005, Blueschists, eclogites, and decompression assemblages of the Zermatt-Saas ophiolite: High-pressure metamorphism of subducted Tethys lithosphere. *American Mineralogist*, v. 90, p. 821-835.
- Debret, B., Andreani, M., Godard, M., Nicollet, C., Schwartz, S. and Lafay, R., 2013, Trace element behavior during serpentinization/de-serpentinization of an eclogitized oceanic lithosphere: A LA-ICPMS study of the Lanzo ultramafic massif (Western Alps). *Chemical Geology*, v. 357, p.117-133.

Debret, B., Andreani, M., Muñoz, M., Bolfan-Casanova, N., Carlut, J., Nicollet, C., Schwartz, S. and Trcera, N., 2014b, Evolution of Fe redox state in serpentine during subduction. *Earth and Planetary Science Letters*, v. 400, p. 206-218

Debret, B., Bolfan-Casanova, N., Padrón-Navarta, J.A., Martín-Hernández, F., Andreani, M., Garrido, C.J., Sánchez-Vizcaíno, V.L., Gómez-Pugnaire, M.T., Muñoz, M. and Trcera, N., 2015, Redox state of iron during high-pressure serpentinite dehydration. *Contributions to Mineralogy and Petrology*, v. 169, p.1-18.

Debret, B., Koga, K.T., Nicollet, C., Andreani, M. and Schwartz, S., 2014a, F, Cl and S input via serpentinite in subduction zones: implications for the nature of the fluid released at depth. *Terra Nova*, v. 26, p.96-101.

Debret, B., Millet, M.A., Pons, M.L., Bouilhol, P., Inglis, E. and Williams, H., 2016, Isotopic evidence for iron mobility during subduction. *Geology*, v. 44, p. 215-218.

Deschamps, F., Godard, M., Guillot, S. and Hattori, K., 2013, Geochemistry of subduction zone serpentinites: A review. *Lithos*, v. 178, p. 96-127.

Deschamps, F., Godard, M., Guillot, S., Chauvel, C., Andreani, M., Hattori, K., Wunder, B. and France, L., 2012, Behavior of fluid-mobile elements in serpentines from abyssal to subduction environments: Examples from Cuba and Dominican Republic. *Chemical Geology*, v. 312, p. 93-117.

Deschamps, F., Guillot, S., Godard, M., Andreani, M. and Hattori, K., 2011, Serpentinites act as sponges for fluid- mobile elements in abyssal and subduction zone environments. *Terra Nova*, v. 23, p.171-178.

Deschamps, F., Guillot, S., Godard, M., Chauvel, C., Andreani, M. and Hattori, K., 2010. In situ characterization of serpentinites from forearc mantle wedges: timing of serpentinization and behavior of fluid-mobile elements in subduction zones. *Chemical Geology*, 269(3), pp.262-277.

Engi, M. and Lindsley, D.H., 1980, Stability of titanian clinohumite: experiments and thermodynamic analysis. *Contributions to Mineralogy and Petrology*, v. 72, p. 415-424.

Evans, B.W. and Trommsdorff, V., 1978. Petrogenesis of garnet lherzolite, Cima di Gagnone, Lepontine Alps. *Earth and Planetary Science Letters*, 40(3), pp.333-348.

Federico, L., Crispini, L., Scambelluri, M. and Capponi, G., 2007. Ophiolite mélange zone records exhumation in a fossil subduction channel. *Geology*, 35(6), pp.499-502.

Guillot, S., Hattori, K.H., de Sigoyer, J., Nägler, T. and Auzende, A.L., 2001. Evidence of hydration of the mantle wedge and its role in the exhumation of eclogites. *Earth and Planetary Science Letters*, 193(1), pp.115-127.

Guillot, S., Schwartz, S., Reynard, B., Agard, P. and Prigent, C., 2015. Tectonic significance of serpentinites. *Tectonophysics*, v. 646, p. 1-19.

Hermann, J., Müntener, O. and Scambelluri, M., 2000. The importance of serpentinite mylonites for subduction and exhumation of oceanic crust. *Tectonophysics*, v. 327, p. 225-238.

John, T., Gussone, N., Podladchikov, Y.Y., Bebout, G.E., Dohmen, R., Halama, R., Klemd, R., Magna, T. and Seitz, H.M., 2012. Volcanic arcs fed by rapid pulsed fluid flow through subducting slabs. *Nature Geoscience*, 5(7), pp.489-492.

John, T., Scambelluri, M., Frische, M., Barnes, J.D. and Bach, W., 2011. Dehydration of subducting serpentinite: implications for halogen mobility in subduction zones and the deep halogen cycle. *Earth and Planetary Science Letters*, 308(1), pp.65-76.

Kendrick, M.A., Honda, M., Pettke, T., Scambelluri, M., Phillips, D. and Giuliani, A., 2013. Subduction zone fluxes of halogens and noble gases in seafloor and forearc serpentinites. *Earth and Planetary Science Letters*, 365, pp.86-96.

Li, X.P., Rahn, M. and Bucher, K., 2004a, Serpentinites of the Zermatt- Saas ophiolite complex and their texture evolution. *Journal of Metamorphic Geology*, v. 22, p. 159-177.

Li, X.P., Rahn, M. and Bucher, K., 2004b, Metamorphic processes in rodingites of the Zermatt-Saas ophiolites. *International Geology Review*, v. 46, p. 28-51.

Magni, V., Bouilhol, P. and van Hunen, J., 2014, Deep water recycling through time. *Geochemistry, Geophysics, Geosystems*, v. 15, p. 4203-4216.

McDonough, W.F. and Sun, S.S., 1995, The composition of the Earth. *Chemical geology*, v. 120, p. 223-253.

Müntener, O., 2010. Serpentine and serpentinization: a link between planet formation and life. *Geology*, v. 38, p. 959-960.

Padrón-Navarta, J.A., Lopez Sanchez-Vizcaino, V., Garrido, C.J. and Gómez-Pugnaire, M.T., 2011, Metamorphic record of high-pressure dehydration of antigorite serpentinite to chlorite harzburgite in a subduction setting (Cerro del Almiraz, Nevado-Filábride Complex, Southern Spain). *Journal of Petrology*, v. 52, p. 2047-2078.

Peacock, S.M., 2001. Are the lower planes of double seismic zones caused by serpentine dehydration in subducting oceanic mantle?. *Geology*, 29(4), pp.299-302.

Plümper, O., John, T., Podladchikov, Y.Y., Vrijmoed, J.C. and Scambelluri, M., 2017, Fluid escape from subduction zones controlled by channel-forming reactive porosity. *Nature Geoscience*, v. 10, p. 150-156.

Poli, S. and Schmidt, M.W., 2002. Petrology of subducted slabs. *Annual Review of Earth and Planetary Sciences*, 30(1), pp.207-235.

Pons, M.L., Debret, B., Bouilhol, P., Delacour, A. and Williams, H., 2016, Zinc isotope evidence for sulfate-rich fluid transfer across subduction zones. *Nature Communications*, v. 7.

Rahn, M.K. and Rahn, K., 1998, Titanian clinohumite formation in the Zermatt-Saas ophiolites, central Alps. *Mineralogy and Petrology*, v. 64, p. 1-13.

Rebay, G., Spalla, M.I. and Zanoni, D., 2012, Interaction of deformation and metamorphism during subduction and exhumation of hydrated oceanic mantle: Insights from the Western Alps. *Journal of Metamorphic Geology*, v. 30, p. 687-702.

Rebay, G., Zanoni, D., Langone, A., Luoni, P., Tiepolo, M. and Spalla, M.I., 2017. Dating of ultramafic rocks from the Western Alps ophiolites discloses Late Cretaceous subduction ages in the Zermatt-Saas Zone. *Geological Magazine*, pp.1-18.

Rüpke, L.H., Morgan, J.P., Hort, M. and Connolly, J.A., 2004, Serpentine and the subduction zone water cycle. *Earth and Planetary Science Letters*, v. 223, p. 17-34.

Sánchez-Vizcaíno, V.L., Trommsdorff, V., Gómez-Pugnaire, M.T., Garrido, C.J., Müntener, O. and Connolly, J.A.D., 2005, Petrology of titanian clinohumite and olivine at the high-pressure breakdown of antigorite serpentinite to chlorite harzburgite (Almirez Massif, S. Spain). *Contributions to Mineralogy and Petrology*, v. 149, p. 627-646.

Sánchez-Vizcaíno, V.L., Gómez-Pugnaire, M.T., Garrido, C.J., Padrón-Navarta, J.A. and Mellini, M., 2009. Breakdown mechanisms of titanclinohumite in antigorite serpentinite (Cerro del Almirez massif, S. Spain): A petrological and TEM study. *Lithos*, 107(3-4), pp.216-226.

Scambelluri, M., Müntener, O., Hermann, J., Piccardo, G.B. and Trommsdorff, V., 1995, Subduction of water into the mantle: history of an Alpine peridotite. *Geology*, v. 23, p. 459-462.

Scambelluri, M. and Philippot, P., 2001a, Deep fluids in subduction zones. *Lithos*, v. 55, p. 213-227.

Scambelluri, M., Bottazzi, P., Trommsdorff, V., Vannucci, R., Hermann, J., Gómez-Pugnaire, M.T. and Vizcaíno, V.L.S., 2001b. Incompatible element-rich fluids released by antigorite breakdown in deeply subducted mantle. *Earth and Planetary Science Letters*, 192(3), pp.457-470.

Scambelluri, M., Strating, E.H., Piccardo, G.B., Vissers, R.L.M. and Rampone, E., 1991, Alpine olivine- and titanian clinohumite-bearing assemblages in the Erro-Tobbio peridotite (Voltri Massif, NW Italy). *Journal of Metamorphic Geology*, v. 9, p. 79-91.

Scambelluri, M., Fiebig, J., Malaspina, N., Müntener, O. and Pettke, T., 2004. Serpentinite subduction: implications for fluid processes and trace-element recycling. *International Geology Review*, 46(7), pp.595-613.

Scambelluri, M. and Tonarini, S., 2012. Boron isotope evidence for shallow fluid transfer across subduction zones by serpentinitized mantle. *Geology*, 40(10), pp.907-910.

Scambelluri, M., Pettke, T. and Cannà, E., 2015. Fluid-related inclusions in Alpine high-pressure peridotite reveal trace element recycling during subduction-zone dehydration of serpentinitized mantle (Cima di Gagnone, Swiss Alps). *Earth and planetary science letters*, 429, pp.45-59.

Shen, T., Hermann, J., Zhang, L., Lü, Z., Padrón-Navarta, J.A., Xia, B. and Bader, T., 2015. UHP metamorphism documented in Ti-chondrodite-and Ti-clinohumite-bearing serpentinitized ultramafic rocks from Chinese southwestern Tianshan. *Journal of petrology*, 56(7), pp.1425-1458.

Schwartz, S., Allemand, P. and Guillot, S., 2001. Numerical model of the effect of serpentinites on the exhumation of eclogitic rocks: insights from the Monviso ophiolitic massif (Western Alps). *Tectonophysics*, 342(1), pp.193-206.

Schwartz, S., Guillot, S., Reynard, B., Lafay, R., Debret, B., Nicollet, C., Lanari, P. and Auzende, A.L., 2013, Pressure–temperature estimates of the lizardite/antigorite transition in high pressure serpentinites. *Lithos*, v. 178, p. 197-210.

Schwartz, S., Lardeaux, J., Guillot, S. and Tricart, P., 2000, The diversity of eclogitic metamorphism in the Monviso ophiolitic complex, western Alps, Italy. *Geodinamica Acta*, v. 13, p. 169-188.

Silverstone, J. and Sharp, Z.D., 2013. Chlorine isotope constraints on fluid- rock interactions during subduction and exhumation of the Zermatt- Saas ophiolite, *Geochemistry, Geophysics, Geosystems*, v. 14, p. 4370-4391.

Skora, S., Mahlen, N.J., Johnson, C.M., Baumgartner, L.P., Lapen, T.J., Beard, B.L. and Szilvagy, E.T., 2015, Evidence for protracted prograde metamorphism followed by rapid exhumation of the Zermatt- Saas Fee ophiolite. *Journal of Metamorphic Geology*, v. 33, p. 711-734

Spandler, C., Pettke, T. and Rubatto, D., 2011. Internal and external fluid sources for eclogite-facies veins in the Monviso meta-ophiolite, Western Alps: implications for fluid flow in subduction zones. *Journal of Petrology*, 52(6), pp.1207-1236.

Tenthorey, E. and Hermann, J., 2004. Composition of fluids during serpentinite breakdown in subduction zones: evidence for limited boron mobility. *Geology*, 32(10), pp.865-868.

Tenthorey, E., Cox, S.F. and Todd, H.F., 2003. Evolution of strength recovery and permeability during fluid–rock reaction in experimental fault zones. *Earth and Planetary Science Letters*, 206(1), pp.161-172.

Trommsdorff, V., Sánchez-Vizcaíno, V.L., Gomez-Pugnaire, M.T. and Müntener, O., 1998, High pressure breakdown of antigorite to spinifex-textured olivine and orthopyroxene, SE Spain. *Contributions to Mineralogy and Petrology*, v. 132, p.139-148.

Ulmer, P. and Trommsdorff, V., 1995, Serpentine stability to mantle depths and subduction-related magmatism. *Science*, v. 268, p. 858.

Ulmer, P. and Trommsdorff, V., 1999. Phase relations of hydrous mantle subducting to 300 km. *Mantle petrology: field observations and high pressure experimentation: a tribute to Francis R.(Joe) Boyd*, 6, pp.259-281.

Zack, T. and John, T., 2007. An evaluation of reactive fluid flow and trace element mobility in subducting slabs. *Chemical Geology*, 239(3), pp.199-216.

Chapter 4.

Iron isotope behaviour accompanying the dehydration of serpentinite during subduction: A mineral scale approach

This chapter is currently in preparation for publication in the journal Earth and Planetary Science Letters.

The following will be included as co-authors on the submitted manuscript:

Edward C. Inglis^{1}, Baptiste Debret², Pierre Bouilhol³, Marc-Alban Millet⁴, Helen M. Williams⁵ and Kevin W. Burton¹*

¹Department of Earth Sciences, Durham University, South Road, Durham, United Kingdom, DH1 3LE

²Laboratoire G-TIME, Université libre de Bruxelles, CP 160/02, Ave. F. Roosevelt 50, B-1050, Brussels, Belgium

³CRPG, Université de Lorraine, UMR7358, Vandoeuvre-Lès-Nancy, F-54501, France

⁴School of Earth and Ocean Science, Cardiff University, Cardiff, United Kingdom, CF10 3AT

⁵Department of Earth Sciences, University of Cambridge, Downing Street, Cambridge, United Kingdom, CB2 3EQ

Abstract

The process of serpentinite dehydration within subduction zones plays a significant role in the transfer of fluids between the subducting oceanic lithosphere and overlying sub-arc mantle. More recently it has been suggested that the process of deserpentinisation can contribute significantly to the redox budget of subduction zones. To further understand the redox potential of subducting serpentinites we have studied a suite of slab serpentinites from the Zermatt-Saas ophiolite. These serpentinites have undergone high-pressure, subduction related metamorphism and display clear evidence for partial dehydration. We have analysed whole-rock antigorite + olivine bearing serpentinites for major and trace element concentrations as well as Fe isotopes. In addition we have selected a set of olivine and Ti-clinohumite bearing metamorphic veins, hosted within the serpentinites. We have subsequently sampled from different vein forming mineral domains using a micro-milling technique. Our results show the mobility of light Fe

isotopes within vein forming minerals, suggesting that serpentinite derived fluids in subduction zones are isotopically light with respect to Fe isotopes. Furthermore we show a striking negative co-variation between the S content of whole-rock antigorite + olivine bearing serpentinites and their Fe isotope compositions, suggesting that Fe isotopes within these rocks is controlled by S mobility. This finding supports previous studies that suggests serpentinite derived fluids within subduction zones are effective carrier of dissolved S species. Such fluids could potentially serve as strong oxidants and are thus capable on contributing significantly to the redox budget of subduction zones.

4.1. Introduction

Devolatilisation of hydrous oceanic lithosphere during subduction zone metamorphism serves as one of the primary mechanisms for chemical mass transfer between Earth's exterior and interior (*Schmidt and Poli, 2014*). Serpentinised slab mantle is thought to play a key role in this global geochemical cycle (e.g. *Scambelluri et al., 2004, Deschamps et al., 2013*). Serpentinisation of the oceanic mantle occurs via a sequence of hydration reactions between ambient mantle peridotite and seawater on the ocean floor, and results in the sequestration of ~13wt% H₂O in within hydrous serpentine group phases (*Ulmer and Tromsdorff, 1995*). Subduction of these serpentinites at convergent plate margins sees progressive dehydration of such lithologies owing to a sequence of metamorphic reactions with increasing pressure and temperature (*P-T*). This metamorphic dehydration sequence culminates in the destabilisation of antigorite under eclogite facies conditions, and is thought to represent one of the most significant fluid fluxes between the slab and sub arc mantle (e.g. *Magni et al., 2014*).

Recently slab serpentinites have received considerable attention from geochemists seeking to elucidate their role in the element cycling that occurs at subduction zones (e.g. *Deschamps et al., 2011; 2013, Hattori and Guillot, 2007, John et al., 2011*) with much emphasis being placed on the potential for such lithologies to contribute significantly to the redox cycle of arcs (*Debret et al., 2015; 2016, Pons et al., 2016, Debret and Sverjensky, 2017*). As a result of this work it has been suggested that the process of deserpentinisation accompanying subduction zone metamorphism can generate highly oxidizing, S-bearing fluids, which in turn can serve as a powerful oxidant of the sub arc mantle, as 1 mol of S⁶⁺ is capable of oxidizing 8 mols of reduced Fe²⁺ to Fe³⁺.

In addition to these geochemical studies, meticulous field and petrological work, and fluid mechanical studies have highlighted the ways in which deep, serpentinite derived fluids are generated and migrate (*Dobson et al., 2002, Tenthorey and Cox, 2003, Plümper*

et al., 2017), with much of our current understanding suggesting that this largely occurs by high permeability channelized fluid flow within the form of metamorphic veins formed during serpentinite dehydration.

This study builds on our understanding of the geochemistry of fluid flow in serpentinites and, in particular, recent work on the Zermatt-Saas serpentinites suggesting that these lithologies have undergone partial dehydration during eclogite facies, subduction zone metamorphism (*Inglis et al.*, *in prep*). We have obtained whole rock major, trace and Fe isotope measurements of olivine + antigorite bearing serpentinites, as well as micro sampling of a series of HP olivine and Ti-clinohumite bearing metamorphic veins and their associated host rocks. The aim of the study is to document grain scale elemental and isotopic variations to trace fluid loss from serpentinite accompanying dehydration during subduction zone metamorphism.

4.2. Geological setting and sample description

4.2.1 The Zermatt-Saas Ophiolite

The Zermatt-Saas region is located in the Western European Alps, occupying a geographic area between Saas-Fee in Switzerland and Valtournenche in Italy (**Figure 4.1**). It is predominantly comprised of metamorphosed ultramafic, mafic and sedimentary units, which once formed a section of Mid-Jurassic Piemonte-Ligurian oceanic lithosphere (*Barnicoat and Fry, 1986, Rubatto et al., 1998*). The ophiolitic rocks of the Zermatt-Saas region all record evidence for high- (H) to ultrahigh- (UH) pressure, subduction-related, eclogite facies metamorphism (*Bearth, 1953; 1959, Barnicoat and Fry, 1986, Rubatto et al., 1998, Bucher et al., 2005, Rebay et al., 2017*), with a metamorphic peak suggested to have occurred by ~65 Ma (*Rebay et al., 2017*). Eocene exhumation of the massif took place as a result of the orogenic Alpine continental collision. Numerous *P-T* estimates for the rocks of the Zermatt-Saas have been derived - all of which suggest a H/UHP peak event, consistent with eclogite facies metamorphism along a subduction zone gradient (see *Rebay et al., 2017* for comprehensive summary). In its current structural configuration Zermatt-Saas currently lies sandwiched between the basal Penninic Monte Rosa and the overlying Austroalpine Dent Blanche nappes (*Pleuger et al., 2007*).

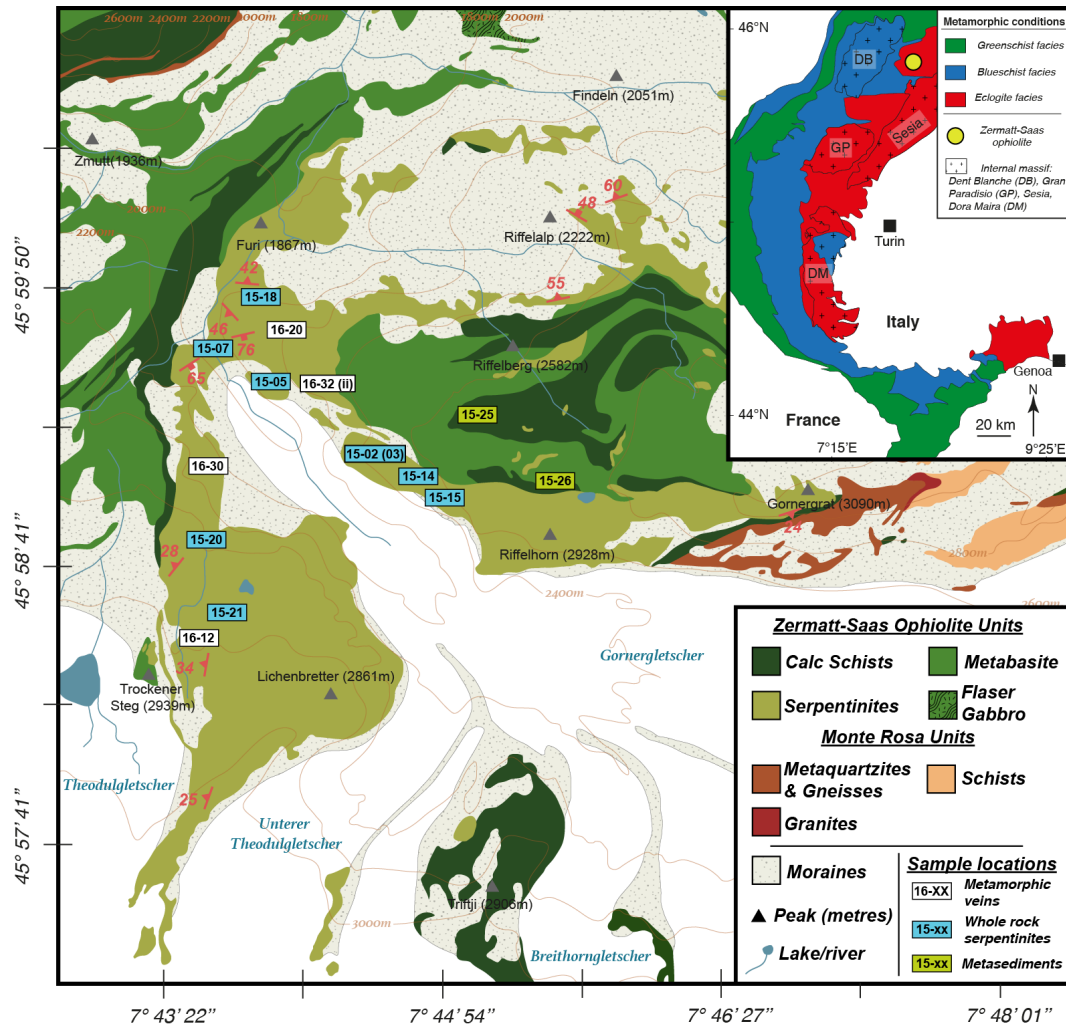


Figure 4.1. The inset map (top right) shows the location of the Zermatt-Saas ophiolite in the context of the European Alps. The main body map is a simplified geological map of the area studied as part of this work. Sample locations are given as white (metamorphic veins), blue (whole-rock antigorite + olivine serpentinites) and green (metasediment) coloured rectangles. The number inside the rectangle corresponds to the sample ID referred to in text. Where two samples have been collected from the same locality the additional ID suffix is given in brackets. Main body map is modified after Bearth, 1953.

4.2.2 Serpentinised ultramafics from the Gornergrat area

This study focuses on a suite of samples collected from the ultramafic sequence of the ophiolite, which outcrops in the Gornergrat valley area, to the south of the town of Zermatt (**Figure 4.1**). This area of the massif preserves a section of well-exposed, variably deformed antigorite dominated serpentinites and grossular-rich meta-rodingities, which sit conformably below the metabasites of the Gornergrat peak. Previous work on the serpentinites from this area had suggested that, despite being metamorphosed under conditions greater than 600 °C and 2.5 GPa,

they had not undergone dehydration and had in fact retained their prograde-related, hydrous, antigorite-rich mineralogy (*Li et al., 2004*). A recent reappraisal of the Gornergrat serpentinites has demonstrated that, contrary to these earlier interpretations; the lithologies from this area show evidence for destabilisation of hydrous phases and partial dehydration accompanying high *P-T* metamorphism (*Inglis et al., in prep*).

As part of this study we have selected samples of antigorite + olivine bearing serpentinites, and a complementary suite of Ti-clinohumite and olivine rich metamorphic veins, which are taken to be representative serpentinites undergoing dehydration and the vein forming minerals crystallising from associated dehydration fluids.

4.2.2.1 Whole rock antigorite + olivine serpentinites

Whole-rock samples containing antigorite and olivine have been selected from the most structurally competent portions of the massif, from outcrops of either massive or foliated serpentinite. These samples typically comprise over 90 % antigorite by modal abundance with minor amounts of magnetite and olivine. The antigorite usually forms as fresh interlocking grains no more than 0.1 mm across. Magnetite either occurs as small ~0.3 mm euhedral, disseminated grains within the groundmass, or within the more foliated samples is seen as ~1 mm long stringers, running parallel to the dominant foliation of the rock. Within all of these samples olivine growth is associated with the antigorite domain. Olivine either occurs as a >0.1 mm disseminated grains within the groundmass antigorite, or occupying small, ~1 mm long pinching veinlets hosted within the antigorite domain. It is not uncommon for both disseminated and veined olivine to be seen within the same sample. In some samples olivine is replaced by laths of antigorite and magnetite.

4.2.2.2 Ti-clinohumite and olivine veins

Samples from Ti-clinohumite- and olivine-rich macroscopic metamorphic veins hosted within antigorite serpentinites have been collected from the massif. To better understand the relationship between the vein and host rock, “in-situ” sample blocks were removed from the outcrop using a portable diamond-tipped rock saw. Once extracted, these blocks were prepared for microanalysis using the methods described in

section 4.3.2. A detailed description of the petrology of these veins is given in Chapter 3 but summarised here.

Ti-clinohumite is a common vein-forming mineral within the Zermatt-Saas serpentinites. As part of this study we have selected one sample for microanalysis (16-20a) that contains anastomosing veinlets of Ti-clinohumite. Within this sample Ti-clinohumite crystals form as 1-2 mm wide anastomosing veins hosted within an antigorite dominated wall rock (**Figure 4.2a**). Individual elongate, reddish-brown Ti-clinohumite grains range between 0.1-0.5 mm in length. Most Ti-clinohumite crystals are subhedral in form and display poorly preserved grain boundaries, which in parts are seen breaking down to coronas of brown and clear olivine and associated grains of magnetite. Rare, fresh Ti-clinohumite grains are observed; these show no evidence of coronitic olivine growth and are filled with needles of antigorite. The host wall rock comprises medium-grained, interlocking crystals of antigorite with subordinate magnetite (**Figure 4.2c**). From this sample we micro-milled one site (16-20a-Ti-Chm) from the centre of a ~0.5 mm wide veined Ti-clinohumite crystal.

Olivine-rich veins are a common feature within the least deformed serpentinites. Typically these occur as pinching, discontinuous features hosted within antigorite-dominated serpentinites (**Figure 4.2b**). We selected four olivine-rich veins for micro-sampling as part of this study. Samples 16-32 and 16-32ii both preserve ~3 cm wide olivine-rich veins. These veins are filled with mm-scale, fresh granoblastic olivine crystals and large, ~1-2 mm, magnetite grains (**Figure 4.2d**). These veins are hosted within wall rock serpentinites that are predominantly made up of fine-grained aggregates of antigorite and subordinate magnetite. For sample wafer 16-32 a total of six sites were sub sampled by micro-milling: 16-32-GM-1, -GM-2 and -GM-3 that represent a progressive transect towards the vein margin (distal to proximal) of the host antigorite serpentinite; 16-32-Ol-1 and -Ol-2, which are sub samples of granoblastic vein forming olivine, and; 16-32-Mag, which is a sub sample of magnetite from within the olivine-rich vein (See Supplementary information Figure 4.1). From sample wafer 16-32ii a total of 3 sites were sub sampled by micro-milling. 16-32ii-GM-2 represents a sub sample from the vein hosting serpentinite, which in this

case comprised of antigorite, magnetite and groundmass olivine. Sub samples 16-32ii-Ol-1 and 16-32ii-Mag are of vein forming granoblastic olivine and associated magnetite, respectively. Sample 16-30 preserves a vein formed of relict Ti-clinohumite surrounded by cm-scale corona of pseudomorphic olivine occurring after Ti-clinohumite. Three sub samples were extracted from 16-30, these being 16-30-TiChm, 16-30-Ol and 16-30-GM-1. Sub sample 16-30-TiChm is of relict Ti-clinohumite from the core of the vein, while 16-30-Ol is taken from the coronitic olivine surrounding the relict Ti-clinohumite. 16-30-GM-1 a groundmass sub sample from the host rock antigorite serpentinite.

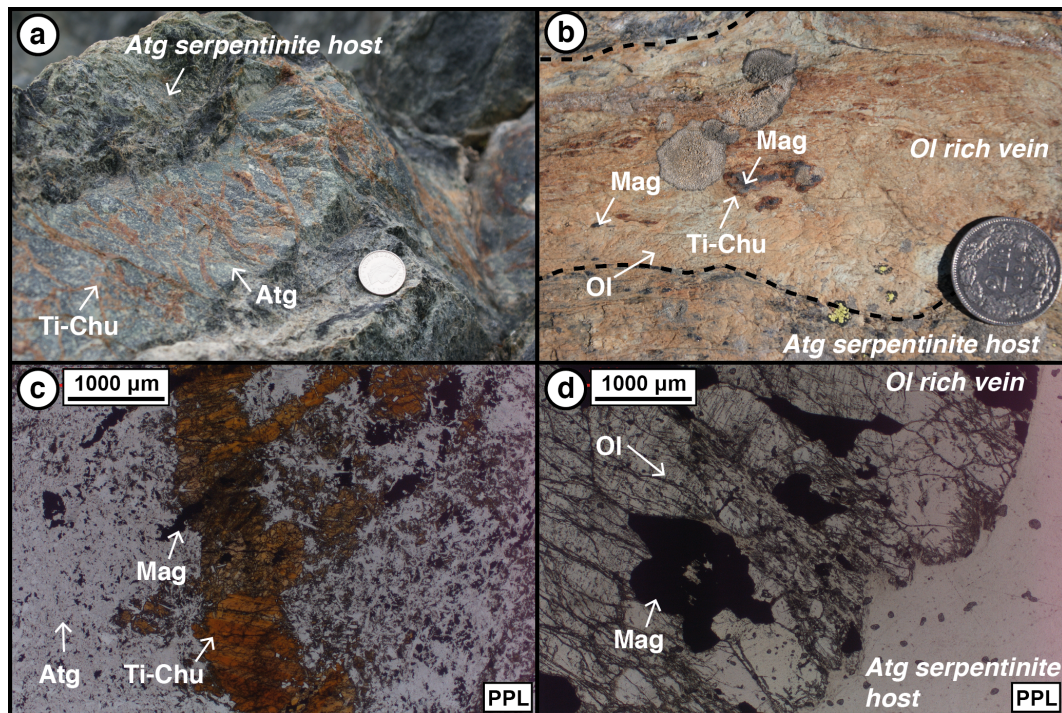


Figure 4.2. Photographs showing macro and micro-scale images that are representative of the types of metamorphic veins studied here. (a) Shows an anastomosing Ti-Chu vein network hosted within variably foliated antigorite serpentinite. (b) Is a photograph showing an olivine dominated metamorphic vein that supports minor magnetite and Ti-chu aggregates. This olivine rich vein is hosted within an antigorite serpentinite. (c) Show a photomicrograph of the same Ti-chu vein from (a). Ti-chu is well preserved and contains inclusions of magnetite. The host rock is dominated by antigorite but also contains high proportions of magnetite. (d) A photomicrograph of a fresh olivine vein hosted with an antigorite serpentinite. Within this sample relative high amounts of magnetite are preserved in association with olivine.

4.2.2.3 Metasediments

Two metasediments, 15-01 and 15-02, were collected from the Riffelberg area of the massif. Both of these samples represent heavily deformed schistose units and are proximal to the upper structural contact of the Gornergrat ultramafic sequence. Sample 15-01 is of a chlorite mica-schist, which comprises fine-grained chlorite with coarse muscovite and subordinate amounts of graphite and opaques. Sample 15-02 is an actinolite schist and is formed almost entirely from fine grained actinolite, with minor muscovite and opaque phases. Previous work examining the nature of the relationship between these sediments and the oceanic basement units in this area has suggested that they are part of a sequence of marine sedimentary cover, coeval, and having undergone the same metamorphic evolution, as the mafic and ultramafic oceanic units that they overlay (*Bearth and Schwander, 1981*).

4.3. Methods

4.3.1 Major and trace element and Fe isotope analysis of whole-rock serpentinites

Whole-rock powders for each sample were produced from slices cut from individual hand specimens. Weathered surfaces were removed from the samples first by cutting on a diamond tipped saw and then by grinding these slices on diamond lap wheel. Prior to powdering these sample slices were cleaned in an ultrasonic bath containing MilliPore Milli-Q® (MQ) ultrapure (>18.2 MΩ) H₂O, before being broken down to <1 cm² chips in a fly press. Fine powdering of these chips was achieved by using a TEMA® agate disk mill at the University of Leeds.

4.3.1.1 Major element concentrations

The powdered whole-rock samples were analysed for major element concentrations (SiO₂, TiO₂, Al₂O₃, Fe₂O₃, MnO, MgO, CaO, Na₂O, K₂O, P₂O₅, CrO₃, NiO) by wavelength dispersive X-Ray Florescence (XRF) analysis using a PANalytical Axios Advanced XRF spectrometer at the University of Leicester, UK as per the method detailed by *Knott et al., 2016*. An external geo-reference material (USGS BHVO-1) was analysed alongside the samples as a check on precision and accuracy. The measured major element concentrations for this geo-reference material is in excellent agreement with the long-term average value obtained at Leicester (<5%) and also with values published elsewhere (*Govindaraju,*

1994; <5%). As part of the same procedure the total loss on ignition (LOI) was also determined and is reported alongside the major element concentrations in Supplementary information 4.2.

4.3.1.2 Trace element concentrations

For the same samples powders the trace element concentrations were measured at the National Oceanography Centre, Southampton by Inductively Coupled Plasma-Mass Spectrometry (ICP-MS). Sample powders were completely digested in Savillex Teflon® vials using concentrated HF and HNO₃ acids before being evaporated to dryness and redissolved in 0.5M HNO₃ spiked with 5 ppb In and Re and 20 ppb Be for use as internal standards. The spiked sample solutions were analysed on a Thermo Scientific® XSERIES-2 quadrupole ICP-MS, which was calibrated at the beginning of the analytical session against 5 international rock standards, with JA-2 and BHVO-2 run as unknowns. Analysis of these unknowns compare well to the published values, with the external reproducibility being <5% for Sc, Ti, V, Ni, Cu, As, Rb, Sr, Y, Cd, Sb, Ba, La, Ce, Nd, Sm, Eu, Gd, Tb, Ho, Tm, Lu, Li, Co, Pr, Dy, Er and Yb and between 5-10% for all other elements reported. The trace element concentrations for these samples are presented alongside the major elements in Supplementary information 4.2.

4.3.1.3 Fe isotope compositions

The Fe isotope composition of the whole-rock samples was carried out at Durham University. The method employed for these analyses is summarized by *Williams et al., 2009* but briefly described here. Between 10 - 20 mg of rock powder was digested in 7 mL Savillex Teflon® square body beakers with wrench-top closures, by the addition of concentrated HF and HNO₃. After initial digestion samples were evaporated to dryness and brought back into solution in 6M HCl. Quantitative purification of Fe from matrix elements was achieved by the chromatographic exchange protocol of *Williams et al., 2009*, which uses BioRad AG1-X4 anion exchange resin on BioRad BioSpin columns in a HCl medium. For these measurements the total procedural blank contribution was <8 ng of Fe. Isotope abundances of pure Fe sample solutions were measured by multiple-collector (MC) ICP-MS (Thermo Scientific® Neptune Plus) using the method of *Weyer and Schwieters,*

2003. Measurements were made with the instrument running in medium-resolution mode using a wet plasma sample introduction system. The mass resolution (mass/ Δ mass at 95% and 5% of the beam intensity of the ^{56}Fe peak edge) typically ranged between 8000-9000, which allowed adequate resolution between the true ^{56}Fe peak and the $^{40}\text{Ar}^{16}\text{O}$ polyatomic interference. The instrumental mass bias was adequately corrected for using a sample-standard bracketing (SSB) approach, whereby individual sample measurements were bracketed by an identical measurement of the IRMM-014 ^{56}Fe reference standard. Final delta values were calculated offline and reported as the permil deviation of the of the sample ratio from the IRMM-014 standard, as shown in **Equation 1**.

$$\text{Equation 1: } \delta^{56}\text{Fe}_{\text{Sample}} = 1000 \times \left[\left(\frac{R^{56/54}\text{Fe}_{\text{Sample}}}{R^{56/54}\text{Fe}_{\text{IRMM-014}}} \right) - 1 \right]$$

Where $R^{56/54}\text{Fe}$ is the measured ratio of $^{56}\text{Fe} / ^{54}\text{Fe}$. When $\delta^{57}\text{Fe}$ is quoted the $R^{56/54}\text{Fe}$ becomes $R^{57/54}\text{Fe}$. All errors reported here, and throughout are two standard deviations (2sd) of the mean of n unless otherwise stated. Both the $\delta^{56}\text{Fe}$ and the $\delta^{57}\text{Fe}$ values are given to demonstrate the mass dependent nature of these measurements.

To check the precision and accuracy both in-house and external reference materials of a known isotopic composition were measured. The in-house FeCl_2 standard was measured a total of 29 times across the 3 analytical sessions from which these data was generated. These repeat measurements gave a $\delta^{56}\text{Fe}$ of $-0.69 \pm 0.06 \text{ ‰}$ and a $\delta^{57}\text{Fe}$ of $-1.04 \pm 0.09 \text{ ‰}$, which is in excellent agreement with other studies (*Mikutta et al., 2009, Inglis et al., 2017a*). Alongside this in-house standard an external geo-reference material, USGS BIR-1, was digested, processed through chemistry and analysed alongside our samples. This yielded a $\delta^{56}\text{Fe}$ of $+0.05 \pm 0.04 \text{ ‰}$ and a $\delta^{57}\text{Fe}$ of $+0.07 \pm 0.05 \text{ ‰}$, and is in excellent agreement with previously published values of BIR-1 (*Millet et al., 2012, Hibbert et al., 2012, Sossi et al., 2015*). The Fe isotope composition of the whole-rock samples is presented alongside the corresponding major and trace element data in Supplementary information 4.3.

4.3.2 Micro-analysis of serpentinite mineral domains

4.3.2.1 Micro-sampling of mineral domains

Both groundmass and vein-forming mineral phases were selected for micro sampling based on prior petrographical investigation of the samples used here (*Inglis et al., in prep*). Individual, ~1 cm thick, wafers of rock were prepared by slicing hand specimens on a diamond tipped saw before flat surfaces were ground and polished on a wet flat lapping wheel. From these blocks a standard 30 μm thick petrographic thin section was made, while the remaining mirror side of the wafer was cleaned in an ultrasonic bath containing MQ H_2O . This technique allowed for clear identification of the target mineral domain from analyzing the thin section on a petrographic microscope before micro-milling of the target domain from the corresponding mirror side “thick section” mounted on the drill stage.

Individual mineral domains were sampled from the polished and cleaned thick section using a New Wave Instruments™ Micro-Mill™ following the technique of *Charlier et al., 2006*. Typically the tungsten carbide mill tip was rastered over the target area ensuring that the Z-axis depth penetration into the sample did not exceed 40 μm . The addition of ~10 μl of MQ H_2O to the area being milled served to lubricate the mill tip and prevented the fine sample powder from being dispersed across the sample stage. Once the target domain has been milled, the resulting powder and MQ H_2O slurry was extracted from the top of the section using a pipette and transferred into individual pre-weighed gold boats. This sample slurry was then dried down in the gold boat under a heat lamp before being weighed on a microbalance to determine the mass of sample extracted from each mineral domain. The gold boats containing the dried sample powders were transferred to clean Savillex Teflon beakers and the sample digested by adding a 1:1 mix of concentrated HF and HNO_3 . With the sample in solution the gold boats were extracted from the beakers.

To ensure that sampling in this way did not introduce an unacceptably high blank contribution to the sample analyte the “full procedural blank” involved milling a high purity quartz microscope slide under the same parameters as used for the samples, with the resulting powder collected,

weighed on a gold boat and brought into solution in the same manner as the sample powders.

4.3.2.2 Mineral trace element concentrations

The mineral samples were analysed for trace element concentrations by ICP-MS at the National Oceanography Centre, Southampton using a similar method to that detailed in 4.3.1.2. Samples were spiked with a mixed In, Re and Be solution to correct for instrumental drift. The instrument was calibrated at the beginning of the analytical session against 5 international geo-reference materials, with JA2 run as an unknown and BAS206 and BRR1 were used as internal standards. Comparison of the JA2 geo-reference material with published inter-laboratory compilation data (*Jochum et al., 2016*) shows <5% deviation for Sc, Ti, V, Ni, Cu, As, Rb, Sr, Y, Cd, Sb, Ba, La, Ce, Nd, Sm, Eu, Gd, Tb, Ho, Tm, Lu, Li, Co, Pr, Dy, Er and Yb and between 5-10% deviation for all other elements reported here. The total procedural blank is below the calculated detection limit for all elements. The trace element concentrations for these samples are presented in Supplementary information 4.4.

4.3.2.3 Mineral Fe isotope compositions

Iron isotope compositions of the minerals were analysed at Durham University in March 2017. The method used for these measurements differed slightly to that used for the whole-rock measurements described in 4.3.1.3. The quantitative purification of Fe from the matrix elements was achieved using a protocol adapted from *Dauphas et al., 2004*. In this method 1.2 ml of BioRad AG1-X8 (200-400 mesh) anion exchange resin was packed onto 11.5 ml total capacity polypropylene columns, which was cleaned with passes of 10 ml MQ H₂O and 10 ml 6 M HCl repeated 4 times each. The resin was preconditioned with 2 ml of 6 M HCl and the sample loaded onto the column in 250 µl of 6 M HCl. The matrix was eluted from the retained Fe species by adding 8 ml of 6 M HCl and discarded. Iron was quantitatively recovered from the column by adding 9 ml 0.4 M HCl, and subsequently collected into clean 15 ml Savillex Teflon beakers. The pure Fe solution was evaporated to dryness and brought back into solution in 2 mls of 0.5 M HNO₃ prior to mass spectrometry. Prior calibration of this chromatographic ion exchange

protocol demonstrated that the recovered Fe fraction was devoid of any isobaric elements (namely Cr and Ni) and totaled >99% of the Fe loaded into the column.

Iron isotope abundances were measured on a Thermo Scientific Neptune Plus MC-ICP-MS at Durham following the procedure of *Weyer and Schwieters, 2003*. The instrument was run in medium-resolution mode which gave a typical mass resolving power of ~6500, adequate to discriminate between the $^{40}\text{Ar}^{14}\text{N}^+$, $^{40}\text{Ar}^{16}\text{O}^+$ and $^{40}\text{Ar}^{16}\text{OH}^+$ polyatomic species that are isobaric on the ^{54}Fe , ^{56}Fe and ^{57}Fe masses respectively. Samples were introduced to the plasma interface using an Elemental Scientific SIS quartz spray chamber coupled with a PFA 50 $\mu\text{l}/\text{min}$ nebulizer. All of the Fe masses were collected, as were ^{53}Cr and ^{60}Ni to correct, using the natural abundances, for any isobaric interference from these elements on the ^{54}Fe and ^{58}Fe masses. In all cases this correction had no effect on the calculated ratio as all Cr and Ni was removed from the sample solution prior to analysis by column chemistry. Instrumental mass bias was corrected using SSB, where IRMM-014 was used as the bracketing standard. Precision and accuracy was assessed by measuring both an in-house secondary reference solution (Durham FeWire) and an external geo-reference material (USGS BIR 1). This study presents the first Fe isotope data for the Durham FeWire in-house reference solution, with a mean $\delta^{56}\text{Fe}$ of $+0.26 \pm 0.06$ ‰ and a $\delta^{57}\text{Fe}$ of $+0.39 \pm 0.09$ ‰ where $n = 179$. Two aliquots of the BIR-1 geo-reference material were processed through two different batches of chemistry and analysed a total of 4 times each. This gave an average $\delta^{56}\text{Fe}$ of $+0.06 \pm 0.04$ ‰ and a $\delta^{57}\text{Fe}$ of $+0.08 \pm 0.06$ ‰, which is in excellent agreement with published values for this standard (*Millet et al., 2012, Hibbert et al., 2012, Sossi et al., 2015*). The Fe isotope data for the minerals analysed as part of this study are reported in Supplementary information 4.5.

4.4. Results

4.4.1 Whole-Rock Major and Trace Element Data

The whole-rock major and trace element data for all of the samples analysed in this study are given in the supplementary information.

Analysis of the antigorite + olivine bearing serpentinites demonstrates an average bulk composition with high Mg# (>80) and Cr# (>60), poor in Ca (<0.15 wt%

CaO), and hydrous (>10.6 wt% LOI). The total variation in Fe₂O₃ within these samples ranges between 5.48 to 20.33 wt%, with an average of 9.64 wt%. When renormalized to anhydrous and stoichiometrically recalculated to an olivine-orthopyroxene-clinopyroxene-spinel componentry, it is apparent that these samples represent the metamorphic product of a harzburgitic protolith. This is in agreement with previous studies of the serpentinites from this area, which suggested formation from an oceanic harzburgite (*Li et al., 2004*).

The metasediment samples display broadly consistent major element values. Sample 15-01 shows notably elevated SiO₂ (50.08 wt%), CaO (9.25 wt%) and Na₂O (0.16 wt%) relative to 15-02, while 15-02 is strongly enriched in C (548.7 ppm) relative to the former. Both samples display major element compositions that are in reasonable agreement with the mean major element composition of globally subducted sediments (*Plank and Langmuir, 1998*).

The whole-rock minor and trace element data for the antigorite + olivine serpentinites is presented as a primitive mantle normalized multi-element spidergram in **Figure 4.3**. The arrangement of elements along the X-axis is taken from *Scambelluri et al., 2014*. All of our samples display generally consistent profiles, which are in good agreement with literature data for the same types of sample (*Debret et al., 2016*). The trace element profiles for these samples range from positive to flat ($Ce_N/Y_N = 0.2-1.1$) with LREE depleted profiles ($La_N/Lu_N = 0.1-0.8$). Striking positive anomalies in fluid mobile B ($B/B^* = 252-7858$), As ($As_N/Pb_N = 19.4-122$) and Sb ($Sb_N/Pr_N = 30.1-4860$) are noted, whilst negative Sr anomalies are apparent for all but one sample. Indeed it should be noted that the total Sr concentration of these samples ranges between 0.13-3.87 ppm, but with an average of 0.6 ppm – significantly lower than the typical range observed in oceanic serpentinites (*Kodolányi et al., 2012*). The behavior of Li is contrasting between the samples - with six showing positive Li anomalies ($Li_N/Y_N = 1.4-3$), whilst the remaining four display negative anomalies ($Li_N/Y_N = 0.1-0.7$). For all samples Zn is enriched relative to Cu ($Zn_N/Cu_N = 1.1-5.3$). The trace element profiles for the metasediment samples analysed here are presented alongside the serpentinites on **Figure 4.3**. The two samples display broadly similar profiles to each other, with 15-01 being more enriched in trace elements (Sm-Zn) than 15-02. Their profiles are characterized by positive trace element ($Ce_N/Y_N = 0.07-0.36$) and REE ($La_N/Lu_N = 0.04-0.17$) patterns. Positive anomalies in B ($B/B^* = 430-519$), As ($As_N/Pb_N = 5.1-67.2$) and Sb ($Sb_N/Pr_N = 80.6-258.4$) are noted,

similar to those seen for the serpentinite samples. Uranium is also enriched ($U_N/Th_N = 2.8-28.2$), whilst Zr ($Zr_N/Nd_N = 0.02-0.17$) and Hf ($Hf_N/Sm_N = 0.04-0.35$) are depleted. Sample 15-26 is strongly enriched in Cu ($Cu_N/Zn_N = 5.8$) relative to the other sediment sample. It is noteworthy that both of the metasediment samples display trace element profiles that are consistent with those observed for the serpentine samples.

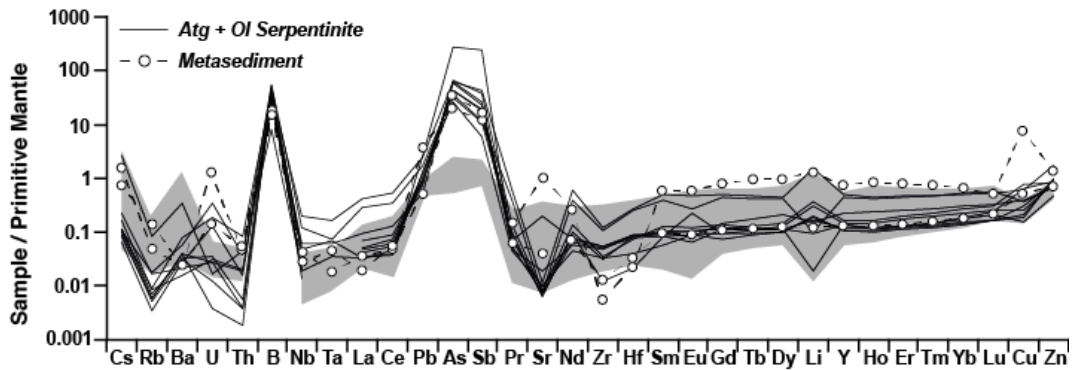


Figure 4.3. Whole-rock minor and trace element profiles for antigorite + olivine serpentinite (black solid lines) and metasediments (dashed lines with closed circles). The grey field represents the range measured for similar antigorite + olivine serpentinites by Debret *et al.*, 2016. Any breaks in the sample profiles represent elements that were not analysed or concentrations that fell below the limit of detection. A full-page version of this figure is included within the supplementary information 4.6.

4.4.2 Mineral Trace Element Data

Trace element data for vein forming and host serpentinite mineral phases are provided in the supplementary information. **Figure 4.4** shows primitive mantle normalized, multi-element spidergrams for each of the types of vein-forming and host rock minerals analysed as part of this study.

Figure 4.4a shows the trace element profiles for the eight micro-milled wall-rock groundmass antigorite samples. Generally all of the samples display profiles that are consistent with one another, albeit with some variation in elemental concentrations. The trace element profiles vary between positive to slightly negative for different samples but on average appear flat (mean $Ce_N/Y_N = 0.9$). Positive anomalies in B ($B_N/Nb_N = 297-2389$), Pb ($Pb_N/Ce_N = 5-425.3$), As, Sb ($Sb_N/Pr_N = 435.4-1320.8$) and Li ($Li_N/Y_N = 2-4.7$) are noted, as, with the

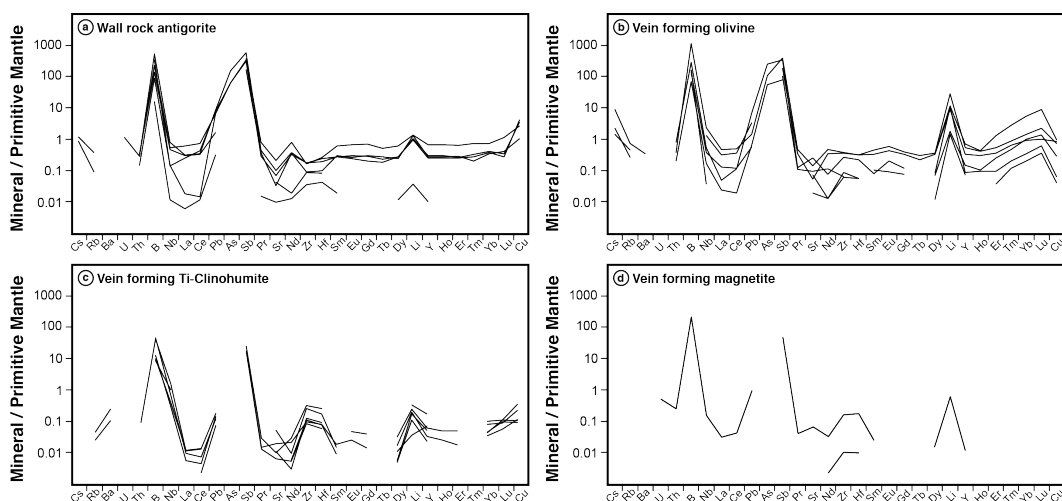


Figure 4.4. Multi-element spidergrams for a selected range of minor and trace element for groundmass or vein-forming minerals analysed as part of this study. All data is normalized to the primitive mantle values for given elements taken from *McDonough and Sun, 1995*. Breaks in the sample profiles indicate elements which were not measured or fell below the limit of detection. A full-page version of this figure is included within the supplementary information 4.7.

exception of two samples, is Nd. An enrichment in Cu is also apparent. The elemental profiles for samples of vein-forming olivine are shown in **Figure 4.4b**. It is apparent that all of the samples display broadly similar profiles, which are dominated by strong positive anomalies in fluid mobile B ($B_N/Nb_N = 360-4429$), As ($As_N/Pb_N = 37-89$), Sb ($Sb_N/Pr_N = 519-2770$) and Li ($Li_N/Y_N = 12.1-123.4$) a significant HREE enrichment ($La_N/Lu_N = 0.3-0.005$) and a depletion in Cu ($Cu_N/Lu_N = 0.1-0.85$). **Figure 4.4c** shows the minor and trace element profiles for vein-forming Ti-Clinohumite. As with vein-forming olivine, all of the samples display profiles consistent with one another. Strong positive enrichments in fluid mobile B ($B_N/Nb_N = 8.4-68.8$), Sb ($Sb_N/Pr_N = 877.4-1339.3$) and, for all but one sample, Li ($Li_N/Y_N = 1.9-5.7$) are noted as well as high-field strength Zr ($Zr_N/Nd_N = 4.5-41.5$) and Hf ($Hf_N/Sm_N = 4.3-11.4$). Three of the samples show enrichment in Cu. Only limited data is reported for minor and trace element concentrations for vein-forming Magnetite, as most elements fall below the limit of detection. As with all other samples, B ($B_N/Nb_N = 1431.5$) and Sb ($Sb_N/Pr_N = 1200.7$) are enriched in one sample measured. Lithium ($Li_N/Y_N = 52.7$), Zr ($Zr_N/Nd_N = 4.9$) and Hf ($Hf_N/Sm_N = 7.2$) are also enriched in this sample, whilst La ($La_N/Ce_N = 0.7$) appears depleted.

4.4.3 Whole Rock and Mineral Fe Isotope Data

The Fe isotope compositions of the whole rock and mineral samples analysed here are presented in the supplementary material. We present the total range in $\delta^{56}\text{Fe}$ values for all of the samples measured on the **Figure 4.5**.

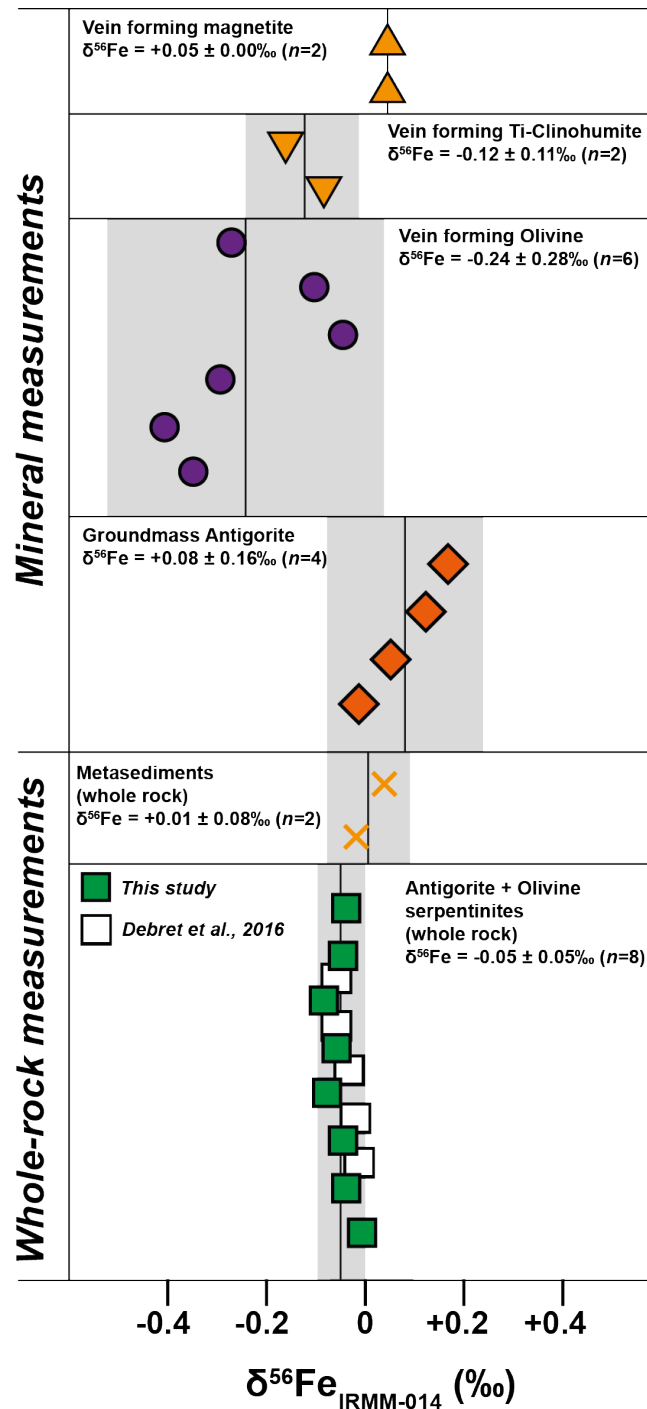


Figure 4.5. Whole rock and mineral Fe isotope measurements for all of the samples analysed as part of this study. Sample symbols occupy an area greater than the error for each measurement. It should be noted that the groundmass antigorite samples (orange diamonds) are the same as the antigorite groundmass samples shown as green circles on Figure 4.6 and the process controlling the variation of these samples is discussed below.

A total of eight whole-rock antigorite + olivine serpentinites were analysed and display a range in $\delta^{56}\text{Fe}$ of between $0.00 \pm 0.04 \text{ ‰}$ and $-0.08 \pm 0.04 \text{ ‰}$, yielding an average $\delta^{56}\text{Fe}$ of $-0.05 \pm 0.05 \text{ ‰}$ (2sd; $n= 8$) for this sample grouping. Our results are in excellent agreement with serpentinite samples analysed by Debret et al. (2016), which yield a mean $\delta^{56}\text{Fe}$ of $-0.03 \pm 0.06 \text{ ‰}$ (2sd; $n= 5$). In addition to these serpentinite samples we also present whole-rock data for the chlorite-mica (15-01) and actinolite schist (15-02) samples. These metasediments yield near indistinguishable $\delta^{56}\text{Fe}$ values of $-0.02 \pm 0.04 \text{ ‰}$ and $+0.04 \pm 0.04 \text{ ‰}$ respectively, giving an average value of $+0.01 \pm 0.08 \text{ ‰}$ (2sd; $n= 2$). This value is in good agreement with data for modern day marine carbonate-rich sediments (Fantle and DePaolo, 2004).

A total of four groundmass antigorite samples were micro-milled from two different wall-rock regions of serpentinite samples that host metamorphic veins (16-30 and 16-32), and subsequently analysed for their Fe isotope composition. These four samples show a range of $\delta^{56}\text{Fe}$ values between $-0.01 \pm 0.04 \text{ ‰}$ to $+0.17 \pm 0.03 \text{ ‰}$ and give an average $\delta^{56}\text{Fe}$ of $+0.08 \pm 0.16 \text{ ‰}$ (2sd; $n= 4$), which is offset towards a heavier average value than seen for the whole-rock antigorite + olivine serpentinite samples. The Fe isotope composition of six different vein-forming olivine grains were analysed from four different veined serpentinite samples (16-12, 16-30, 16-32 and 16-32ii). These olivines give a range in $\delta^{56}\text{Fe}$ of between $-0.05 \pm 0.05 \text{ ‰}$ to $-0.40 \pm 0.03 \text{ ‰}$, and yield an average $-0.24 \pm 0.28 \text{ ‰}$ (2sd; $n= 6$), markedly lighter than that of the groundmass antigorite. Two sub-samples of vein-forming Ti-Clinohumite were taken from two different samples (16-20 and 16-30), these show consistent $\delta^{56}\text{Fe}$ values of $-0.08 \pm 0.02 \text{ ‰}$ to $-0.16 \pm 0.01 \text{ ‰}$, and an average value of $-0.12 \pm 0.11 \text{ ‰}$ (2sd; $n= 6$), indistinguishable from the range exhibited by the vein-forming olivine, and lighter than that of the groundmass antigorite. The two vein-forming magnetite grains analysed here (taken from samples 16-32 and 16-32ii) yielded near identical $\delta^{56}\text{Fe}$ values of $+0.04 \pm 0.04 \text{ ‰}$ and $+0.05 \pm 0.05 \text{ ‰}$, giving an average of $0.05 \pm 0.00 \text{ ‰}$, which is offset to a slightly heavier average than vein-forming olivine and Ti-Clinohumite, but in agreement with the average $\delta^{56}\text{Fe}$ of the groundmass antigorite.

Within sample 16-32, a progressive transect was milled across the groundmass antigorite host from distal to proximal of an olivine bearing vein (described in

section 4.3.2.1). Within these three sub samples of the groundmass antigorite a resolvable variation is apparent with increasing proximity to the vein wall, with the $\delta^{56}\text{Fe}$ varying between -0.01 ± 0.04 ‰ 1.6cm from the vein wall, to $+0.12 \pm 0.01$ ‰ 0.1 cm from the vein wall. The two samples of vein forming olivine from this sample yield an average $\delta^{56}\text{Fe}$ of -0.07 ± 0.08 ‰. The results from this transect are shown in **Figure 4.6**.

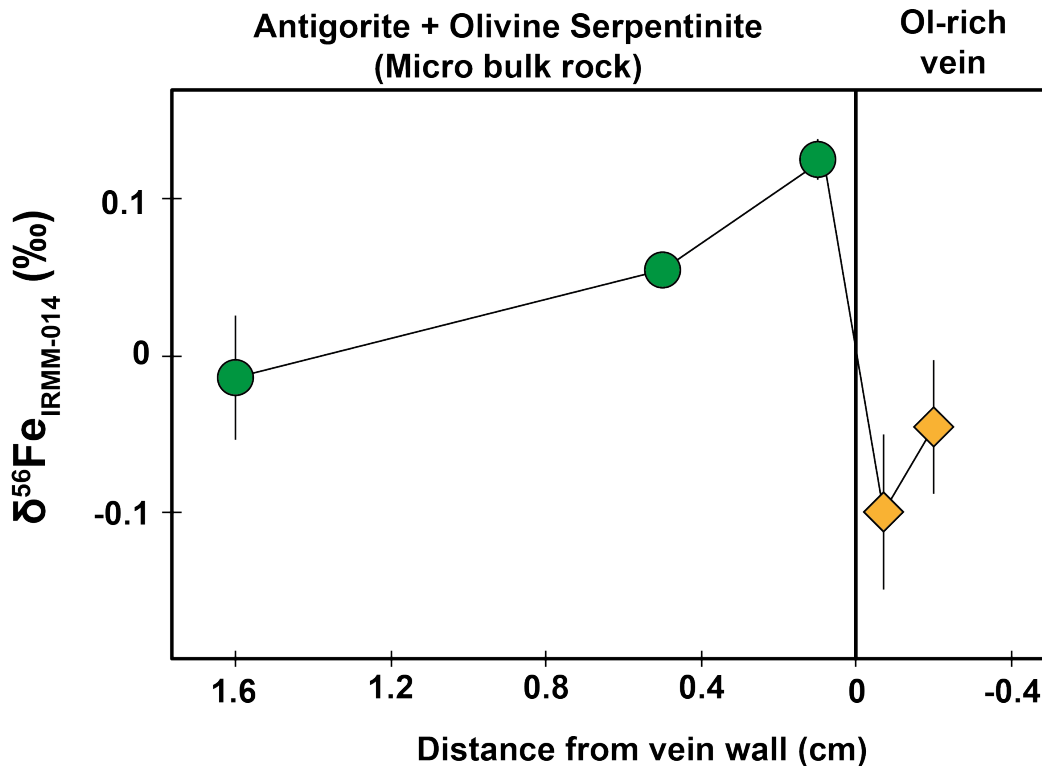


Figure 4.6. A plot showing the change in Fe isotope composition of the host antigorite serpentinite with proximity to vein wall. Green circles represent measurements of the antigorite and olivine host rock, while yellow diamonds are measurements of vein forming olivine. Error bars represents the 2sd error of each measurement, when not present this indicates that errors fall within the symbol.

4.5. Discussion

The goal of this study is to examine, at the mineral scale, the effect of serpentinite dehydration on the behavior of Fe isotopes. In line with this aim we have characterized a suite of serpentinites that have undergone H/UHP, subduction zone metamorphism and record evidence for the destabilisation of hydrous phases, which has resulted in the mobilization of free fluids at depth, preserved in a series of olivine and Ti-clinohumite-rich metamorphic veins. Additionally we present elemental data for whole rock serpentinites and metasediments, alongside key mineral phases.

4.5.1 Trace Element Behavior During High-Pressure Metamorphism of the Zermatt-Saas Serpentinities

The elemental data for antigorite + olivine bearing serpentinites obtained here is in excellent agreement with that for similar serpentinites from different Alpine ophiolites (e.g. *Debret et al., 2016*) and shown in **Figure 4.3**.

Of significant interest is the behavior of fluid mobile B, As and Sb within the serpentinites. The large B anomaly of the antigorite + olivine serpentinites relative to the primitive mantle, represents an average B concentration of 11.35 $\mu\text{g/g}$ for this sample set. This concentration is significantly higher than estimates for the primitive mantle, e.g. 0.3 $\mu\text{g/g}$ (*McDonough and Sun, 1995*), but lower than that for oceanic serpentinites, e.g. $\sim 60 \mu\text{g/g}$ (*Kodolányi et al., 2012*). Taking this into account, we suggest that the concentrations of B observed within the Zermatt antigorite + olivine serpentinites represents $\sim 80\%$ loss of B between initial seafloor fixation and mobilization during partial dehydration of these lithologies accompanying HP metamorphism. This is in line with measurements of vein forming olivine, which shows strong enrichments in B relative to primitive mantle (**Figure 4.4b**). This corresponds to a range in concentrations of between 20.5-331.7 $\mu\text{g/g}$, significantly higher than measurements of B in mantle derived olivine (e.g. *Debret et al., 2013*). Wall-rock antigorite, proximal to olivine bearing metamorphic veins, shows a depletion in B relative to the vein-forming olivine that they host. Indeed our data show that on average the $[\text{B}]_{\text{wall-rock antigorite}}/[\text{B}]_{\text{vein-forming olivine}} = 0.5$, suggesting that B is strongly partitioned into metamorphic olivine, and removed from the residual antigorite.

Like B, the whole-rock antigorite + olivine serpentinites are strongly enriched in fluid mobile As and Sb relative to the primitive mantle and similar antigorite + olivine bearing serpentinites as studied by *Debret et al., 2016*. Comparison with compilations of abyssal serpentinites (*Deschamps et al., 2013*) show that while our samples fall within a similar range of Sb concentrations, they are strongly enriched in As relative to their oceanic counterparts. When compared to the metasediments analysed as part of this study we show that they display similar concentrations for both As and Sb, suggesting that mixing between a sediment derived component and the serpentinites may have occurred. Consequently we present a simple two-component mixing model between primitive mantle and representative seafloor sediment end members in **Figure 4.7**, derived as per

Equation 2:

$$\text{Equation 2: } C_m^x = C_{\text{sediment}}^x \times f + C_{PM}^x(1 - f)$$

Where C_m^x is the proportion of x (either As or Sb) within the mixture; C_{sediment}^x is the concentration of x (either As or Sb) in the sediment end member; C_{PM}^x is the concentration of x (either As or Sb) in the primitive mantle end member, and; f is the proportion, as a percentage, of the given end member in the mixture. The As and Sb concentrations for the primitive mantle were taken from *McDonough and Sun, 1995*, while the ODP Leg 123 abyssal sediment average was calculated from data taken from *Plank and Ludden, 1992*.

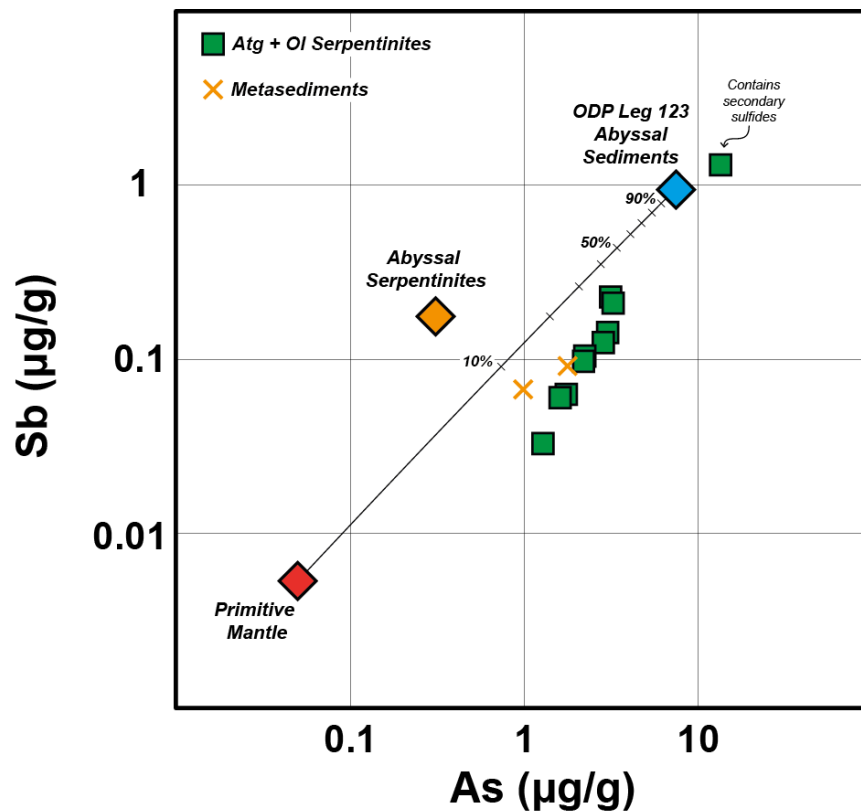


Figure 4.7. A mixing plot showing the sediment contribution to serpentinites for As and Sb. Mixing between the two end members (ODP abyssal sediments and primitive mantle) is denoted by the black line with each tick mark representing mixing at 10% increments. Primitive mantle values are taken from *McDonough and Sun, 1995*. The abyssal serpentinite average value is taken from the compilation of *Deschamps et al., 2011*, where $n = 27$. The value presented for ODP Leg 123 abyssal sediments represents the average Sb and As concentrations of 101 samples of various marine sediments taken from

Plank and Ludden, 1992. Our data are shown as green closed squares (antigorite + olivine serpentinites) and orange crosses (metasediments).

Modeling this exchange shows that our analysed antigorite + olivine samples plot away from the calculated mixing line between the two end members, ultimately suggesting that sediment interaction during subduction zone metamorphism does not solely control the As and Sb concentrations observed within these samples. One antigorite + olivine serpentinite shows whole rock As and Sb concentrations substantially greater than the other antigorite + olivine serpentinites from Zermatt, the metasediment samples and the average value for the ODP Leg 123 abyssal sediments. The high As and Sb concentrations within this sample are attributed to the presence of secondary sulfide minerals, which form as small stringers within the groundmass antigorite. It should be noted that this is the only serpentinite sample analysed as part of this study to contain sulfides as part of their mineralogy, that are visible with a petrographic microscope.

Despite the apparent enrichment within these samples our measurements of vein-forming olivine suggest that they too are enriched in As and Sb relative to primitive mantle. When considering this with respect to partitioning of elements between antigorite and secondary olivine we show that $[As]_{\text{wall-rock antigorite}}/[As]_{\text{vein-forming olivine}} = 0.6$, suggesting that As is indeed lost from the residual antigorite and incorporated into vein forming olivine. When considering the same effect for Sb we show that $[Sb]_{\text{wall-rock antigorite}}/[Sb]_{\text{vein-forming olivine}} = 1.2$, consequently showing that Sb is weakly retained within wall-rock antigorite, relative to vein forming olivine. When considering the behavior of fluid mobile Li, we show that contrasting behavior is observed within the whole rock antigorite + olivine samples, with some samples enriched in Li relative to primitive mantle, whilst some are depleted. Analysis of vein forming olivine demonstrates high concentrations (2.29-44.59 $\mu\text{g/g}$) relative to the host antigorite (0.06-2.04 $\mu\text{g/g}$) and the whole rock antigorite + olivine serpentinite (0.16-2.38 $\mu\text{g/g}$). The $[Li]_{\text{wall-rock antigorite}}/[Li]_{\text{vein-forming olivine}} = 0.07$, thus allowing us to conclude that Li is stripped from the serpentinites and strongly partitioned into the vein-forming olivine.

4.5.2 Iron Isotope Systematics During Serpentine Dehydration

4.5.2.1 Whole-rock Fe isotope behavior

The whole-rock antigorite + olivine samples analysed here preserve a

narrow range of $\delta^{56}\text{Fe}$ values of between -0.08 ± 0.04 ‰ to 0.00 ± 0.04 ‰, which is indistinguishable from measured $\delta^{56}\text{Fe}$ values for similar samples from different alpine ophiolites *Debret et al., 2016*. In their study *Debret et al., 2016* demonstrated a progressive shift towards heavier $\delta^{56}\text{Fe}$ values with increasing prograde metamorphism of Alpine serpentinites, suggesting that isotopically light Fe is lost from the serpentinites during progressive dehydration across a subduction zone gradient. Furthermore they suggested that these similar olivine + antigorite serpentinites represented serpentinites that were undergoing dehydration and consequently recorded the light “fluid signature” (e.g. fluids trapped during their escape from the rock) with respect to Fe isotopes, rather than a fully dehydrated residue, which would be expected to record a heavy Fe isotope composition. It is apparent that our data support these earlier suggestions.

Iron isotope fractionation can occur due to variations in redox, with the heavier isotope mirroring Fe^{3+} when a system is in equilibrium (*Polyakov and Mineev, 2000*). Alongside this, the coordination chemistry and bonding environments are also known to control stable isotope behaviour (*Schauble, 2004*). Indeed the effect of S-bearing species on Fe isotopes is well known, with stable isotope theory predicting preferential complexing of light Fe isotopes within S-bearing fluids in the form of Fe-S complexes (*Hill et al., 2010*). Our data show a strong co-variation between S content of the antigorite and olivine bearing serpentinites and their $\delta^{56}\text{Fe}$ isotope composition, demonstrating that those samples with the lowest S contents preserve the heaviest Fe isotope compositions (**Figure 4.8**). This finding is in excellent agreement with predictions from previous workers who demonstrated a progressive shift in the stable isotope composition of whole-rock subducted serpentines, and argued that loss of $\text{SO}_x\text{-Fe}$ complexes could be controlling the Fe isotope systematics of subduction zone serpentinites (*Debret et al., 2016*). It is further reinforced by findings from recent Zn isotope measurements on Alpine serpentinites, that also demonstrated that Zn isotope were fractionated in response to S loss (*Pons et al., 2016*).

Sulfur storage in mantle peridotite is generally thought to be controlled by the presence of sulfide (*Alt and Shanks, 2003*), where the oxidative

process of serpentinisation converts such sulfides to sulfates prior to subduction. Additionally recent work has demonstrated that serpentinite minerals serve as a powerful sink for oxidized sulfur (S^{6+}) and could account for 60-100% of the abyssal serpentinite S budget (Debret *et al.*, 2017). Given that S appears homogeneously distributed between different serpentinite phases, and that, with the exception of one sample, the whole-rocks contain no sulfide or sulfate phases, we suggest that the dominant carrier of S within our whole-rock samples is antigorite. As our samples are representative of partial antigorite breakdown we argue that S mobilization results from antigorite breakdown. Given that S is poorly compatible within olivine, which here is the metamorphic product of antigorite breakdown, it is likely that S released during this reaction is strongly partitioned into the resulting fluid phase. As S bearing fluids are known to complex isotopically light Fe in the form of Fe^{2+} -SO- $X_{(aqueous)}$ complexes, this serves as a viable mechanism for the whole rock Fe isotope fractionation observed.

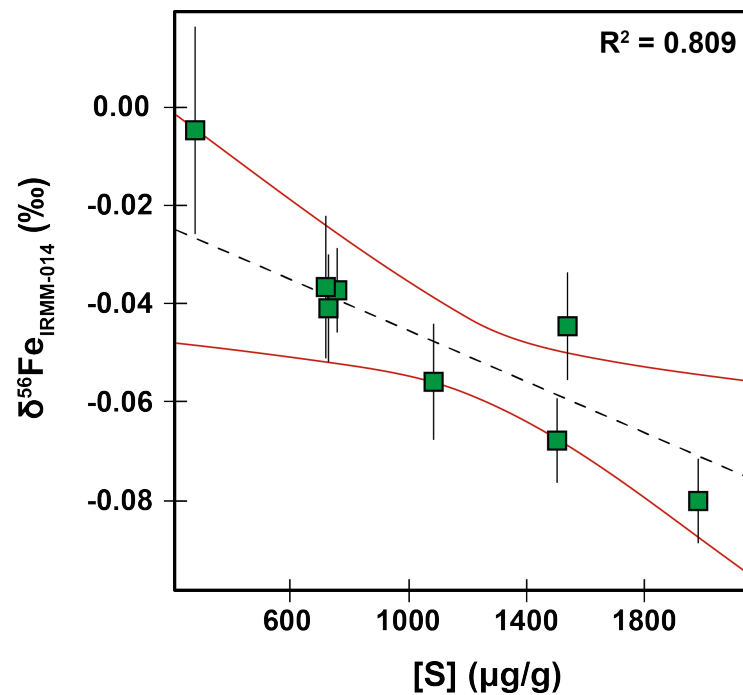


Figure 4.8. A plot showing the co-variation between S content and Fe isotope composition of whole rock olivine and antigorite bearing serpentinites. The dashed black line represents a linear regression of the dataset, which displays an R^2 value of 0.809. The curved red lines represent an error envelope at the 95% confidence level. Individual errors associated with data point represent the 2sd of the mean of n .

4.5.2.2 Mineral-scale control on Fe isotope behavior

To assess the effect of metamorphic dehydration of serpentinite on Fe isotopes we have specifically targeted samples of antigorite serpentinite, which host metamorphic veins. Using microdrilling techniques we have sampled different at the grain scale different vein forming phases (olivine, Ti-chu and magnetite) alongside a spatial sequence of samples from the adjacent antigorite dominated host serpentinite to assess the local effect of the veins.

Firstly, the groundmass antigorite shows a range of $\delta^{56}\text{Fe}$ values, of the four antigorite samples analysed a resolvable and significant isotope variation is apparent. As we do not present Fe concentration data for these samples we are unable to conclude to what degree this covariation accompanies Fe mobility. Despite this we are able to comment on possible mechanism for this variation. The sample closest to the vein displays the heaviest value ($\delta^{56}\text{Fe} = 0.17 \pm 0.03 \text{ ‰}$) (**Figure 4.6**) which is inline with other measurements of antigorite-dominated serpentinites (*Debret et al., 2016*). This Fe isotope composition most likely reflects the effect of progressive removal of light Fe during subduction by previous fluid loss. Such an interpretation is consistent with the data for sample 16-32, which represents a progressive transect across the antigorite serpentinite host towards an olivine bearing metamorphic vein (as described in section 4.2.2.2). The three groundmass antigorite samples display a resolvable and systematic shift to heavier values towards the host-vein interface (see **Figure 4.6**), whereas the two samples of vein forming olivine possess notably light $\delta^{56}\text{Fe}$ isotope compositions. One possible interpretation of the observed isotope variations between vein and antigorite host is that this results from dehydration and recrystallisation of the antigorite domain to form metamorphic olivine. In this scenario, the partial recrystallisation of the host antigorite to olivine - serves to generate fluid that is, in turn, supplied to the vein. If this fluid is a carrier of dissolved S species then it could act to complex isotopically light Fe, preferentially taking this Fe from the residual wall rock, and enriching the vein forming minerals in isotopically light Fe. In this scenario it is assumed that the wall rock closest to the vein has undergone a higher degree of fluid loss than the more distal samples. Indeed this interpretation is reinforced by petrographic observations that sub sample 16-32GM3 contains the most disseminated groundmass olivine.

Alternatively, the Fe isotope variations may result from disequilibrium or kinetic effects. In this scenario diffusion of light Fe between the wall rock and vein serves to drive the wall rock closest to the vein towards a heavier Fe isotope composition, due to greater diffusive loss of light Fe proximal to the vein. Indeed diffusive behavior of Fe isotopes has been documented in single-crystal studies (*Teng et al., 2011, Sio et al., 2013, Collinet et al., 2017*), but Fe isotope diffusion across lithological interfaces remains undocumented at the time of writing. As such we suggest that our data could provide the first evidence for Fe isotope diffusion between wall rock and vein lithologies, but cannot conclusively comment on this without either invoking another stable isotope system, whereby we would expect the two systems to co-vary, or correlating the Fe isotope variation with trace element diffusion models. It should be noted however that no co-variation between the Fe isotope values of these samples and trace elements known to exhibit diffusive behavior (i.e. Li) is observed.

Irrespective of the mechanism responsible for the Fe isotope variations in the host serpentinite vein forming olivine and Ti-Chu preserve light $\delta^{56}\text{Fe}$ values – clearly offset from both the antigorite wall-rock and antigorite + olivine samples. This observation confirms that isotopically light Fe is indeed mobilized as a result of serpentinite dehydration. For the moment S concentration data is unavailable for the vein forming phases, but the high concentrations of chalcophile elements within these minerals supports the suggestion that such fluids are indeed S bearing.

4.5.3 Implications for the Nature of Fluids Released During Deserpentinisation

Detailed micro-sampling has revealed the mobility of isotopically light Fe at the grain scale within partially dehydrated antigorite serpentinite. This data confirms suggestions from earlier studies based on whole-rock measurements of similar samples that isotopically light Fe is mobilized in the fluid phases during such metamorphic reactions (*Debret et al., 2016*). Given that serpentinites are thought to contribute significantly to the fluid budget of subduction zones we argue that the process of deserpentinisation could serve as a key mechanism for supplying light Fe to the sub-arc mantle. Indeed it is well documented that arc lavas display a light Fe isotope composition relative to MORBs (*Nebel et al., 2015, Sossi et al., 2016*) and it has been suggested that mass transfer of isotopically light Fe

between the subducting slab and sub arc mantle source could be responsible for this isotopic variation. Here we are able to confirm that the process of serpentinite dehydration may well contribute to the Fe isotope systematics of arc lavas, and serve as a potential candidate for the source of isotopically light Fe within the arc system.

The relationship between Fe isotopes and redox mediating components can also be remarked upon. An ongoing debate within earth sciences is the redox nature of the sub-arc mantle, and the tracing of oxidized components during subduction zone mass transfer. The simplest interpretation of the results presented here is that the Fe isotope variations reflect the mobilization and loss of S bearing fluids during deserpentinisation. The source of S is most likely antigorite and this is released during partial breakdown of this phase. In accord with previous studies (*Debret et al., 2016, Pons et al., 2016, Debret and Sverjensky, 2017*) we conclude that SO_x release during antigorite breakdown occurs, and the transfer of these oxidized species can serve as a powerful oxidant within the sub-arc mantle.

4.6. Conclusions

Using combined whole-rock and micro scale measurements this study has demonstrated the mobility of key elements in a series of metamorphic veins within a section serpentinite that has experienced dehydration during subduction zone metamorphism.

The Fe isotope data presented for whole rock antigorite + olivine serpentinites shows a strong correlation with S content of these samples, suggesting that those samples which have undergone S loss also display the heaviest Fe isotope compositions. Again this finding confirms previous suggestions that serpentinite dehydration fluids are carriers of dissolved S. We interpret this process to serve as the primary mechanism for Fe isotope fractionation within these rocks.

Metamorphic vein forming olivine and Ti-clinohumite, which form due to fluid release during partial dehydration of serpentinite, show enrichments in B, Sb and Li suggesting that, for these samples at least, we are able to trace the mobility of these elements within subduction zones down to the vein scale. These results, therefore, provide strong support to the hypothesis that serpentinite dehydration within subduction zones acts as an effective mechanism for the transfer of these mobile elements between the subducting slab and sub-arc mantle.

These data also demonstrate that isotopically light Fe is incorporated within both vein forming olivine and Ti-clinohumite, relative to host antigorite serpentinite. This result confirms previous suggestions that isotopically light Fe is mobilized in serpentinite-derived fluid in subduction zones. This result is significant, as it reveals a possible source of isotopically light Fe within subduction zones – a potential “smoking gun” to explain the Fe isotope compositions of arc lavas. Additionally it confirms that the progressive shift in whole rock serpentinite samples across a subduction zone *P-T* gradient as reported by *Debret et al., 2016* may well result from the mobilization of light Fe in dehydration fluids.

References Cited

- Alt, J.C. and Shanks, W.C., 2003. Serpentinization of abyssal peridotites from the MARK area, Mid-Atlantic Ridge: sulfur geochemistry and reaction modeling. *Geochimica et cosmochimica Acta*, 67(4), pp.641-653.
- Barnicoat, A.C. and Fry, N., 1986. High-pressure metamorphism of the Zermatt-Saas ophiolite zone, Switzerland. *Journal of the Geological Society*, 143(4), pp.607-618.
- Bearth, P. and Schwander, H., 1981. The post-Triassic sediments of the ophiolite zone Zermatt-Saas Fee and the associated manganese mineralizations. *Ecol. Geol. Helve.*, 74, 198–205.
- Bearth, P., 1953. *Geologischer Atlas der Schweiz*. Schweizerische Geologische Komm.
- Bearth, P., 1959. Über Eklogite, Glaukophanschiefer und metamorphe Pillowlaven. *Schweizerische Mineralogische und Petrographische Mitteilungen*, 39, pp.267-286.
- Bucher, K., Fazis, Y., Capitani, C.D. and Grapes, R., 2005. Blueschists, eclogites, and decompression assemblages of the Zermatt-Saas ophiolite: High-pressure metamorphism of subducted Tethys lithosphere. *American mineralogist*, 90(5-6), pp.821-835.
- Charlier, B.L.A., Ginibre, C., Morgan, D., Nowell, G.M., Pearson, D.G., Davidson, J.P. and Ottley, C.J., 2006. Methods for the microsampling and high-precision analysis of strontium and rubidium isotopes at single crystal scale for petrological and geochronological applications. *Chemical Geology*, 232(3), pp.114-133.
- Collinet, M., Charlier, B., Namur, O., Oeser, M., Médard, E. and Weyer, S., 2017. Crystallization history of enriched shergottites from Fe and Mg isotope fractionation in olivine megacrysts. *Geochimica et Cosmochimica Acta*, 207, pp.277-297.
- Craddock, P.R. and Dauphas, N., 2011. Iron isotopic compositions of geological reference materials and chondrites. *Geostandards and Geoanalytical Research*, 35(1), pp.101-123.
- Dauphas, N., Van Zuilen, M., Wadhwa, M., Davis, A.M., Marty, B. and Janney, P.E., 2004. Clues from Fe isotope variations on the origin of early Archean BIFs from Greenland. *Science*, 306(5704), pp.2077-2080.

Debret, B. and Sverjensky, D.A., 2017. Highly oxidising fluids generated during serpentinite breakdown in subduction zones. *Scientific Reports*, 7.

Debret, B., Andreani, M., Delacour, A., Rouméjon, S., Trcera, N. and Williams, H., 2017. Assessing sulfur redox state and distribution in abyssal serpentinites using XANES spectroscopy. *Earth and Planetary Science Letters*, 466, pp.1-11.

Debret, B., Andreani, M., Godard, M., Nicollet, C., Schwartz, S. and Lafay, R., 2013. Trace element behavior during serpentinization/de-serpentinization of an eclogitized oceanic lithosphere: A LA-ICPMS study of the Lanzo ultramafic massif (Western Alps). *Chemical Geology*, 357, pp.117-133.

Debret, B., Bolfan-Casanova, N., Padrón-Navarta, J.A., Martin-Hernandez, F., Andreani, M., Garrido, C.J., Sánchez-Vizcaíno, V.L., Gómez-Pugnaire, M.T., Muñoz, M. and Trcera, N., 2015. Redox state of iron during high-pressure serpentinite dehydration. *Contributions to Mineralogy and Petrology*, 169(4), p.36.

Debret, B., Millet, M.A., Pons, M.L., Bouilhol, P., Inglis, E. and Williams, H., 2016. Isotopic evidence for iron mobility during subduction. *Geology*, 44(3), pp.215-218.

Deschamps, F., Godard, M., Guillot, S. and Hattori, K., 2013. Geochemistry of subduction zone serpentinites: A review. *Lithos*, 178, pp.96-127.

Deschamps, F., Guillot, S., Godard, M., Andreani, M. and Hattori, K., 2011. Serpentinites act as sponges for fluid-mobile elements in abyssal and subduction zone environments. *Terra Nova*, 23(3), pp.171-178.

Dobson, D.P., Meredith, P.G. and Boon, S.A., 2002. Simulation of subduction zone seismicity by dehydration of serpentine. *Science*, 298(5597), pp.1407-1410.

Fantle, M.S. and DePaolo, D.J., 2004. Iron isotopic fractionation during continental weathering. *Earth and Planetary Science Letters*, 228(3), pp.547-562.

Govindaraju, K., 1994. 1994 compilation of working values and sample description for 383 geostandards. *Geostandards and Geoanalytical Research*, 18(S1), pp.1-158.

Hattori, K.H. and Guillot, S., 2007. Geochemical character of serpentinites associated with high- to ultrahigh-pressure metamorphic rocks in the Alps, Cuba, and the Himalayas: Recycling of elements in subduction zones. *Geochemistry, Geophysics, Geosystems*, 8(9).

Hibbert, K.E.J., Williams, H.M., Kerr, A.C. and Puchtel, I.S., 2012. Iron isotopes in ancient and modern komatiites: evidence in support of an oxidised mantle from Archean to present. *Earth and Planetary Science Letters*, 321, pp.198-207.

Hill, P.S., Schauble, E.A. and Young, E.D., 2010. Effects of changing solution chemistry on Fe 3+/Fe 2+ isotope fractionation in aqueous Fe–Cl solutions. *Geochimica et Cosmochimica Acta*, 74(23), pp.6669-6689.

Inglis et al., in prep. Chapter 3 – this thesis

Inglis, E.C., Debret, B., Burton, K.W., Millet, M.A., Pons, M.L., Dale, C.W., Bouilhol, P., Cooper, M., Nowell, G.M., McCoy-West, A. and Williams, H.M., 2017. The behaviour of iron and zinc stable isotopes accompanying the subduction of mafic oceanic crust: A case study from Western Alpine Ophiolites. *Geochemistry, Geophysics, Geosystems*.

John, T., Scambelluri, M., Frische, M., Barnes, J.D. and Bach, W., 2011. Dehydration of subducting serpentinite: implications for halogen mobility in subduction zones and the deep halogen cycle. *Earth and Planetary Science Letters*, 308(1), pp.65-76.

Kodolányi, J., Pettke, T., Spandler, C., Kamber, B.S. and Gméling, K., 2011. Geochemistry of ocean floor and fore-arc serpentinites: constraints on the ultramafic input to subduction zones. *Journal of Petrology*, 53(2), pp.235-270.

Li, X.P., Rahn, M. and Bucher, K., 2004. Serpentinites of the Zermatt-Saas ophiolite complex and their texture evolution. *Journal of Metamorphic Geology*, 22(3), pp.159-177.

Magni, V., Bouilhol, P. and van Hunen, J., 2014. Deep water recycling through time. *Geochemistry, Geophysics, Geosystems*, 15(11), pp.4203-4216.

McDonough, W.F. and Sun, S.S., 1995. The composition of the Earth. *Chemical geology*, 120(3-4), pp.223-253.

Mikutta, C., Wiederhold, J.G., Cirpka, O.A., Hofstetter, T.B., Bourdon, B. and Von Gunten, U., 2009. Iron isotope fractionation and atom exchange during sorption of ferrous iron to mineral surfaces. *Geochimica et Cosmochimica Acta*, 73(7), pp.1795-1812.

Millet, M.A., Baker, J.A. and Payne, C.E., 2012. Ultra-precise stable Fe isotope measurements by high resolution multiple-collector inductively coupled plasma mass spectrometry with a ^{57}Fe - ^{58}Fe double spike. *Chemical Geology*, 304, pp.18-25.

Nebel, O., Sossi, P.A., Benard, A., Wille, M., Vroon, P.Z. and Arculus, R.J., 2015. Redox-variability and controls in subduction zones from an iron-isotope perspective. *Earth and Planetary Science Letters*, 432, pp.142-151.

Plank, T. and Langmuir, C.H., 1998. The chemical composition of subducting sediment and its consequences for the crust and mantle. *Chemical geology*, 145(3), pp.325-394.

Plank, T. and Ludden, J.N., 1992. Geochemistry of sediments in the Argo abyssal plain at Site 765; a continental margin reference section for sediment recycling in subduction zones. In *Proc. Ocean Drill. Program Sci. Results* (Vol. 123, pp. 167-189).

Pleuger, J., Roller, S., Walter, J.M., Jansen, E. and Froitzheim, N., 2007. Structural evolution of the contact between two Penninic nappes (Zermatt-Saas zone and Combin zone, Western Alps) and implications for the exhumation mechanism and palaeogeography. *International Journal of Earth Sciences*, 96(2), pp.229-252.

Plümper, O., John, T., Podladchikov, Y.Y., Vrijmoed, J.C. and Scambelluri, M., 2017. Fluid escape from subduction zones controlled by channel-forming reactive porosity. *Nature Geoscience*, 10(2), pp.150-156.

Polyakov, V.B. and Mineev, S.D., 2000. The use of Mössbauer spectroscopy in stable isotope geochemistry. *Geochimica et Cosmochimica Acta*, 64(5), pp.849-865.

Pons, M.L., Debret, B., Bouilhol, P., Delacour, A. and Williams, H., 2016. Zinc isotope evidence for sulfate-rich fluid transfer across subduction zones. *Nature communications*, 7, p.13794.

Rebay, G., Zanoni, D., Langone, A., Luoni, P., Tiepolo, M. and Spalla, M.I., 2017. Dating of ultramafic rocks from the Western Alps ophiolites discloses Late Cretaceous subduction ages in the Zermatt-Saas Zone. *Geological Magazine*, pp.1-18.

Rubatto, D., Gebauer, D. and Fanning, M., 1998. Jurassic formation and Eocene subduction of the Zermatt–Saas-Fee ophiolites: implications for the geodynamic evolution of the Central and Western Alps. *Contributions to Mineralogy and Petrology*, 132(3), pp.269-287.

Scambelluri, M., Fiebig, J., Malaspina, N., Müntener, O. and Pettke, T., 2004. Serpentinite subduction: implications for fluid processes and trace-element recycling. *International Geology Review*, 46(7), pp.595-613.

Scambelluri, M., Pettke, T., Rampone, E., Godard, M. and Reusser, E., 2014. Petrology and trace element budgets of high-pressure peridotites indicate subduction dehydration of serpentinitized mantle (Cima di Gagnone, Central Alps, Switzerland). *Journal of Petrology*, 55(3), pp.459-498.

Schauble, E.A., 2004. Applying stable isotope fractionation theory to new systems. *Reviews in Mineralogy and Geochemistry*, 55(1), pp.65-111.

Schmidt, M.W. and Poli, S., 2014. 4.19. Devolatilization during subduction. *The Crust, Treatise on Geochemistry (eds. HD Holland and KK Turekian, Second Edition)*, Elsevier-Pergamon, Oxford, pp.669-701.

Sio, C.K.I., Dauphas, N., Teng, F.Z., Chaussidon, M., Helz, R.T. and Roskosz, M., 2013. Discerning crystal growth from diffusion profiles in zoned olivine by in situ Mg–Fe isotopic analyses. *Geochimica et Cosmochimica Acta*, 123, pp.302-321.

Sossi, P.A., Halverson, G.P., Nebel, O. and Eggins, S.M., 2015. Combined separation of Cu, Fe and Zn from rock matrices and improved analytical protocols for stable isotope determination. *Geostandards and Geoanalytical Research*, 39(2), pp.129-149.

Sossi, P.A., Nebel, O. and Foden, J., 2016. Iron isotope systematics in planetary reservoirs. *Earth and Planetary Science Letters*, 452, pp.295-308.

Teng, F.Z., Dauphas, N., Helz, R.T., Gao, S. and Huang, S., 2011. Diffusion-driven magnesium and iron isotope fractionation in Hawaiian olivine. *Earth and Planetary Science Letters*, 308(3), pp.317-324.

Tenthorey, E. and Cox, S.F., 2003. Reaction-enhanced permeability during serpentinite dehydration. *Geology*, 31(10), pp.921-924.

Ulmer, P. and Trommsdorff, V., 1995. Serpentine stability to mantle depths and subduction-related magmatism. *Science*, pp.858-858.

Weyer, S. and Schwieters, J.B., 2003. High precision Fe isotope measurements with high mass resolution MC-ICPMS. *International Journal of Mass Spectrometry*, 226(3), pp.355-368.

Williams, H.M. and Bizimis, M., 2014. Iron isotope tracing of mantle heterogeneity within the source regions of oceanic basalts. *Earth and Planetary Science Letters*, 404, pp.396-407.

Williams, H.M., Nielsen, S.G., Renac, C., Griffin, W.L., O'Reilly, S.Y., McCammon, C.A., Pearson, N., Viljoen, F., Alt, J.C. and Halliday, A.N., 2009. Fractionation of oxygen and iron isotopes by partial melting processes: implications for the interpretation of stable isotope signatures in mafic rocks. *Earth and Planetary Science Letters*, 283(1), pp.156-166.

Chapter 4. Supplementary Information

Supplementary information 4.1 (Figure) – Vein and host microdrill transect

Supplementary information 4.2 (Table) – Whole rock major and trace elements

Supplementary information 4.3 (Table) – Whole rock Fe isotopes

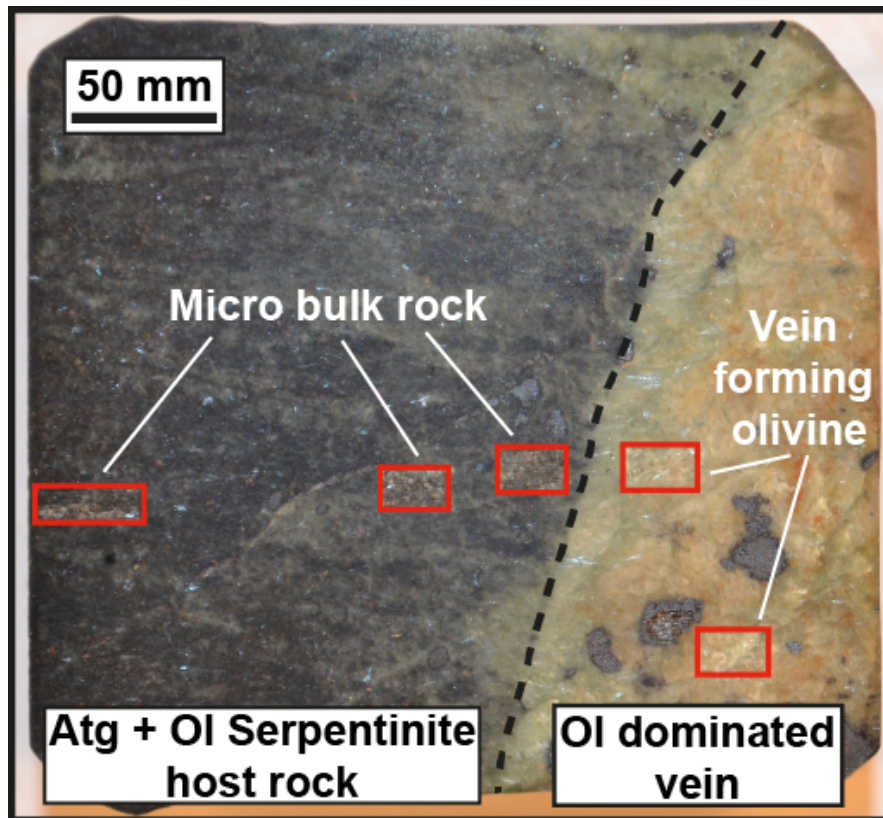
Supplementary information 4.4 (Table) – Mineral trace elements

Supplementary information 4.5 (Table) – Mineral Fe isotopes

Supplementary information 4.6 (Figure) – Full-page whole rock trace element profile

Supplementary information 4.7 (Figure) – Full-page mineral trace element profiles

Supplementary information 4.1 (Figure) – Vein and host microdrill transect



An unmagnified photograph of sample billet/wafer 16-32. The micro-drill sites are highlighted with red rectangles. Towards the left side of the photograph is the antigorite + olivine dominated serpentinite host. The right side of the photograph shows an olivine-dominated vein.

Supplementary information 4.2 – Whole rock major and trace element concentrations**Table 4.2a (All major elements, C & S and trace elements Li to Zr)**

Sample	Major elements and Loss on Ignition (by XRF) – weight percent (wt%)													Carbon a & Sulfur (ppm)		Trace Elements (by ICP-MS) – Parts Per Million (ppm)						
	SiO ₂	TiO ₂	Al ₂ O ₃	Fe ₂ O ₃	MnO	MgO	CaO	Na ₂ O	K ₂ O	P ₂ O ₅	CrO ₃	NiO	LOI	C	S	Li	Sc	Rb	Sr	Y	Zr	
<i>Whole-rock antigorite + olivine serpentinites</i>																						
15-05	36.427	0.022	1.261	12.706	0.132	37.118	0.034	<0.009	0.004	0.004	0.167	0.072	10.116	b.d.1	1983	0.31	6.75	0.001	0.21	0.46	0.34	
15-14	40.236	0.015	2.106	5.483	0.096	38.969	0.897	<0.008	0.005	0.004	0.023	0.031	11.085	b.d.1	1540	0.24	12.83	0.001	0.37	0.96	0.50	
15-02	34.043	0.045	1.446	20.366	0.166	33.040	0.013	<0.009	<0.001	<0.001	0.793	0.366	8.358	591	280	2.38	5.05	0.01	0.23	2.13	1.30	
15-18	37.546	0.022	1.933	10.741	0.142	39.730	0.031	<0.009	0.007	0.004	0.387	0.095	9.235	349	729	0.49	9.75	0.001	0.13	0.64	0.13	
15-15	39.016	0.033	1.549	8.880	0.119	37.255	0.352	<0.008	0.004	0.003	0.377	0.294	11.110	1180	759	0.58	10.12	0.05	3.87	0.70	0.57	
15-19	39.797	0.027	1.866	6.593	0.122	39.185	0.029	<0.009	0.004	0.004	0.445	0.311	11.660	1163	721	0.03	11.57	0.01	0.13	0.61	0.32	
15-20	39.056	0.036	1.276	7.358	0.119	39.921	0.007	<0.009	0.002	0.004	0.332	0.260	10.785	410	1085	0.32	8.00	0.001	0.15	0.46	0.53	
15-21	39.407	0.024	1.313	6.762	0.114	40.307	0.024	<0.009	0.002	0.004	0.399	0.327	10.980	497	1503	0.27	7.81	0.001	0.19	0.54	0.56	
<i>Metasediments</i>																						
15-25	50.078	0.024	3.912	6.761	0.124	24.380	9.248	0.161	0.049	0.004	0.018	0.640	0.367	3.32	b.d.1	2.14	12.46	0.09	22.6	3.38	0.06	
15-26	40.165	0.042	2.215	8.208	0.104	36.877	0.068	<0.008	0.006	0.004	0.019	0.346	0.246	11.2	b.d.1	0.21	13.54	0.03	0.83	0.60	0.14	

Metasediment samples 15-25 and 15-26 are referred to elsewhere as Rif15-01 and Rif15-02 respectively

bd1 –below detection limit

Table 4.2b (Trace elements Nb to Pb)

Trace Elements (by ICP-MS) – Parts Per Million (ppm)																					
Sample	Nb	Sn	Cs	Ba	La	Ce	Pr	Nd	Sm	Eu	Gd	Tb	Dy	Ho	Er	Tm	Yb	Lu	Hf	Ta	Pb
Whole-rock antigorite + olivine serpentinites																					
15-05	0.01	12.16	0.00	0.22	0.02	0.06	0.01	0.06	0.02	0.01	0.04	0.01	0.07	0.02	0.05	0.01	0.07	0.01	0.01	bdl	0.20
15-14	0.01	16.20	0.00	0.10	0.02	0.07	0.01	0.07	0.04	0.01	0.08	0.02	0.14	0.03	0.11	0.02	0.14	0.02	0.03	0.00	0.39
15-02	0.13	15.88	0.00	0.52	0.28	0.89	0.15	0.74	0.21	0.07	0.27	0.05	0.30	0.07	0.20	0.03	0.22	0.04	0.08	0.01	0.38
15-18	0.01	16.20	0.00	0.27	0.05	0.14	0.02	0.11	0.03	0.04	0.05	0.01	0.09	0.02	0.08	0.01	0.10	0.02	0.01	bdl	0.14
15-15	0.01	8.98	0.06	2.32	0.03	0.10	0.02	0.09	0.03	0.01	0.06	0.01	0.10	0.03	0.09	0.02	0.12	0.02	0.03	bdl	0.12
15-19	0.03	11.88	0.00	0.14	0.03	0.12	0.02	0.13	0.04	0.02	0.07	0.01	0.08	0.02	0.06	0.01	0.08	0.02	0.02	bdl	0.13
15-20	0.03	14.63	0.00	0.21	0.02	0.07	0.01	0.08	0.03	0.01	0.05	0.01	0.07	0.02	0.05	0.01	0.06	0.01	0.02	0.00	0.16
15-21	0.03	34.28	0.00	0.26	0.03	0.09	0.02	0.10	0.04	0.02	0.06	0.01	0.08	0.02	0.06	0.01	0.07	0.01	0.02	bdl	0.19
Metasediments																					
15-25	0.02	13.63	0.02	0.16	0.01	0.10	0.04	0.33	0.25	0.09	0.44	0.10	0.66	0.13	0.36	0.05	0.30	0.04	0.01	0.00	0.58
15-26	0.03	17.64	0.03	0.16	0.02	0.08	0.02	0.10	0.04	0.01	0.06	0.01	0.09	0.02	0.07	0.01	0.08	0.01	0.01	0.00	0.08

Metasediment samples 15-25 and 15-26 are referred to elsewhere as Rif15-01 and Rif15-02 respectively

bdl –below detection limit

Table 4.2b (Trace elements Th to Te)

Trace Elements (by ICP-MS) – Parts Per Million (ppm)													
Sample	Th	U	V	Cr	Co	Ni	Cu	Zn	B	As	Se	Sb	Te
Whole-rock antigorite + olivine serpentinites													
15-05	0.001	0.001	46.66	2282	132.	2618	9.38	46.94	14.67	1.28	0.07	0.03	0.01
15-14	0.001	0.001	47.30	2436	83.54	1934	12.00	38.29	9.44	13.36	0.01	1.31	0.001
15-02	0.01	0.001	71.00	5159	140.7	2645	17.73	96.93	11.60	3.14	0.07	0.23	0.01
15-18	0.001	0.001	50.08	2838	107.4	2166	7.50	46.56	13.98	1.61	0.02	0.06	0.01
15-15	0.001	0.001	44.20	2192	108.7	2200	22.68	46.45	2.36	3.03	0.02	0.14	0.01
15-19	0.001	0.001	44.04	2221	95.36	1717.0	18.84	47.54	15.45	2.83	0.10	0.12	0.01
15-20	0.001	0.001	31.12	2680	109.3	2300	5.57	53.96	10.30	2.20	0.05	0.10	0.01
15-21	0.001	0.001	29.20	2394	118.9	2504	6.30	52.60	8.04	2.21	0.02	0.10	0.01
Metasediments													
15-25	0.001	0.03	46.15	2633	76.57	1776	245.6	77.27	4.79	0.99	0.10	0.07	0.03
15-26	0.001	0.001	61.97	2524	100.9	2168	15.96	39.38	5.79	1.77	bdl	0.09	0.02

Metasediment samples 15-25 and 15-26 are referred to elsewhere as Rif15-01 and Rif15-02 respectively

bdl –below detection limit

Supplementary information 4.3 Whole rock Fe isotope compositions

Sample	Fe isotopes (*relative to IRMM-14)				
	$\delta^{56}/^{54}\text{Fe}^*$	2sd	$\delta^{57}/^{54}\text{Fe}^*$	2sd	n
Whole-rock antigorite + olivine serpentinites					
15-05	-0.08	0.04	-0.14	0.04	4
15-14	-0.04	0.01	-0.06	0.04	4
15-02	0.00	0.04	-0.02	0.08	4
15-18	-0.04	0.04	-0.05	0.07	3
15-15	-0.04	0.04	-0.06	0.10	5
15-19	-0.04	0.03	-0.08	0.05	4
15-20	-0.06	0.01	-0.10	0.07	4
15-21	-0.07	0.02	-0.13	0.03	4
Metasediments					
15-25	-0.02	0.04	-0.04	0.07	4
15-26	0.04	0.04	0.06	0.07	3

Supplementary information 4.4 Mineral trace element data**Table 4.4a (Mineral trace element data Cs to Sm)**

Sample	Trace Elements (by ICP-MS) – Parts Per Million (ppm)																	
	Cs	Rb	Ba	U	Th	B	Nb	La	Ce	Pb	As	Sb	Pr	Sr	Nd	Zr	Hf	Sm
16-32ii																		
16 32ii Atg GM2	b.d.l	0.01	b.d.l	0.001	0.001	4.58	0.01	0.001	0.02	0.04	b.d.l	b.d.l	0.00	0.19	0.01	0.36	0.01	0.01
16 32ii Atg GM3	0.02	0.05	b.d.l	0.001	0.001	95.32	0.09	0.16	0.68	1.09	2.92	1.66	0.07	1.31	0.39	1.73	0.05	0.11
16 32ii MAG	b.d.l	0.01	b.d.l	b.d.l	0.001	2.08	b.d.l	0.001	0.11	0.00	b.d.l							
16 32ii OL	b.d.l	0.06	b.d.l	0.001	0.001	40.68	0.25	0.08	0.19	0.08	b.d.l	0.55	0.03	1.86	0.14	0.67	b.d.l	0.04
16-32																		
16 32i Atg GM1	b.d.l	0.03	b.d.l	0.001	0.03	40.59	0.30	0.18	0.52	0.23	b.d.l	0.86	0.09	0.62	0.43	0.91	0.03	0.12
16 32i Atg GM2	0.02	0.22	b.d.l	0.001	0.02	65.99	0.34	0.38	1.15	0.94	b.d.l	1.99	0.19	3.94	0.94	1.63	0.07	0.24
16 32i Atg GM3	b.d.l	0.61	b.d.l	0.02	0.02	154.44	0.50	0.19	0.54	1.23	7.44	3.09	0.11	1.90	0.45	1.75	0.06	0.11
16 32i O11	b.d.l	0.09	b.d.l	0.001	0.02	b.d.l	0.86	0.20	0.60	0.49	b.d.l	0.99	0.09	1.04	0.42	3.75	0.09	0.13
16 32i O12	0.03	0.27	b.d.l	0.00	0.03	331.67	1.52	0.30	0.83	0.21	5.36	2.14	0.12	2.74	0.60	3.90	0.09	0.18
16 32i MAG	b.d.l	0.08	b.d.l	0.01	0.02	69.07	0.11	0.02	0.07	0.15	b.d.l	0.28	0.01	1.39	0.04	1.76	0.05	0.01
16-12																		
16 12 Atg GM1	b.d.l	0.09	b.d.l	0.001	0.01	25.93	0.09	0.01	0.02	0.92	3.03	1.78	0.00	0.82	0.02	0.85	0.02	b.d.l
16 12 O11	0.19	0.44	2.26	0.001	0.06	86.55	0.34	0.03	0.19	1.00	12.57	1.88	0.03	4.92	0.09	2.79	0.06	0.03
16 12 O12	0.05	0.16	b.d.l	0.001	0.02	20.48	0.11	0.02	0.03	0.09	2.77	0.42	0.00	1.42	0.02	0.90	0.02	b.d.l
16-24ii																		
16 24ii GM1	0.01	0.04	b.d.l	0.001	0.01	16.28	0.09	0.01	0.09	0.10	b.d.l	0.21	0.02	0.38	0.15	0.65	0.01	0.05
16 24ii Chm1	b.d.l	0.01	b.d.l	0.001	b.d.l	4.24	0.22	0.001	0.01	0.02	b.d.l	b.d.l	0.00	0.25	0.01	1.30	0.02	0.00
16 24ii Chm2	b.d.l	0.02	b.d.l	0.001	0.01	14.03	1.15	0.01	0.02	b.d.l	b.d.l	0.15	0.01	0.22	0.04	3.79	0.08	b.d.l
16-20A																		
16 20A Chm1	b.d.l	0.02	0.79	0.001	0.001	b.d.l	1.30	b.d.l	0.00	0.01	b.d.l	0.10	0.00	0.24	0.00	1.46	0.03	b.d.l
16 20A Chm2	b.d.l	0.01	b.d.l	b.d.l	b.d.l	2.85	0.75	b.d.l	0.02	b.d.l	b.d.l	0.11	0.00	0.14	0.01	0.99	0.02	b.d.l
16 20A Chm3	b.d.l	0.03	1.79	0.001	0.001	3.25	0.29	0.01	0.03	0.03	b.d.l	0.11	0.00	0.43	0.03	1.13	0.03	0.01
16-30																		
16 30 Atg GM1	0.01	0.09	b.d.l	b.d.l	b.d.l	33.88	0.06	0.01	0.03	0.36	b.d.l	0.36	0.00	1.08	0.04	1.39	0.04	0.01
16 30 Chm1	b.d.l	0.07	b.d.l	0.001	0.001	15.82	0.50	0.01	0.01	0.02	b.d.l	0.19	0.001	1.14	0.01	2.96	0.05	0.01
16 30 O11	b.d.l	0.01	b.d.l	b.d.l	b.d.l	48.17	0.02	b.d.l	b.d.l	0.03	b.d.l	b.d.l	b.d.l	0.37	0.02	0.64	0.02	b.d.l

bdl –below detection limit

Table 4.4b (Mineral trace element data Eu to Cu)

Sample	Trace Elements (by ICP-MS) – Parts Per Million (ppm)											
	Eu	Gd	Tb	Dy	Li	Y	Ho	Er	Tm	Yb	Lu	Cu
16-32ii												
16 32ii Atg GM2	0.000 1	0.007	0.000	0.007	0.056	0.041	0.0001	0.004	0.000 1	0.007	0.000 1	3.699
16 32ii Atg GM3	0.035	0.105	0.018	0.175	1.453	1.033	0.035	0.105	0.018	0.158	0.018	116.816
16 32ii MAG	b.d.l	b.d.l	b.d.l	0.000	b.d.l	0.003	b.d.l	0.000	b.d.l	b.d.l	b.d.l	0.190
16 32ii OL	0.014	0.041	0.000 1	0.055	17.058	0.371	0.014	0.041	0.014	0.151	0.041	1.857
16-32												
16 32i Atg GM1	0.039	0.156	0.026	0.156	1.991	1.145	0.039	0.117	0.013	0.143	0.026	30.229
16 32i Atg GM2	0.096	0.360	0.048	0.384	2.042	2.787	0.096	0.264	0.048	0.312	0.072	76.757
16 32i Atg GM3	0.043	0.151	0.022	0.173	1.557	1.211	0.043	0.108	0.022	0.173	0.022	101.146
16 32i O11	0.066	0.177	0.022	0.221	13.932	1.435	0.044	0.155	0.044	0.397	0.066	25.038
16 32i O12	0.089	0.208	0.030	0.238	44.599	2.292	0.060	0.238	0.060	0.625	0.149	21.645
16 32i MAG	0.000 1	0.011	0.000 1	0.011	1.037	0.053	0.0001	0.000	b.d.l	b.d.l	b.d.l	3.693
16-12												
16 12 Atg GM1	b.d.l	0.011	0.000 1	0.011	b.d.l	0.102	0.0001	0.011	0.000	0.023	0.000	12.932
16 12 O11	0.031	0.063	0.000 1	0.219	18.243	2.978	0.063	0.564	0.188	2.382	0.596	28.619
16 12 O12	0.000	0.016	0.000 1	0.047	2.868	0.639	0.016	0.109	0.031	0.436	0.094	8.651
16-24ii												
16 24ii GM1	0.022	0.072	0.007	0.072	b.d.l	0.598	0.014	0.029	0.000	0.029	0.007	5.521
16 24ii Chm1	0.000	0.008	0.000	0.008	0.065	0.335	0.000	0.008	0.000	0.012	0.000	12.498
16 24ii Chm2	0.008	0.024	0.000	0.024	0.429	0.291	0.008	0.024	0.000	0.049	0.008	11.963
16-20A												
16 20A Chm1	0.000 1	0.004	0.000	0.004	0.309	0.246	0.0001	0.008	0.000 1	0.021	0.008	3.591
16 20A Chm2	0.000 1	0.004	0.000	0.004	0.199	0.111	0.0001	0.007	0.000	0.022	0.007	3.014
16 20A Chm3	0.004	0.009	0.000	0.013	0.345	0.162	0.004	0.009	0.000	0.017	0.004	3.912
16-30												

Chapter 4

16 30 Atg GM1	0.000 1	0.015	0.000 1	0.044	b.d.1	0.385	0.015	0.044	0.015	0.074	0.015	11.985
16 30 Chm1	b.d.1	0.007	0.000	0.000	0.585	0.840	0.0001	0.007	0.000 1	0.040	0.007	7.480
16 30 O11	b.d.1	b.d.1	b.d.1	0.008	2.290	0.310	0.0001	0.016	0.008	0.087	0.024	1.209

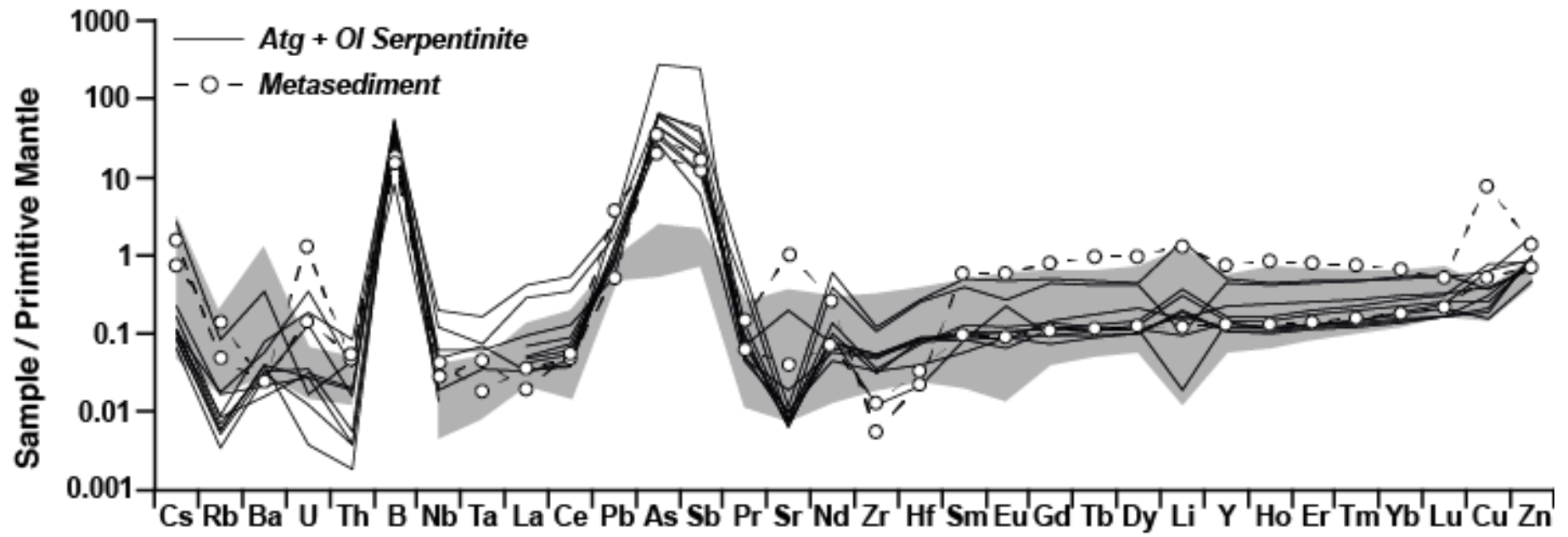
bd1 –below detection limit

Supplementary information 4.5 Mineral Fe isotope data

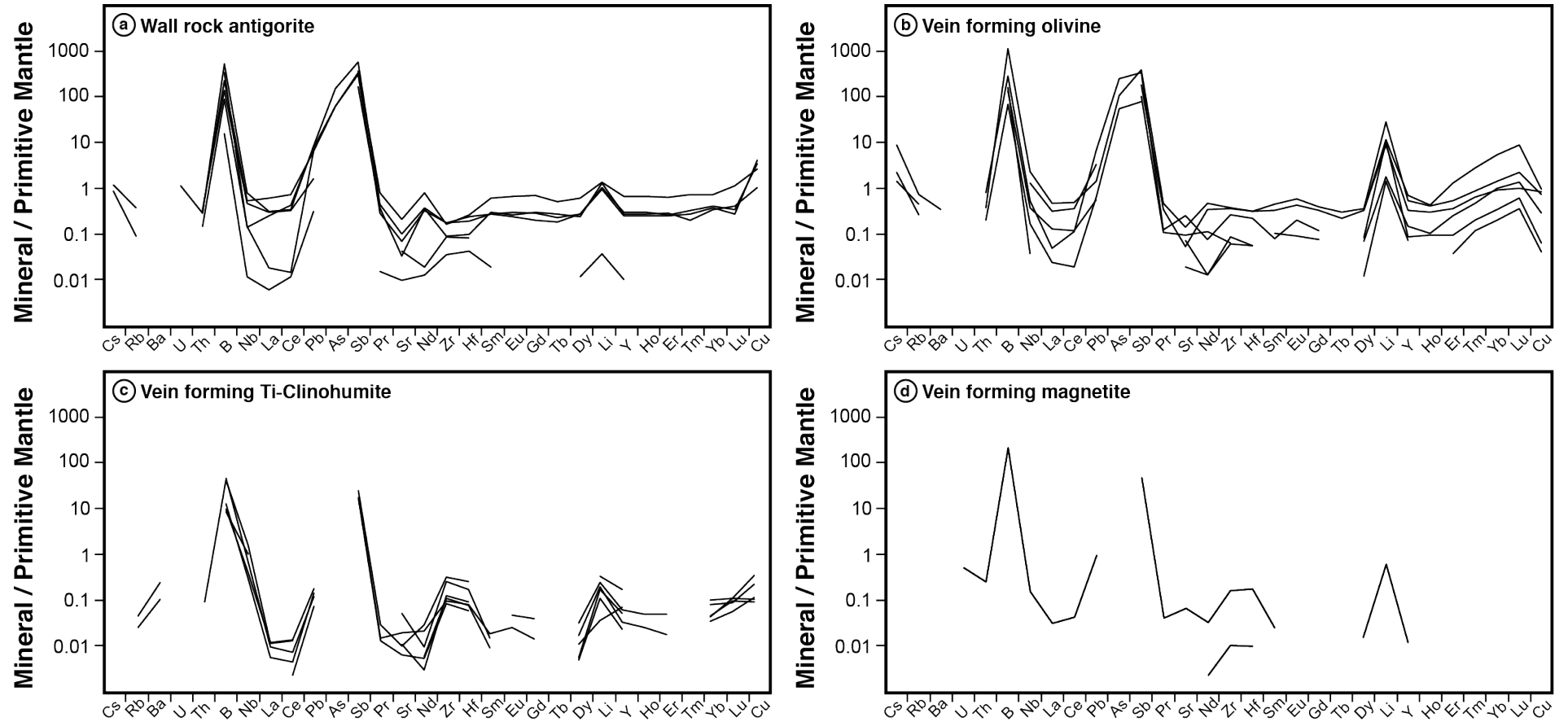
<i>Sample</i>	<i>Fe isotopes (*relative to IRMM-14)</i>				
	$\delta^{56}/^{54}\text{Fe}^*$	2sd	$\delta^{57}/^{54}\text{Fe}^*$	2sd	n
16-32ii					
16 32ii Atg GM2	-	-	-	-	-
16 32ii Atg GM3	-	-	-	-	-
16 32ii Mag	0.05	0.05	0.05	0.07	4
16 32ii Ol	-0.29	0.05	-0.45	0.08	4
16-32					
16 32i Atg GM1	-0.01	0.04	-0.02	0.06	4
16 32i Atg GM2	0.05	0.01	0.10	0.01	4
16 32i Atg GM3	0.12	0.01	0.18	0.05	4
16 32i Ol1	-0.05	0.05	-0.06	0.07	4
16 32i Ol2	-0.10	0.05	-0.15	0.07	4
16 32i Mag	0.04	0.04	0.07	0.06	4
16-12					
16 12 Atg GM1	-	-	-	-	-
16 12 Ol1	-0.40	0.03	-0.63	0.02	4
16 12 Ol2	-0.35	0.00	-0.53	0.02	4
16-24ii					
16 24ii GM1	-	-	-	-	-
16 24ii Chm1	-	-	-	-	-
16 24ii Chm2	-	-	-	-	-
16-20A					
16 20A Chm1	-0.08	0.02	-0.13	0.02	4
16 20A Chm2	-	-	-	-	-
16 20A Chm3	-	-	-	-	-
16-30					
16 30 Atg GM1	0.17	0.03	0.24	0.05	4
16 30 Chm1	-0.16	0.01	-0.23	0.03	4
16 30 Ol1	-0.27	0.04	-0.42	0.07	4

- represents samples that were not analysed

Supplementary information 4.6 - Full-page whole-rock trace element profile



Supplementary information 4.7 - Full-page mineral trace element profiles



Chapter 5.

Conclusions and Synthesis

5.1 Key aims of this work

The overarching goal of this thesis was to understand and quantify the processes of geochemical mass transfer occurring in subduction zones, with particular respect to the role of devolatilisation of the subducting slab. To this end two key aspects have been focussed upon. The first of these is the petrographic characterisation of exhumed subduction zone lithologies - the rationale of which is to provide an understanding of how subduction zone mass transfer can occur within natural samples. The second aspect has been the application of different geochemical tracers, namely metal stable isotopes, within these natural samples, in order to ascertain the mobility of key redox mediating elements during the subduction of oceanic lithosphere.

5.2 Overview of chapters

Here a brief overview is provided of each of the scientific chapters presented within this thesis. Summarising each and linking it to the main objective of this study

5.2.1 The behaviour of iron and zinc stable isotopes accompanying the subduction of mafic oceanic crust: A case study from Western Alpine ophiolites

This paper, presented in **Chapter 2**, gives whole rock data for a range of metabasalts and metagabbros taken from three different Alpine meta-ophiolites. These different meta-ophiolite bodies have been metamorphosed under conditions ranging between greenschist, blueschist and eclogite facies, and are subsequently interpreted to be representative of different, prograde metamorphic regions of the subducting oceanic lithosphere.

Major element data for these samples demonstrates that there are no significant differences between this suite and similar abyssal samples, thus suggesting that no, large-scale, major element variations occur as a result of subduction zone metamorphism. In contrast, variations are observed with respect to trace element concentrations. Greenschist facies meta-gabbros display trace element concentrations in good agreement with other abyssal gabbros, and other trace element measurements of samples from the same meta-ophiolite. The blueschist

facies meta-gabbros show a striking enrichment in fluid-mobile elements (e.g. B, Sb, As and Cs), suggesting interaction between proximal meta-sedimentary lithologies and the meta-gabbros during blueschist facies metamorphism. Meta-basalts and meta-gabbros from the H/UH-*P* Zermatt-Saas ophiolite display a range of different trace element profiles - the metagabbros appear to preserve profiles broadly consistent with abyssal gabbros, while meta-basalts show a depletion of some fluid mobile elements, suggesting loss of aqueous fluids during subduction zone metamorphism.

In addition to elemental concentrations this paper also draws upon Fe and Zn stable isotope data for the same sample suite. The rationale behind measuring Fe and Zn isotopes within these samples is that these isotope systems can be fractionated in response to the mobility of oxidised Fe³⁺ and/or oxidising S and C species, respectively. As such the aim was to trace the mobility of these key redox-mediating components during the prograde evolution of subduction zone rocks. The key findings for this aspect of the study is that Fe and Zn show no resolvable variations between metamorphic facies, and both the Fe and Zn isotope compositions of basaltic and gabbroic eclogites overlap with values observed for MORB. This finding is significant with respect to two aspects. Firstly, we show that Fe isotopes are not fractionated in response to loss of Fe during dehydration of mafic lithologies during dehydration. Secondly, it is demonstrated that the lack of Zn isotope variation consistent with indices of prograde metamorphism suggests that fluids released from these lithologies during metamorphism are not major carriers of dissolved Zn-SO_x/CO_x complexes. It should be noted that the Fe isotope composition of the blueschist facies meta-gabbros show covariations with fluid mobile element concentrations, suggesting that there is a metasomatic control on Fe isotopes within these samples.

The key results from this paper are that, if these samples are representative of globally subducting oceanic crust, then we see no evidence for the mobility of Fe accompanying prograde metamorphism. The most like control on this is the low solubility of Fe within aqueous fluids coupled with the relatively low volume of H₂O stored within such rocks. Consequently, we conclude that Fe behaves conservatively during the metamorphic dehydration of mafic lithologies within subduction zones. Furthermore, we suggest that it is unlikely that these lithologies contribute significantly to the fluxes of dissolved S or C within

subduction zones. Taken together our results suggest that metamorphism of crustal basalts and gabbros serves as a poor mechanism for the oxidation of the sub-arc mantle.

5.2.2 Relicts of High-Pressure Serpentinite Dehydration in the Zermatt-Saas Ophiolite (Western Alps, Switzerland)

Building on our results from the previous chapter, where we examined the effect of mafic lithologies on the redox budget of subduction zones, the next logical step was to consider the rest of the oceanic crust. In particular, to examine the potential role of the associated serpentinised mantle lithologies from the Zermatt-Saas ophiolite, which form part of the same oceanic lithosphere, that have also experienced H/UH-*P*, eclogite facies metamorphism during subduction.

As part of this study we identified a series of metamorphic veins and associated dehydration textures within the Zermatt serpentinites from the Gornergrat area of the ophiolite. Olivine and Titanian-clinohumite occur as the main vein forming phases and are also observed alongside chlorite growth in distinctive macroscopic textural arrangements, termed here, the “python-pattern”. Throughout the massif the occurrence of both metamorphic veins and the python-pattern is pervasive and suggests high degrees of fluid flow. Taken together these features are interpreted to reflect partial dehydration of the serpentinite body during H/UH-*P* metamorphism, likely resulting from the breakdown of antigorite near to the metamorphic climax of the massif.

This finding is significant because it demands a revision of the P-T conditions experienced by the Zermatt-Saas ophiolite, which, up until now, has been considered as an example of a deeply subducted section of oceanic lithosphere but that displays little evidence for serpentinite breakdown (e.g. *Li et al., 2004*). Contrary to this our findings suggest otherwise, and in fact, present a strong case for partial deserpentinisation of these lithologies. As such we argue that the Zermatt-Saas serves as an excellent example of a H/UH-*P* subduction zone terrane, which can be utilised as a case study to understand and quantify subduction zone fluid flow and mass transfer resulting from serpentinite breakdown.

5.2.3 Iron isotope behaviour accompanying the dehydration of serpentinite during subduction: A mineral scale approach

This chapter presents a detailed trace element and isotopic study of the serpentinites and associated metamorphic veins from the Zermatt-Saas ophiolite, and builds on the petrographic characterisation of such features as described in the previous chapter.

In order to understand the nature of fluids that are released during the process of deserpentinisation during subduction zone metamorphism, we selected a suite of whole-rock antigorite and olivine bearing samples, alongside sections comprising olivine and Ti-clinohumite bearing metamorphic veins and associated host wall rocks. The whole-rock antigorite and olivine bearing samples were analysed for their bulk major, trace and Fe isotope composition, while the olivine and Ti-clinohumite veins were sampled using a micro-mill to extract material from each vein forming and wall rock domain. The resultant powders were then analysed for their trace element and Fe isotope compositions. The combined approach of whole rock and mineral scale analysis has allowed us to document the trace element and Fe isotope systematics during the breakdown of antigorite and expulsion of serpentinite derived fluids.

Our data show a strong co-variation between the bulk S content and Fe isotope composition of the whole rock antigorite and olivine serpentinites, with the samples that display the lowest S concentrations also having the heaviest Fe isotope composition. These results suggest that isotopically light Fe is lost, alongside S from the serpentinites and that the resulting fluids would not only be enriched in light Fe isotopes but also contain dissolved S. This suggestion is supported by the measurements of vein forming olivine and Ti-clinohumite, both of which preserve light Fe isotope values with respect to their associated wall rocks. Seeing as isotopically light Fe is preferentially incorporated within aqueous Fe-S complexes, it is likely that these vein forming minerals record the mobilisation of isotopically light Fe, S bearing fluids during antigorite breakdown. In addition we also show that vein forming phases are strongly enriched in key fluid mobile elements, such as B, and we suggest that these elements can be mobilised within serpentinite derived fluids in subduction zones.

The key finding from this chapter is that our data provide strong evidence that deserpentinisation of the subducting slab mantle is a viable mechanism for S release and mobilisation within resulting serpentinite derived fluids. In this case S mobility is traceable with Fe isotopes.

5.3 Synthesis of key findings

The main objective of this thesis was to consider, from a slab perspective, the role of different metamorphic fluid fluxes on redox cycling within subduction zones. In satisfaction of this goal we have dissected different metamorphic terranes, comprising both crustal and mantle sequences of sections of oceanic lithosphere, which have been exhumed from subduction zones. Using different stable isotope tracers we have shown how these different metamorphic terranes contribute to fluxes of redox mediating elements. Our findings suggest that fluids derived from devolatilisation of crustal metabasalts and meta-gabbros are poor agents for the mobilisation of Fe. It is likely that during eclogitization of the oceanic crust Fe behaves conservatively, consequently aqueous Fe^{3+} is likely not liberated from these lithologies and, as such the transfer of Fe^{3+} to the sub-arc mantle does not occur. Additionally our data suggest that the fluids liberated during prograde metamorphism crustal rocks, are not major carriers of dissolved SO_x and/or CO_x bearing complexes. Taken together we conclude that devolatilisation of crustal lithologies during subduction zone metamorphism does not provide a major mechanism for oxidation of the sub-arc mantle.

In support of this work we have analysed a section of complementary serpentinised slab mantle. We first show strong field and petrographic evidence that these slab serpentinites have undergone partial dehydration accompanying prograde, subduction zone metamorphism. A finding noteworthy within itself, as previous workers had argued that the Zermatt-Saas serpentinite body had retained its hydrous mineralogy despite enduring H/UH-*P* metamorphism (*Li et al., 2004*). Building on these findings our detailed, micro-analytical study of these serpentinites and associated metamorphic veins has revealed that the breakdown of antigorite within these rocks is accompanied by a release of S within serpentinite-derived fluids, and that this mobility is traceable with Fe isotopes. As such, we conclude that not only do slab serpentinites play a key role in redox cycling in subduction zones, but that it is likely that they are accountable for the release of multi-valent S species, capable of exerting a control on the redox state of the sub-arc mantle.

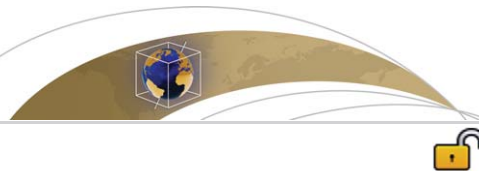
5.4 Future perspectives

This thesis has provided a detailed elemental and isotopic insight into metamorphic dehydration occurring during the subduction of oceanic lithosphere. Future work relating to the key findings would centre around detailed mineral chemistry analyses and the construction of quantitative *P-T* paths for the Zermatt ultramafics. It would be interesting to link this to detailed geochronology of vein forming minerals to better constrain the

timings of metamorphic dehydration in this setting – ultimately allowing one to comment on the chronometry of subduction zone dehydration. Additionally, detailed Zn isotope analyses of metamorphic veins from the Zermatt ultramafics would allow for tracing of redox sensitive S and C aqueous species.

References Cited

Li, X.P., Rahn, M. and Bucher, K., 2004. Serpentinites of the Zermatt-Saas ophiolite complex and their texture evolution. *Journal of Metamorphic Geology*, 22(3), pp.159-177.



RESEARCH ARTICLE

10.1002/2016GC006735

The behavior of iron and zinc stable isotopes accompanying the subduction of mafic oceanic crust: A case study from Western Alpine ophiolites

Edward C. Inglis¹ , Baptiste Debret^{1,2}, Kevin W. Burton¹, Marc-Alban Millet^{1,3} , Marie-Laure Pons^{1,2}, Christopher W. Dale¹ , Pierre Bouilhol^{1,4} , Matthew Cooper⁵ , Geoff M. Nowell¹, Alex J. McCoy-West¹ , and Helen M. Williams^{1,2}

¹Department of Earth Sciences, Science Labs, Durham University, Durham, UK, ²Department of Earth Sciences, University of Cambridge, Cambridge, UK, ³School of Earth and Ocean Science, Cardiff University, Cardiff, UK, ⁴Université Clermont Auvergne, CNRS, IRD, OPGC, Laboratoire Magmas et Volcans, Clermont-Ferrand, France, ⁵Ocean and Earth Science, National Oceanography Centre Southampton, University of Southampton, Southampton, UK

Key Points:

- Iron and zinc stable isotope and elemental data are presented for a prograde suite of metabasalts and metagabbros from Western Alpine ophiolite complexes
- Bulk rock $\delta^{56}\text{Fe}$ and $\delta^{66}\text{Zn}$ do not vary across metamorphic facies and the eclogitic samples show a MORB-like isotope composition
- Blueschist facies metagabbros preserve evidence for infiltration of sediment derived fluids that impart a light $\delta^{56}\text{Fe}$ isotope composition to the gabbro

Supporting Information:

- Supporting Information S1
- Table S1
- Table S2

Correspondence to:

E. C. Inglis,
e.c.inglis@durham.ac.uk

Citation:

Inglis, E. C., et al. (2017), The behavior of iron and zinc stable isotopes accompanying the subduction of mafic oceanic crust: A case study from Western Alpine ophiolites, *Geochem. Geophys. Geosyst.*, 18, 2562–2579, doi:10.1002/2016GC006735.

Received 16 NOV 2016

Accepted 2 JUN 2017

Accepted article online 9 JUN 2017

Published online 13 JUL 2017

© 2017. The Authors.

This is an open access article under the terms of the Creative Commons Attribution License, which permits use, distribution and reproduction in any medium, provided the original work is properly cited.

Abstract

Arc lavas display elevated $\text{Fe}^{3+}/\Sigma\text{Fe}$ ratios relative to MORB. One mechanism to explain this is the mobilization and transfer of oxidized or oxidizing components from the subducting slab to the mantle wedge. Here we use iron and zinc isotopes, which are fractionated upon complexation by sulfide, chloride, and carbonate ligands, to remark on the chemistry and oxidation state of fluids released during prograde metamorphism of subducted oceanic crust. We present data for metagabbros and metabasalts from the Chenaillet massif, Queyras complex, and the Zermatt-Saas ophiolite (Western European Alps), which have been metamorphosed at typical subduction zone *P-T* conditions and preserve their prograde metamorphic history. There is no systematic, detectable fractionation of either Fe or Zn isotopes across metamorphic facies, rather the isotope composition of the eclogites overlaps with published data for MORB. The lack of resolvable Fe isotope fractionation with increasing prograde metamorphism likely reflects the mass balance of the system, and in this scenario Fe mobility is not traceable with Fe isotopes. Given that Zn isotopes are fractionated by S-bearing and C-bearing fluids, this suggests that relatively small amounts of Zn are mobilized from the mafic lithologies in within these types of dehydration fluids. Conversely, metagabbros from the Queyras that are in proximity to metasediments display a significant Fe isotope fractionation. The covariation of $\delta^{56}\text{Fe}$ of these samples with selected fluid mobile elements suggests the infiltration of sediment derived fluids with an isotopically light signature during subduction.

1. Introduction

Oceanic lithosphere formed at mid-ocean ridges is progressively hydrated, altered, and oxidized by interaction with seawater before being recycled into the deep mantle at convergent plate margins. During the subduction of oceanic lithosphere, the increase in pressure and temperature (*P-T*) conditions leads to the destabilization of hydrous mineral phases via a series of metamorphic reactions and the release of dehydration fluids and/or slab derived melts into the overlying crust and subarc mantle [e.g., Schmidt and Poli, 2014; Hermann and Green, 2001; Bouilhol et al., 2015]. Alongside the release of structurally bound H_2O from subducted sediments, mafic and ultramafic sections of the slab, the mechanical compaction of sediments at shallower depths (<20 km) can result in pore fluid expulsion in the fore arc region [Hensen et al., 2004; Rüpke et al., 2004] and localized metasomatism of lithologies in the residual subducting slab [e.g., Marshall et al., 2009; Penniston-Dorland et al., 2012; Vitale Brovarone and Beyssac, 2014; Debret et al., 2016a]. The release of slab derived subcritical [Hermann et al., 2006] or supercritical [Kessel et al., 2005] fluids, and melts [Foley et al., 2000] has been invoked to explain a number of distinct geochemical signatures observed in arc lavas relative to mid-ocean ridge (MORB) and Ocean Island Basalts (OIB), including the enrichment of fluid mobile elements [Hawkesworth et al., 1993] and their elevated $\text{Fe}^{3+}/\Sigma\text{Fe}$ ratios [Brandon and Draper, 1996; Frost and Ballhaus, 1998; Parkinson and Arculus, 1999; Kelley and Cottrell, 2009]. At the same time, residual oceanic crust is ultimately recycled back into the deep mantle, providing a source for the geochemical heterogeneity that is sampled by MORBs and OIBs. Consequently, developing a clear understanding of the processes that govern element mobility during subduction zone metamorphism and metasomatism is crucial

for elucidating both the controls on arc magmatism and the long-term chemical evolution of the mantle [Magni *et al.*, 2014]. This study aims to examine the effect of subduction zone metamorphism and metasomatism on the redox budget of subducted mafic oceanic crust using the stable iron (Fe) and zinc (Zn) isotopes as tracers of elemental mobility, which are thought to be sensitive to complexation by aqueous sulfate (SO_x) and carbonate (CO_x) ligands [Fujii *et al.*, 2011; Hill *et al.*, 2010; Black *et al.*, 2011].

Recent advances in mass spectrometric techniques have seen the emerging field of nontraditional stable isotope geochemistry applied to numerous scientific problems in both high-temperature and low-temperature natural settings. Theory predicts that equilibrium stable isotope fractionation decreases with increasing temperature ($1/T^2$) [Urey, 1947; Schauble, 2004]. Nonetheless, high-precision Fe and Zn stable isotope measurements have shown that both of these systems are sensitive to high-temperature petrogenetic processes, such as mantle melting [Weyer *et al.*, 2005; Williams *et al.*, 2004, 2005, 2009; Williams and Bizimis, 2014; Weyer and Ionov, 2007; Dauphas *et al.*, 2014; Konter *et al.*, 2016], igneous differentiation [Telus *et al.*, 2012; Chen *et al.*, 2013; Schuessler *et al.*, 2009; Teng *et al.*, 2011, 2013; Doucet *et al.*, 2016] and for Fe, changes in redox state [Williams *et al.*, 2004; Dauphas *et al.*, 2009]. It is now well established from both radiogenic and stable isotopes that the loss of fluid mobile elements from sediments imparts a distinct signature to arc lavas [e.g., Pearce, 1982; Plank and Langmuir, 1993; Elliott *et al.*, 1997; Nebel *et al.*, 2010; Freymuth *et al.*, 2015], and the dissolution of carbonate sediments during subduction may play a role in controlling the redox budget of the subarc mantle [Frezzotti *et al.*, 2011; Evans, 2012]. Despite this, it has been suggested that subducted sediments exert little influence on the Fe isotope composition of arc lavas, and that Fe isotope variations in erupted arc products result from depletion of the mantle source and fractional crystallization of the resulting melt [Nebel *et al.*, 2015]. Additionally, the release of sulfur from the subducting slab could serve as a powerful oxidizing agent in this setting, as if sulfur was to be released from the slab as sulfate, then 1 mol of sulfur could serve to oxidize 8 mol of reduced Fe²⁺ to oxidized Fe³⁺.

More recently, both Fe and Zn stable isotopes have been utilized to trace the mobility of Fe and oxidizing sulfate (SO_x) and/or carbonate (CO_x) species during the prograde devolatilization of subducted slab serpentinites [Debret *et al.*, 2016b; Pons *et al.*, 2016]. However, while element depletion has been shown to occur from some parts of the mafic oceanic crust [e.g., Dale *et al.*, 2007], the nature of those fluids remains poorly constrained. This study aims to examine the effect of subduction zone metamorphism on redox sensitive elements in mafic oceanic crust. To this end, we have measured stable Fe and Zn isotope in the metamorphic rocks of an exhumed subducted slab to trace the mobility of redox sensitive Fe and oxidizing SO_x/CO_x-rich fluids during the subduction-related, prograde metamorphism and metasomatism of the mafic oceanic crust.

One approach to assessing the controls on Fe and Zn isotopes during subduction-related metamorphism is to compare their behavior in oceanic crustal rocks across a range of *P-T* conditions. This study uses samples of metabasalts and metagabbros from three meta-ophiolite massifs in the Western European Alps—Chenaillet, Queyras, and Zermatt-Saas. These meta-ophiolites record prograde metamorphic conditions that range from greenschist to blueschist to eclogite that are taken to be representative of a *P-T* path for subducting mafic oceanic crust [e.g., Guillot *et al.*, 2009] (Figure 1a). Samples have also been selected based on varying degree of fluid related slab metasomatism (i.e., those that show evidence for interaction with externally derived fluids released from proximal subducting sediments), thus allowing us to not only examine the effect of prograde metamorphism but also how metasomatic modification could potentially alter the Fe and Zn isotope composition of downgoing mafic lithologies.

2. Geological Setting and Sample Petrology

The ophiolite complexes of the Western European Alps provide a unique insight into the processes acting upon oceanic lithosphere during subduction [e.g., Scambelluri and Philippot, 2001; Guillot *et al.*, 2009; Debret *et al.*, 2013; Vils *et al.*, 2011; Evans *et al.*, 1979; Hermann *et al.*, 2000; Scambelluri *et al.*, 2001, 2014]. These meta-ophiolites were formed in a magma-poor setting, i.e., a slow or ultra-slow-spreading center or an ocean-continent transition, during the opening of the Ligurian Ocean in the Jurassic [Lagabrielle and Canat, 1990; Bernoulli *et al.*, 2003; Lagabrielle *et al.*, 2015], before being subsequently metamorphosed at various *P-T* conditions and exhumed during the Alpine orogeny [Rubatto *et al.*, 1998; Brouwer *et al.*, 2004]. This study is focused on three Alpine ophiolitic complexes that record different *P-T* paths during Alpine

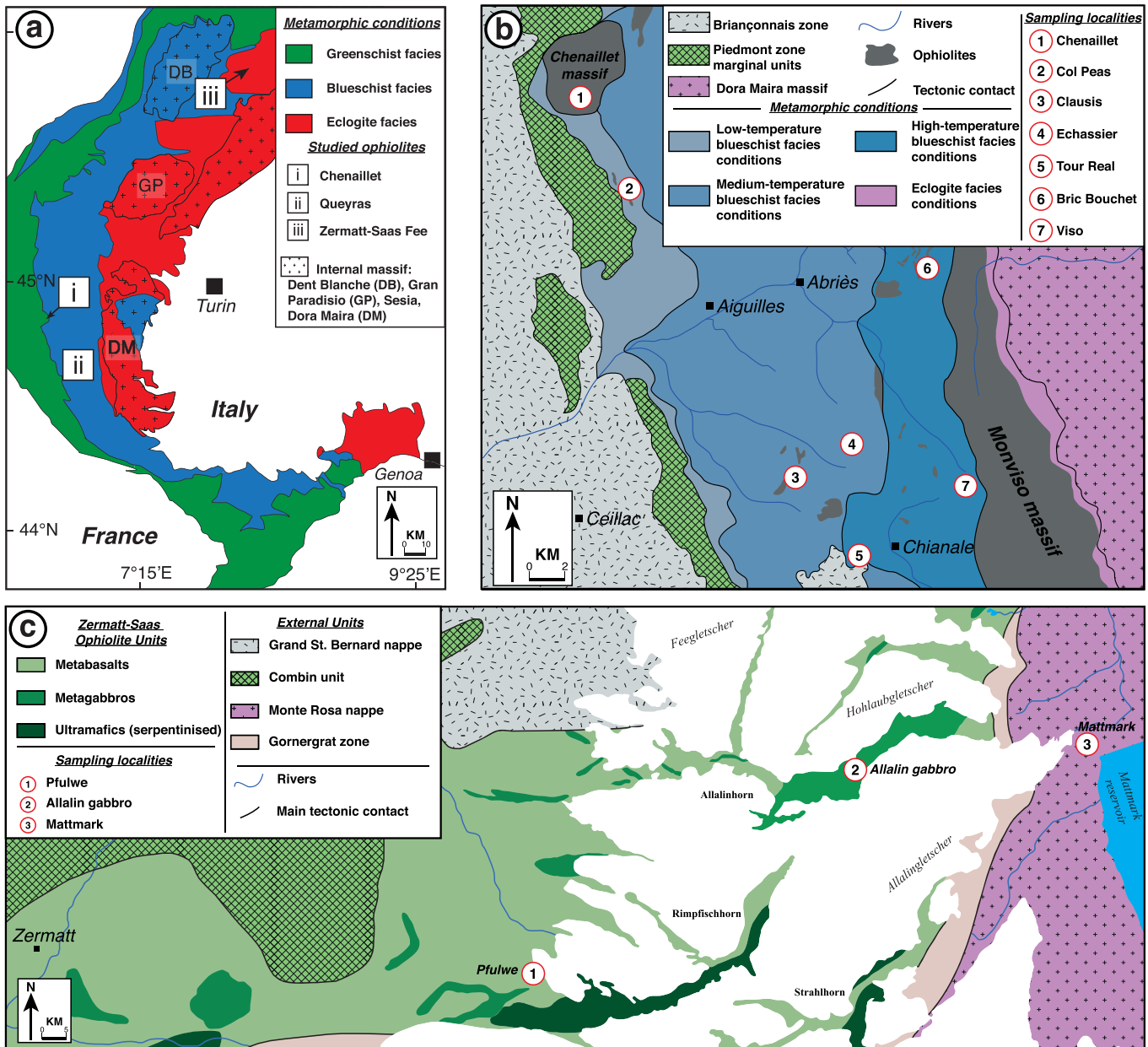


Figure 1. (a) The location of the three Western Alps ophiolitic complexes (Chenaillet, Queyras Schiste Lustrés, and Zermatt Saas) that were sampled as part of this study, within the context of Alpine metamorphic conditions. (b) The sampling localities for the Chenaillet massif and Queyras Schiste Lustré complex and the tectonometamorphic conditions within the area (modified after Schwartz *et al.* [2013]). (c) The sampling localities for the Zermatt-Saas area and the key lithological units of the complex.

evolution (Figure 1a). These are the Chenaillet massif, the Queyras Schiste-Lustrés, and Zermatt-Saas ophiolitic complexes. The Chenaillet massif mainly preserves low-pressure “ocean floor” parageneses, while the Queyras Schiste-Lustrés and Zermatt-Saas ophiolite complexes record the high-pressure transformation of subducted oceanic lithosphere, ranging from blueschist to eclogite facies, respectively.

2.1. The Chenaillet Massif

The Chenaillet massif is located in the external Piedmont zone, 6 km west of Briançon (Figure 1b). It is a structural klippe, overlying the Lago Nero-Replatte unit [Caby, 1995]. The massif preserves a classic sequence of oceanic lithosphere comprising, from top to bottom, oceanic sediments and/or basalts overlying gabbroic pods and serpentinized mantle peridotite. Detailed petrological, geochemical, and structural studies have suggested that this ophiolite represents a fossil oceanic core complex, likely formed at a slow-

spreading ridge setting [Lagabrielle *et al.*, 1990; Chalot-Prat, 2005; Manatschal *et al.*, 2011]. Unlike the majority of the Western Alpine ophiolites, the Chenaillet massif was only weakly affected by Alpine subduction [Mevel *et al.*, 1978; Debret *et al.*, 2016a]. Instead, the metagabbros here mainly record a low-pressure metamorphic overprint, ranging from amphibolite to greenschist facies conditions [Mevel *et al.*, 1978; Debret *et al.*, 2016a]. One coarse-grained metagabbro sample (PR4) was analyzed in this study. This sample represents an undeformed metagabbro, mainly composed of plagioclase and clinopyroxene. The clinopyroxene crystals display small ($\sim 20 \mu\text{m}$) coronas of green and brown amphibole. Minor amounts ($< 10\%$) of actinolite are also observed, both within the plagioclase domain and associated with the amphibole coronas.

2.2. Queyras Schiste lustrés Complex

The Queyras Schiste lustrés complex is located in the Piedmont zone of the south-western Alps (Figure 1b). It comprises units belonging to the distal European margin and from the nearby oceanic domain [Lemoine *et al.*, 1987] that were juxtaposed during Alpine subduction and collision in the Late Cretaceous to Tertiary [Tricart, 1984]. This complex comprises $\sim 10\%$ meta-ophiolite bodies embedded in a sedimentary-rich environment, consisting of Jurassic to Lower Cretaceous clastic and metasedimentary rocks [Lagabrielle *et al.*, 1984; Lemoine *et al.*, 1987] and has previously been interpreted to represent a paleosedimentary wedge [Tricart and Schwartz, 2006].

Three tectonometamorphic domains have been identified within the complex by Schwartz *et al.* [2013]. The P - T conditions of these domains range from low-temperature blueschist facies conditions ($P = 0.9$ – 1.1 GPa, $T = 320$ – 340°C) in the west, to medium-temperature blueschist facies conditions ($P = 1.$ – 1.2 GPa, $T = 340$ – 360°C) and high-temperature blueschist facies conditions ($P = 1.2$ – 1.5 GPa, $T = 380$ – 470°C) toward the east (Figure 1b).

Eight metagabbros were collected from the medium-temperature and high-temperature blueschist domains within five different metagabbroic massifs. Four metagabbro samples were collected from the Echassier (CE7 and CE12) and Clausis (QE1 and QE10) meta-ophiolites that belong to the medium-temperature domain (Figure 1b). These samples predominantly display coarse-grained textures and are typically composed of clinopyroxene, partially recrystallized to glaucophane, while plagioclase is no longer present and is replaced by fine aggregate of lawsonite, chlorite and albite with minor amounts of ilmenite, titanite and late zoisite. Within these massifs the interface between metasedimentary lithologies and metagabbros is demarked by metasomatic contacts, which represent a zone of intense localized fluid circulation, which has occurred during subduction [Debret *et al.*, 2016a]. In order to constrain the nature of the fluid circulating within these zones during subduction, we selected a sample from one metasomatic contact (CE8a) from the Echassier meta-ophiolite. This sample comprises glaucophane, chlorite, quartz, epidote, and titanite. Four samples from the high-temperature domain were collected from the Refuge du Viso (RV7), Tour Real (TR6 and TR9), and the Bric Bouchet (BB1) meta-ophiolites (Figure 1b). The sample RV7 preserves relicts of brown amphibole associated with green amphibole coronas and partially recrystallized into glaucophane, while the plagioclase domain is recrystallized to fine aggregates ($< 10 \mu\text{m}$) of lawsonite, chlorite, quartz, and magnetite. Samples TR6 and TR9 consist of lawsonite, magnetite, chlorite, and glaucophane without any low-pressure relicts, while BB1 displays a similar coarse-grained texture as the Tour Real samples but is composed of stretched porphyroblasts of brown amphibole in association with needles of tremolite and actinolite. In this sample, the plagioclase domain is finely recrystallized to aggregates of cloudy plagioclase and zoisite.

In addition to the metagabbro samples, two sedimentary lithologies from the low-temperature and high-temperature domains were also collected. One sediment sample (CP1) was taken from the Col Peas area within the low-temperature blueschist domain, while the second sediment sample (RV5) comes from the Refuge du Viso within the high-temperature domain. These samples are proximal within tens of meters to the sampled metagabbros. Both of these samples are similar in mineralogy and are comprised of calcite, quartz aggregates, stringy magnetite, phengite, chlorite, and titanite, with both preserving a well-developed foliation.

2.3. Zermatt-Saas

The Zermatt-Saas complex of Alpine Switzerland (Figure 1c) represents a continuous slice of oceanic lithosphere, including ultramafic, mafic, and metasedimentary lithologies, which have been metamorphosed

under eclogite facies conditions during subduction [Bucher *et al.*, 2005]. The Zermatt-Saas ophiolite is preserved within a collisional nappe stack, underlain by the Monte Rosa continental basement, and overlain by the Dent Blanche nappe [Angiboust *et al.*, 2009]. Twelve metabasaltic and metagabbroic rocks were sampled in three different areas of the complex, which record various *P-T* conditions (Figure 1c): the Pfulwe area located to the east of the town of Zermatt which records a metamorphic climax of 24–26 kbar and 550–600°C [Bucher *et al.*, 2005]; the Allalin gabbro which is situated between Zermatt and Saas-Fee and records a metamorphic climax of 2.5 GPa and 610°C [Bucher and Grapes, 2009]; and the terminal moraine of the Hohlaub and Allalin glaciers at the Mattmark dam area, which derives from the Allalin gabbro and corresponds to the same peak metamorphic conditions as given for the Allalin gabbro [Dale *et al.*, 2007]. These samples are discussed in detail in Dale *et al.* [2007, 2009].

Two different types of metabasalt were collected at Pfulwe. The first of these being samples of eclogitized pillow basalts that comprise garnet, omphacite, quartz, zoisite, paragonite, and phengite. Samples were collected from both the core (S02/75iiiC) and rim (S02/75iiR and S02/75iiiR) of individual pillows. The second type of metabasalt collected at Pfulwe are massive basaltic eclogites (S02/41ii and S02/41v), which comprise garnet, omphacite, glaucophane, epidote, paragonite, and phengite. In addition to the basaltic eclogites, a range of metagabbros from the Allalin and Mattmark areas has also been studied. The three metagabbro samples collected from the Allalin gabbro body display a range in mineralogy. Samples S01/5G and S02/83viiiG consist of olivine, fresh and dusty plagioclase and pyroxene without any evidence of an eclogitic overprint, while sample S01/35iix is a gabbroic eclogite and is composed of garnet, glaucophane, talc, zoisite, omphacite, paragonite, and rutile. The occurrence of both primary gabbroic and metamorphic eclogitic assemblages within the Allalin metagabbros has been noted before [Meyer, 1983; Dale *et al.*, 2007; Bucher and Grapes, 2009] and is attributed to a combination of the relatively anhydrous nature of the gabbroic protolith, and the short period and only moderate peak temperature of metamorphism. Of the samples collected from the Mattmark moraine, three (S01/40viii, S02/85ixE, and S01/40vx) display typical eclogitic assemblages of coranitic garnet, omphacite, paragonite, glaucophane, phengite, and quartz, while S02/85ixB shows evidence for late retrogression (barroisite, talc, zoisite, and chlorite).

3. Analytical Methods

3.1. Major and Trace Element Concentrations

Samples from Zermatt-Saas have been previously characterized for major and trace element concentrations by Dale *et al.* [2007]. Samples from the Chenaillet and Queyras meta-ophiolites were analyzed for major element concentration by wavelength dispersive X-ray fluorescence at the University of Edinburgh after the method detailed by Fitton *et al.* [1998]. An external international rock standard (USGS BHVO-1) was measured alongside the samples as a check on precision and accuracy. Measured major element values of this geostandard compare well with the average values obtained in Edinburgh (<5%) and with accepted values published elsewhere [Govindaraju, 1994] (<5%). The loss on ignition corrected major element concentrations of the samples and standards analyzed as part of this study are presented in supporting information Table A1.

Trace element concentrations for the Chenaillet and Queyras samples were determined at the National Oceanography Centre, Southampton. Sample powders were digested using concentrated HF and HNO₃ acids, evaporated to dryness and redissolved in 3% HNO₃ spiked with 5 ppb In and Re and 20 ppb Be for use as internal standards. The samples were analyzed on a Thermo X-Series 2 Quadrupole Inductively Coupled Plasma-Mass Spectrometer (ICP-MS), calibrated against five international rock standards, with JA-2 and BHVO-2 run as unknowns. Analysis of these unknowns compare well to the published values, with the external reproducibility being <5% for Sc, Ti, V, Ni, Cu, As, Rb, Sr, Y, Cd, Sb, Ba, La, Ce, Nd, Sm, Eu, Gd, Tb, Ho, Tm, Lu, Li, Co, Pr, Dy, Er, and Yb and between 5 and 10% for all other elements. The trace element concentrations are presented in supporting information Table A1.

3.2. Fe Isotope Measurements

The Fe isotope measurements were carried out on whole-rock powders at Durham University. Isotope ratios are reported as $\delta^{56}\text{Fe}$ in permil notation relative to IRMM-014 external standard, and $\delta^{57}\text{Fe}$ is given to demonstrate mass dependency of the measurements. All reported errors are 2SD unless stated otherwise.

$$\delta^{56}\text{Fe} = \left(\frac{{}^{56}\text{Fe}/{}^{54}\text{Fe}_{\text{sample}}}{{}^{56}\text{Fe}/{}^{54}\text{Fe}_{\text{IRMM-014}}} - 1 \right) \times 1000$$

$$\delta^{57}\text{Fe} = \left(\frac{{}^{57}\text{Fe}/{}^{54}\text{Fe}_{\text{sample}}}{{}^{57}\text{Fe}/{}^{54}\text{Fe}_{\text{IRMM-014}}} - 1 \right) \times 1000$$

The procedure for the chemical separation of Fe is described in detail by *Williams et al.* [2009] but is briefly outlined here. Samples were dissolved using concentrated HF and HNO₃ acids in 7 mL PTFE Teflon square body beakers with wrench top closures in an oven at 165°C for 3 days. These were then further attacked with a 1:1 mix of concentrated HCl and HNO₃ to ensure all refractory phases, such as spinel and rutile, were fully digested. Finally, samples were brought into solution in 6 M HCl prior to column chemistry. Quantitative purification of Fe was achieved by chromatographic exchange, using Biorad AG1-X4 anion exchange resin in an HCl medium. All reagents used in the chemistry and mass spectrometry procedures were distilled in subboiling Teflon two-bottle stills at Durham University. The total amount of Fe processed through the columns was typically around 650 μg. The total procedural blank contribution was <10 ng of Fe, which is negligible compared to the amount of Fe in the samples. Isotope measurements follow that of *Weyer and Schwieters* [2003] but briefly described here. Measurements were performed by multiple-collector (MC) ICP-MS (Thermo Scientific Neptune Plus) in medium-resolution mode, using an Elemental Scientific Instruments Apex HF desolvating nebulizer for sample introduction. The mass resolution, which is defined as mass/Δmass at 95% and 5% of the beam intensity of the ⁵⁶Fe peak edge, ranged between 7500 and 9000 depending on daily tuning of the instrument as well as the age of the medium resolution beam slit. At this resolution, it was possible to adequately resolve the ⁴⁰Ar¹⁶O⁺, ⁴⁰Ar¹⁶O¹H⁺, ⁴⁰Ar¹⁸O⁺, and ⁴⁰Ar¹⁴N⁺ polyatomic species that can interfere on the ⁵⁶Fe, ⁵⁷Fe, ⁵⁸Fe, and ⁵⁴Fe masses, respectively. Instrumental mass bias was corrected for by sample-standard bracketing, where the beam intensities of the bracketing standard and sample were matched to within 10%. Both sample and standard solutions were run at 2 ppm, giving a beam intensity of between 35 and 50 V on ⁵⁶Fe, depending on daily sensitivity. In addition to all Fe masses, ⁵³Cr and ⁶⁰Ni were also monitored and an online Cr and Ni correction was applied to account for any isobaric interferences from ⁵⁴Cr and ⁵⁸Ni on the ⁵⁴Fe and ⁵⁸Fe masses. These corrections were either negligible or nonexistent due to the effective separation of Fe from Cr and Ni during column chemistry. An in-house standard of FeCl₂ was analyzed throughout each analytical sessions giving a mean δ⁵⁶Fe value of -0.70 ± 0.06‰ and mean δ⁵⁷Fe value of -1.05 ± 0.06, where *n* = 69, these values are in excellent agreement with previously published measurements of this standard [*Mikutta et al.*, 2009]. In addition to this internal standard, an external geostandard, USGS BIR-1, was processed through chemistry and analyzed alongside samples. The BIR-1 analysis gave a mean value of +0.06 ± 0.02‰ for δ⁵⁶Fe and +0.08 ± 0.03‰ for δ⁵⁷Fe based on nine measurements from different analytical sessions on the same dissolution. This value is in good agreement with previously published values [*Millet et al.*, 2012; *Hibbert et al.*, 2012; *Sossi et al.*, 2015], which notably were carried out at both high-resolution and low-resolution modes on Nu Plasma and Thermo Neptune instruments.

3.3. Zn Isotope Measurements

The method used for the chemical purification of Zn is based on that of *Moynier et al.* [2006], adapted by *Pons et al.* [2011]. Depending on the Zn concentration of samples, between 30 and 50 mg of rock powder was digested in a 2:1 mix of concentrated HF-HNO₃ in 7 mL PTFE Teflon square body beakers with wrench top closures in an oven at 165°C for 3 days. As Zn is likely to partition into the fluoride phase as ZnF₂, it is important that all fluorides are fully decomposed prior to column separation, and this was achieved by repeated refluxes of the sample residue in 6 M and concentrated HCl. All samples were visually inspected for the presence of fluorides before being evaporated to dryness and brought back into solution in 1.5 M HBr, ready for column chemistry.

Quantitative separation of Zn from matrix elements was achieved using Teflon shrink fit columns filled with 0.5 mL of Biorad AG1-X4 anion exchange resin. The resin was cleaned on the column by four repeated passes of 0.5 M HNO₃ and Milli-Q (MQ) ultrapure (18.2 MΩ) H₂O, before conditioning in 3 mL of 1.5 M HBr. The sample solution was then added to the column and the matrix eluted in 3 mL of 1.5 M HBr. Zn was collected from the column in 0.5 M HNO₃. To ensure total separation of Zn from matrix elements, this column separation procedure was repeated twice. With the exception of the HBr, which was purchased from ROMIL Ltd. at ultra pure "UpA" grade, all reagents were distilled by subboiling in Teflon stills at Durham University. The total procedural blank is <20 ng of Zn, which is negligible compared to the >2 μg of sample Zn processed.

Isotope ratio measurements were performed on a Thermo Scientific Neptune Plus MC-ICPMS at Durham University running in low-resolution mode. Samples were introduced via an ESI PFA 50 $\mu\text{L}/\text{min}$ nebulizer attached to an ESI cinnabar glass spray chamber. Sample solutions were run at a concentration of 750 ppb Zn in 0.5 M HNO_3 , this typically gives signal intensities of $\sim 3\text{--}4$ V on ^{64}Zn . To correct for the effect of instrumental mass bias a combined standard-sample bracketing and empirical external normalization method was adopted. This method applies an external normalization correction [Maréchal *et al.*, 1999; Mason *et al.*, 2004; Chen *et al.*, 2009] by doping both sample and standard solutions with a pure Cu solution (Alfa-Aesar) at a Zn/Cu ratio of 3/1. In addition, each sample analysis was bracketed against measurement of Alfa-Aesar pure Zn standard solution, which had been matched to the same concentration as the sample. During analysis, the masses of ^{63}Cu , ^{64}Zn , ^{65}Cu , ^{66}Zn , ^{67}Zn , and ^{68}Zn were collected, as well as ^{62}Ni to correct, using Ni natural abundances, for ^{64}Ni that is isobaric on ^{64}Zn . In all cases no online or off-line Ni correction was performed, as the calculated contribution of ^{64}Ni to the 64 mass peaks was always lower than 0.5% of the total beam intensity.

The Zn isotope composition of the sample is presented as a delta value in permil notation relative to the JMC-Lyon isotopic standard.

$$\delta^{66}\text{Zn} = \left(\frac{{}^{66}\text{Zn}/{}^{64}\text{Zn}_{\text{sample}}}{{}^{66}\text{Zn}/{}^{64}\text{Zn}_{\text{JMC-Lyon}}} - 1 \right) \times 1000$$

Due to a limited supply of the JMC-Lyon standard solution, samples were measured relative to an Alfa-Aesar pure Zn solution. This standard is offset from JMC-Lyon by 0.27‰ for $\delta^{66}\text{Zn}$ (2sd = 0.04‰ ; $n = 87$; over four different analytical sessions); as such we were able to correct our measured value by this factor and present our data relative to JMC-Lyon, as is widely accepted. Precision and accuracy were assessed using the international rock reference material, USGS BCR-2. This rock was processed through chemistry alongside sample powders and measured during analytical sessions. The value obtained for $\delta^{66}\text{Zn}$ was $+0.30\text{‰} \pm 0.04\text{‰}$ based on five measurements of the same sample aliquot during two analytical sessions. This value agrees well with published results of BCR-2 [Herzog *et al.*, 2009; Moeller *et al.*, 2012].

4. Results

4.1. Major and Trace Element Data

Major and trace element data for all samples analyzed in this study are given in the supporting information Table A1. With respect to Figures 2b and 2c, it is apparent that the range in Mg# ($[\text{Mg}_{\text{Moles}}]/([\text{Mg}_{\text{Moles}}] + [\text{Fe}_{\text{Moles}}])$) (51–84), MgO (5.6–14.3 wt %), FeO (4.1–9.6 wt %), and Ni (45–385 ppm) is consistent with the fields defined for gabbronorite, gabbro, and olivine gabbro by previous work [Godard *et al.*, 2009], with the majority of samples falling within the gabbro field. The Ca# ($[\text{Ca}_{\text{Moles}}]/([\text{Ca}_{\text{Moles}}] + [\text{Na}_{\text{Moles}}])$) of the analyzed samples are lower than those of seafloor oceanic gabbros (Figure 2a), with a range between 36 and 73.

The major element composition of the metasediments (RV5 and CP1) and metasomatic contact zone (CE8a) from Queyras is not shown but presented alongside the data for the metabasalt and metagabbros samples in supporting information Table A1. With the exception of SiO_2 , CaO, and Na_2O , the two metasediment samples are broadly similar to estimates of the mean major element composition of global subducted sediments [Plank and Langmuir, 1998]. The metasomatic contact zone (CE8a) is best compared directly to metagabbros from the same meta-ophiolite (CE7 and CE12). Relative to these samples CE8a shows depletion in SiO_2 (37.1 wt %), Al_2O_3 (11.3 wt %), CaO (10.4 wt %), K_2O (<0.1 wt %), and Na_2O (2.5 wt %), while it is enriched in Fe_2O_3 (23.9 wt %), TiO_2 (3.9 wt %), MnO (0.4 wt %), and P_2O_5 (0.3 wt %) and a consistent MgO concentration (8.4 wt %).

Trace element data are presented for all of the samples used for this study, grouped by locality, in the form of multielement spidergrams (Figure 3). Where available, relevant published data are presented alongside our sample data for comparison. The Chenaillet metagabbros elemental patterns (PR1 and PR4) are in good agreement with previous studies [e.g., Chalot-Prat, 2005] (Figure 3a). They are characterized by a relatively flat trace element profile ($\text{Ce}_N/\text{Y}_N = 0.8\text{--}1.4$; N: primitive mantle normalized), with notable depletions in Li ($\text{Li}_N/\text{Y}_N = 0.2\text{--}0.3$) and an enrichment in Sr ($\text{Sr}_N/\text{Nd}_N = 1.5\text{--}2.9$). The blueschist facies metagabbros (CE7, CE12, QE1, QE10, RV7, TR6, TR9, and BB1) (Figure 3b) and metasomatic contact (CE8a) (Figure 3c) from the Queyras display similar trace element patterns to those of Chenaillet samples, but show significant

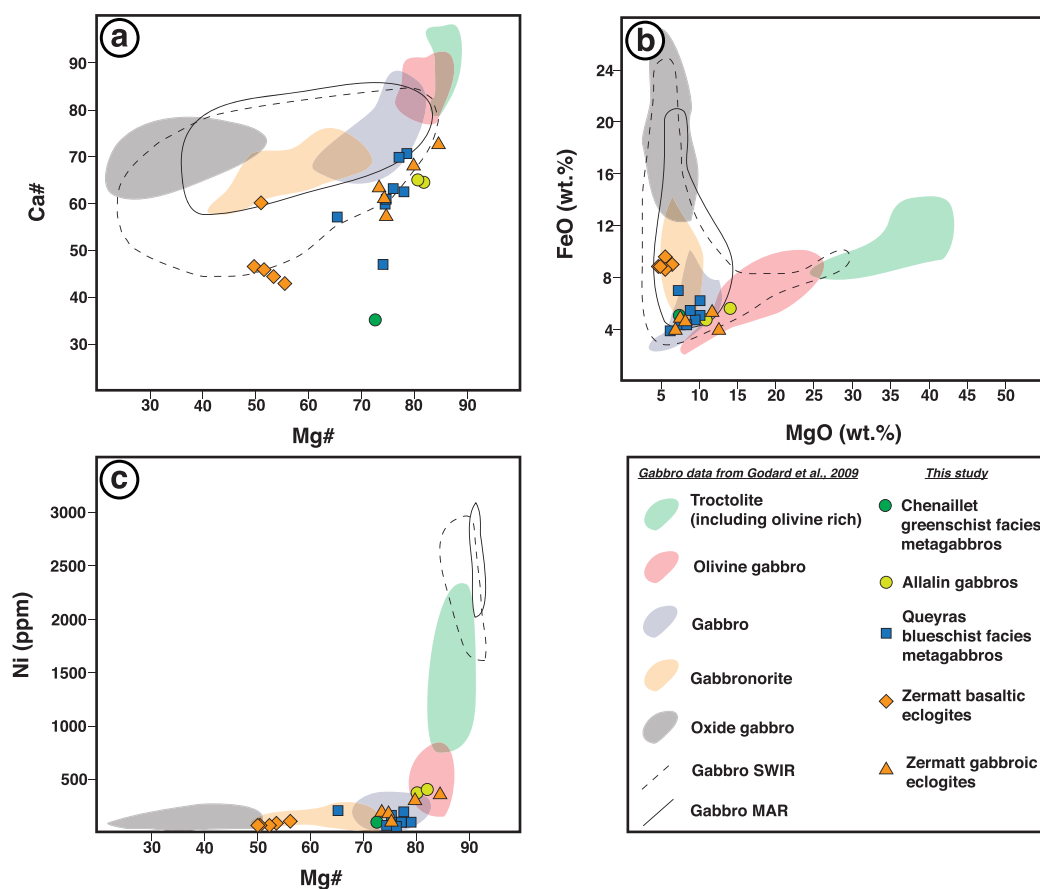


Figure 2. Major element plots of the metagabbroic and metabasaltic samples analyzed as part of this study. The samples are compared to the fields for oceanic gabbros defined by Godard *et al.* [2009]. Ca# is defined as $\text{Ca}_{\text{TOT}} [\text{mol}] / \text{Ca}_{\text{TOT}} [\text{mol}] + \text{Na}_{\text{TOT}} [\text{mol}]$ and Mg# as $\text{Mg}_{\text{TOT}} [\text{mol}] / \text{Mg}_{\text{TOT}} [\text{mol}] + \text{Fe}_{\text{TOT}} [\text{mol}]$. The field defined by the black dashed line is compiled data from Mid-Atlantic Ridge gabbros, while the field defined by the black solid line is compiled data from South-West Indian Ridge gabbros. Both of these compilations are taken from Godard *et al.* [2009].

enrichment in fluid mobile elements (e.g., $\text{Sb}_N/\text{Pr}_N = 1.3\text{--}42.3$, $\text{B}_N/\text{K}_N = 1.5\text{--}30.5$, and $\text{Li}/\text{Li}^* = 1.8\text{--}25.8$; supporting information Table A1).

The trace element profiles for the Zermatt-Saas samples are presented in Figures 3d and 3e. The two samples from the Allalin gabbro are plotted alongside additional data from Dale *et al.* [2007] and compared to the Chenaillet metagabbros (grey field). All of the Allalin gabbros display trace element profiles that are consistent with each other, but are overall of lower concentrations than the patterns of the Chenaillet metagabbros. The trace element profiles are characterized by an enrichment in LREE relative to HREE ($\text{La}_N/\text{Lu}_N = 2.2\text{--}3.3$), positive anomalies in Sr ($\text{Sr}_N/\text{Nd}_N = 21.3\text{--}22$), Ba ($\text{Ba}_N/\text{Th}_N = 25.7\text{--}49.1$), and Eu ($\text{Eu}_N/\text{Ti}_N = 3.5\text{--}3.8$) and negative anomalies in U ($\text{U}_N/\text{K}_N = 0.1$) and Nb ($\text{Nb}_N/\text{La}_N = 0.1$). The Zermatt gabbroic eclogites (Figure 3e) display similar trace element patterns to that of the Allalin gabbros (Figure 3d), with positive anomalies in Sr ($\text{Sr}_N/\text{Nd}_N = 2.7\text{--}25.5$), Eu ($\text{Eu}_N/\text{Ti}_N = 2.2\text{--}3.9$), and Ba ($\text{Ba}_N/\text{Th}_N = 2\text{--}9.5$) and depletions in Rb ($\text{Rb}_N/\text{Ba}_N = 0.29\text{--}0.3$) and Nb ($\text{Nb}_N/\text{La}_N = 0.1\text{--}0.4$). The basaltic eclogites from Zermatt are shown in Figure 3f. With the exception of K, they show consistent profiles for all elements, this is marked by broadly flat lying profile between LREE to HREE ($\text{La}_N/\text{Lu}_N = 1.5\text{--}2.1$) and varying depletions in Ba ($\text{Ba}_N/\text{Th}_N = 0.01\text{--}0.6$), Sr ($\text{Sr}_N/\text{Nd}_N = 0.5\text{--}0.7$), and Li ($\text{Li}_N/\text{Y}_N = 0.6\text{--}1$).

4.2. Fe and Zn Stable Isotopes

The whole-rock Fe isotope compositions are reported as $\delta^{56}\text{Fe}$ and all errors as two standard deviations (2sd) of repeat analyses of the same sample aliquot. The $\delta^{56}\text{Fe}$ values are presented in the supporting information Table A2. The range of $\delta^{56}\text{Fe}$ values for all samples analyzed here is between $-0.02 \pm 0.03\text{‰}$ and $+0.30 \pm 0.06\text{‰}$. The only greenschist facies metagabbro from the Chenaillet that has been analyzed for Fe

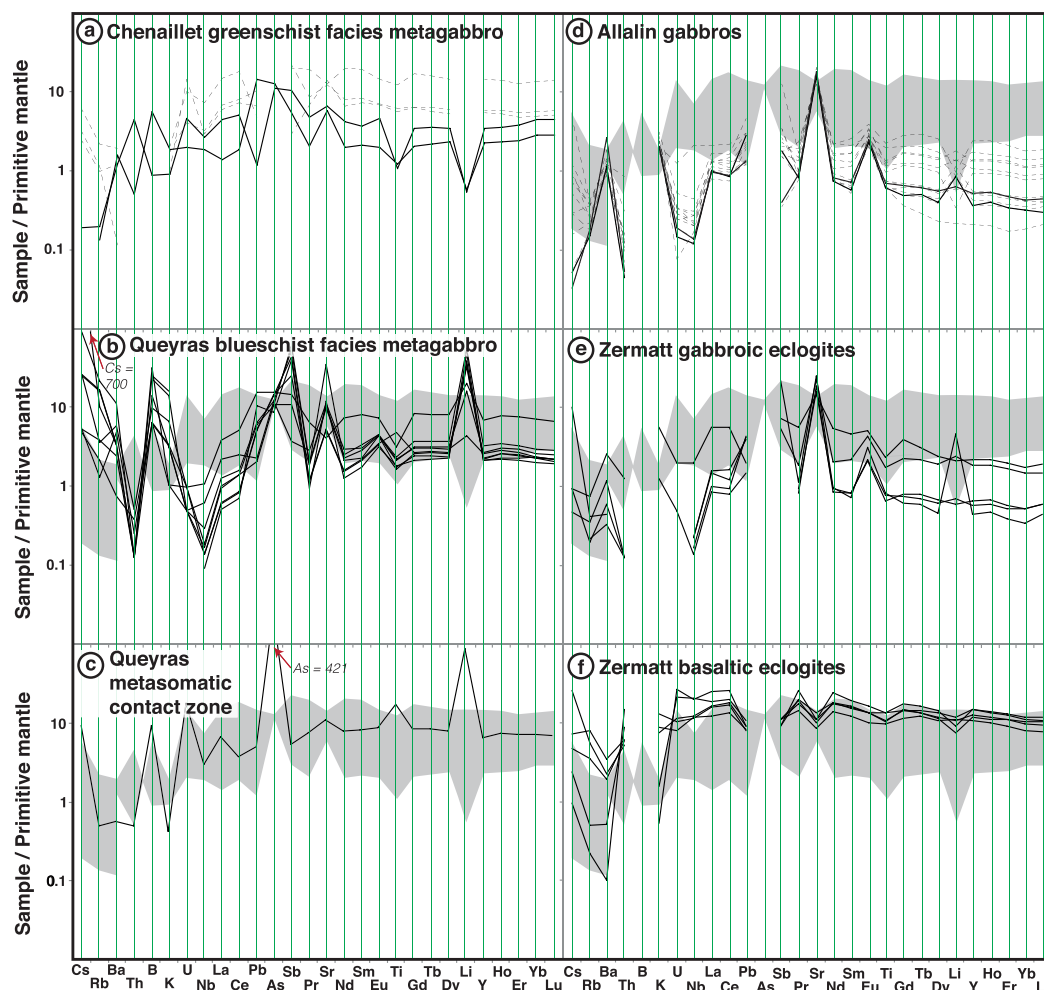


Figure 3. Multi-element spidergrams of selected elements for samples analyzed as part of this study. Elements are arranged along the horizontal axis according to degree of compatibility. The grey field shown in Figure 3b–3f outline the “oceanic field” compiled from the Chenaillet metagabbros. Solid black lines denote samples used as part of this study. Dashed black lines represent literature data of comparable samples. The dashed black lines in Figure 3a are metagabbro data for the Chenaillet taken from *Charlot-Prat et al.* [2005], while the dashed black lines in Figure 3d are literature data for the Allalin gabbros taken from *Dale et al.* [2007]. Breaks in the sample profiles indicate elements that were not analyzed. The primitive mantle normalization factors are taken from *McDonough and Sun* [1995].

isotopes (PR4) yields a $\delta^{56}\text{Fe}$ of $+0.14 \pm 0.06\text{‰}$, which is in good agreement with MORB analyzed by *Teng et al.* [2013] and other basaltic rocks [*Sossi et al.*, 2015]. The blueschist facies metagabbros from the Queyras display a range of $\delta^{56}\text{Fe}$ of between $0.00 \pm 0.06\text{‰}$ and $+0.16 \pm 0.04\text{‰}$, with no systematic covariation between metamorphic facies. The metasomatic contact zone sample, CE8a, yields the lightest $\delta^{56}\text{Fe}$ observed: $-0.02 \pm 0.03\text{‰}$. The two metasediments from the Queyras, RV5 and CP1 display $\delta^{56}\text{Fe}$ values of $+0.09 \pm 0.03\text{‰}$ and $+0.05 \pm 0.04\text{‰}$ respectively. The samples from the Zermatt-Saas ophiolite display the greatest range in Fe isotope composition ($\delta^{56}\text{Fe} = +0.03 \pm 0.04\text{‰}$ to $+0.29 \pm 0.04\text{‰}$). Of the two Allalin gabbros selected, one—S02/83viiiG, displays the heaviest $\delta^{56}\text{Fe}$ value of any of the samples ($+0.30 \pm 0.06\text{‰}$), while the other preserves a value indistinguishable from MORB ($+0.11 \pm 0.04\text{‰}$). The $\delta^{56}\text{Fe}$ values of the gabbroic eclogites from Zermatt ranges between $+0.03 \pm 0.04\text{‰}$ and $+0.29 \pm 0.04\text{‰}$, while the basaltic eclogites show similar $\delta^{56}\text{Fe}$ values ranging between $+0.05 \pm 0.07\text{‰}$ and $+0.18 \pm 0.02\text{‰}$.

The zinc isotope composition is reported as $\delta^{66}\text{Zn}$, with all errors again being given as 2sd of n . The $\delta^{66}\text{Zn}$ values of all of the samples analyzed here are presented alongside the Fe isotope compositions in the supporting information Table A2. The $\delta^{66}\text{Zn}$ values of the samples analyzed here ranges from $0.00 \pm 0.02\text{‰}$ to $+0.33 \pm 0.03\text{‰}$. As with Fe isotopes, there is no covariation between $\delta^{66}\text{Zn}$ and metamorphic facies. The greenschist facies metagabbro displays a $\delta^{66}\text{Zn}$ value of $+0.20 \pm 0.04\text{‰}$, lower than the suggested MORB

value of $+0.27 \pm 0.03\text{‰}$ [Wang *et al.*, 2017]. Significant variation is observed within the blueschist facies metagabbros, which range between $+0.03 \pm 0.02\text{‰}$ and $+0.26 \pm 0.03\text{‰}$. The metasomatic contact zone from the Queyras has a $\delta^{66}\text{Zn}$ of $+0.03 \pm 0.02\text{‰}$, while the two metasediments show $\delta^{66}\text{Zn}$ of $0.00 \pm 0.02\text{‰}$ to $+0.13 \pm 0.02\text{‰}$. Samples from Zermatt display the greatest overall range in $\delta^{66}\text{Zn}$, being between $+0.05 \pm 0.03\text{‰}$ and $+0.33 \pm 0.03\text{‰}$.

5. Discussion

The overall goal of this study is to examine the effects of prograde metamorphism and metasomatism on the Zn and Fe isotope budget of the oceanic crust. To this end we have characterized a suite of metagabbros and metabasalts from three Western Alps ophiolite complexes. These samples display different parageneses from greenschist facies in the Chenaillet massif, representative of seafloor fluid interaction and oceanic crust hydration, to blueschist facies in the Queyras complex, which shows evidence for sediment interaction during subduction, through to high-pressure eclogite facies in the Zermatt-Saas ophiolite. This transect is taken to be representative of *P-T* path for subducting oceanic lithosphere and allows us to assess the effect of subduction zone metamorphism on the mafic portion of the subducting slab [e.g., Guillot *et al.*, 2009; Schwartz *et al.*, 2013]. Furthermore, samples from the Queyras meta-ophiolites were selected as they have previously been demonstrated on the basis of strong enrichments in fluid mobile elements to have been affected by fluid metasomatism from proximal devolatilization of metasedimentary rocks [Debret *et al.*, 2016a].

5.1. The Effect of High-Pressure Metamorphism and Eclogitization of Mafic Lithologies on Fe Isotopes: Zermatt Eclogites

The basaltic eclogites from Zermatt show MORB-like $\delta^{56}\text{Fe}$ (between 0.07 and 0.14‰) [Teng *et al.*, 2013], ranging between $+0.05$ and $+0.18\text{‰}$, with an average of $+0.12 \pm 0.11\text{‰}$ (2sd, $n = 5$) suggesting that they retain their primary magmatic composition. To full examine the effect of high-pressure dehydration we present a simple Rayleigh distillation model (shown in supporting information A3), which has been calculated according to the equation below.

$$\delta_{\text{final}} - \delta_{\text{initial}} = (1000 + \delta_{\text{initial}})(F^{\alpha} - 1)$$

where δ_{final} and δ_{initial} are taken as the average Zermatt basaltic eclogite composition and the average MORB value taken from Teng *et al.* [2013], respectively. The variable *F* represents the amount of Fe removed from the rock, and α is the fractionation factor between the rock and fluid. Here we have derived the α empirically, choosing to match the modeled $\delta^{56}\text{Fe}$ to our average measured $\delta^{56}\text{Fe}$ from the Zermatt basaltic eclogites.

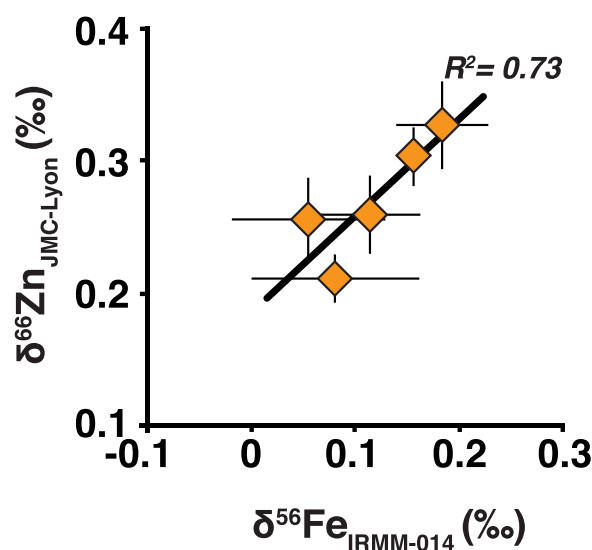


Figure 4. The strong correlation ($R^2 = 0.73$) between the $\delta^{56}\text{Fe}$ and $\delta^{66}\text{Zn}$ of the basaltic eclogites from the Zermatt-Saas suggest that both the Fe and Zn stable isotopes composition of these samples is controlled by the same process. All errors are 2sd of the mean of *n*.

Given that the solubility of Fe in aqueous Cl-poor subduction zone fluids is low [Kessel *et al.*, 2004], and considering the relatively small volume of H_2O released during eclogite facies dehydration, it can be taken that the loss of Fe would not exceed 1 wt %. Across the range of possible Fe concentrations (*F*) we show that the derived fractionation factor is insufficient to significantly perturb the whole-rock Fe isotope composition of the fully dehydrated eclogite, even with the maximum loss of Fe possible. Thus, we suggest that, owing to mass balance constraints, Fe isotopes serve as poor tracers of Fe mobility within these

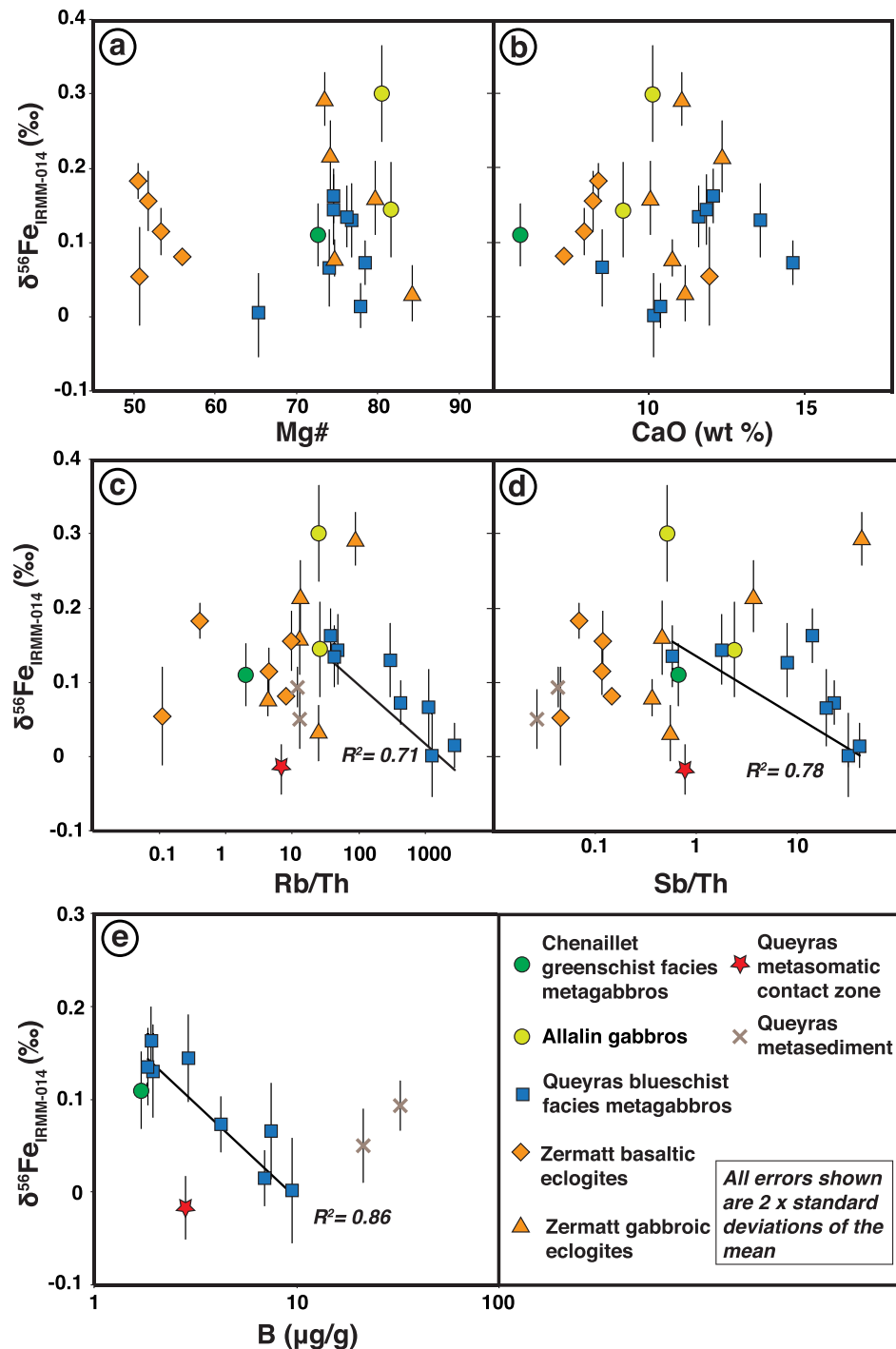


Figure 5. Iron isotope compositions ($\delta^{56}\text{Fe}$) plotted against (a, b) indices of magmatic differentiation and (c–e) fluid-rock interaction. The Queyras metasomatic contact zone and the metasediments are not plotted in Figures 5a and 5b as they have not undergone magmatic differentiation. Figures 5c and 5d present ratios of fluid mobile (Rb and Sb) and immobile (Th) elements. The linear regression lines and associated R^2 values plotted in Figures 5c–5e are for the Queyras blueschist metagabbro data only. Boron concentration data were only available for the Chenaillet and Queyras samples. Error bars represent two standard deviations of the mean of n .

particular rocks. Similarly the positive correlation ($R^2 = 0.78$) between the $\delta^{56}\text{Fe}$ and $\delta^{66}\text{Zn}$ values of basaltic eclogite (Figure 4) suggests that both isotope systems are little affected by prograde metamorphism during subduction. In agreement with this hypothesis, is the observation that $\delta^{56}\text{Fe}$ and $\delta^{66}\text{Zn}$ values of the studied eclogitic basalts show a degree of covariation with indices of magmatic differentiation such as Mg# and

CaO (Figure 2), suggesting that both the $\delta^{56}\text{Fe}$ and $\delta^{66}\text{Zn}$ in these samples are largely controlled by primary magmatic differentiation.

Many of the Zermatt metagabbro samples display $\delta^{56}\text{Fe}$ values outside of the range seen in MORB (between 0.07 and 0.14‰) [Teng *et al.*, 2013]. Although Fe isotopes can be fractionated in response to magmatic differentiation [Schuessler *et al.*, 2009; Weyer and Seitz, 2012; Teng *et al.*, 2008], there are no systematic covariations between the $\delta^{56}\text{Fe}$ of the gabbroic eclogites and any indicator of magmatic differentiation (Mg# and CaO) (Figures 5a and 5b). One possible explanation for the level of $\delta^{56}\text{Fe}$ variation observed is seafloor fluid interaction and alteration of gabbroic oceanic crust, and in particular the incorporation of isotopically light Fe into secondary alteration minerals (including hydrothermal sulfides), which leaves the residual highly altered silicate minerals enriched in heavier Fe isotopes [Rouxel *et al.*, 2003]. Although this could account for such isotopic compositions, the absence of chalcophile element enrichment within the whole rock make it unlikely that these lithologies have been affected by hydrothermal alteration and the formation of secondary sulfides. Another possibility is that Fe isotope fractionation took place during prograde metamorphism and associated metasomatism or dehydration of the Zermatt metagabbro protoliths. However, no covariation between metamorphic grade and Fe isotope composition is observed. It should be noted, however, that the gabbroic eclogite with the heaviest $\delta^{56}\text{Fe}$ (S02/85ixB) shows the most evidence for blueschist facies retrogression, and it is possible that retrograde processes could have modified the $\delta^{56}\text{Fe}$ of these samples.

5.2. Fe Isotope Fractionation in Response to Fluid Metasomatism at Blueschist Facies: The Queyras Meta-Ophiolites

A single metagabbro sample from the Chenaillet possesses a $\delta^{56}\text{Fe}$ value of $+0.11 \pm 0.04\text{‰}_{\text{oor}}$ which is in good agreement with published values obtained for MORB of between $+0.11$ and $+0.17\text{‰}_{\text{oo}}$ [Teng *et al.*, 2013]. The blueschist metagabbros from the Queyras meta-ophiolites display a similar range of Fe isotope compositions to the gabbroic eclogites from Zermatt but, on average are offset toward lighter $\delta^{56}\text{Fe}$ values, with a mean $\delta^{56}\text{Fe}$ of $+0.09 \pm 0.12\text{‰}_{\text{oor}}$ (2sd, $n = 8$) as opposed to $+0.16 \pm 0.21\text{‰}_{\text{oor}}$ (2sd, $n = 5$) for the Zermatt gabbroic eclogites.

A notable feature of the samples from the Queyras is the substantial enrichment in fluid mobile elements, such as Rb, B, Sb, and Li (Figure 3b). This enrichment is thought to result from fluid infiltration from the surrounding metasediments and the incorporation of fluid mobile elements during recrystallization under blueschist facies conditions. This type of high-pressure interaction between external fluids and surrounding lithologies, which results in the enrichment in fluid mobile elements has been noted elsewhere globally [Marshall *et al.*, 2009; Penniston-Dorland *et al.*, 2012; Vitale Brovarone and Beysac, 2014]. Consequently, it is possible to use these samples to document the effect of high-pressure fluid infiltration during subduction on the behavior of Fe (and Zn) isotopes. Owing to the low solubility of Th and B relative to Rb and Sb in aqueous fluids [e.g., Kessel *et al.*, 2005; Zack and John, 2007], we have used the ratios of Rb/Th and Sb/Th alongside elemental concentrations of B in these samples as an indicator of fluid-rock interaction occurring during subduction. A negative correlation is observed between indices of fluid-rock interaction (Rb/Th, Sb/Th, and B) and the $\delta^{56}\text{Fe}$ values of the samples (Figures 5c–5e). This correlation provides evidence for a relationship between fluid infiltration and Fe isotope systematics in the blueschist facies metagabbros in the Queyras. The perturbation of the bulk rock $\delta^{56}\text{Fe}$ by an external fluid can be accounted for by two possible mechanisms: (1) isotopically heavy Fe is preferentially complexed into the fluid and lost from the metagabbros, leaving the residual rock enriched in light Fe isotopes or (2) isotopically light Fe is transported via the external fluid and incorporated into one or more of the blueschist facies minerals that make up the metagabbros, thus enriching the bulk rock in light Fe isotopes. Mechanism 1, the loss of isotopically heavy Fe, appears unlikely, because previous work has demonstrated the preferential mobility of isotopically light Fe in slab derived dehydration fluids [Debret *et al.*, 2016b]. Specifically, it would be expected that the heavy isotopes of Fe would have a preference for Fe^{3+} complexes [Polyakov and Mineev, 2000], and the solubility of Fe^{3+} relative to Fe^{2+} in aqueous solution is known to be low [Ding and Seyfried, 1992]. Consequently, it seems much more likely that the light Fe isotope composition of the metagabbros is caused by the incorporation of externally derived low- $\delta^{56}\text{Fe}$ fluids (mechanism 2).

Fluids can acquire distinctively light Fe isotope compositions through different means. These include kinetic processes (i.e., enhanced mobility of isotopically light Fe); preferential dissolution of low- $\delta^{56}\text{Fe}$ phases; or, equilibrium partitioning, where isotopically light Fe is preferentially complexed by aqueous SO_x [Hill *et al.*, 2010] and Cl [Testemale *et al.*, 2009] ligands, as suggested to be the case for Western Alps subducted

serpentinites [Debret *et al.*, 2016b]. Because there is no observed covariation between the $\delta^{56}\text{Fe}$ and $\delta^{66}\text{Zn}$ of the blueschist facies metagabbros, we suggest that kinetic processes are not responsible, as if this was to be the case we would expect to see the two systems covary accordingly. Alternatively, it could be considered that preferential dissolution of a low- $\delta^{56}\text{Fe}$ phase within the sediments, such as a sulfide, could result in an isotopically light metasomatizing fluid. The metasediments analyzed here do show isotopically light Fe isotope compositions relative to the metagabbros from the same area, but show no evidence of sulfur bearing phase dissolution (supporting information A1 and A2). In order to test this further, we have applied a simple mass balance calculation using the equation shown below.

$$\delta^{56}\text{Fe}_{\text{mixture}} = \left(\frac{([\text{Fe}]_{\text{rock}} \times \delta^{56}\text{Fe}_{\text{rock}}) + ([\text{Fe}]_{\text{fluid}} \times \delta^{56}\text{Fe}_{\text{fluid}})}{([\text{Fe}]_{\text{rock}} + [\text{Fe}]_{\text{fluid}})} \right)$$

If we were to take the sediment composition as being representative of the fluid compositions, then mass balance suggests that we would have to add near $\sim 60\%$ of the sediment to the metagabbro reservoir to generate the lightest $\delta^{56}\text{Fe}$ observed. As this is unrealistic, we can only suggest that the Fe isotope composition of the bulk sediments analyzed does not reflect that of the fluid. Hence, we are unable to precisely identify which reaction in the metasedimentary rocks could generate a fluid with an isotopically light Fe signature. Hydrothermal fluids from mid-ocean ridges are known to be isotopically light with respect to Fe [Rouxel *et al.*, 2003, 2008; Beard *et al.*, 2003], if we were to assume that these fluids are representative of the type of fluids cycling in subduction zones, and that have been responsible for metasomatizing the metagabbros in the Queyras, the mass balance suggests that addition of $\sim 20\%$ fluid with a $\delta^{56}\text{Fe}$ of -0.5% to the metagabbro could account for the light $\delta^{56}\text{Fe}$ observed. The role of infiltrating fluids derived from other lithologies such as serpentinites could also be considered here. Indeed, it has been shown that the devolatilization of serpentinitized ultramafic rocks can release fluids enriched in isotopically light Fe and heavy Zn, interpreted to reflect the release of sulfate-bearing fluids during serpentinite devolatilization [Debret *et al.*, 2016b; Pons *et al.*, 2016]. If such fluids were to be released from proximal serpentinite bodies in the Queyras, and be the key metasomatic agent for the metagabbros here then we would expect to see a consistent, coupled Fe and Zn isotope variation. As we only see the process of fluid metasomatism reflected in the Fe isotope composition of the metagabbros, then we can only suggest that the fluids, and associated isotopically light Fe originates from the sediments.

5.3. Zn Isotope Systematics of Metabasalts and Metagabbros From the Queyras and Zermatt-Saas Ophiolites

The igneous samples (metabasalts and metagabbros) analyzed here possess $\delta^{66}\text{Zn}$ isotope compositions that range from $+0.03 \pm 0.02\%$ to $+0.30 \pm 0.02\%$, with a mean $\delta^{66}\text{Zn}$ value of $+0.21 \pm 0.16\%$ (2sd; $n = 21$). Recent work by Wang *et al.* [2017] suggests that MORB possesses a Zn isotope composition of $\delta^{66}\text{Zn} = +0.28 \pm 0.03\%$ ($n = 6$; samples from Carlsberg and North Atlantic), which is indistinguishable within error of the studied samples. The absence of any variation between Zn concentration and $\delta^{66}\text{Zn}$ within the sample set suggests that the overall $\delta^{66}\text{Zn}$ is not the result of Zn mobility during fluid loss under eclogite facies conditions. To demonstrate this we have modeled the evolution of $\delta^{66}\text{Zn}$ within the dehydrated eclogite according to the same Rayleigh distillation equation given in section 5.1, the result of which is shown in the supporting information A4. This model confirms that the solubility of Zn, even in the presence of aqueous SO_x and/or CO_x species, is too low to lead to a significant fractionation of zinc isotopes in the metabasaltic eclogites during prograde metamorphism.

In the case of the Queyras blueschist facies metagabbros, the lack of a correlation between $\delta^{66}\text{Zn}$ and fluid mobile elements (supporting information A5), suggests that the blueschist facies sediment interaction, which has affected Fe isotopes, has not perturbed the whole-rock Zn isotope systematics of these samples. However, it is possible that the external metasomatic fluid either possesses Zn concentrations that are too low to significantly affect the Zn isotope composition of the metagabbros, or else that the sediment derived fluid preserves a Zn isotope composition indistinguishable to that of the metagabbros, and owing to the mass balance this interaction is not traceable with Zn isotopes. It is notable that the metasomatic contact between metagabbros and metasedimentary rocks analyzed here preserves the lightest $\delta^{66}\text{Zn}$ ($+0.03 \pm 0.02\%$) and $\delta^{56}\text{Fe}$ ($-0.02 \pm 0.03\%$) values. Previous studies have shown that kinetic fractionation can occur along such type of metasomatic interfaces [Teng *et al.*, 2006; Marschall *et al.*, 2007; Penniston-Dorland *et al.*, 2010; Pogge von Strandman *et al.*, 2015] resulting in a decrease of isotopic values. These compositions arise from a preferential diffusive partitioning of the lighter isotopes relative to the heavier isotopes. It is thus conceivable that similar processes locally occur in the Queyras, however, further work would be required to comment on this conclusively.

Recently Zn isotopes have been shown to be sensitive to mantle partial melting [Doucet *et al.*, 2016; Wang *et al.*, 2017] and igneous differentiation [Chen *et al.*, 2013], but owing to the complex metasomatic and metamorphic history of the studied samples, coupled with the lack of a comprehensive study of Zn isotopes in global MORB and oceanic gabbros, it is difficult to conclude if the variations in Zn isotope composition observed here reflect primary magmatic process or modification by late stage alteration and metasomatic processes. While it has previously been stated that the process of low-temperature seafloor alteration of the upper, basaltic oceanic lithosphere has little effect on Zn isotopes, the same study demonstrated that high-temperature (>350°C) hydrothermal circulation and complexing of light Zn isotopes in hydrothermal fluids could drive the Zn isotope composition toward heavier $\delta^{66}\text{Zn}$ values in the gabbroic portion of the oceanic lithosphere [Huang *et al.*, 2016]. This observation could be invoked to explain the range of $\delta^{66}\text{Zn}$ values observed in the Zermatt and Queyras metagabbros, but as the samples now preserve a subduction-related, Alpine overprint to their mineralogy it is not possible to unambiguously conclude on the effect of seafloor hydrothermal activity on the Zn isotope compositions of these rocks.

5.4. Implications for Slab Dehydration and the Redox Budget of the Subarc Mantle

Mass transfer from the subducted slab can be considered with respect to three components: sediments; mafic oceanic crust, and the serpentinized slab mantle. Of these, the serpentinized slab mantle has received much attention as the main carrier of fluids into subduction zones, as hydrated peridotite can contain up to 13 wt % H_2O [Ulmer and Trommsdorff, 1995]. Indeed, the prograde dehydration of subducting serpentinites has been demonstrated to contribute significantly to the fluid budget of the subarc mantle [Scambelluri and Tonarini, 2012]. When considered with the findings of Debret *et al.* [2016b] and Pons *et al.* [2016], who show clear fractionation of both Fe and Zn stable isotopes with increasing subduction metamorphism, it is likely that serpentinite-derived fluids, in combination with sediment melts, exert a strong control on the transfer of redox mediating elements between the slab and overlying subarc-arc. This is consistent with the results of many studies that have highlighted the importance of distinct contributions from serpentinite-derived slab fluids and sediment melts in the source regions of arc lavas [e.g., Plank and Langmuir, 1993; Elliott *et al.*, 1997; Freymuth *et al.*, 2015; Nebel *et al.*, 2015; Sossi *et al.*, 2016].

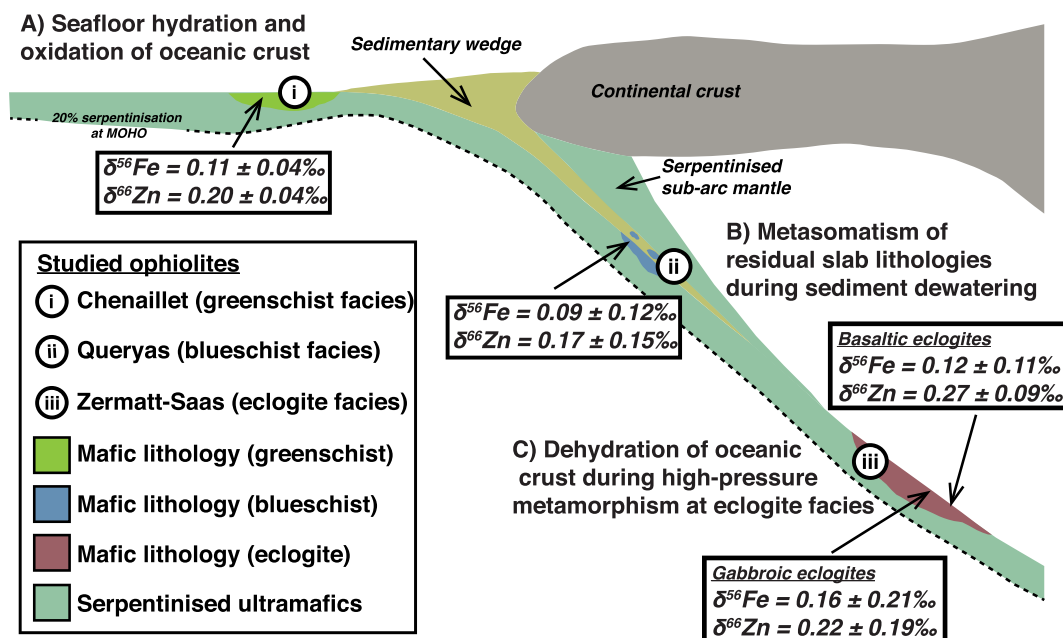


Figure 6. Schematic diagram (modified after Debret *et al.* [2016a]) showing the approximate location of the meta-ophiolites studied as part of this work: (i) Chenaillet massif; (ii) Queryas complex; and (iii) Zermatt-Saas ophiolite. Each of these meta-ophiolites has been metamorphosed under conditions representative of a subduction gradient (greenschist to blueschist to eclogite) and allows us to examine the effect of slab metamorphism and metasomatism on the mafic oceanic crust. For each of these ophiolites, the average $\delta^{56}\text{Fe}$ and $\delta^{66}\text{Zn}$ values are presented.

We have demonstrated that the effect of high-pressure subduction zone metamorphism and associated dehydration at eclogite facies, has no detectable effect on the whole-rock Fe and Zn stable isotope composition of subducted metabasalts and metagabbros (Figure 6). This is significant with respect to two aspects. First, we show that an absence of resolvable Fe isotope variation at eclogite facies, with respect to a MORB protolith, demonstrates that Fe isotopes are not fractionated in response to loss of Fe during dehydration of mafic lithologies in subduction. Secondly we show that Zn isotopes remain unfractionated, suggesting that the dehydration fluids released by the process of eclogitization are not major carriers of aqueous Zn-SO_x and/or Zn-CO_x complexes.

The results from this study, at least, suggest that high-pressure subduction zone metamorphism has no detectable effect on Fe or Zn isotope composition of the mafic lithologies within the subducting slab. Consequently, the mafic slab component that is recycled back into the mantle preserves a MORB-like Fe and Zn isotope signature.

6. Conclusions

We have analyzed a suite of metagabbros and metabasalts, which have been metamorphosed under the different conditions of a subduction zone gradient, and are taken to be representative of the mafic oceanic crust during subduction. Our data show that fluids released from subducting sediments can interact and metasomatize mafic slab lithologies. This metasomatism is capable of modifying bulk rock Fe isotope composition, with the samples displaying the most evidence for fluid interaction recording the lightest Fe isotope compositions. This is likely due to the incorporation of an isotopically light Fe component, which is derived from the associated subducted sediments. Within the same samples zinc isotopes show no evidence of being perturbed by this metasomatic process. Consequently, we conclude that Fe isotopes in subducting oceanic crust are sensitive tracers of slab metasomatism, relating to fluid released from subducting sediments.

Contrary to this it is apparent that no systematic variation in isotopic composition across metamorphic grade is observed, suggesting that the mobility of Fe during the dehydration of the mafic lithologies in subduction zones is too low to lead to significant isotopic variations within the dehydrated lithologies. Additionally our Zn isotope data demonstrate that the fluids released by these dehydration reactions are not major carriers of dissolved Zn-SO_x/CO_x complexes.

Acknowledgments

This work was supported by an ERC Starting grant (HabitablePlanet; 306655) and a NERC Deep Volatiles Consortium grant (NE/M0003/1) awarded to H.W. B.D. and M.L.P. were supported as PDRAs on the HabitablePlanet grant, while the PhD studentship to E.I. was funded as part of the same project. PB acknowledges support from ERC Starting Grant (MASE; 279828), and his Auvergne Fellowship (French Government Laboratory of Excellence initiative no. ANR-10-LABX-0006; ClerVolc contribution no. 253). M.A.M. was funded by a Durham University International Junior Fellowship. Careful and constructive reviews from Oliver Nebel, Paolo Sossi, Horst Marschall, and an anonymous reviewer greatly improved the quality of this manuscript. Janne Blichert-Toft is also acknowledged for her patient editorial handling. We thank Christian Nicollet (LMV, Clermont-Ferrand, France) for discussions in the field and for providing the metagabbro samples from the Queyras and Chenaillat ophiolites. The full major and trace element composition of all of the samples presented in this study can be found within the supporting information. The Fe and Zn isotope data are also included within the supporting information.

References

- Angiboust, S., P. Agard, L. Jolivet, and O. Beyssac (2009), The Zermatt-Saas ophiolite: The largest (60-km wide) and deepest (c. 70–80 km) continuous slice of oceanic lithosphere detached from a subduction zone?, *Terra Nova*, 21(3), 171–180.
- Beard, B. L., C. M. Johnson, K. L. Von Damm, and R. L. Poulson (2003), Iron isotope constraints on Fe cycling and mass balance in oxygenated Earth oceans, *Geology*, 31(7), pp. 629–632.
- Bernoulli, D., G. Manatschal, L. Desmurs, and O. Muntener (2003), Where did Gustav Steinmann see the trinity? Back to the roots of an Alpine ophiolite concept, *Geol. Soc. Am. Spec. Pap.*, 373, 93–110.
- Black, J. R., A. Kavner, and E. A. Schauble (2011), Calculation of equilibrium stable isotope partition function ratios for aqueous zinc complexes and metallic zinc, *Geochim. Cosmochim. Acta*, 75(3), 769–783.
- Bouilhol, P., V. Magni, J. van Hunen, and L. Kaislaniemi (2015), A numerical approach to melting in warm subduction zones, *Earth Planet. Sci. Lett.*, 411, 37–44.
- Brandon, A. D., and D. S. Draper (1996), Constraints on the origin of the oxidation state of mantle overlying subduction zones: An example from Simcoe, Washington, USA, *Geochim. Cosmochim. Acta*, 60(10), 1739–1749.
- Brouwer, F. M., D. M. A. Van De Zedde, M. J. R. Wortel, and R. L. M. Vissers (2004), Late-orogenic heating during exhumation: Alpine PTt trajectories and thermomechanical models, *Earth Planet. Sci. Lett.*, 220(1), 185–199.
- Bucher, K., and R. Grapes (2009), The eclogite-facies Allalin Gabbro of the Zermatt-Saas ophiolite, Western Alps: A record of subduction zone hydration, *J. Petrol.*, 50(8), 1405–1442.
- Bucher, K., Y. Fazis, C. D. Capitani, and R. Grapes (2005), Blueschists, eclogites, and decompression assemblages of the Zermatt-Saas ophiolite: High-pressure metamorphism of subducted Tethys lithosphere, *Am. Mineral.*, 90(5–6), 821–835.
- Caby, R. (1995), Plastic deformation of gabbros in a slow-spreading Mesozoic ridge: Example of the Montgenevre ophiolite, Western Alps, in *Mantle and Lower Crust Exposed in Oceanic Ridges and in Ophiolites*, pp. 123–145, Springer, Netherlands.
- Chalot-Prat, F. (2005), An undeformed ophiolite in the Alps: Field and geochemical evidence for a link between volcanism and shallow plate tectonic processes, *Geol. Soc. Am. Spec. Pap.*, 388, 751–780.
- Chen, H., P. S. Savage, F. Z. Teng, R. T. Helz, and F. Moynier (2013), Zinc isotope fractionation during magmatic differentiation and the isotopic composition of the bulk Earth, *Earth Planet. Sci. Lett.*, 369, 34–42.
- Chen, J., J. Gaillardet, P. Louvat, and S. Huon (2009), Zn isotopes in the suspended load of the Seine River, France: Isotopic variations and source determination, *Geochim. Cosmochim. Acta*, 73(14), 4060–4076.
- Dale, C. W., A. Gannoun, K. W. Burton, T. W. Argles, and I. J. Parkinson (2007), Rhenium–osmium isotope and elemental behaviour during subduction of oceanic crust and the implications for mantle recycling, *Earth Planet. Sci. Lett.*, 253(1), 211–225.

- Dale, C. W., K. W. Burton, D. G. Pearson, A. Gannoun, O. Alard, T. W. Argles, and I. J. Parkinson (2009), Highly siderophile element behaviour accompanying subduction of oceanic crust: Whole rock and mineral-scale insights from a high-pressure terrrain, *Geochim. Cosmochim. Acta*, 73(5), 1394–1416.
- Dauphas, N., P. R. Craddock, P. D. Asimow, V. C. Bennett, A. P. Nutman, and D. Ohnenstetter (2009), Iron isotopes may reveal the redox conditions of mantle melting from Archean to Present, *Earth Planet. Sci. Lett.*, 288(1), 255–267.
- Dauphas, N., M. Roskosz, E. E. Alp, D. R. Neuville, M. Y. Hu, C. K. Sio, and F. L. H. Tissot (2014), Magma redox and structural controls on iron isotope variations in Earth's mantle and crust, *Earth Planet. Sci. Lett.*, 398, 127–140.
- Debret, B., C. Nicollet, M. Andreani, S. Schwartz, and M. Godard (2013), Three steps of serpentinization in an eclogitized oceanic serpentinitization front (Lanzo Massif–Western Alps), *J. Metamorph. Geol.*, 31(2), 165–186.
- Debret, B., K. T. Koga, F. Cattani, C. Nicollet, G. Van den Bleeken, and S. Schwartz (2016a), Volatile (Li, B, F and Cl) mobility during amphibole breakdown in subduction zones, *Lithos*, 244, 165–181.
- Debret, B., M. A. Millet, M. L. Pons, P. Bouilhol, E. Inglis, and H. Williams (2016b), Isotopic evidence for iron mobility during subduction, *Geology*, 44(3), 215–218.
- Ding, K., and W. E. Seyfried (1992), Determination of Fe-Cl complexing in the low pressure supercritical region (NaCl fluid): Iron solubility constraints on pH of seafloor hydrothermal fluids, *Geochim. Cosmochim. Acta*, 56(10), 3681–3692.
- Doucet, L. S., N. Mattielli, D. A. Ionov, W. Debouge, and A. V. Golovin (2016), Zn isotopic heterogeneity in the mantle: A melting control?, *Earth Planet. Sci. Lett.*, 451, 232–240.
- Elliott, T., T. Plank, A. Zindler, W. White, and B. Bourdon (1997), Element transport from slab to volcanic front at the Mariana arc, *J. Geophys. Res.*, 102(B7), 14,991–15,019.
- Evans, B. W., V. Trommsdorff, and W. Richter (1979), Petrology of an eclogite-metarodngite suite at Cima di Gagnone, Ticino, Switzerland, *Am. Mineral.*, 64(1–2), 15–31.
- Evans, K. A. (2012), The redox budget of subduction zones, *Earth Sci. Rev.*, 113(1), 11–32.
- Fitton, J. G., A. D. Saunders, L. M. Larsen, B. S. Hardarson, and M. J. Norry (1998), Volcanic rocks from the southeast Greenland margin at 63°N: composition, petrogenesis, and mantle sources, edited by A. D. Saunders, H. C. Larsen, and S. W. Wise, Jr., pp. 331–350, *Proc. ODP, Sci. Results*, 152, Ocean Drill. Program, College Station, Tex.
- Foley, S. F., M. G. Barth, and G. A. Jenner (2000), Rutile/melt partition coefficients for trace elements and an assessment of the influence of rutile on the trace element characteristics of subduction zone magmas, *Geochim. Cosmochim. Acta*, 64(5), 933–938.
- Freyruth, H., F. Vils, M. Willbold, R. N. Taylor, and T. Elliott (2015), Molybdenum mobility and isotopic fractionation during subduction at the Mariana arc, *Earth Planet. Sci. Lett.*, 432, 176–186.
- Frezzotti, M. L., J. Selverstone, Z. D. Sharp, and R. Compagnoni (2011), Carbonate dissolution during subduction revealed by diamond-bearing rocks from the Alps, *Nat. Geosci.*, 4(10), 703–706.
- Frost, B. R., and C. Ballhaus (1998), Comment on "Constraints on the origin of the oxidation state of mantle overlying subduction zones: An example from Simcoe, Washington, USA" by A. D. Brandon and D. S. Draper, *Geochim. Cosmochim. Acta*, 62, 329–332.
- Fujii, T., F. Moynier, M. L. Pons, and F. Albarède (2011), The origin of Zn isotope fractionation in sulfides, *Geochim. Cosmochim. Acta*, 75(23), 7632–7643.
- Godard, M., et al. (2009), Geochemistry of a long in-situ section of intrusive slow-spread oceanic lithosphere: Results from IODP Site U1309 (Atlantis Massif, 30 N Mid-Atlantic-Ridge), *Earth Planet. Sci. Lett.*, 279(1), 110–122.
- Govindaraju, K. (1994), Compilation of working values and sample descriptions for 383 geostandards, *Geostand. Newsl.*, 18, 1–55.
- Guillot, S., K. Hattori, P. Agard, S. Schwartz, and O. Vidal (2009), Exhumation processes in oceanic and continental subduction contexts: A review, in *Subduction Zone Geodynamics*, pp. 175–205, Springer, Berlin Heidelberg.
- Hawkesworth, C. J., K. Gallagher, J. M. Hergt, and F. McDermott (1993), Mantle and slab contribution in arc magmas, *Annu. Rev. Earth Planet. Sci.*, 21, 175–204.
- Hensen, C., K. Wallmann, M. Schmidt, C. R. Ranero, and E. Suess (2004), Fluid expulsion related to mud extrusion off Costa Rica—A window to the subducting slab, *Geology*, 32(3), 201–204.
- Hermann, J., and D. H. Green (2001), Experimental constraints on high pressure melting in subducted crust, *Earth Planet. Sci. Lett.*, 188(1), 149–168.
- Hermann, J., O. Müntener, and M. Scambelluri (2000), The importance of serpentinite mylonites for subduction and exhumation of oceanic crust, *Tectonophysics*, 327(3), 225–238.
- Hermann, J., C. Spandler, A. Hack, and A. V. Korsakov (2006), Aqueous fluids and hydrous melts in high-pressure and ultra-high pressure rocks: Implications for element transfer in subduction zones, *Lithos*, 92(3), 399–417.
- Herzog, G. F., F. Moynier, F. Albarède, and A. A. Berezhnoy (2009), Isotopic and elemental abundances of copper and zinc in lunar samples, Zagami, Pele's hairs, and a terrestrial basalt, *Geochim. Cosmochim. Acta*, 73(19), 5884–5904.
- Hibbert, K. E. J., H. M. Williams, A. C. Kerr, and I. S. Puchtel (2012), Iron isotopes in ancient and modern komatiites: Evidence in support of an oxidised mantle from Archean to present, *Earth Planet. Sci. Lett.*, 321, 198–207.
- Hill, P. S., E. A. Schauble, and E. D. Young (2010), Effects of changing solution chemistry on Fe³⁺/Fe²⁺ isotope fractionation in aqueous Fe-Cl solutions, *Geochim. Cosmochim. Acta*, 74(23), 6669–6689.
- Huang, J., S.-A. Liu, Y. Gao, Y. Xiao, and S. Chen (2016), Copper and zinc isotope systematics of altered oceanic crust at IODP Site 1256 in the eastern equatorial Pacific, *J. Geophys. Res. Solid Earth*, 121, 7086–7100, doi:10.1002/2016JB013095.
- Kelley, K. A., and E. Cottrell (2009), Water and the oxidation state of subduction zone magmas, *Science*, 325(5940), 605–607.
- Kessel, R., P. Ulmer, T. Pettke, M. W. Schmidt, and A. B. Thompson (2004), A novel approach to determine high-pressure high-temperature fluid and melt compositions using diamond-trap experiments, *Am. Mineral.*, 89(7), 1078–1086.
- Kessel, R., M. W. Schmidt, P. Ulmer, and T. Pettke (2005), Trace element signature of subduction-zone fluids, melts and supercritical liquids at 120–180 km depth, *Nature*, 437(7059), 724–727.
- Konter, J. G., A. J. Pietruszka, B. B. Hanan, V. A. Finlayson, P. R. Craddock, M. G. Jackson, and N. Dauphas (2016), Unusual $\delta^{56}\text{Fe}$ values in Samoan rejuvenated lavas generated in the mantle, *Earth Planet. Sci. Lett.*, 450, 221–232.
- Lagabrielle, Y., and M. Cannat (1990), Alpine Jurassic ophiolites resemble the modern central Atlantic basement, *Geology*, 18(4), 319–322.
- Lagabrielle, Y., et al. (1984), Les témoins d'une tectonique intra-océanique dans le domaine téthysien: Analyse des rapports entre les ophiolites et leurs couvertures métasédimentaires dans la zone piémontaise des Alpes franco-italiennes, *Ofoliti*, 9, 67–88.
- Lagabrielle, Y., S. Fudraland, and J. R. Kienast (1990), La couverture océanique des ultrabasites de Lanzo (Alpes occidentales): Arguments lithostratigraphiques et pétrologiques, *Geodin. Acta*, 4(1), 43–55.
- Lagabrielle, Y., A. Vitale Brovarone, and B. Ildefonse (2015), Fossil oceanic core complexes recognized in the blueschist metaophiolites of Western Alps and Corsica, *Earth Sci. Rev.*, 141, 1–26.

- Lemoine, M., P. Tricart, and G. Boillot (1987), Ultramafic and gabbroic ocean floor of the Ligurian Tethys (Alps, Corsica, Apennines): In search of a genetic imodel, *Geology*, *15*(7), 622–625.
- Magni, V., P. Bouilhol, and J. van Hunen (2014), Deep water recycling through time, *Geochem. Geophys. Geosyst.*, *15*, 4203–4216, doi: 10.1002/2014GC005525.
- Manatschal, G., D. Sauter, A. M. Karpoff, E. Masini, G. Mohn, and Y. Lagabrielle (2011), The Chenaillet ophiolite in the French/Italian Alps: An ancient analogue for an oceanic core complex?, *Lithos*, *124*(3), 169–184.
- Maréchal, C. N., P. Télouk, and F. Albarède (1999), Precise analysis of copper and zinc isotopic compositions by plasma-source mass spectrometry, *Chem. Geol.*, *156*(1), 251–273.
- Marschall, H. R., P. A. E. Pogge von Strandmann, H.-M. Seitz, T. Elliott, and Y. Niu (2007), The lithium isotopic composition of orogenic eclogites and deep subducted slabs, *Earth Planet. Sci. Lett.*, *262*(3), 563–580.
- Marschall, H. R., R. Altherr, K. Gmélung, and Z. Kasztovszky (2009), Lithium, boron and chlorine as tracers for metasomatism in high-pressure metamorphic rocks: A case study from Syros (Greece), *Mineral. Petrol.*, *95*(3–4), 291–302.
- Mason, T. F., D. J. Weiss, M. Horstwood, R. R. Parrish, S. S. Russell, E. Mullane, and B. J. Coles (2004), High-precision Cu and Zn isotope analysis by plasma source mass spectrometry. Part 2. Correcting for mass discrimination effects, *J. Anal. At. Spectrom.*, *19*(2), 218–226.
- McDonough, W. F., and S. S. Sun (1995), The composition of the Earth, *Chem. Geol.*, *120*(3), 223–253.
- Mevel, C., R. Caby, and J. R. Kienast (1978), Amphibolite facies conditions in the oceanic crust: Example of amphibolitized fiaser-gabbro and amphibolites from the Chenaillet ophiolite massif (Hautes Alpes, France), *Earth Planet. Sci. Lett.*, *39*(1), 98–108.
- Meyer, J. (1983), The development of the high-pressure metamorphism in the Allalin metagabbro (Switzerland), *Terra Cognita*, *3*(2–3), 187.
- Mikutta, C., J. G. Wiederhold, O. A. Cirpka, T. B. Hofstetter, B. Bourdon, and U. Von Gunten (2009), Iron isotope fractionation and atom exchange during sorption of ferrous iron to mineral surfaces, *Geochim. Cosmochim. Acta*, *73*(7), 1795–1812.
- Millet, M. A., J. A. Baker, and C. E. Payne (2012), Ultra-precise stable Fe isotope measurements by high resolution multiple-collector inductively coupled plasma mass spectrometry with a ^{57}Fe – ^{58}Fe double spike, *Chem. Geol.*, *304*, 18–25.
- Moeller, K., R. Schoenberg, R. B. Pedersen, D. Weiss, and S. Dong (2012), Calibration of the new certified reference materials ERM-AE633 and ERM-AE647 for copper and IRMM-3702 for zinc isotope amount ratio determinations, *Geostand. Geoanal. Res.*, *36*(2), 177–199.
- Moynier, F., F. Albarède, and G. F. Herzog (2006), Isotopic composition of zinc, copper, and iron in lunar samples, *Geochim. Cosmochim. Acta*, *70*(24), 6103–6117.
- Nebel, O., P. Z. Vroon, D. F. Wiggers de Vries, F. E. Jenner, and J. A. Mavrogenes (2010), Tungsten isotopes as tracers of core–mantle interactions: The influence of subducted sediments, *Geochim. Cosmochim. Acta*, *74*(2), 751–762.
- Nebel, O., P. A. Sossi, A. Benard, M. Wille, P. Z. Vroon, and R. J. Arculus (2015), Redox-variability and controls in subduction zones from an iron-isotope perspective, *Earth Planet. Sci. Lett.*, *432*, 142–151.
- Parkinson, I. J., and R. J. Arculus (1999), The redox state of subduction zones: Insights from arc-peridotites, *Chem. Geol.*, *160*(4), 409–423.
- Pearce, J. A. (1982), Trace element characteristics of lavas from destructive plate boundaries, *Andesites*, *8*, 525–548.
- Penniston-Dorland, S. C., S. S. Sorensen, R. D. Ash, and S. V. Khadke (2010), Lithium isotopes as a tracer of fluids in a subduction zone mélange: Franciscan Complex, CA, *Earth Planet. Sci. Lett.*, *292*(1), 181–190.
- Penniston-Dorland, S. C., G. E. Bebout, P. A. P. von Strandmann, T. Elliott, and S. S. Sorensen (2012), Lithium and its isotopes as tracers of subduction zone fluids and metasomatic processes: Evidence from the Catalina Schist, California, USA, *Geochim. Cosmochim. Acta*, *77*, 530–545.
- Plank, T., and C. H. Langmuir (1993), Tracing trace elements from sediment input to volcanic output at subduction zones, *Nature*, *362*(6422), 739–743.
- Plank, T., and C. H. Langmuir (1998), The chemical composition of subducting sediment and its consequences for the crust and mantle, *Chem. Geol.*, *145*(3), 325–394.
- Pogge von Strandmann, P. A., R. Dohmen, H. R. Marschall, J. C. Schumacher, and T. Elliott (2015), Extreme magnesium isotope fractionation at outcrop scale records the mechanism and rate at which reaction fronts advance, *J. Petrol.*, *56*(1), 33–58.
- Polyakov, V. B., and S. D. Mineev (2000), The use of Mössbauer spectroscopy in stable isotope geochemistry, *Geochim. Cosmochim. Acta*, *64*(5), 849–865.
- Pons, M. L., G. Quitté, T. Fujii, M. T. Rosing, B. Reynard, F. Moynier, C. Douchet, and F. Albarède (2011), Early Archean serpentine mud volcanoes at Isua, Greenland, as a niche for early life, *Proc. Natl. Acad. Sci. U. S. A.*, *108*(43), 17,639–17,643.
- Pons, M. L., B. Debret, P. Bouilhol, A. Delacour, and H. Williams (2016), Zinc isotope evidence for sulfate-rich fluid transfer across subduction zones, *Nat. Commun.*, *7*, 13794.
- Rouxel, O., N. Dobbek, J. Ludden, and Y. Fouquet (2003), Iron isotope fractionation during oceanic crust alteration, *Chem. Geol.*, *202*(1), 155–182.
- Rouxel, O., W. C. Shanks, W. Bach, and K. J. Edwards (2008), Integrated Fe- and S-isotope study of seafloor hydrothermal vents at East Pacific Rise 910 N, *Chem. Geol.*, *252*(3), 214–227.
- Rubatto, D., D. Gebauer, and M. Fanning (1998), Jurassic formation and Eocene subduction of the Zermatt–Saas-Fee ophiolites: Implications for the geodynamic evolution of the Central and Western Alps, *Contrib. Mineral. Petrol.*, *132*(3), 269–287.
- Rüpke, L. H., J. P. Morgan, M. Hort, and J. A. Connolly (2004), Serpentine and the subduction zone water cycle, *Earth Planet. Sci. Lett.*, *223*(1), 17–34.
- Scambelluri, M., and P. Philippot (2001), Deep fluids in subduction zones, *Lithos*, *55*(1), 213–227.
- Scambelluri, M., E. Rampono, and G. B. Piccardo (2001), Fluid and element cycling in subducted serpentinite: A trace-element study of the Erro–Tobbio high-pressure ultramafites (Western alps, NW Italy), *J. Petrol.*, *42*(1), 55–67.
- Scambelluri, M., T. Pettke, E. Rampono, M. Godard, and E. Reusser (2014), Petrology and trace element budgets of high-pressure peridotites indicate subduction dehydration of serpentinitized mantle (Cima di Gagnone, Central Alps, Switzerland), *J. Petrol.*, *55*(3), 459–498.
- Scambelluri, M., and S. Tonarini (2012), Boron isotope evidence for shallow fluid transfer across subduction zones by serpentinitized mantle, *Geology*, *40*(10), 907–910.
- Schauble, E. A. (2004), Applying stable isotope fractionation theory to new systems, *Rev. Mineral. Geochem.*, *55*, 65–102.
- Schmidt, M. W., and S. Poli (2014), Devolatilisation during subduction, in *The Crust, Treatise on Geochemistry*, edited by H. D. Holland and K. K. Turekian, pp. 669–701, Elsevier-Pergamon, Oxford, U. K.
- Schuessler, J. A., R. Schoenberg, and O. Sigmarsson (2009), Iron and lithium isotope systematics of the Hekla volcano, Iceland—Evidence for Fe isotope fractionation during magma differentiation, *Chem. Geol.*, *258*(1), 78–91.
- Schwartz, S., S. Guillot, B. Reynard, R. Lafay, B. Debret, C. Nicollet, P. Lanari, and A. L. Auzende (2013), Pressure–temperature estimates of the lizardite/antigorite transition in high pressure serpentinites, *Lithos*, *178*, 197–210.

- Sossi, P. A., G. P. Halverson, O. Nebel, and S. M. Eggin (2015), Combined separation of Cu, Fe and Zn from rock matrices and improved analytical protocols for stable isotope determination, *Geostand. Geoanal. Res.*, *39*(2), 129–149.
- Sossi, P. A., O. Nebel, and J. Foden (2016), Iron isotope systematics in planetary reservoirs, *Earth Planet. Sci. Lett.*, *452*, 295–308.
- Teng, F.-Z., W. F. McDonough, R. L. Rudnick, and R. J. Walker (2006), Diffusion-driven extreme lithium isotopic fractionation in country rocks of the Tin Mountain pegmatite, *Earth Planet. Sci. Lett.*, *243*(3), 701–710.
- Teng, F. Z., N. Dauphas, and R. T. Helz (2008), Iron isotope fractionation during magmatic differentiation in Kilauea Iki lava lake, *Science*, *320*(5883), 1620–1622.
- Teng, F. Z., N. Dauphas, R. T. Helz, S. Gao, and S. Huang (2011), Diffusion-driven magnesium and iron isotope fractionation in Hawaiian olivine, *Earth Planet. Sci. Lett.*, *308*(3), 317–324.
- Telus, M., N. Dauphas, F. Moynier, F. L. Tissot, F. Z. Teng, P. I. Nabelek, P. R. Craddock, and L. A. Groat (2012), Iron, zinc, magnesium and uranium isotopic fractionation during continental crust differentiation: The tale from migmatites, granulites, and pegmatites, *Geochim. Cosmochim. Acta*, *97*, 247–265.
- Teng, F. Z., N. Dauphas, S. Huang, and B. Marty (2013), Iron isotopic systematics of oceanic basalts, *Geochim. Cosmochim. Acta*, *107*, 12–26.
- Testemale, D., J. Brugger, W. Liu, B. Etschmann, and J. L. Hazemann (2009), In-situ X-ray absorption study of iron (II) speciation in brines up to supercritical conditions, *Chem. Geol.*, *264*(1), 295–310.
- Tricart, P. (1984), From passive margin to continental collision; a tectonic scenario for the Western Alps, *Am. J. Sci.*, *284*(2), 97–120.
- Tricart, P., and S. Schwartz (2006), A north-south section across the Queyras Schistes lustrés (Piedmont zone, western Alps): Syn-collision refolding of a subduction wedge, *Eclogae Geol. Helv.*, *99*(3), 429–442.
- Ulmer, P., and V. Trommsdorff (1995), Serpentine stability to mantle depths and subduction-related magmatism, *Science*, *268*(5212), 858.
- Urey, H. C. (1947), The thermodynamic properties of isotopic substances, *J. Chem. Soc.*, *0*, 562–581.
- Vils, F., O. Müntener, A. Kalt, and T. Ludwig (2011), Implications of the serpentine phase transition on the behaviour of beryllium and lithium–boron of subducted ultramafic rocks, *Geochim. Cosmochim. Acta*, *75*(5), 1249–1271.
- Vitale Brovarone, A., and O. Beyssac (2014), Lawsonite metasomatism: A new route for water to the deep Earth, *Earth Planet. Sci. Lett.*, *393*, 275–284.
- Wang, Z.-Z., S.-A. Liu, J. Liu, J. Huang, Y. Xiao, Z.-Y. Chu, X.-M. Zhao, and L. Tang (2017), Zinc isotope fractionation during mantle melting and constraints on the Zn isotope composition of Earth's upper mantle, *Geochim. Cosmochim. Acta*, *198*, 151–167.
- Weyer, S., and D. A. Ionov (2007), Partial melting and melt percolation in the mantle: The message from Fe isotopes, *Earth Planet. Sci. Lett.*, *259*(1), 119–133.
- Weyer, S., and J. B. Schwieters (2003), High precision Fe isotope measurements with high mass resolution MC-ICPMS, *Int. J. Mass Spectrom.*, *226*(3), 355–368.
- Weyer, S., and H. M. Seitz (2012), Coupled lithium and iron isotope fractionation during magmatic differentiation, *Chem. Geol.*, *294*, 42–50.
- Weyer, S., A. D. Anbar, G. P. Brey, C. Münker, K. Mezger, and A. B. Woodland (2005), Iron isotope fractionation during planetary differentiation, *Earth Planet. Sci. Lett.*, *240*(2), 251–264.
- Williams, H. M., and M. Bizimis (2014), Iron isotope tracing of mantle heterogeneity within the source regions of oceanic basalts, *Earth Planet. Sci. Lett.*, *404*, 396–407.
- Williams, H. M., C. A. McCammon, A. H. Peslier, A. N. Halliday, N. Teutsch, S. Levasseur, and J. P. Burg (2004), Iron isotope fractionation and the oxygen fugacity of the mantle, *Science*, *304*(5677), 1656–1659.
- Williams, H. M., A. H. Peslier, C. McCammon, A. N. Halliday, S. Levasseur, N. Teutsch, and J. P. Burg (2005), Systematic iron isotope variations in mantle rocks and minerals: The effects of partial melting and oxygen fugacity, *Earth Planet. Sci. Lett.*, *235*(1), 435–452.
- Williams, H. M., S. G. Nielsen, C. Renac, W. L. Griffin, S. Y. O'Reilly, C. A. McCammon, N. Pearson, F. Viljoen, J. C. Alt, and A. N. Halliday (2009), Fractionation of oxygen and iron isotopes by partial melting processes: Implications for the interpretation of stable isotope signatures in mafic rocks, *Earth Planet. Sci. Lett.*, *283*(1), 156–166.
- Zack, T., and T. John (2007), An evaluation of reactive fluid flow and trace element mobility in subducting slabs, *Chem. Geol.*, *239*(3), 199–216.